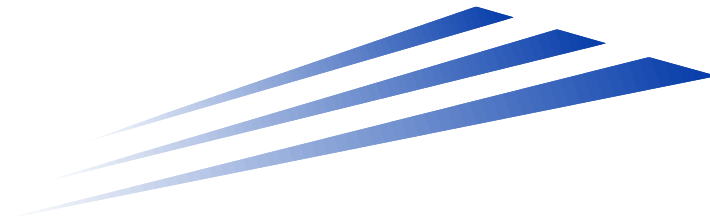


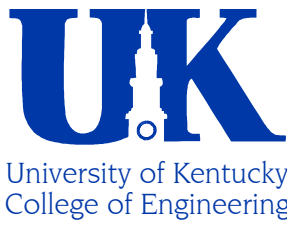
KENTUCKY TRANSPORTATION CENTER

College of Engineering

**GFRP REINFORCED CONCRETE
BRIDGE DECKS**



UNIVERSITY OF KENTUCKY



KENTUCKY TRANSPORTATION CENTER

Our Mission

We provide services to the transportation community through research, technology transfer and education. We create and participate in partnerships to promote safe and effective transportation systems.

We Value...

Teamwork -- Listening and Communicating, Along with Courtesy and Respect for Others
Honesty and Ethical Behavior
Delivering the Highest Quality Products and Services
Continuous Improvement in All That We Do

For more information or a complete publication list, contact us

Kentucky Transportation Center
176 Raymond Building
University of Kentucky
Lexington, Kentucky 40506-0281

(859) 257-4513
(859) 257-1815 (FAX)
1-800-432-0719
www.ktc.uky.edu
ktc@enr.uky.edu

Research Report
KTC-00-9

GFRP REINFORCED CONCRETE BRIDGE DECKS (KYSPR 96-169)

By

David Deitz

Former Research Student, Kentucky Transportation Center

Issam E. Harik

Professor of Civil Engineering and Head, Structures Section,
Kentucky Transportation Center

and

Hans Gesund

Professor of Civil Engineering

Kentucky Transportation Center
College of Engineering, University of Kentucky

in cooperation with

Transportation Cabinet
Commonwealth of Kentucky

and

Federal Highway Administration
U.S. Department of Transportation

The contents of this report reflect the views of the authors who are responsible for the facts and accuracy of the data presented herein. The contents do not necessarily reflect the official views or policies of the University of Kentucky, the Kentucky Transportation Cabinet, nor the Federal Highway Administration. This report does not constitute a standard, specification or regulation. The inclusion of manufacturer names or trade names are for identification purposes and are not to be considered as endorsement.

July 2000

Mr. Jose M. Sepulveda

July
2000

Division Administrator
Federal Highway Administration
330 West Broadway
Frankfort, KY 40602

Subject: - Implementation Statement for Final Report entitled "GFRP
Reinforced Concrete Bridge Decks"
- Study number: KYSPR 96-169
- Study title: Innovative Solution to Corrosion Related
Degradation of
Kentucky's Decks

Dear Mr. Sepulveda:

This study was conducted to investigate the feasibility of using glass fiber reinforced polymer (GFRP) rebars as reinforcement in concrete bridge decks. The objective set forth has been achieved by conducting series of experiments in the Structural Engineering Laboratory at the University of Kentucky.

Several recommendations are proposed for construction and repair of bridge decks reinforced with GFRP rebars. Modifications are suggested to improve existing theoretical expressions for predicting ultimate shear strength and maximum crack width for bridge decks. The behavior of bridge deck overhangs during vehicle-barrier wall impact was experimentally investigated. Results of the testing showed that GFRP rebars can be used to reinforce concrete bridge decks.

Sincerely,

J. M. Yowell, P.E.
State Highway Engineer

cc: John Carr

Technical Report Documentation Page

1. Report No. KTC-00-9		2. Government Accession No.		3. Recipient's Catalog No.	
4. Title and Subtitle GFRP REINFORCED CONCRETE BRIDGES (KYSPR 96-169)				5. Report Date July 2000	
				6. Performing Organization Code	
7. Author(s): David Deitz, Issam Harik, and Hans Gesund				8. Performing Organization Report No. KTC-00-9	
9. Performing Organization Name and Address Kentucky Transportation Center College of Engineering University of Kentucky Lexington, Kentucky 40506-0281				10. Work Unit No. (TRAIS)	
				11. Contract or Grant No. KYSPR 96-169	
				13. Type of Report and Period Covered Final	
12. Sponsoring Agency Name and Address Kentucky Transportation Cabinet State Office Building Frankfort, Kentucky 40622				14. Sponsoring Agency Code	
15. Supplementary Notes Prepared in cooperation with the Kentucky Transportation Cabinet and the U.S. Department of Transportation, Federal Highway Administration.					
16. Abstract <p>This report investigates the application of glass fiber reinforced polymer (GFRP) rebars in concrete bridge decks as a potential replacement or supplement to conventional steel rebars. Tests were conducted to determine the material properties of the GFRP reinforcement, and experiments were performed to study aspects of GFRP rebar placement in actual bridge decks. These included observation of GFRP rebar handling characteristics and worker response during construction. Load tests of full-scale reinforced concrete specimens were conducted to evaluate the characteristics of three reinforcing schemes: (1) an epoxy coated steel (ECS) reinforcing scheme; (2) a GFRP reinforcing scheme, and (3) a Hybrid reinforcing scheme combining GFRP and ECS rebars.</p> <p>Results of the investigation showed that the moduli of elasticity in tension and compression for the GFRP rebars were approximately the same, but the ultimate strength in compression was 50% of the ultimate strength in tension. Several recommendations were made for construction and repair procedures for decks reinforced with GFRP rebars. Modifications are suggested to existing theoretical expressions for predicting ultimate shear strength and maximum crack width of GFRP reinforced concrete members.</p> <p>The results of this study show that bridge decks reinforced with GFRP rebars satisfy the AASHTO specifications for strength. AASHTO's crack width requirements were not satisfied.</p>					
17. Key Words Glass Fiber Reinforced Polymer, Epoxy Coated Steel, Corrosion, Ultimate shear strength, Crack Width, Barrier wall			18. Distribution Statement Unlimited with approval of Kentucky Transportation Cabinet		
19. Security Classif. (of this report) Unclassified		20. Security Classif. (of this page) Unclassified		21. No. of Pages 183	22. Price

TABLE OF CONTENTS

LIST OF TABLES	vi
LIST OF FIGURES	viii
EXECUTIVE SUMMARY	xiv
ACKNOWLEDGEMENTS	xvii
1.0 INTRODUCTION	
1.1 BACKGROUND	1
1.1.1 The Electrochemical Corrosion Process in Steel Reinforced Concrete	1
1.1.2 Chloride Contamination, Delamination, and Spalling	3
1.2 POTENTIAL SOLUTIONS TO ELECTROCHEMICAL CORROSION	3
1.2.1 Coating of Reinforcing Steel	3
1.2.2 Non-Metallic Fiber Reinforced Polymer Reinforcements	5
1.2.3 Hybrid Reinforcing Scheme	5
1.3 REVIEW OF PREVIOUS RESEARCH	7
1.3.1 Construction with GFRP Rebars	7
1.3.2 Bond of Rebars to Concrete	8
1.3.3 Tensile Properties of GFRP Rebars	8
1.3.4 Compressive Properties of GFRP Rebars	9
1.3.5 Experimental Studies of Concrete Beams Reinforced with GFRP Rebars	9
1.3.6 Design Recommendations for Concrete Members Reinforced with GFRP Rebars	12
1.4 RESEARCH OBJECTIVES	14
1.5 RESEARCH SIGNIFICANCE	14
1.6 CHAPTER OUTLINE	14
2.0 REBAR MATERIAL PROPERTIES	
2.1 INTRODUCTION	16
2.2 MATERIAL PROPERTIES	16
2.3 TENSILE TESTS	18
2.3.1 Ultimate Tensile Strength	18
2.3.2 Tensile Modulus of Elasticity	21
2.4 COMPRESSION TESTING	23
2.4.1 Ultimate Compressive Strength	23
2.4.2 Compressive Modulus of Elasticity of the GFRP Rebars	26
2.4.3 GFRP Rebar Compressive Design Curve	27
2.5 SUMMARY AND CONCLUSIONS	28
3.0 CONSTRUCTABILITY ASSESSMENT	
3.1 INTRODUCTION	30

3.2	DESCRIPTION OF BRIDGE DECKS	33
3.2.1	Mock Bridge Decks	33
3.2.2	Roger's Creek Bridge Deck	33
3.3	FLEXIBILITY	37
3.3.1	Mock Bridge Decks	37
3.3.2	Roger's Creek Bridge Deck	38
3.4	FLOATATION	38
3.5	REBAR DAMAGE DURING CONSTRUCTION	40
3.6	CONTRACTOR/ENGINEER COMMENTS ON THE ROGER'S CREEK BRIDGE DECK	40
3.7	BRIDGE DECK REPAIR	40
3.7.1	Jackhammer	41
3.7.2	Hydro-Demolition	44
3.7.3	Recommended Repair Procedure	46
3.8	CONCLUSIONS AND RECOMMENDATIONS	46
4.0	EXPERIMENTAL DECK PANEL TESTING	
4.1	INTRODUCTION	48
4.2	DECK PANEL SPECIMEN DESCRIPTION	49
4.2.1	Deck Panel Dimensions	49
4.2.2	Reinforcement Patterns	49
4.2.3	Moment Orientations in a Bridge Deck	51
4.2.4	Specimen Labeling	52
4.2.5	Material Properties	53
4.2.6	Preparation of Deck Panel Specimens	55
4.3	DECK PANEL TEST SETUP	55
4.3.1	Test Frame	55
4.3.2	Instrumentation and Measurements Recorded	57
4.3.2.1	Strain Measurements	58
4.3.2.2	Crack Measurements	59
4.4	DECK PANEL LOAD TEST RESULTS	61
4.4.1	Load versus Midspan Displacement	61
4.4.2	Moment versus Maximum Compressive Strain in Concrete	65
4.4.3	Maximum Crack Widths	70
4.5	DECK PANEL LOAD TEST RESULTS (COMPARISON OF DECK PANEL TYPES)	73
4.5.1	Load versus Displacement	73
4.5.2	Moment versus Maximum Compressive Strain in the Concrete	76
4.5.3	Moment versus Maximum Crack Width	78
4.5.4	Average Crack Spacing	80
4.5.5	Crack Patterns	81
4.5.6	Failure Mode	83
4.6	SUMMARY & CONCLUSIONS	84

5.0	DECK PANEL THEORETICAL CORRELATION	
5.1	INTRODUCTION	87
5.2	CONCRETE REINFORCED WITH GFRP VERSUS ECS REBARS	88
5.3	REVIEW OF EXPERIMENTAL PROCEDURE	91
	5.3.1 Deck Panel Geometry	91
	5.3.2 Material Properties	94
	5.3.3 Deck Panel Test Setup	95
	5.3.4 Dead Load Considerations	96
5.4	CORRELATION OF ULTIMATE LOAD WITH CODE PROVISIONS & THEORY	96
	5.4.1 AASHTO Design Load Requirements	97
	5.4.2 Correlation of Experimental Ultimate Load with Theory	100
	5.4.2.1 Flexural failure mode	100
	5.4.2.2 Flexural shear failure mode	101
	5.4.2.3 Proposed shear equation modifications	102
5.5	PREDICTION OF MIDSPAN DISPLACEMENT	104
	5.5.1 AASHTO & ACI Maximum Displacements at Service Load	104
	5.5.2 Moment Curvature Analysis	106
	5.5.3 Theoretical Estimates of Displacement for Deck Panels with ECS Tensile Reinforcement	109
	5.5.4 Theoretical Estimates of Displacement for Deck Panels with GFRP Tension Reinforcement	112
5.6	CRACK WIDTH CORRELATION	115
	5.6.1 AASHTO and ACI Maximum Crack Widths	115
	5.6.2 Theoretical Estimates of Maximum Crack Width for Deck Panels with ECS Tensile Reinforcement	118
	5.6.3 Theoretical Estimates of Maximum Crack Width for Specimens with GFRP Tensile Reinforcement	121
5.7	SUMMARY AND CONCLUSIONS	127

6.0	BARRIER WALL IMPACT SIMULATION	
6.1	INTRODUCTION	129
6.2	BARRIER WALL SPECIMEN DESCRIPTION	130
	6.2.1 Barrier Wall Dimensions	130
	6.2.2 Reinforcement Layout	131
	6.2.3 Specimen Labeling	133
	6.2.4 Material Properties	133
	6.2.5 Test Specimen Preparation	135
6.3	BARRIER WALL TEST SETUP & INSTRUMENTATION	136
6.4	COMPARISON OF BARRIER WALL STIFFNESS	139
	6.4.1 Load versus Displacement at Top of Barrier Wall	139
	6.4.2 Vertical Displacement at Toe of Barrier Wall	142
	6.4.3 Load versus Curvature	146

6.5	FAILURE OF BARRIER WALL SPECIMENS	150
6.5.1	AASHTO Load Requirements	150
6.5.2	Ultimate Strength of Barrier Wall Specimens	150
6.5.3	Failure Mode	151
6.6	SUMMARY AND CONCLUSIONS	155
7.0 CONCLUSIONS, RECOMMENDATIONS, AND FUTURE RESEARCH		
7.1	OBJECTIVES	158
7.2	SUMMARY OF RESEARCH FINDINGS	158
7.2.1	Constructability Assessment	158
7.2.2	Rebar Material Properties	158
7.2.3	Testing of Bridge Deck Panels	159
7.2.3.1	Comparison with AASHTO Specifications	159
7.2.4	Barrier Wall Impact Simulation	160
7.3	RECOMMENDED REINFORCING SCHEME	160
	REFERENCES	161

LIST OF TABLES

TABLE 1.1	DIFFUSION-CRACKING-DETERIORATION MODEL PARAMETERS	7
TABLE 1.2	AVERAGE PROPERTIES FOR #15 GFRP C-BAR REINFORCING RODS TESTED BY BENMOKRANE AND MASMOUDI (1996)	9
TABLE 2.1	PHYSICAL COMPOSITION (WEIGHT %) OF C-BAR GFRP REINFORCING RODS	17
TABLE 2.2	MATERIAL PROPERTIES OF REBARS USED IN STUDY	17
TABLE 2.3	SUMMARY OF TENSILE TEST RESULTS FOR THE GFRP REBARS	20
TABLE 2.4	SUMMARY OF TENSILE TEST RESULTS FOR THE ECS REBARS	20
TABLE 2.5	EXPERIMENTAL MODULUS OF ELASTICITY	23
TABLE 2.6	SUMMARY OF GFRP REBAR COMPRESSION MODULUS OF ELASTICITY	27
TABLE 2.7	SUMMARY OF REBAR PROPERTIES	29
TABLE 3.1	PROPERTIES OF ECS AND GFRP REBARS USED IN THE STUDY	31
TABLE 4.1	SUMMARY OF DECK PANELS TESTED	53
TABLE 4.2	CONCRETE MIX DESIGN	54
TABLE 4.3	CONCRETE CYLINDER COMPRESSION STRENGTHS	54
TABLE 4.4	REBAR PROPERTIES	54
TABLE 4.5	SUMMARY OF DECK PANEL SPECIMENS LOAD VERSUS DISPLACEMENT BEHAVIOR	62
TABLE 4.6	SUMMARY OF MAXIMUM CRACK WIDTH DATA	71
TABLE 4.7	DECK PANEL SPECIMENS LOAD VERSUS DISPLACEMENT BEHAVIOR	75
TABLE 4.8	SUMMARY OF FAILURE MODES	84
TABLE 5.1	DECK PANELS IDENTIFICATION AND PROPERTIES	93
TABLE 5.2	CONCRETE CYLINDER COMPRESSIVE STRENGTH	94
TABLE 5.3	REBAR PROPERTIES	94

TABLE 5.4	RESULTS OF PROPOSED SHEAR EQUATION	103
TABLE 6.1	SUMMARY OF BARRIER WALL SPECIMEN REINFORCEMENT	132
TABLE 6.2	CONCRETE MIX DESIGN	134
TABLE 6.3	CONCRETE CYLINDER COMPRESSION STRENGTHS	134
TABLE 6.4	REBAR PROPERTIES	134
TABLE 6.5	SUMMARY OF FAILURE LOADS OBSERVED	151
TABLE 6.6	SUMMARY TEST RESULTS	157

LIST OF FIGURES

Figure 1.1	Electrochemical Corrosion Circuit	2
Figure 1.2	Typical Bridge Deck Cross Section Showing Deck Reinforcement	6
Figure 2.1	Cross Section of C-BAR Reinforcing Rod Used in Study	18
Figure 2.2	Split Steel Pipe Grips for Tensile Testing of GFRP Rebars	19
Figure 2.3	Steel Pipe Halves Epoxied to the GFRP Rebars during Tensile Tests	20
Figure 2.4	GFRP Tensile Specimen after Failure	21
Figure 2.5	Tensile Stress Strain Properties for the #15 GFRP Rebars	22
Figure 2.6	Tensile Stress Strain Properties of the #16 ECS Rebars	22
Figure 2.7	Apparatus used During the Tests of GFRP Rebars in Compression	24
Figure 2.8	Ultimate Compressive Strength versus Unbraced Length of the GFRP Rebars used in the Study	25
Figure 2.9	Crushing Failure Mode	25
Figure 2.10	Buckling Failure Mode	25
Figure 2.11	Compressive Stress versus Strain Results for the GFRP Rebars	26
Figure 2.12	Proposed Design Ultimate Strengths for #15 GFRP Rebar used in the Study	28
Figure 3.1	Deflection of an ECS Rebar under the Weight of a Construction Worker	31
Figure 3.2	Deflection of a GFRP Rebar under the Weight of the Same Construction Worker	32
Figure 3.3	Two Mock Bridge Decks Constructed as Slabs on Grade (Foreground--ECS Reinforced) (Background--GFRP Reinforced)	32
Figure 3.4	Details of the Mock Bridge Deck Reinforcing Schemes	34
Figure 3.5	Detail of Glass Fiber Reinforced Plastic Reinforcement	35
Figure 3.6	Detail of Epoxy Coated Steel Reinforcement	35
Figure 3.7	Plan View of Bridge Deck Showing Location of the GFRP Rebars	36
Figure 3.8	Photograph of Bridge Deck prior to Concrete Placement Dots were Sketched in to Identify the Location of the GFRP Rebars in the Top Mat	36
Figure 3.9	Photograph showing the Epoxy Coated Steel Runner Chairs supporting GFRP rebar in the Construction of the Roger's Creek Bridge Deck	37
Figure 3.10	Concrete Core Removed from the GFRP Reinforced Mock Bridge Deck	39
Figure 3.11	Measuring to Determine the Vertical Location of the GFRP Rebars in the Mock Bridge Deck (Note: Ruler dimensions are in inches, 1 inch = 25.4 mm)	39

Figure 3.12	Hammering Concrete during Repair Feasibility Study. A GFRP Rebar is Exposed near the Hammer Tip	42
Figure 3.13	Second Hole Hammered into Mock Bridge Deck Reinforced with GFRP Rebars	43
Figure 3.14	Detail of Jackhammer Damage to the GFRP Mock Bridge Deck	43
Figure 3.15	Hole Hammered into Mock Bridge Deck Reinforced with ECS Rebars	44
Figure 3.16	Hydro-Demolition Equipment	45
Figure 3.17	Rebar after being Exposed to the Hydro-Demolition Equipment	45
Figure 4.1	Bridge Deck Cross Section Showing Regions of Interest	48
Figure 4.2	Deck Panel Dimensions	49
Figure 4.3	Deck Panel Cross Sections	50
Figure 4.4	Plan View of Reinforcing Pattern	50
Figure 4.5	Deck Panel Cross Sections	51
Figure 4.6	Moment Orientations in an Actual Bridge Deck	52
Figure 4.7	Stress versus Strain Properties of the Rebars Used	55
Figure 4.8	Deck Panel Load Test Setup	56
Figure 4.9	Deck Panel Load Test Setup	56
Figure 4.10	Instrumentation Locations	57
Figure 4.11	Reusable Strain Gage	59
Figure 4.12	Crack Recording Grid & Measurement Locations	60
Figure 4.13	Crack Comparator used to Measure Crack Widths during the Deck Panel Testing	60
Figure 4.14	Load versus Midspan Displacement for the Negative Moment ECS Reinforced Deck Panels	63
Figure 4.15	Load versus Midspan Displacement for the Positive Moment ECS Reinforced Deck Panels	63
Figure 4.16	Load versus Midspan Displacement for the GFRP Reinforced Panels	64
Figure 4.17	Load versus Midspan Displacement for the Negative Moment Hybrid Reinforced Deck Panels	64
Figure 4.18	Load versus Midspan Displacement for the Positive Moment Hybrid Reinforced Deck Panels	65
Figure 4.19	Moment versus Maximum Compressive Strain in Concrete for the Negative Moment ECS Reinforced Deck Panels	67
Figure 4.20	Moment versus Maximum Compressive Strain in Concrete for the Positive Moment ECS Reinforced Deck Panels	67
Figure 4.21	Moment versus Maximum Compressive Strain in Concrete for the GFRP Reinforced Deck Panel F1	68
Figure 4.22	Moment versus Maximum Compressive Strain in Concrete for the GFRP Reinforced Panels F2 & F3	68
Figure 4.23	Moment versus Maximum Compressive Strain in Concrete for the Negative Moment Hybrid Deck Panels	69

Figure 4.24	Moment versus Maximum Compressive Strain in Concrete for the Positive Moment Hybrid Deck Panels	69
Figure 4.25	Moment versus Crack Width Illustrating Maximum and Average Crack Width Results for Deck Panels EP1 and F2	71
Figure 4.26	Moment versus Maximum Crack Width for the ECS Reinforced Deck Panels	72
Figure 4.27	Moment versus Maximum Crack Width for the GFRP Reinforced Deck Panels	72
Figure 4.28	Moment versus Maximum Crack Width for the Hybrid Reinforced Deck Panels	73
Figure 4.29	Load versus Displacement for Negative Moment Deck Panels	75
Figure 4.30	Load versus Displacement for Positive Moment Deck Panels	76
Figure 4.31	Moment versus Maximum Compressive Strain for the Negative Moment Deck Panels	77
Figure 4.32	Moment versus Maximum Compressive Strain for the Positive Moment Deck Panels	78
Figure 4.33	Moment versus Maximum Crack Width for the Negative Moment Deck Panels	79
Figure 4.34	Moment versus Maximum Crack Width for the Positive Moment Deck Panels	80
Figure 4.35	Average Crack Spacing for Deck Panels at a Moment of 14,200 kN-mm	81
Figure 4.36	Crack Pattern for Deck Panel F2 at Approximately 60% of the Ultimate Load	82
Figure 4.37	Crack Pattern for Deck Panel HP1 at Approximately 60% of the Ultimate Load	82
Figure 4.38	Shear – Diagonal Tension Failure of Deck Panels with GFRP Tensile Reinforcement	84
Figure 4.39	Flexural Failure of Deck Panels with ECS Tensile Reinforcement	84
Figure 5.1	Bridge Superstructure Cross Section	88
Figure 5.2	Qualitative Strain Compatibility for Concrete Reinforced with ECS and GFRP rebars at the Same Applied Moment	89
Figure 5.3	Theoretical Compressive Depth versus Moment for ECS and GFRP Reinforced Concrete Deck Panels	89
Figure 5.4	Shear Resisting Mechanisms in a Reinforced Concrete Deck Panel (Adapted from MacGregor (1992))	90
Figure 5.5	Qualitative Cracked Transformed Sections	91
Figure 5.6	Deck Panel Cross Sections	93
Figure 5.7	Stress versus Strain Properties of the Rebars Used	95
Figure 5.8	Elevation View of Test Setup	95
Figure 5.9	Qualitative Load, Shear, and Bending Moment Diagrams for the Load Test Setup	96

Figure 5.10	Assumed Dead Load Moment versus Actual Dead Load Moment	97
Figure 5.11	Comparison of Experimental Ultimate Moment and AASHTO Service Moment	98
Figure 5.12	Comparison of Experimental Ultimate Moment and AASHTO Factored Moment	99
Figure 5.13	Comparison of Experimental Ultimate Load to Predicted Ultimate Load based on ACI Provisions Flexural Failures	101
Figure 5.14	Summary of Comparisons of Experimental Ultimate Load to Predicted Shear Capacity (Flexural Shear Failures)	104
Figure 5.15	Span Length, L, to Service Live Load Displacement, $D_{LL-Service}$, Ratios of Deck Panels	106
Figure 5.16	Kent Park Model for Concrete in Compression	108
Figure 5.17	Theoretical Moment Curvature for Negative Moment Deck Panels	108
Figure 5.18	Theoretical Moment versus Curvature for Positive Moment Deck Panels	109
Figure 5.19	Comparison of Experimental and Theoretical Load versus Displacement for Deck Panel EM2	111
Figure 5.20	Comparison of Experimental and Theoretical Load versus Displacement for Deck Panel EP1	111
Figure 5.21	Comparison of Experimental and Theoretical Load versus Displacement for Deck Panel HP1	112
Figure 5.22	Comparison of Experimental and Theoretical Load versus Displacement for Deck Panel F2	114
Figure 5.23	Comparison of Experimental and Theoretical Load versus Displacement for Deck Panel HM1	115
Figure 5.24	Ratio of Experimental Crack Width at Service Load to ACI Specified Maximum Crack Width	117
Figure 5.25	Ratio of Experimental Crack Width at Service Load to AASHTO Apparently Intended Maximum Crack Width	118
Figure 5.26	Experimental and Theoretical Maximum Crack Width for Negative Moment ECS Deck Panel EM3	119
Figure 5.27	Experimental and Theoretical Maximum Crack Width for Positive Moment ECS Deck Panel EP1	120
Figure 5.28	Experimental and Theoretical Maximum Crack Width for Positive Moment Hybrid Deck Panel HP1	120
Figure 5.29	Experimental and Theoretical Maximum Crack Width for the GFRP Deck Panel F1 Tested with a Reduced Span Length of 2130 mm	122
Figure 5.30	Experimental and Theoretical Maximum Crack Width for the GFRP Reinforced Deck Panel F2	123
Figure 5.31	Experimental and Theoretical Maximum Crack Width for the Negative Moment Hybrid Deck Panel HM2	123
Figure 5.32	$\frac{f_s(d_c A)^{1/3}}{w}$ versus Maximum Crack Width for Deck Panels with GFRP Tensile Reinforcement	125

Figure 5.33	Experimental and Predicted Maximum Crack Width for the GFRP Reinforced Deck Panel Tested with a Reduced Span of 2130 mm	125
Figure 5.34	Experimental and Predicted Maximum Crack Width for the GFRP Reinforced Deck Panel F2	126
Figure 5.35	Experimental and Predicted Maximum Crack Width for the Negative Moment Hybrid Reinforced Deck Panel HM2	126
Figure 6.1	Typical Bridge Superstructure Cross Section	129
Figure 6.2	Relation of a Test Specimen to an Actual Bridge (Reinforcement details are given in Figure 6.3)	130
Figure 6.3	Barrier Wall Specimen Dimensions	131
Figure 6.4	Cross Section of Barrier Wall Specimen Deck	133
Figure 6.5	Stress versus Strain for ECS and GFRP Rebars (Refer to Chapter 2 for the derivation of these curves)	135
Figure 6.6	Barrier Wall Test Setup	136
Figure 6.7	Barrier Wall Test Setup	137
Figure 6.8	Barrier Wall Test Setup	137
Figure 6.9	Qualitative Shear, Axial, and Moment Diagrams for the Barrier Wall Subjected to Load P	138
Figure 6.10	Illustration of Instrumentation Locations	139
Figure 6.11	Load versus Displacement at Barrier Top, ECS Barriers	140
Figure 6.12	Load versus Displacement at Barrier Top, GFRP Barriers	141
Figure 6.13	Load versus Displacement at Barrier Top, Hybrid Barriers	141
Figure 6.14	Comparison of Load versus Displacement at Barrier Top for the ECS, GFRP, and Hybrid Specimens; BE3, BF2, and BH2 Respectively	142
Figure 6.15	Detail showing Parameters used to compute Vertical Displacement at the Toe of the Barrier	143
Figure 6.16	Load versus Vertical Displacement at Toe of Barrier, ECS Barriers	144
Figure 6.17	Load versus Vertical Displacement at Toe of Barrier, GFRP Barriers (Note: Data for Specimen BF1 were accidentally erased and are not shown)	144
Figure 6.18	Load versus Vertical Displacement at Toe of Barrier, Hybrid Barriers	145
Figure 6.19	Load versus Vertical Displacement at Toe of Barrier for the ECS, GFRP, and Hybrid Specimens; BE3, BF2, and BH2 Respectively	145
Figure 6.20	Detail showing Parameters used to Compute Curvature at Section A-A	147
Figure 6.21	Load versus Curvature of Deck, ECS Barriers	148
Figure 6.22	Load versus Curvature of Deck, GFRP Barriers (Note: Data for Specimen BF1 were accidentally erased and is not shown)	148
Figure 6.23	Load versus Curvature of Deck, Hybrid Barriers	149

Figure 6.24	Load versus Curvature of Deck Top for the ECS, GFRP, and Hybrid Specimens; BE3, BF2, and BH2 Respectively	149
Figure 6.25	Comparison of Experimental Load Ultimate Load and AASHTO Service Design Load	152
Figure 6.26	Comparison of Experimental Ultimate Load and AASHTO Factored Design Load	152
Figure 6.27	Crack Pattern of Anchorage Failure beneath the Barrier Wall	154
Figure 6.28	Crack Pattern of Combined Shear-Tension-Bond Failure	154
Figure 6.29	Crack Pattern of Combined Flexural-Tension Failure	155

EXECUTIVE SUMMARY

The objective of this study is to evaluate the use of glass fiber reinforced polymer (GFRP) rebars in concrete bridge decks. The objective was achieved by conducting the following tasks: (1) Constructability assessment; (2) Laboratory testing of GFRP rebars to determine their material properties; (3) Laboratory testing of concrete deck panels and barrier walls reinforced with GFRP and/or epoxy coated steel to evaluate the behavior and compliancy with the AASHTO and ACI Codes; and (4) Deployment of the GFRP rebars in a portion of the top reinforcing mat in the Roger's Creek deck.

CONSTRUCTABILITY ASSESSMENT

The constructability assessment phase of the research project proved that GFRP rebars can withstand bridge deck construction with very few changes from conventional construction techniques. In addition, results show that GFRP rebar mats can support construction loads.

Recommendations based on the research findings include the use of ECS chairs and plastic coated steel wire ties with GFRP rebars. It is estimated that approximately twice as many ECS chairs will be required to achieve adequate mat stiffness in a GFRP rebar mat.

No floatation of the reinforcing mat was observed during the constructability assessment; however, this problem could be encountered during placement of high slump concrete. To avoid floatation, the GFRP reinforcing mat could be tied to the concrete forms.

In case repairs on a deck are needed (e.g. potholes), the use of a jackhammer was identified as a viable method for removing concrete from a GFRP reinforced bridge deck during repair operations. Hydro-demolition was also considered as a repair procedure but was found to damage the GFRP rebars during the concrete removal process. Therefore, it should not be considered for removal of deteriorated concrete reinforced with GFRP rebars.

REBAR MATERIAL PROPERTIES

Standard methods are not available for determining the compression elastic modulus and compression strength of GFRP rebars. A method was developed to experimentally determine these parameters. Based on the test results of more than 50 GFRP rebar specimens in compression, an ultimate compression strength versus unbraced length design curve is proposed. Test results also show that the compression modulus of elasticity is approximately the same as the tensile modulus of elasticity for

the GFRP rebars used in the study. However, for design, the compression strength of the GFRP rebars should be 50% of the tension strength.

TESTING OF BRIDGE DECK PANELS

Twelve full-scale reinforced concrete deck panels were tested to simulate transverse bridge deck load conditions. Three different reinforcing schemes were evaluated in the study: (1) an ECS reinforcing scheme with a top and bottom mat of ECS rebars, (2) a GFRP reinforcing scheme with a top and bottom mat of GFRP rebars, and (3) a Hybrid reinforcing scheme with a top mat of GFRP rebars and a bottom mat of ECS rebars.

Results show that the ultimate load, load versus displacement at service levels (i.e. prior to yielding), moment versus maximum concrete compression strain, and deck panel failure mode were governed by the type of tensile reinforcement. The type of compression reinforcement had little effect on these parameters. Compression reinforcement did have a limited effect on the ductility of the deck panels with ECS tension reinforcement and the maximum observed crack widths.

Observations show that all twelve deck panels exhibited the same load versus displacement and moment versus strain characteristics prior to cracking. After cracking, the deck panels with ECS tension reinforcement exhibited significantly greater stiffness and smaller crack widths than the deck panels with GFRP tensile reinforcement.

All of the deck panels with ECS tension reinforcement failed in a flexural mode. The failure mode exhibited ductility and provided adequate warning of failure through apparent yielding of the reinforcement. All deck panels with GFRP reinforcement collapsed in a combined flexure and shear failure mode. The failure of these deck panels was ductile, and provided warning of impending collapse with large crack widths and displacements.

COMPARISON WITH AASHTO SPECIFICATIONS

Comparisons of the deck panel results to current AASHTO provisions for bridge deck design show that all of the deck panels met AASHTO guidelines for ultimate load. However, AASHTO specifications are based on under-reinforced concrete specimens with steel reinforcement, failing after yielding of the reinforcing steel. Since GFRP specimens do not exhibit yielding, and in this study failed in shear, it is recommended that specifications be broadened to include a shear failure mode.

ACI-318M-95 design specifications accurately predicted the failure load of the ECS reinforced deck panels, which failed in flexure. However, neither current ACI provisions nor a model developed by other researchers adequately predicted the

combined shear and flexural failure strength of the GFRP reinforced deck panels. Two equations for predicting the shear strength of the specimens are proposed in this study.

Experimental maximum crack widths were compared to theoretical models developed by others, and the result show that these models adequately predicted crack widths for the GFRP reinforced deck panel with a span length of 2130 mm. However, these models did not predict crack widths for the deck panels with the longer span length of 2740 mm. A maximum crack width model based on the results of this study is proposed based on the Gergely-Lutz expression.

BARRIER WALL IMPACT SIMULATION

In addition to the deck panel specimens, nine barrier wall specimens were constructed and tested to evaluate the behavior of concrete bridge deck overhangs with the three different reinforcing schemes discussed in Section 7.1.3. Results show that all of the specimens met AASHTO load specifications. In addition, all of the specimens exhibited a ductile failure type that provided adequate warning of the impending failure. The ECS reinforced specimens exhibited ductility through apparent reinforcement yielding, large displacements, and large crack widths, while the GFRP reinforced deck panels exhibited ductility through large displacements and crack widths.

RECOMMENDED REINFORCING SCHEME

Results of this study show that both the GFRP and Hybrid deck panel reinforcing schemes meet all AASHTO load requirements. Either of these reinforcing schemes can be depended on from a strength standpoint. However, the results also show that the GFRP and Hybrid deck panels did not meet AASHTO requirements for maximum crack widths. In addition, though AASHTO does not specify maximum displacements for concrete bridge decks, the displacements observed for the GFRP and Hybrid deck panels were significantly greater than those of the ECS reinforced deck panels and warrant consideration.

The Hybrid reinforcing scheme is recommended for use in bridge decks even though it did not meet serviceability requirements. This reinforcing scheme provides the dependability of ECS rebars with the corrosion immunity of the GFRP rebars. Since reinforced concrete bridge decks transfer load transversely over main support girders as a continuous beam, ECS rebars in the bottom of the bridge deck will decrease the deflection of the deck under loading observed in this study. In addition, crack width limitations for the top reinforcing mat could be increased for GFRP reinforced deck panels due to their immunity from corrosion.

ACKNOWLEDGMENTS

The financial support for this project was provided by the Kentucky Transportation Cabinet and Federal Highway Administration. The authors would like to acknowledge the cooperation, suggestions, and advice of the members of the study advisory committee: Dale Carpenter (Committee Chair), Steve Criswell, Ray Greer, Donald Herd, Don Miracle. The authors would also like to acknowledge Chris Hill for his support and guidance throughout this study, and Dr. P. Alagusundaramoorthy for his assistance in preparing this report.

The authors would also like to acknowledge the partial support for equipment by the National Science Foundation under grant CMS-9601674-ARI Program.

1.0 INTRODUCTION

1.1 BACKGROUND

A major maintenance expense for many transportation departments is the replacement of bridge decks to repair corrosion induced deterioration. “Chloride-ion-induced corrosion damage of reinforced concrete bridges is the single most costly deterioration mechanism facing state highway agencies in the United States” (Weyers et al., 1993). It is estimated that about 40% of the current backlog of bridge repairs are a direct result of chloride-ion-induced corrosion of steel reinforcement in concrete bridge components (Weyers et al., 1993). Corrosion deterioration of reinforced concrete is brought about by the application of deicing salts to bridge deck to melt ice during winter months. Bridge decks are very susceptible to chloride ion damage because the deicing salts are placed directly on the riding surface.

The most common solution to the corrosion deterioration problem is the use of coated steel reinforcements such as epoxy coated steel (ECS) rebars or galvanized rebars. However, experience has shown that these coatings cannot completely prevent deterioration.

Another potential solution to deterioration of reinforced concrete structures is the use of fiber reinforced polymer (FRP) rebars. In addition to being corrosion resistant, FRP rebars have high strength and high stiffness to weight ratios. The most common FRPs used in structural systems are aramid (AFRP), carbon (CFRP), and glass (GFRP). Of these GFRP has the least initial cost.

1.1.1 The Electrochemical Corrosion Process in Steel Reinforced Concrete

Steel reinforced concrete is an environmentally stable and corrosion resistant material combination. Steel deteriorates quickly when exposed to oxygen and moisture, while well made concrete is stable in most environments. In steel reinforced concrete systems, the concrete protects the steel physically by encasing the steel reinforcement, limiting the amount of oxygen and moisture in direct contact with the steel (Purvis et al., 1994). In addition to protecting the steel by physically encapsulating it, the concrete protects the steel electrochemically.

The corrosion of steel is an electrochemical process, meaning that the chemical reaction proceeds similar to an electric circuit. The electric circuit can be illustrated as shown in Figure 1.1. The anode is the positive side of the circuit where compounds are undergoing chemical reactions. The cathode is the negative side of the circuit, where other reactions are occurring. Exact chemical formulations of these reactions are not discussed herein.

As Figure 1.1 illustrates, the current flows from the anode to the cathode through the steel reinforcement. Then the current flows back from the cathode to the anode through the concrete pore water, completing the electric circuit. Concrete protects the steel electrochemically by forming a very thin passive layer around the reinforcement preventing the flow of electric current through the concrete-rebar circuit. The passive layer is a very thin layer, on the order of 30 angstroms, formed because of the concrete's high alkali content (Fraczek 1987).

While concrete provides good protection for the steel in most environments, it cannot protect the steel reinforcement completely. First, the concrete cannot completely block all oxygen and moisture from reaching the steel reinforcement. Both of these can exist in gaseous form, so even the best concrete cannot prevent the corrosion cycle. Second, the passive layer formed by the concrete can be broken down, defeating the electrochemical protection. Most frequently in cold climates, the passive layer is broken down by the introduction of aggressive chloride ions to the bridge deck in the form of deicing salts. For a more detailed discussion of the steel reinforcement corrosion cycle in concrete refer to Deitz (1995).

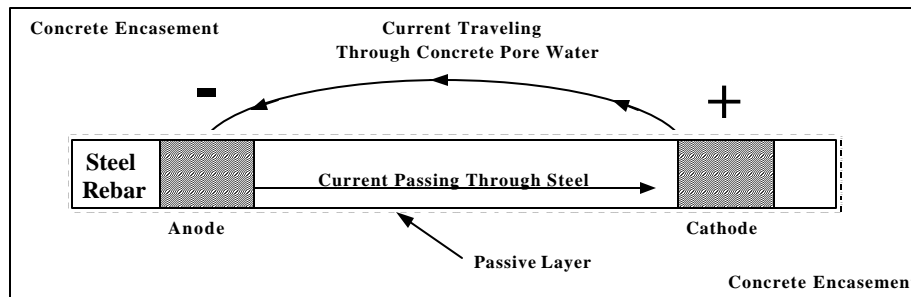


Figure 1. 1: Electrochemical Corrosion Circuit

Before the corrosion process can occur, the free chloride ion concentration must reach a certain level, referred to as the corrosion threshold value typically given as 7.0 N/m^3 or 0.031% of the concrete weight (Weyers et al., 1993). Once the corrosion threshold value is reached the steel can oxidize because the passive layer is broken down. In addition, the chloride ions are recycled in the electrochemical corrosion process. So when the corrosion threshold value is reached, there is no need for additional chloride ions to continue the corrosion process.

In summary, three things are required for the deterioration of steel in reinforced concrete. First, water must be present in some form to allow the electrochemical current to flow allowing the reaction to take place. Second, oxygen is required to react with the steel. Third, chloride ions are needed to break down the protective passive layer of the concrete.

1.1.2 Chloride Contamination, Delamination, and Spalling

Chloride contamination is the driving mechanism for corrosion associated with delamination and spalling. The presence of chlorides breaks down the passive layer allowing the steel reinforcement to corrode. The corrosion products have a much greater volume than the original steel, up to 10 times its volume. The concrete cannot resist the expansive forces generated by the increased volume without cracking and spalling. Cracking of the concrete results in easier access of salt water, hastening deterioration of the bridge deck in the form of delaminations and spalls. A “delamination occurs when layers of concrete separate at or near the level of the top of the outermost layer of reinforcing steel” (Hartle et al., 1990). The delamination need not crack the concrete at the surface, making delaminations difficult to find by visual inspection. Eventually, the delaminated portions of the deck break away from the bridge forming a spall. The spall often appears as “a roughly circular depression in the concrete” (Hartle et al., 1990).

1.2 POTENTIAL SOLUTIONS TO ELECTROCHEMICAL CORROSION

Many passive solutions to the corrosion of steel reinforcement have been developed. One method is to coat the steel reinforcement with a material to prevent the corrosion circuit from developing. Another potential solution that has recently become feasible is the use of non-metallic reinforcement in bridge decks.

1.2.1 Coating of Reinforcing Steel

One of the most widely adopted solutions to steel corrosion problems today is epoxy coated reinforcing steel (ECS), in which steel rebars are coated with a powdered epoxy resin. ECS rebars were thought to be an affordable, simple, solution to the corrosion of steel rebars in concrete until 1987 when the Florida Department of Transportation reported corrosion problems with the use of ECS rebars in marine substructures after only four to seven years of service (Burke 1994). Because of these findings several research projects were implemented to study how long ECS rebars could prevent deterioration of bridge components exposed to chloride environments.

Twelve ECS reinforced bridge deck project sites with service lives ranging from 17 to 19 years were investigated by the West Virginia Department of Transportation Division of Highways (1994). Each bridge deck was inspected including a visual condition survey, a complete delamination survey, and chloride sampling. Results showed that no spalling or measurable reinforcement associated delamination of the decks was observed at the test sites. This can be compared to previous experience on bridge decks containing ordinary rebars where percentages of delamination reached as high as 60% to 80%. This led the investigators to the conclusion that the corrosion process is not occurring or is occurring at a reduced rate due to the use of the ECS reinforcement.

A similar study was performed by the Indiana Department of Transportation and the Federal Highway Administration (Hasan, Ramirez, and Cleary 1995). The field investigation included identification of delaminated and spalled areas, measurements of concrete cover, and concrete powder sampling to determine chloride concentrations at various depths. Six bridges were included, ranging in service life from 6 to 18 years at the time of the study. Observations found that all but two of the bridges had chloride ion contents well above the accepted corrosion threshold value at the level of the reinforcing steel. No sign of disbondment of coating or corrosion was observed in the reinforcement in the bridge decks investigated. It was concluded that epoxy coated steel had performed satisfactorily in the bridge decks surveyed.

Drawbacks to ECS rebars include problems during construction which can lead to nicks and cuts in the epoxy coating leaving portions of the rebars vulnerable to chloride ion induced corrosion. To reestablish the corrosion protection epoxy must be applied in the field, which can take up valuable time during construction. In addition, experimental tests have shown that epoxy coating significantly reduces bond strength of rebars (Treece and Jirsa 1989). Results showed that the development length of epoxy coated rebars should be increased by 15% when adequate rebar cover and spacing are available and by 50% in other cases compared with uncoated rebars.

Another potential solution to the corrosion of steel reinforcement is zinc coated rebars, or galvanized rebars. This option is not as prevalent as ECS rebars, but has occasionally been used. To prepare galvanized reinforcement, rebars are cleaned thoroughly and dipped into a molten zinc bath. The zinc offers sacrificial protection of the steel by acting as anode in place of the base steel. That is, the zinc coating will deteriorate prior to deterioration of the steel (Galvanized Rebar Advisory Board 1995). Another advantage of the galvanized coating is that if the coating is scratched or cut, the zinc sacrificial protection will still act to prevent corrosion of the steel rebar. The biggest disadvantage of this alternative is galvanized rebars lack of availability.

Copper-clad reinforcing bars have also been studied as a solution to the deterioration of steel reinforcement in aggressive environments. This alternative has never been applied in the field and the rebars are not commercially available (McDonald, Virmani, and Pfeifer 1996). McDonald et al. (1996) performed tests on slabs reinforced with copper-clad rebars and black steel rebars over a thirteen year period of outdoor exposure. Results showed that that after the exposure period the copper-clad rebars were far more corrosion resistant than the black bars.

1.2.2 Non-Metallic Fiber Reinforced Polymer Reinforcements

Another solution to the deterioration of steel in concrete bridge decks is to remove all reinforcing steel from the deck and use non-metallic fiber reinforced polymer (FRP) reinforcement. FRP rebars are available in different forms, possessing different mechanical properties, including carbon fiber reinforced polymer (CFRP) rebars, aramid fiber reinforced polymer (AFRP) rebars, and glass fiber reinforced polymer (GFRP) rebars. Due economic considerations, GFRP rebars are the predominant choice of reinforcement for structural applications to date and were used in this study. Other types of FRP may become more promising if material prices continue to fall.

Advantages of GFRP rebars include high strength to weight ratio, light weight (facilitating construction), and resistance to chemical attack. Disadvantages of GFRP rebars include, low elastic modulus, and no ductility. In addition, engineers are unfamiliar with the GFRP rebars compared to steel rebars that have been in use for many years making them familiar and reliable.

GFRP rebars are resistant to the electrochemical process that deteriorates steel rebars in concrete bridge decks. Since they will not deteriorate, problems associated with corrosion of steel rebars will not be encountered, increasing the time between costly bridge deck repairs thereby increasing the overall service life of the bridge deck.

1.2.3 Hybrid Reinforcing Scheme

A combination of reinforcement types, hybrid reinforcements, could provide another promising solution to the deterioration of concrete bridge decks. This study explores one possible Hybrid reinforcing scheme made up of GFRP rebars and ECS rebars. Figure 1.2 shows a cross section of a typical Kentucky bridge containing a top and bottom reinforcing mat. The proposed hybrid bridge deck reinforcing layout would consist of a top mat of GFRP rebars and a bottom mat of ECS rebars. This combination would provide advantages inherent in both materials. The corrosion resistance of GFRP rebars and the familiarity and ductility of ECS rebars.

Since the top mat of reinforcement in the Hybrid reinforcing scheme consists of GFRP rebars that are chemically inert, the aggressive chloride ions have to travel farther to reach the steel reinforcement. This would increase the service life of the bridge deck considerably. In order to investigate the increase in life span brought about by the use of the Hybrid reinforcing scheme, the Diffusion-Cracking-Deterioration Model presented in SHRP-360 (Weyers et al., 1993) was used.

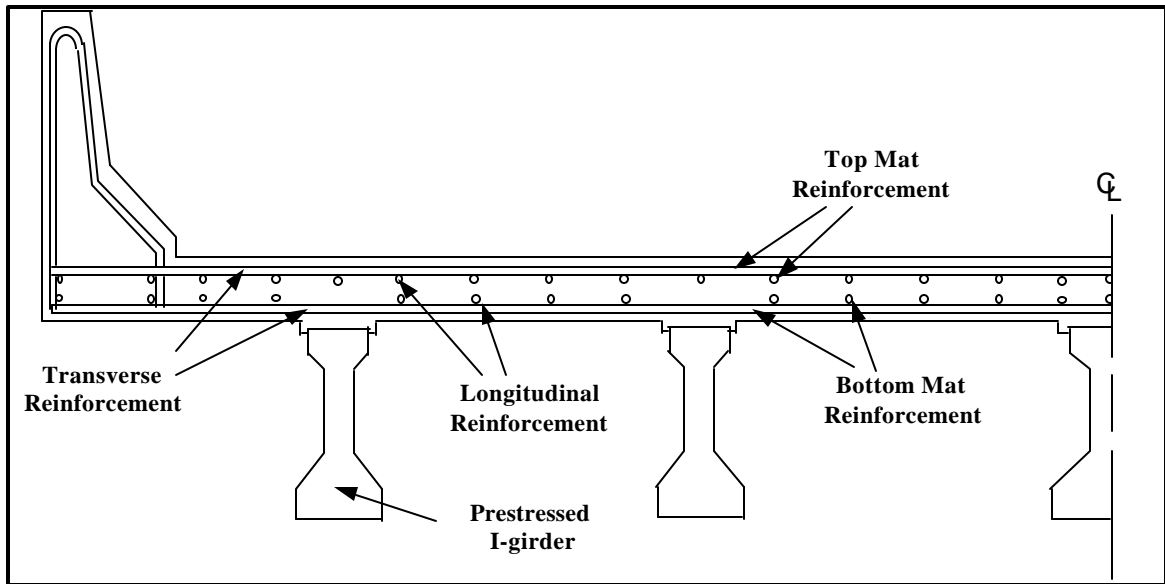


Figure 1. 2: Typical Bridge Deck Cross Section Showing Deck Reinforcement

The model is based on the standard solution to Fick's Second Law for diffusion through a porous medium, as follows:

$$C_{(x,t)} = C_o \left(1 - \operatorname{erf} \frac{X}{2\sqrt{D_c t}} \right) \quad (1.1)$$

where,

- $C_{(x,t)}$ = chloride concentration at depth X after time t for an equilibrium concentration C_o at the surface (based on salt exposure)
- erf = error function (from standard mathematical tables)
- D_c = chloride diffusion constant (based on regional climatic conditions, and concrete properties)

SHRP-360 provides values for the above coefficients for several states. The model was used to predict the time required for chloride ions at the top level of steel reinforcement to reach the corrosion threshold level (see Section 1.1.1) for the ECS and Hybrid reinforcing schemes. Specific values of the coefficients used in the model were not provided for Kentucky. Therefore, values were estimated by using an average of the values for the adjacent states of West Virginia and Indiana, D_c equal to $0.45 \text{ cm}^2/\text{year}$ and $0.58 \text{ cm}^2/\text{year}$ respectively. Coefficients used in the computations, and results, are provided in Table 1.1.

For the conventional ECS reinforced bridge deck, the chloride ions must permeate through the concrete a depth of 60 mm (the top mat clear cover) to reach the rebars. The model estimated that it would take approximately 4.1 years for the chloride ion concentration to reach the threshold level at this depth. In the case of the Hybrid reinforced deck, the chlorides ions must permeate through the deck a depth of 145 mm

(distance from the deck surface to the top of the bottom mat). The model estimated it would require 23.3 years for the ion concentration to reach the threshold value and begin corroding the reinforcement in the Hybrid reinforced deck.

The model does not account for the presence of the coating on the ECS rebars. Results of the model estimated how long it would take for the chloride ion concentration at the level of the rebars to reach the corrosion threshold level, allowing active corrosion of the reinforcement to take place. If the ECS rebars are well coated, with no imperfections, corrosion of the steel may never occur. However, if imperfections exist in the epoxy coating, corrosion of the steel could readily occur if the corrosion threshold value has been reached.

TABLE 1.1 DIFFUSION-CRACKING-DETERIORATION MODEL PARAMETERS

Reinforcing Scheme	X (mm)	Time Until the Chloride Ion Concentration Reaches the Corrosion Threshold Value (years)
ECS	60	4.1
Hybrid	145	23.3
Coefficients Used: $D_c = 52 \text{ mm}^2/\text{year}$ $C_o = 52 \text{ N/m}^3$ Corrosion Threshold Value = 7.0 N/m^3		

1.3 REVIEW OF PREVIOUS RESEARCH

1.3.1 Construction with GFRP Rebars

Research performed by Thippeswamy, Franco, and GangaRao (1998) led to the construction of a bridge deck reinforced with GFRP rebars. The bridge was a 54 m long three span continuous steel girder bridge. During the construction of the bridge the GFRP rebars were found to be light weight and easy to handle. However, construction workers stated that the edges of the rebars were sharp resulting in numerous cuts during construction. Consequently, it was recommended that leather gloves be used while handling the GFRP rebars. Reinforcing chair supports were spaced at approximately 1.2 m during construction to decrease displacements of the GFRP rebars under construction loads. In addition, the reinforcing mat was tied to the forms during construction to prevent movement of the reinforcement while vibrating etc.

1.3.2 Bond of Rebars to Concrete

Cosena et. al., (1997) identify two bond mechanisms for GFRP rebars, friction-resistant and bearing-resistance (mechanical interlock). Friction-resistant mechanisms are predominant in smooth and sand coated GFRP rebars while the bearing-resistant mechanisms is available for deformed rebars including glued on spirals, twisted fiber strands, and rib and indented rebars. Results from the research study showed that the bond of smooth FRP rebars is inadequate for use as concrete reinforcement. Sand covered continuous fiber rebars showed good bond resistance. However, the adhesion between the sand grains and the bars can fail abruptly, leading to a brittle bond failure.

The report also stated that deformations obtained by gluing a spiral to the FRP rebar do not improve the bond behavior over that of the smooth rebars, making them inadequate as concrete reinforcement, also. Rebars manufactured by twisting strands of fibers show slightly larger bond strengths compared to those of smooth rebars. Good bond performance is obtained by use of both indented and deformed GFRP rebars. Although the maximum bond strengths of the GFRP rebars were similar to those of uncoated deformed steel bars, the free end slips of the GFRP type reinforcement, at the same bond stresses, were greater than those of steel bars. The best performance in terms of bond stiffness was found with GFRP rebars with a deformed surface and coated with sand. However, the bond failures for these rebar types were brittle.

1.3.3 Tensile Properties of GFRP Rebars

One of the greatest difficulties in determining the tensile properties of GFRP rebars is proper gripping of the rebars during testing. Since GFRP rebars have little resistance to transverse compressive forces occurring in grip regions during tests, rebars tend to rupture inside the grips. Test results can only be considered valid if the rebar specimen ruptures away from the mechanical grips. Several methods have been proposed to prevent transverse crushing of the rebars inside of the grips during testing. The method selected for this study was developed at the Constructed Facilities Center at the University of West Virginia (Kumar 1996). The method involves the use of a split steel pipe to distribute the load to the GFRP rebar.

Tensile tests on the particular GFRP rebars used in this study were performed by Benmokrane and Masmoudi (1996) at the University of Sherbrooke. Steel barrel and wedge grips were used in the testing. Test results identified the ultimate tensile strength, modulus of elasticity, ultimate tensile strain, Poisson's ratio, and failure mode, and are summarized in Table 1.2. Tests also showed that the rebars exhibit a linear stress strain behavior up until failure.

TABLE 1.2 AVERAGE PROPERTIES FOR #15 GFRP C-BAR REINFORCING RODS TESTED BY BENMOKRANE AND MASMOUDI (1996)

	Ultimate Tensile Strength (MPa)	Young's Modulus ^a (MPa)	Calculated Failure Strain (%)	Poisson's Ratio
Average	773.32 ^b	37.65 ^b	2.05 ^b	0.27 ^c
Std. Dev.	52.58	1.13	0.13	0.01
^a Derived from Strain Gage Measurements ^b Average of seven specimens ^c Average of three specimens				

1.3.4 Compressive Properties of GFRP Rebars

Few research studies have been performed to determine the compressive properties of FRP rebars. Kobayashi and Fujisaki (1995) performed tests to determine the compressive properties of several different types of FRP rebars including carbon, aramid, and glass. Ends of the test specimens were cast in concrete block grips. The study found that the GFRP reinforcing rods used in the study had a compression strength equal to approximately 30% of their tensile strength. In addition, GFRP reinforcing rods were affected by cyclic loading. A 20% to 50% reduction in the compressive capacity of the reinforcing rods was observed under repeated loading.

1.3.5 Experimental Studies of Concrete Beams Reinforced with GFRP Rebars

Bank, Frostig, and Shapira (1997) studied the behavior of concrete beams with a three dimensional GFRP reinforcing grid under flexural loading. The specimens had a depth of 300 mm, width of 200 mm, and span length of 2400 mm with 600 mm between active load points. Reinforcing ratios of the specimens tested ranged from 0.7% to 2.1%. The specimens were tested under a four point loading and exhibited a linear load-displacement relationship up to failure. No significant strength loss or deflection increase were observed during repeated loading, and the specimens failed in a brittle mode by rupture of the tension reinforcement.

To avoid the sudden brittle failure resulting from the tensile rupturing of GFRP reinforcement, Alsayed et al., (1995) tested over-reinforced specimens. Over-reinforcement of the section took advantage of the ductility inherent in concrete itself to produce reserve capacity after reaching ultimate load. Three specimen types were tested under a four point loading with 200 mm between active load points. Steel stirrups were provided at a 120 mm spacing, which is greater than the ACI code maximum of $d/2$ for most specimens. The specimens had widths of 200 mm, heights ranging from 210 mm to 260 mm, and a span length of 2700 mm. Specimens failed as over-reinforced concrete specimens, by concrete compressive rupture. The specimens did possess reserve capacity

after reaching ultimate load. However, the post-ultimate capacity was less than the ultimate load.

An experimental study by Benmokrane, Chaallal, and Masmoudi (1996) compared concrete beams reinforced with FRP rebars and beams reinforced with identical arrangements of steel reinforcing rods. The beams used in the study had depths of 300 mm and 550 mm with reinforcing ratios of 1.102% and 0.562% respectively. All of the beams tested had a width of 200 mm and a span length of 3300 mm under four point loading with 1000 mm between active load points. Steel stirrups to resist shear were provided at a spacing of 100 mm for the beams tested. Results showed that the average crack spacing was similar for beams reinforced with GFRP and steel longitudinal reinforcement under low loading (25% of ultimate). However, at moderate and high loadings, the spacing on average for the GFRP reinforced beams was about 65% that of the steel beams. A compression failure mode was observed in all of the over-reinforced specimens. Tension failure of the GFRP and yielding of the steel was observed in the under-reinforced specimens. The GFRP reinforced beams exhibited a linear load displacement relationship after cracking up to failure. Finally, the experimental strain data showed “the (GFRP) tension reinforcement behaved in a similar manner as in a tension test, implying a perfect bond between the reinforcing bar and the concrete” (Benmokrane, Chaallal, and Masmoudi (1996)).

Brown and Bartholomew (1996) performed studies on long-term deflections of GFRP reinforced concrete beams under sustained loading. Both steel and GFRP reinforced specimens with identical reinforcement schemes were used in the study. Test beams were 150 mm deep, 100 mm wide, and reinforced with 2 #10 (metric) rebars. The beams were tested with 1830 mm span length under a four point loading with 305 mm between load points. Test results showed that the initial deflections under service load of the GFRP reinforced specimens averaged 3.76 times higher those of the steel reinforced specimens. The study concluded that the long-term deflections of the beams could be predicted using modified techniques for predicting long-term deflections of steel reinforced specimens.

Experimental tests were performed by Faza and GangaRao (1991) on 305 mm deep by 150 mm wide beams reinforced with different reinforcing ratios and reinforcement types. The beams were tested under a 2750 mm span four point loading. All of the specimens contained shear stirrups. The types of reinforcement used in the study included smooth, sand coated, and deformed GFRP rebars and stirrups as well as conventional deformed steel rebars and stirrups. Results showed that cracks in the GFRP reinforced specimens tested initiated suddenly and were larger than corresponded cracks in steel reinforced beams. Flexural cracks were found to occur at uniform intervals giving “clear indication that there was no bond failure between the deformed FRP rebars and concrete” (Faza and GangaRao 1991). Bond failure of smooth GFRP rebars and stirrups was observed during testing that was not encountered during the testing of deformed GFRP stirrups. For this reason, the authors advised against the use of smooth GFRP rebars and stirrups.

Masmoudi, Benmokrane, and Chaallal (1996) studied cracking behavior of concrete beams reinforced with FRP rebars. Four point load tests were performed on beams with a 3300 mm span with 500 mm between active load points. The specimen cross sections were 300 mm deep and 200 mm wide with reinforcement ratios ranging from 0.50% to 1.07%. Stirrups were provided in the specimens at an 80 mm spacing. Results showed that as the reinforcement ratio increased the number of cracks increased while their spacing decreased. Results also showed that as the reinforcement ratio increased crack width decreased.

Therault and Benmokrane (1998) tested six concrete beams reinforced with GFRP rebars. Specimens were 180 mm high, 130 mm wide, and 1800 mm long. They were tested under equally spaced four point loads with a 1500 mm span length. Smooth steel stirrups were provided at an 80 mm spacing in all specimens. Two reinforcing ratios were used in the study, 1.16% and 2.77%. Results showed that the effects of concrete strength and reinforcement ratio on the crack spacing were negligible. In addition, the crack width was found to be independent of concrete strength and decreased as the reinforcing ratio increased. Under cyclic loading the beams exhibited increasing crack width but no reduction in flexural stiffness. Finally, increases in concrete strength were found to have no effect on the overall stiffness of a concrete beam, while increasing the reinforcing ratio increased the stiffness significantly.

In an experimental study by Masmoudi, Therault, and Benmokrane (1996) eight concrete beams reinforced with GFRP rebars were tested along with two steel reinforced beams. The beams were tested with a 3300 mm span length with 500 mm between active load points and steel stirrups spaced at 80 mm throughout the shear spans. The beams had cross sections 200 mm wide and 300 mm deep. Reinforcing ratios for the GFRP reinforced specimens ranged between 0.56% to 2.15% while the reinforcing ratios for the steel specimens were between 0.42% and 2.00%. Results showed that the maximum observed crack widths in beams reinforced with GFRP rebars were three to five times those of identical beams with steel rebars.

1.3.6 Design Recommendations for Concrete Members Reinforced with GFRP Rebars

Results from experimental tests performed by GangaRao and Faza (1991) on GFRP reinforced concrete beams were used to derive theoretical relations for predicting flexural strength of GFRP reinforced concrete members, flexural crack widths, deflections, bond strength, and development lengths of the rebars in concrete. The authors found that the flexural strength of GFRP reinforced concrete beams could be adequately predicted using the ACI Ultimate Strength Design relations with an effective yield stress of the rebars. The effective yield stress was recommended to be 85% of the ultimate rebar strength in tension. Conclusions from comparisons of experimental results of the study to theoretical predictions of crack widths found that a modified Watstein and Bresler relationship best agreed with the experimental results. The modification took into account the reduced modulus of elasticity of GFRP rebars. Finally, a modified moment of inertia was derived to predict deflections of GFRP reinforced concrete specimens under load.

Nanni (1994) provided flexural design recommendations for concrete specimens reinforced with GFRP rebars. His recommendations included:

Ultimate Strength Design Method:

A strength reduction factor for flexure, N , should be taken as 0.7 since no yield plateau is obtainable in GFRP reinforced members.

No upper limit on reinforcing ratio should be specified, allowing designers to take advantage of the relatively more ductile concrete compressive failure compared to the brittle GFRP reinforcement tensile failure.

Deflection under service loads should always be considered a design parameter.

Working Stress Design Method:

This design methodology could be more practical at this stage of GFRP reinforced concrete development. It is recommended that this design methodology be used in place of Ultimate Strength Design.

The recommended allowable compressive stress for the concrete was $0.45f'_c$, where f'_c is the compressive strength of the concrete.

The recommended allowable tensile stress in GFRP reinforcement was $0.45f_{tu}$, where f_{tu} is the ultimate tensile strength of the GFRP reinforcement. "Based on available data on stress rupture (static fatigue) of GFRP, this coefficient appears to be appropriate for design life up to 100 years."

It was also recommended that GFRP reinforcement be used with high strength concrete because the strength of a GFRP reinforced concrete member is sensitive to the concrete strength.

Michaluk (1996) tested one way slabs under equally spaced four point loadings with a span length of 3000 mm. The slabs had a width of 1000 mm and depths varying between 150 mm and 200 mm. Transverse reinforcement was included in the specimens with longitudinal reinforcing ratios 0.23% to 0.955% for the GFRP reinforced specimens tested. Results showed that the shear strength predictions of current code equations significantly overestimated the shear capacity of the specimens tested. The author recommended the modification of the existing ACI equations by the ratio of the elastic moduli of GFRP and steel reinforcements, $E_{\text{GFRP}}/E_{\text{STEEL}}$.

Benmokrane, Chaallal, and Masmoudi (1996) found that ultimate moments of the beams used in their experimental study could accurately be predicted using ACI Ultimate Strength Design assumptions. They recommend a strength reduction factor for flexure, ϕ , of 0.75 for GFRP reinforced concrete specimens. The study also found that the expression developed by Branson adopted by the ACI code for estimating deflections, overestimates the effective moment of inertia for beams with GFRP reinforcement. The authors recommended modification of the Branson expression using a cracking moment reduction factor to correlate with the experimental findings of the study.

Research on cracking behavior performed by Masmoudi, Benmokrane, and Chaallal (1996) determined that crack widths could be predicted for GFRP reinforced concrete specimens using modified Gergley-Lutz and European code equations. However, for every new product introduced to the market experimental studies would be required to determine modification coefficients for the equations. The cracking moment relation provided in ACI could adequately predict cracking moment of GFRP reinforced sections with no modifications.

Research by Theriault and Benmokrane (1998) found that the modified Gergley-Lutz relation developed by Masmoudi, Benmokrane, and Chaallal (1996) accurately predicted the crack widths observed in their experimental research program. In addition, they found that the model developed by Faza and GangaRao (1991) best predicted the load-displacement behavior of the GFRP reinforced concrete specimens used in the study after calibrating the relationship for the actual deflections observed at cracking.

Masmoudi, Theriault, and Benmokrane (1996) concluded that the limitation of crack widths specified by the ACI code and Canadian code for structures reinforced with conventional steel should not apply to structures with GFRP reinforcement. There are no corrosion problems in GFRP reinforced concrete specimens. Therefore, the limiting crack width should be controlled by aesthetic requirements.

1.4 RESEARCH OBJECTIVES

The objectives of this research are two fold. First, to determine if GFRP rebars are a viable alternative to ECS rebars as bridge deck reinforcement. Second, to compare the experimental results of the study to theoretical predictions of GFRP reinforced concrete behavior. In situations where theoretical predictions are found to be inadequate, new theories or suggestions for modifications of existing theories will be provided.

1.5 RESEARCH SIGNIFICANCE

Though many experimental studies have been performed on GFRP reinforced concrete members, the design information available to engineers is limited compared to more conventional materials such as steel reinforced concrete, wood, and structural steel. Results of this study will serve to increase design information available to engineers in the form of equations for predicting GFRP reinforced concrete behavior. The experimental results will also serve to increase the amount of test data available to research institutions developing guidelines for GFRP reinforced concrete.

In addition, there have been relatively few field applications of GFRP rebars in concrete bridge decks. Construction observations made during the study will be directly applicable to the implementation of GFRP reinforced concrete bridge decks.

1.6 CHAPTER OUTLINE

Chapter 1 of this report provides a background to the bridge deck reinforcement corrosion problem and potential solutions including a summary of related research projects. Chapter 2 summarizes the material properties of the rebar types used in the study including ECS and GFRP rebars. An experimental study was conducted to determine tensile properties of the rebars. A test method developed to determine compressive properties of GFRP rebars is also discussed in detail.

In Chapter 3, constructability testing of GFRP reinforced concrete is discussed. A summary of the test method used and results of the study are provided. In addition to testing the behavior of the GFRP rebars during construction, various repair procedures for concrete reinforced with GFRP rebars were tested and results are presented.

Chapter 4 provides a summary of the experimental strength testing of twelve full scale reinforced concrete deck panels. The deck panels tested were reinforced with GFRP, ECS and the Hybrid reinforcing layouts discussed in Section 1.2. Results of the study are discussed and comparisons are made between the different reinforcement schemes. Chapter 5 presents comparisons of the deck panel test results and current analytical models and code provisions. New analytical models and recommendations for improvement of current models for shear strength and crack widths are proposed.

Chapter 6 discusses the simulated barrier wall impact study. Summaries of the experimental test methods and assumptions, as well as test results are provided. Results included comparison of the experimental results to current AASHTO code specifications for the design of barrier wall overhangs. Finally, Chapter 7 summarizes important results of the study and provides recommendations for future research.

2.0 REBAR MATERIAL PROPERTIES

2.1 INTRODUCTION

This chapter identifies structural properties of the GFRP and ECS rebars used in the study. Descriptions of the experimental methods used to determine the tensile properties of the ECS and GFRP rebars and the compressive properties of the GFRP rebars are presented.

Currently, no ASTM standard test methods exist for testing of GFRP rebars in tension or compression. Several test methods have been developed for tensile testing by researchers such as Nanni, GangaRao and Faza, Erci and Rizkalla (Castro and Carino (1998)). However, little work has been done to characterize the properties of GFRP rebars in compression. This is largely due to the fact that the effect of the GFRP in compression rebars is ignored during design of reinforced concrete members.

In bridge decks, some reinforcement is in compression in both the transverse and longitudinal directions of the bridge slab. To perform a refined analytical study of bridge decks compressive properties of GFRP rebars are required.

In this chapter, specific tensile and compressive properties of the ECS and GFRP rebars are determined from the lots of the reinforcement used in this study to conduct comparisons between experimental and analytical results. An apparatus and method for testing of GFRP rebars in compression was developed. A proposed GFRP rebar compression design curve was developed from the compression test results.

2.2 MATERIAL PROPERTIES

Grade B C-BAR reinforcing rods produced by Marshall Industries were selected for the GFRP reinforcement in this study. The Physical composition of the rebars is provided in Table 2.1. These materials integrate into rebars with the physical characteristics shown in Table 2.2 which also gives the properties of the epoxy coated steel rebars used in the study.

Cross sectional design of the rebars is illustrated in Figure 2.1. An article published by Loud in 1995 outlines the rebar manufacturing process consisting of three process stages. In the first process stage, the E-glass fiber rovings used in the rebar pass through a typical pultrusion process, the fibers are passed through a wet out station and shaped with forming guides. Next, a circumferential winding is added in the form of helical fiberglass wraps oriented at approximately +/- 45 degree angles to the core fibers, as illustrated in Figure 2.1.

In process stage two, a sheet molded compound is added to define the irregular cross sectional shape of the rebars, a deformation pattern similar to typical steel rebars.

The semicured rod is passed through a compression molding system that applies two sheet molded compounds to the rod resulting in the final rebar product. In the third process stage, a printer applies a lot code to the rebars and they are cut to the desired length. The rebars are then off loaded to a banding table and packaged for shipping.

TABLE 2.1 PHYSICAL COMPOSITION (WEIGHT %) OF C-BAR GFRP REINFORCING RODS

(Adapted from Standard Specifications for C-BAR Reinforcing Rod for Concrete Reinforcement)

Reinforcing Fiber	Urethane Modified Vinyl Ester	Recycled P.E.T.	Ceramic Reinforcement	Corrosion Inhibitor
70%	15%	10%	3.5%	1.5%

TABLE 2.2 MATERIAL PROPERTIES OF REBARS USED IN STUDY (C-BAR Reinforcing Rod Properties Provided by Manufacturer ECS Rebar Properties from CSRI Interim Specifications)

	#15 C-BAR GFRP Rebar	#16 Epoxy Coated Steel Rebar
Cross Section Diameter	15 mm	16 mm
Area of Reinforcement	176 mm ²	199 mm ²
Mass	0.37 kg/m	1.552 kg/m
Water Absorption	0.25% maximum	N. A.
Ultimate Tensile Strength	713 MPa	620 MPa
Yield Strength	N. A.	420 MPa
Modulus of Elasticity	42,000 MPa	200,000 MPa

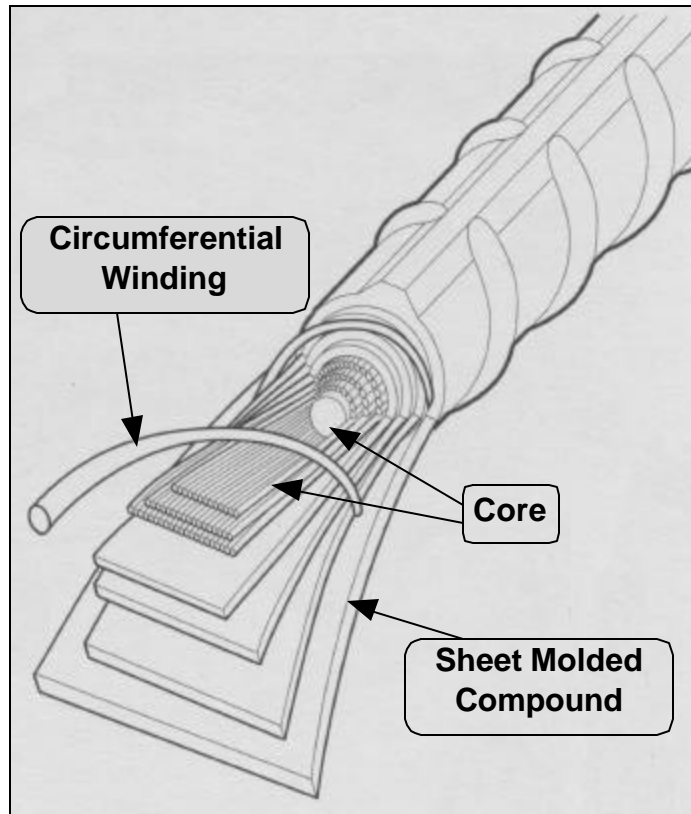


**Figure 2.1: Cross Section of C-BAR Reinforcing Rod Used in Study
(Adapted from a Marshall Industries Publication)**

2.3 TENSILE TESTS

Tensile tests were conducted on both GFRP and ECS rebar samples taken from the lots used in the reinforced concrete specimens discussed in Chapters 4, 5 and 6 to determine specific tensile properties. Tests to measure ultimate tensile strength, yield strength of the ECS rebars, and Young's modulus were conducted on the full section rebar specimens.

2.3.1 Ultimate Tensile Strength

Ultimate strength of the GFRP rebars was determined by averaging the results of four specimens. Special measures were taken to properly grip the GFRP specimens. Standard gripping devices used on conventional steel rebars during tensile tests would crush the GFRP rebars inside the grips prior to tensile failure. Figure 2.2 shows the gripping mechanism used during the tests developed at the West Virginia University's Constructed Facilities Center (Kumar 1996).

To grip the GFRP rebar specimens, a steel pipe with a length of 305 mm was cut lengthwise into two pieces, as illustrated in Figure 2.2. The inner surface of the pipe halves was cleaned with a wire brush mounted on a hand drill to remove rust and other debris and then wiped with mineral spirits to remove residue that might prevent bonding of epoxy to the pipe surface. Next, the inner surfaces of the pipe halves were coated with a generic two part metal epoxy and then clamped at the ends of the GFRP rebar until the epoxy was fully cured. The total length of the rebar specimens tested was approximately 1500 mm. Figure 2.4 shows a photo of completed grips at one side of a test specimen.

Once the epoxy cured, the rebars were tested in a hydraulic testing machine with wedge type grips as shown in Figure 2.2. Table 2.3 shows the results of the five specimens tested. Each specimen failed near the center of the rebar length, as shown in Figure 2.3. Similar tensile tests were performed on the same type and size of rebar used in this study by Benmokrane and Masmoudi (1996). For comparison purposes, tensile strength results from their study are shown along with the present study in Table 2.3.

Three ECS rebars were tested to determine yield strength and ultimate strength of the rebars used in the reinforced concrete specimens. No special gripping devices were used in the testing of the ECS rebars. Results of the tensile tests are provided in Table 2.4.

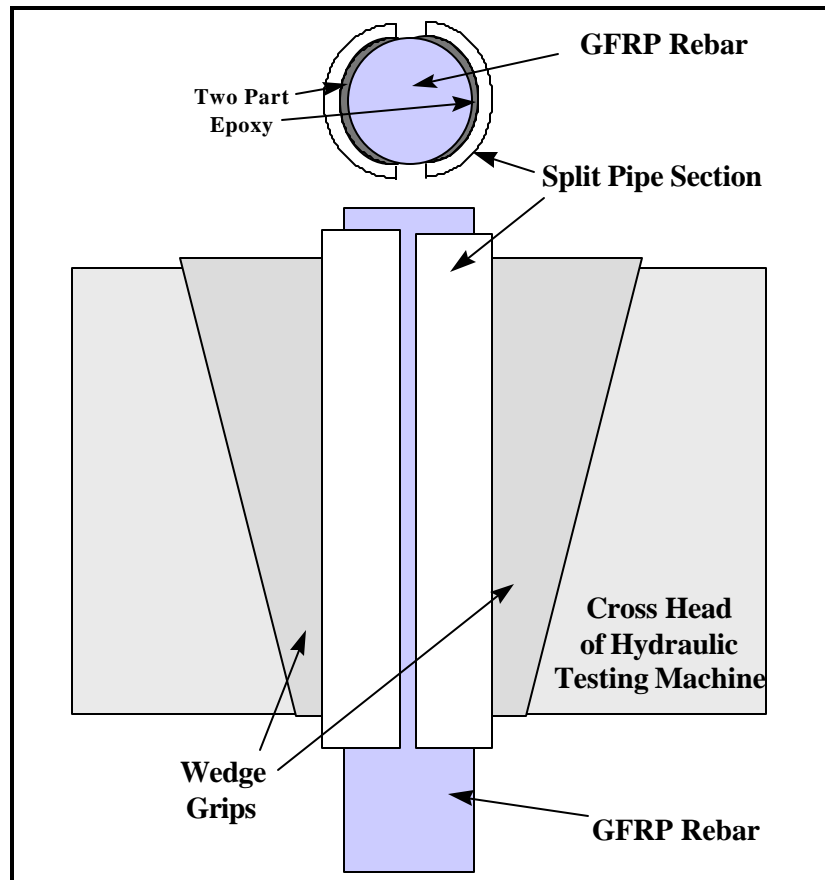


Figure 2.2: Split Steel Pipe Grips for Tensile Testing of GFRP Rebars

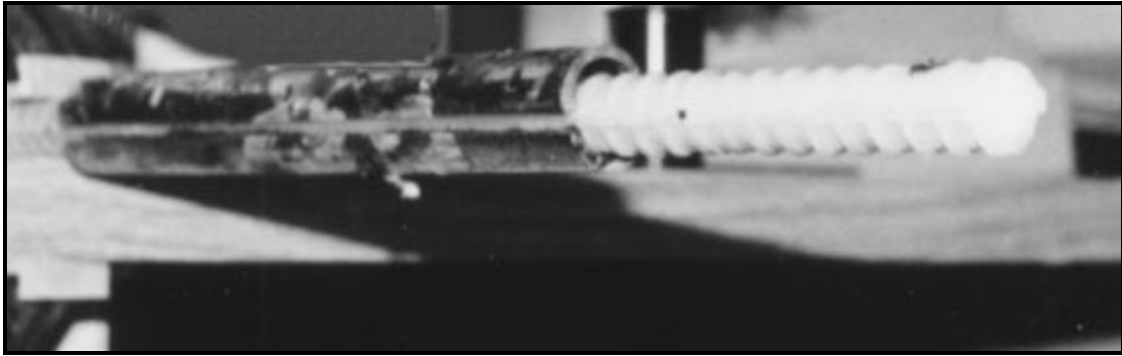


Figure 2.3: Steel Pipe Halves Epoxied to the GFRP Rebars during Tensile Tests

TABLE 2.3 SUMMARY OF TENSILE TEST RESULTS FOR THE GFRP REBARS

Specimen	Ultimate Tensile Capacity (kN)	Ultimate Tensile Strength* (MPa)
1	122.0	693
2	95.5	543
3	105.0	596
4	108.5	614
Average	108.0	612
Benmokrane & Masmoudi (1996)	_____	773

* Computed Using Manufacturer Specified Area in Table 2.2

TABLE 2.4 SUMMARY OF TENSILE TEST RESULTS FOR THE ECS REBARS

Specimen	Yield (kN)	Yield Strength (MPa)	Ultimate Tensile Capacity (kN)	Ultimate Tensile Strength* (MPa)
1	95.6	480.4	128.2	644.0
2	93.0	467.4	128.2	644.0
3	102.1	513.0	133.8	672.2
Average	96.9	486.9	130.1	653.4

* Computed Using an Area of 199 mm²

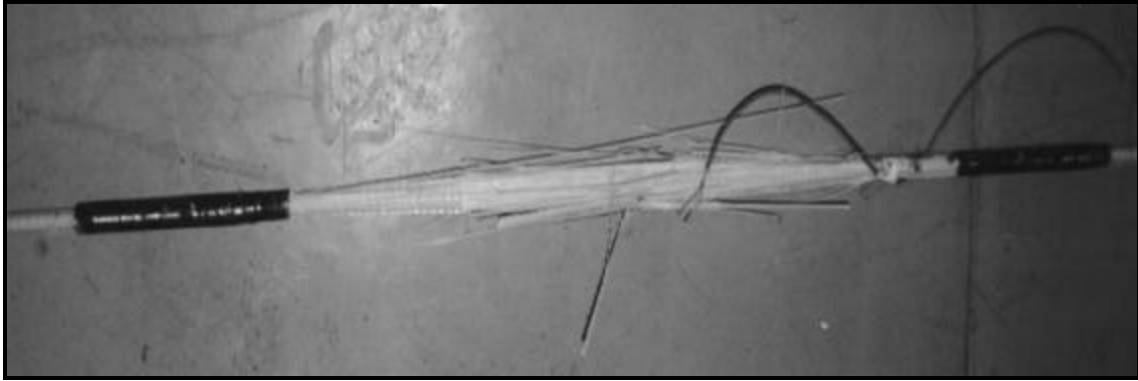


Figure 2. 4: GFRP Tensile Specimen after Failure

2.3.2 Tensile Modulus of Elasticity

The modulus of elasticity in tension for the GFRP and ECS rebars was determined by tensile tests. Tensile specimens were prepared in three steps. First, rebar deformations were removed with a belt sander over a small length to apply one strain gage to the surface. Second, the cross section diameter of the rebar where the deformations were removed was measured using a dial caliper. Third, a 6 mm foil strain gage was attached to the rebars.

The specimens were tested using methods described in Section 2.3.1 with a hydraulic testing machine with wedge type grips. The grips were checked for misalignment to minimize the amount of bending moment present in the specimens. Stress versus strain results of the four GFRP and three ECS rebar specimens tested are shown in Figures 2.5 and 2.6 respectively. Termination of the graphs represents the capacity of the data acquisition equipment rather than the rupture of the rebars in every case.

The test results were used in the analytical studies of the reinforced concrete specimens discussed in Chapters 4, 5, and 6. The modulus of elasticity of the GFRP rebars was computed using the average modulus of the four specimens tested. During the analysis of the reinforced concrete specimens, post yield information was required for the ECS rebars. Since strain measurements were taken at different stress levels after yielding, it was difficult to obtain an accurate average of results for the three specimens. Therefore, the post yield stress strain results of specimen E2 were used. The post yield behavior of this specimen closely approximated the average of the three specimens tested. Table 2.5 provides a summary of the results for the modulus of elasticity of the specimens tested. In addition, the table provides a comparison of test data from this study and a study by Benmokrane and Masmoudi (1996) (see Section 2.3.1).

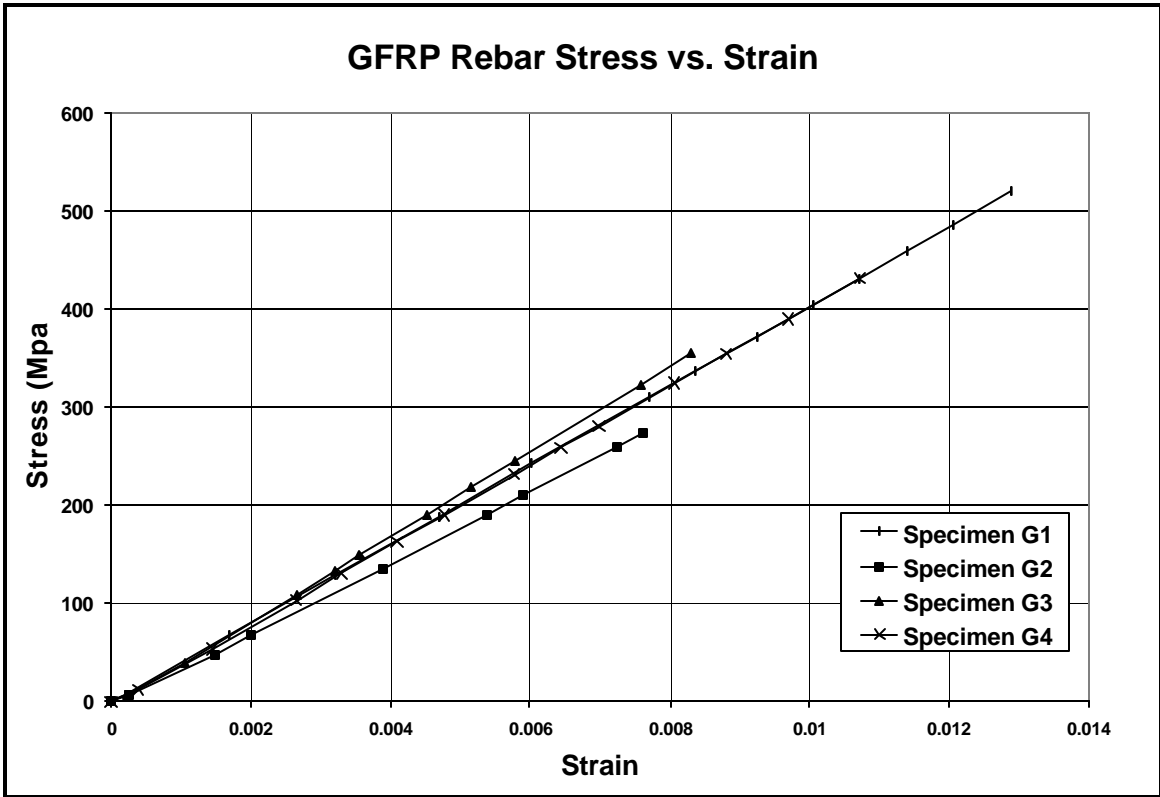


Figure 2.5: Tensile Stress Strain Properties for the #15 GFRP Rebars

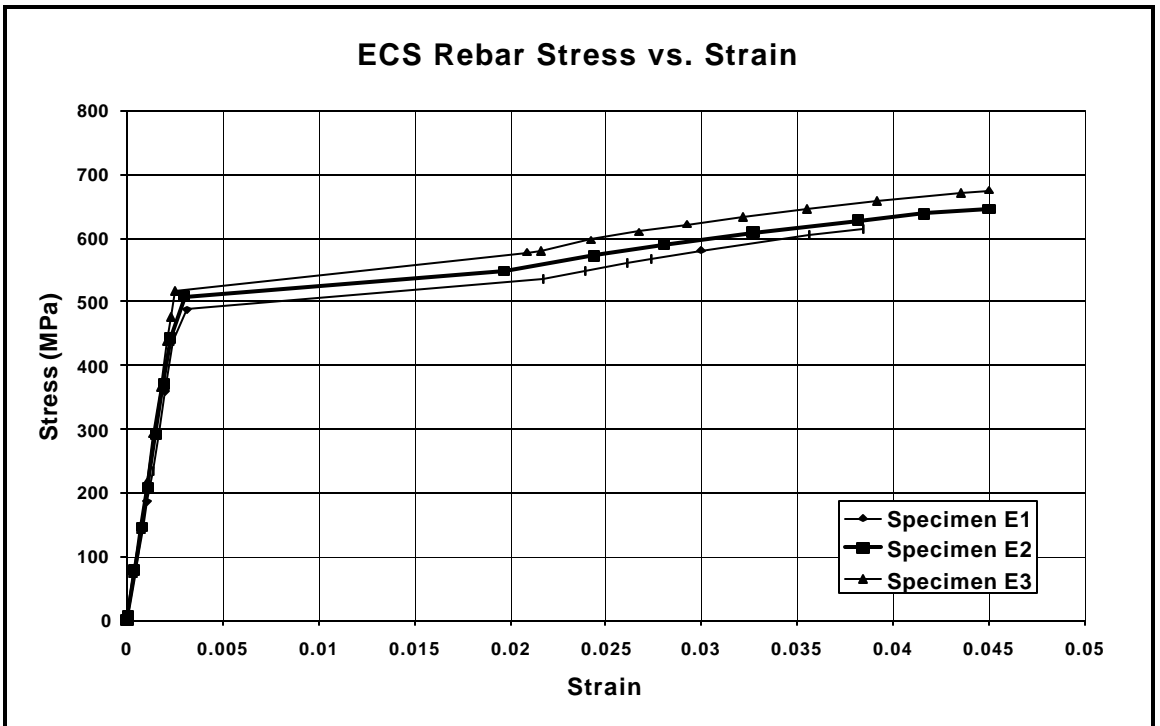


Figure 2.6: Tensile Stress Strain Properties of the #16 ECS Rebars

TABLE 2.5 EXPERIMENTAL MODULUS OF ELASTICITY

Specimen	E_{GFRP} #15 GFRP Rebar (MPa)	E_{ECS} #16 ECS Rebar (MPa)
1	40,400	185,760
2	36,140	195,930
3	42,960	207,610
4	40,610	-----
Modulus Used	Average = 40,000	Specimen #2 = 196,000
Benmokrane & Masmoudi (1996)	Average = 37,650	_____

2.4 COMPRESSION TESTING

The ECS rebars are known to have similar properties in both tension and compression. However, GFRP rebars could have significantly different material properties in tension and compression. Tests were performed to determine ultimate compressive strength and compressive modulus of elasticity for the rebars used in the study.

2.4.1 Ultimate Compressive Strength

The methods used to test the GFRP rebars in tension could not be used to test the rebars in compression because of difficulties with the test equipment. First, the equipment used to test the GFRP rebars in tension could not test the smaller specimens used in the compression tests. Second, the wedge grips used in the tensile test (see Figure 2.2) could not be used in compression.

To determine compressive properties of the GFRP rebars the testing apparatus shown in Figure 2.7 was developed. The apparatus consisted of two 135 mm rods with an outside diameter of 50 mm designed to thread into the hydraulic testing machine used in the study. Each of the threaded rods was drilled with a 17.5 mm diameter hole in the center, slightly larger than the 15 mm diameter of the #15 GFRP rebars. The holes were drilled to a depth of 65 mm to provide some fixity at the specimen ends.

Specimens were tested with unbraced lengths ranging from 50 mm to 380 mm. Ultimate compressive strength results are depicted in Figure 2.8 for the lengths tested. Three distinct failure modes were observed during the tests and occurred based on the unbraced length of the specimens. The ranges of unbraced length for the three failure modes are identified in Figure 2.8 along with a 4th order best fit curve. The first type of failure was found in the tests of the shorter specimens ranging in unbraced length from 50 mm to 110 mm. These specimens failed by crushing. The second failure type observed

was buckling and was exhibited by the longer specimens with unbraced lengths from 210 mm to 380 mm. Figures 2.9 and 2.10 show specimens exhibiting crushing and buckling failure modes respectively.

The third failure type was a combination of the crushing and buckling failure modes. Specimens with unbraced lengths ranging from 110 mm to 210 mm would fail in either mode. In some cases buckling failure would occur and then under continued loading a crushing type failure would occur for the same specimen.

Scatter of the specimen data was also consistent for the different failure types. A wide scatter was exhibited by the shorter specimens failing by crushing. Specimens failing by buckling had little scatter. The specimens in the combination failure region had varied scatter as shown in Figure 2.8.

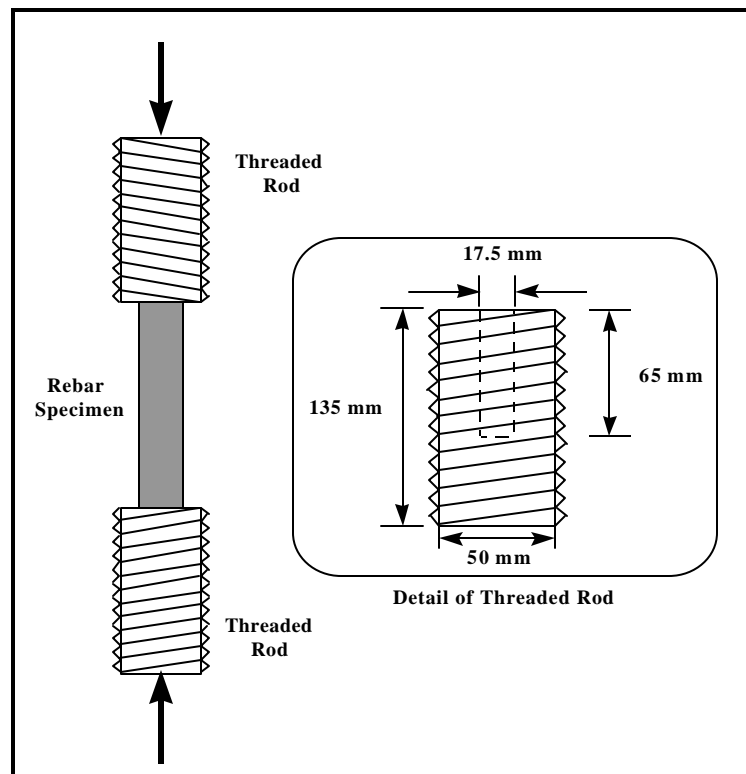


Figure 2.7: Apparatus used During the Tests of GFRP Rebars in Compression

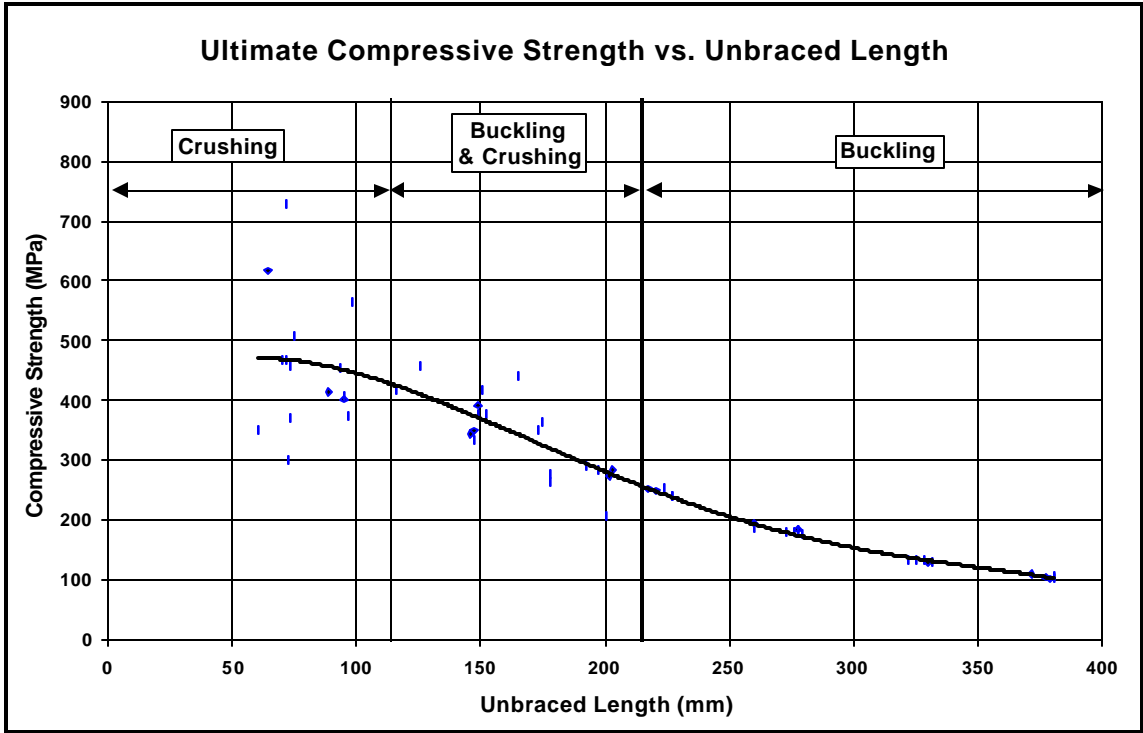


Figure 2. 1: Ultimate Compressive Strength versus Unbraced Length of the GFRP Rebars used in the Study

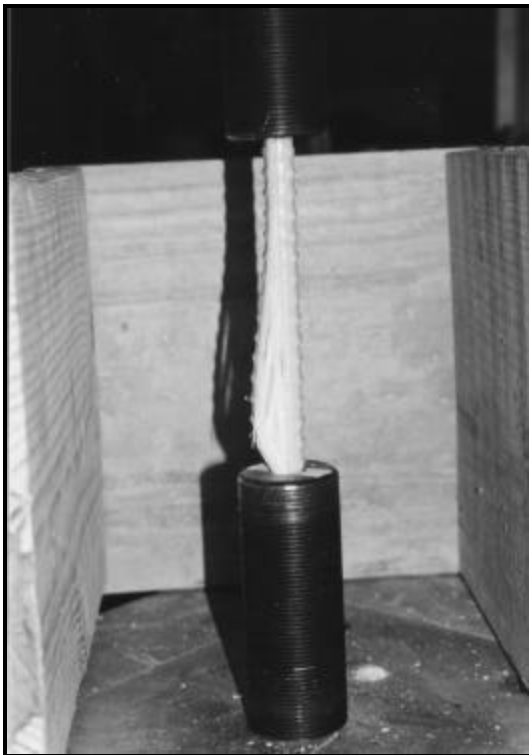


Figure 2. 9: Crushing Failure Mode

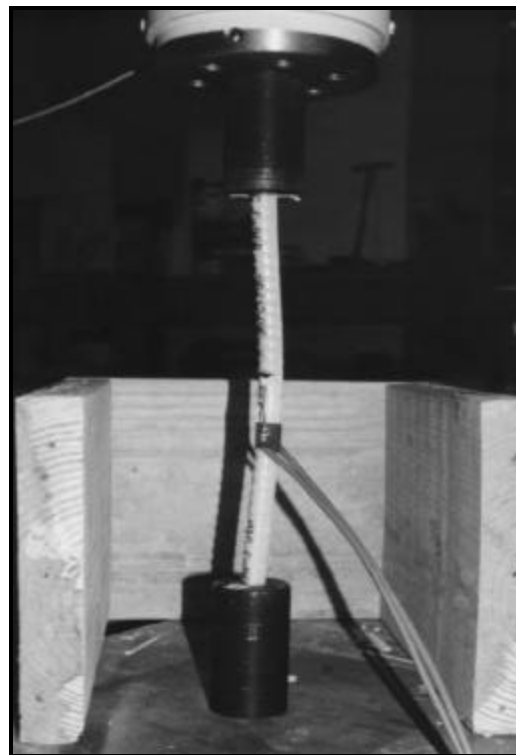


Figure 2. 10: Buckling Failure Mode

2.4.2 Compressive Modulus of Elasticity of the GFRP Rebars

The compressive modulus of elasticity of the GFRP rebars was determined experimentally using the compression testing procedures discussed in Section 2.4.2. Three specimens were tested with lengths chosen to represent the three failure modes shown in Figure 2.8. Unbraced lengths of the three specimens tested were 80 mm, 200 mm, and 300 mm corresponding to the crushing, combined crushing and buckling, and buckling failure regions respectively.

To prepare the GFRP rebar test specimens, the surface deformations were removed in a small area using a belt sander providing a smooth surface to attach two 6.35 mm strain gages to each of the three specimens. Diameter of the rebar in the section where the deformations were removed was measured using calipers to account for the small section loss during sanding.

Since the moment applied by the hydraulic testing machine during the test was significant, a strain gage was placed on each side of the specimens. This allowed for the separation of axial and flexural strains in the test data. To obtain the axial compressive strains data from the two strain gages on each specimen was averaged.

Figure 2.11 shows the stress strain results of the three specimens tested. The results showed good agreement in modulus of elasticity regardless of specimen length.

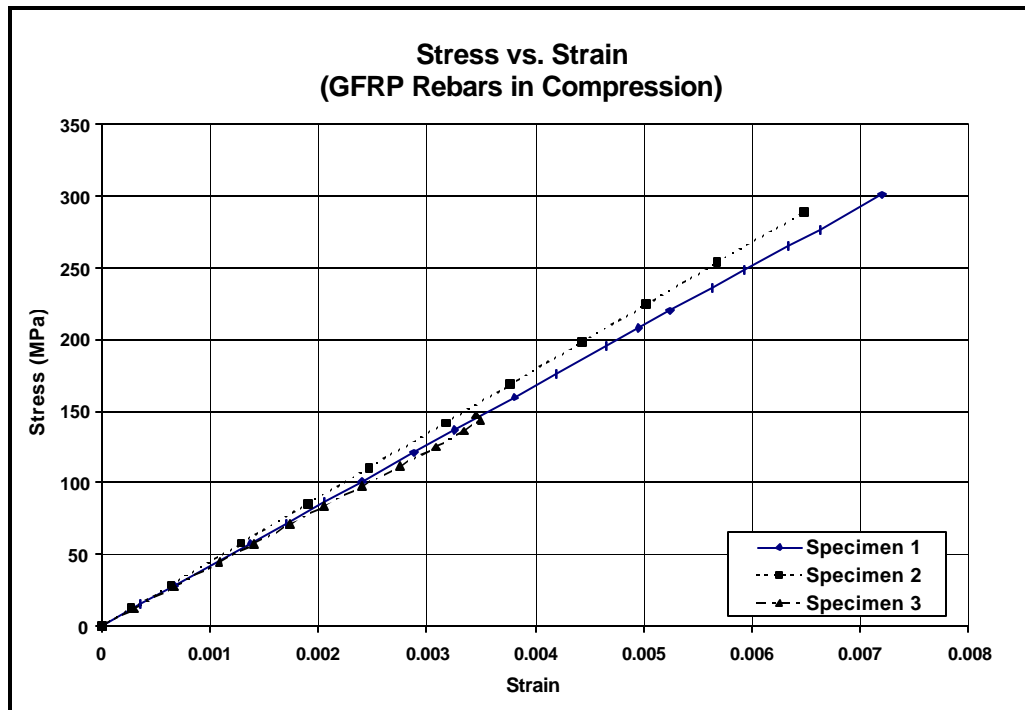


Figure 2.11: Compressive Stress versus Strain Results for the GFRP Rebars

TABLE 2.6 SUMMARY OF GFRP REBAR COMPRESSION MODULUS OF ELASTICITY

Specimen	Length (mm)	Modulus of Elasticity (N/mm ²)
1	80	41,730
2	200	44,585
3	300	41,220
Average	-----	42,510

2.4.3 GFRP Rebar Compressive Design Curve

Proposed design curves for the GFRP rebars under compression were developed using the experimental test data discussed in Sections 2.4.1 and 2.4.2. Figure 2.10 shows the three functions developed to predict the behavior of the #15 GFRP rebar in the three failure regions observed during the tests. The following three relations are proposed:

Crushing Failure

$$\sigma = 325 \qquad 0 \text{ mm} \leq L \leq 110 \text{ mm} \qquad (2.1)$$

Combined Crushing and Buckling Failure

$$\sigma = 325 - \frac{1}{2}(L - 110) \qquad 110 \text{ mm} \leq L \leq 210 \text{ mm} \qquad (2.2)$$

Buckling Failure

$$\sigma = \frac{\pi^2 E}{\left(\frac{kL}{r}\right)^2} \qquad L > 210 \text{ mm} \qquad (2.3)$$

where,

σ	=	ultimate compressive stress
L	=	unbraced length
E	=	compressive modulus of elasticity
k	=	effective length factor for buckling
r	=	radius of gyration of the GFRP rebar

A maximum value of 325 MPa was selected for the crushing failure region. This lower than average value was selected due to the limited amount of test results. A GFRP rebar encased in concrete can intuitively be expected to have a greater strength than the test results show and this value will most likely be increased as more test data becomes available.

In the combined buckling crushing region, a linear relation described by Equation (2.2) was derived to describe the ultimate strength of the rebar. The Euler buckling relation was used to predict the ultimate compressive strength of the rebar in the buckling failure region. The value of k used was selected on data best fit, a value of 0.65, and the radius of gyration, $r=3.6$, was computed based on the barrel diameter specified by the GFRP rebar manufacturer.

For the design of reinforced concrete members the crushing properties should be used since the concrete cover will provide full lateral bracing. In cases where spalling of the concrete cover might be expected, the unbraced length should be taken as the distance between transverse rebars.

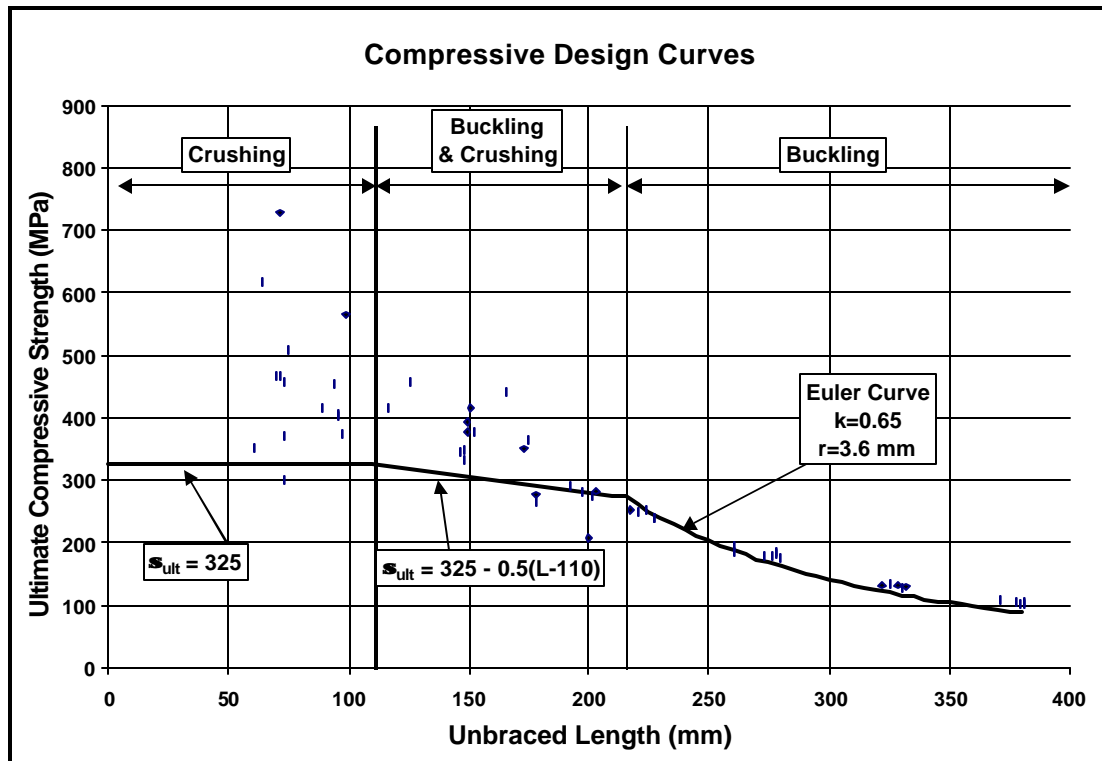


Figure 2. 12: Proposed Design Ultimate Strengths for #15 GFRP Rebar used in the Study

2.5 SUMMARY AND CONCLUSIONS

This chapter summarized the properties of the #15 GFRP and #16 ECS rebars used in the study. Tensile modulus of elasticity, yield strength (of the ECS rebars), and ultimate strength of the GFRP and ECS rebars were determined experimentally. Compressive modulus of elasticity and ultimate strengths were determined for the GFRP rebars. A compressive design curve for the GFRP rebars was proposed based on experimental results of the study.

A gripping mechanism developed at West Virginia University was used during the experimental determination of the GFRP tensile properties. Split pipe halves were epoxied to the ends of the rebar specimens preventing transverse crushing failure of the GFRP rebars in the wedge grips prior to tensile failure of the rebar.

Table 2.7 shows the experimental results of the tensile tests. There was a 15% difference between the manufacturer specified ultimate tensile strength and the experimental tensile strength. Specified and experimental tensile modulus of elasticity showed better agreement with a 4.8% difference. Properties of the ECS rebars correlated well with values commonly used.

No manufacturer specified properties for the GFRP rebars in compression were available. The compressive modulus and tensile modulus of the GFRP rebars determined experimentally are approximately the same. However, the ultimate strength in compression of the GFRP rebar is approximately 53% of the ultimate strength in tension for the compressive specimen identified in Table 2.7.

Results of compression tests were used to develop a proposed ultimate strength design curve for the GFRP rebars used in the study. The proposed design curve was based on the observed failure mode and unbraced length.

In most cases GFRP rebars in reinforced concrete members should be considered fully braced for compression. Therefore, the crushing compressive properties should be used in design. In cases where concrete cover could spall off the unbraced length of the rebars in compression can be taken as the distance between transverse rebars or ties.

TABLE 2.7 SUMMARY OF REBAR PROPERTIES

	Tension			Compression
	Manufacturer Specified # 15 GFRP	#15 GFRP	#16 ECS	#15 GFRP
Ultimate Strength (N/mm ²)	713	612	653.4	325*
Yield Strength (N/mm ²)	N. A.	N. A.	486.9	N. A.
Modulus of Elasticity (N/mm ²)	42,000	40,030	195,930	42,510
*Property for Crushing Failure, Unbraced Length < 110 mm				

3.0 CONSTRUCTABILITY ASSESSMENT

3.1 INTRODUCTION

The issues related to the construction of bridge decks, from rebar placement to placement of concrete, are evaluated for decks reinforced with glass fiber reinforced polymer (GFRP) rebars and epoxy coated steel (ECS) rebars. Properties of these two rebar types are presented in Table 3.1.

The modulus of elasticity in tension, E , of the GFRP rebars ($E_{\text{GFRP}} = 40,000$ MPa) is low when compared to that of steel rebars ($E_{\text{ECS}} = 196,000$ MPa). The low modulus GFRP rebar deflects more under weight than an equivalent ECS rebar, as shown in Figures 3.1 and 3.2. The flexibility of the GFRP rebars raises issues regarding the ability of GFRP rebars to adequately support construction workers during placement of concrete (e.g. loss of balance).

Floation of GFRP rebars in wet concrete was investigated since the specific gravity of GFRP rebars, 1.92, is less than that of fresh concrete, 2.4, and consequently the rebars could potentially float before the concrete has set. Another factor of concern during construction with GFRP rebars is possible rebar damage due to construction mishaps. Dropping of shovels or other construction equipment could scratch the outer surface of the rebar applied to protect the GFRP rebar from the highly alkaline environment in a concrete bridge deck. Some resins and E-glass fibers used in GFRP rebars have been found to deteriorate in these environments (Anderson, Bank and Munley 1994).

To investigate the behavior of the GFRP rebars and other plastic construction components (e.g. plastic chairs and ties) a constructability assessment was conducted. During the study two mock bridge decks were built as slabs on grade (see Figure 3.3). The first mock bridge deck was constructed with GFRP rebars, plastic ties, and plastic chairs. The second mock bridge deck was constructed using conventional reinforcing components common in bridge decks. These components included epoxy coated steel rebars, plastic coated steel ties, and epoxy coated steel chairs. The repair of concrete decks reinforced with GFRP rebars was also considered. The study was primarily concerned with potholes that could form in a bridge deck due to causes unrelated to corrosion of the reinforcement. Because the hardness of the GFRP rebars is low compared to that of steel it is easier for a jackhammer to cut through the GFRP rebar. The difficulty in repairing decks reinforced with GFRP rebar is further compounded by the fact that GFRP rebars cannot be detected using pachometers prior to concrete removal. This makes the rebars difficult to avoid during removal operations.

TABLE 3.1 PROPERTIES OF ECS AND GFRP REBARS USED IN THE STUDY

Rebar Type	Diameter of Rebar (mm)	Area of Rebar (mm ²)	Specific Gravity	Yield Strength (MPa)	Ultimate Strength (MPa)	Modulus of Elasticity (MPa)
#16 ECS	16	199	7.85	487 ^a	653 ^a	196,000 ^a
#15 GFRP	15	176	1.92	N. A.	612 ^b	40,000 ^b

^a Average of three specimens
^b Average of four specimens



Figure 3.1: Deflection of an ECS Rebar under the Weight of a Construction Worker

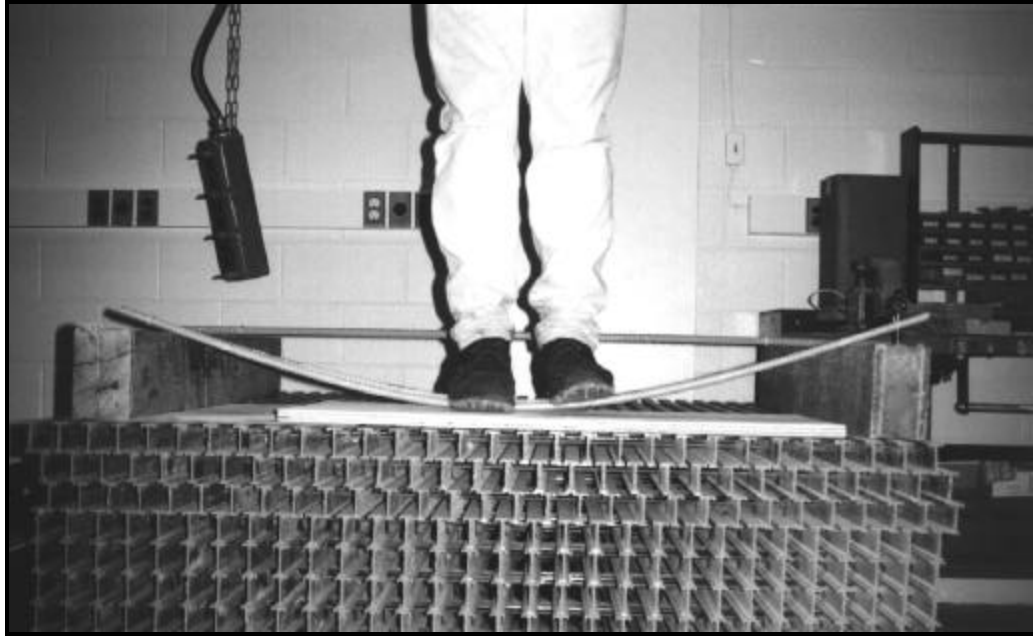


Figure 3.2: Deflection of a GFRP Rebar under the Weight of the Same Construction Worker



**Figure 3.3: Two Mock Bridge Decks Constructed as Slabs on Grade
Foreground--ECS Reinforced
Background--GFRP Reinforced**

3.2 DESCRIPTION OF BRIDGE DECKS

3.2.1 Mock Bridge Decks

Figure 3.3 shows the two mock bridge decks that were constructed as slabs on grade during the constructability assessment. One of the bridge decks was reinforced with GFRP rebars using plastic ties and chairs. The second bridge deck was constructed using conventional ECS rebars with coated steel ties and chairs, and served as a benchmark of the study since it represents typical bridge deck construction in Kentucky.

Both mock bridge decks had the same longitudinal and transverse rebar spacing, shown in Figure 3.4. The spacings were based on a typical Kentucky ECS reinforced bridge deck. Identical spacings were used for both bridge decks to facilitate comparison of test results. In the actual design of a GFRP reinforced bridge deck, the spacing is likely to be smaller. It should be noted that Kentucky suggests a minimum spacing of 125 mm to facilitate deck construction. The transverse rebars in the bottom mat of the mock bridge decks were spaced at 127 mm.

Figure 3.5 shows the components used in the construction of the first deck reinforced with GFRP rebars. The reinforcement consisted of #15 GFRP rebars tied with plastic zip ties and supported by individual plastic chairs. The plastic zip ties were purchased at a local hardware store. The components used in the second deck reinforced with ECS rebars are shown in Figure 3.6 and consisted of #16 ECS rebars, plastic coated steel ties, and individual epoxy coated steel chairs.

3.2.2 Roger's Creek Bridge Deck

After the completion of the later stages of this research study (Chapters 4 and 5 of this report) it was decided to place GFRP rebars in a region of the top reinforcing mat in the Roger's Creek bridge deck. The bridge is an 11,125 mm simply supported PCI beam structure with a width of 10,975 mm. Figure 3.7 shows the region of the top reinforcing mat, 2735 mm by 4725 mm, where GFRP rebars were placed. The remainder of the top mat was reinforced with ECS rebars.

Figure 3.8 shows a photograph of the bridge deck reinforcement. The lighter area of the mat close to the center of the bridge, highlighted with dots, is the GFRP rebar area. ECS rebars in the mat are darker in color. Information from the mock bridge deck studies was provided to the contractors prior to the construction of the Roger's Creek bridge deck.

During the construction of the Roger's Creek bridge deck, contractors used runner chairs, shown in Figure 3.9. The runner chairs were much longer than the individual chairs used in the mock bridge deck, shown in Figure 3.6. Runner chairs were not used in the mock deck study because plastic runner chairs required for a direct comparison of reinforcement components could not be obtained.

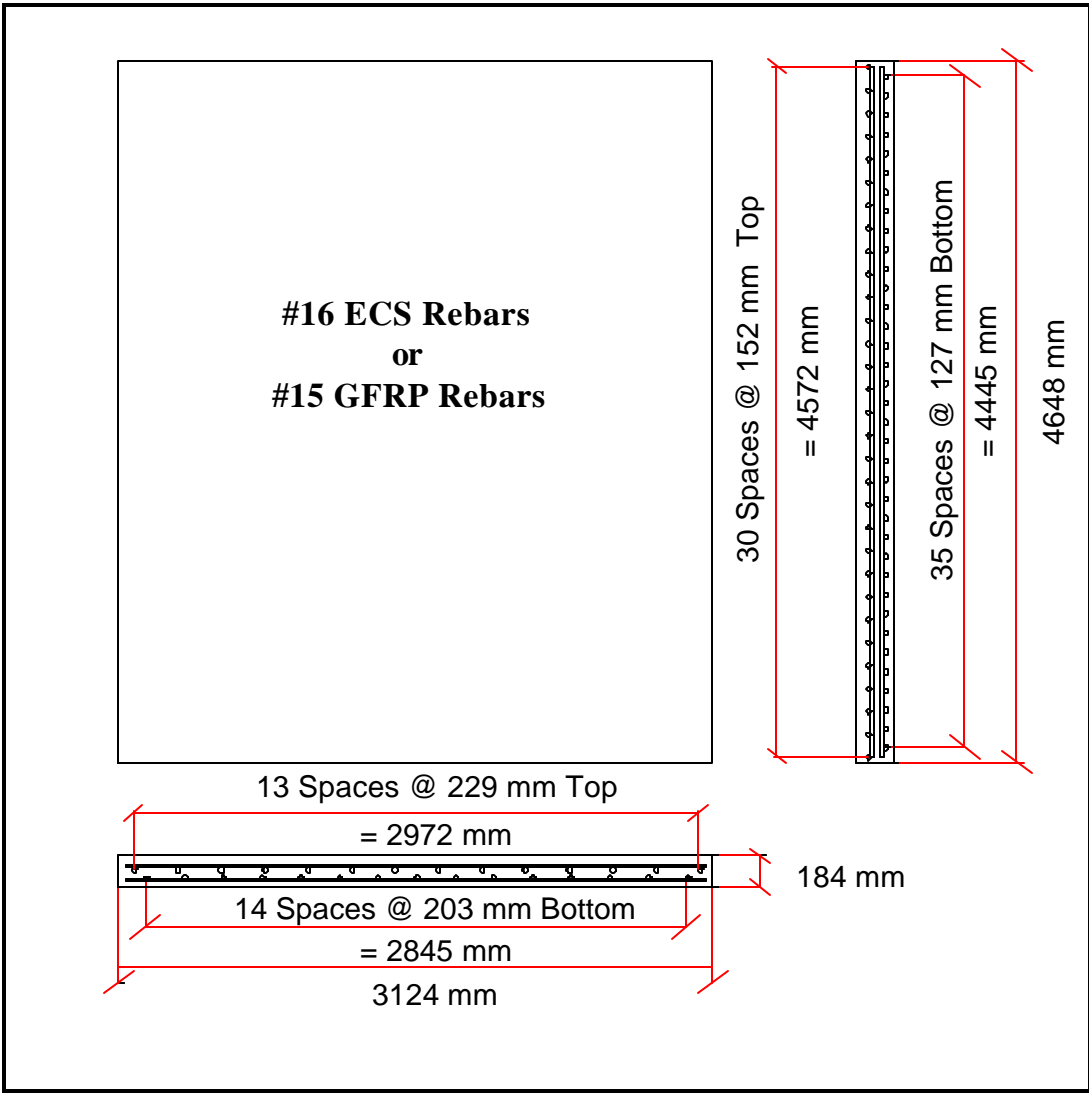


Figure 3.4: Details of the Mock Bridge Deck Reinforcing Schemes

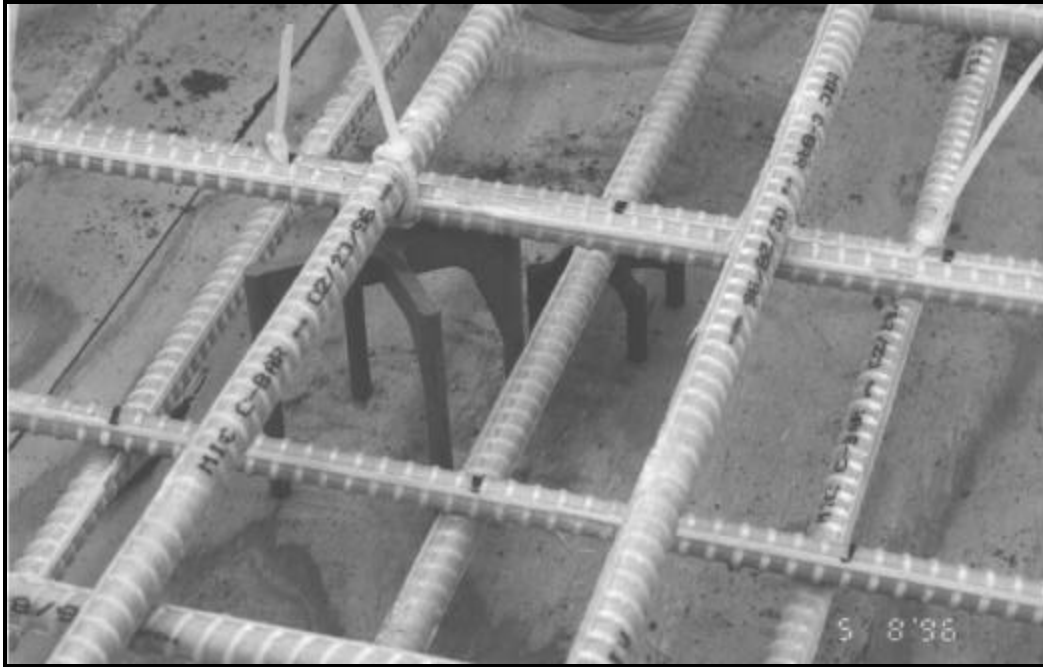


Figure 3.5: Detail of Glass Fiber Reinforced Plastic Reinforcement

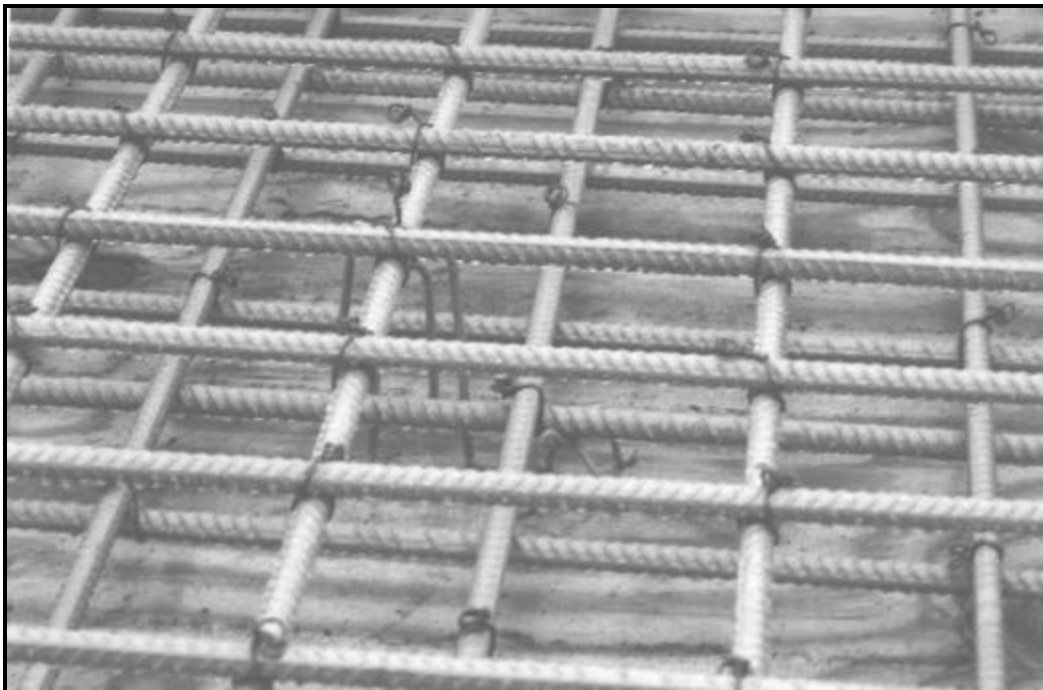


Figure 3.6: Detail of Epoxy Coated Steel Reinforcement

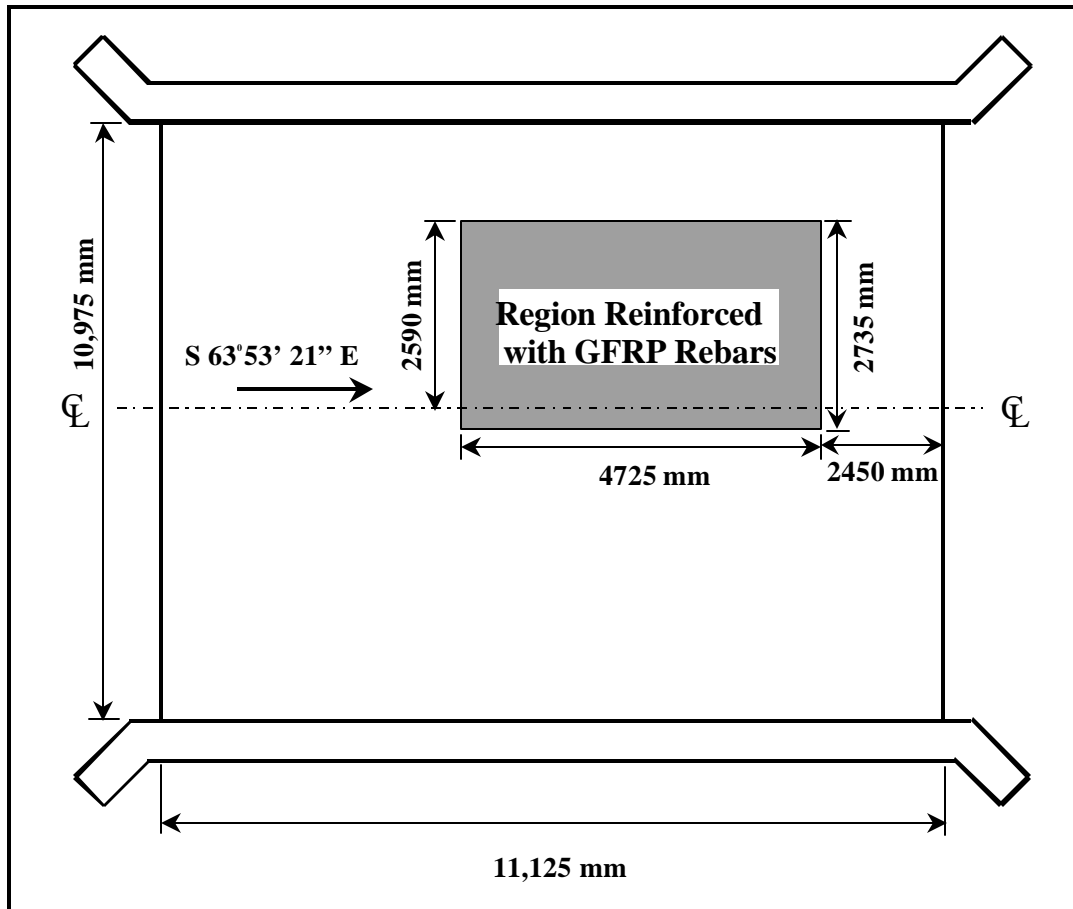


Figure 3.7: Plan View of Bridge Deck Showing Location of the GFRP Rebars



Figure 3.8: Photograph of Bridge Deck prior to Concrete Placement. Dots were Sketched in to Identify the Location of the GFRP Rebars in the Top Mat

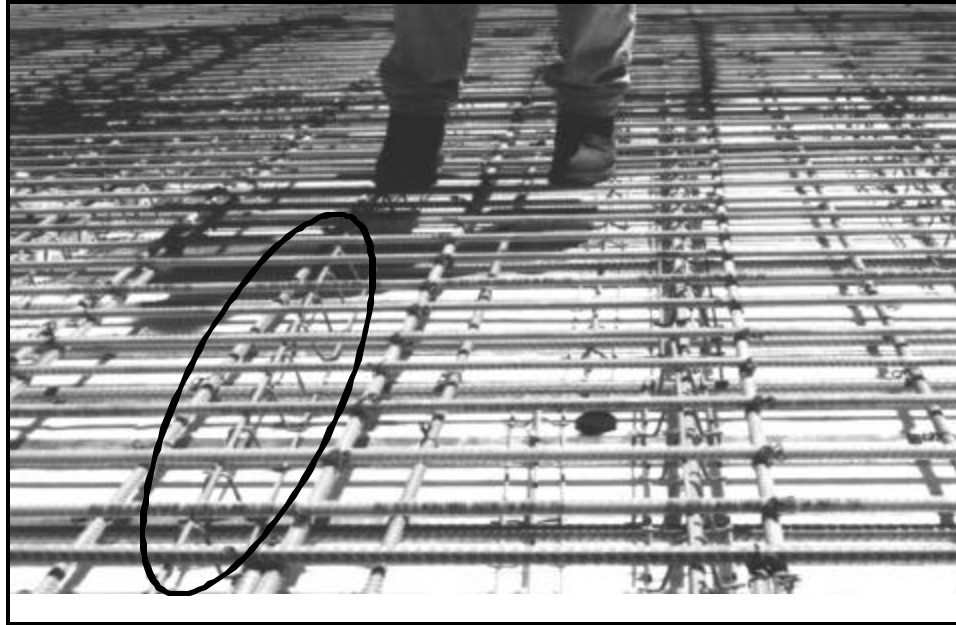


Figure 3.9: Photograph showing the Epoxy Coated Steel Runner Chairs Supporting GFRP rebars in the Construction of the Roger's Creek Bridge Deck

3.3 FLEXIBILITY

3.3.1 Mock Bridge Decks

In most cases, reinforcing mats are required to support the weight of construction workers and their equipment during the placement of both reinforcement and concrete. Flexibility and strength problems were encountered during construction of the GFRP reinforcing mat due to the flexibility GFRP rebars, individual plastic reinforcing chairs, and plastic zip ties.

The GFRP rebars were sufficiently strong to support the construction loads. However, the plastic zip ties and the individual plastic chairs used were not. The zip ties would frequently unzip or snap under the construction workers. To prevent this problem two ties were required at each tie point, increasing construction time. The individual plastic chairs used in the study frequently broke. Increasing the number of chairs alleviated the problem somewhat, but they would still break if a construction worker stepped directly on them. The GFRP rebars, individual plastic chairs, and the plastic ties made it difficult for construction workers to maneuver on the reinforcing mat. No problems with strength and flexibility were encountered during the construction of the mock deck reinforced with ECS rebars.

3.3.2 Roger's Creek Bridge Deck

In the Roger's Creek bridge deck, approximately twice as many steel runner chairs were used in the GFRP area as the ECS reinforced area. The greater number of stiffer steel runner chairs in addition to the use of coated steel ties enhanced the stiffness of the GFRP portion of the mat. In fact workers did not notice any difference in stiffness between the GFRP and ECS portions of the mat.

Based on observations during the construction of the mock bridge decks and the Roger's Creek bridge deck, the following is recommended for construction with GFRP rebar:

1. ECS steel runner chairs are recommended to support the GFRP rebars
2. Approximately twice as many steel runner chairs should be used to support GFRP rebars as to support ECS rebars of the same cross section.
3. Plastic coated steel ties are recommended for tying GFRP rebars.

3.4 FLOATATION

The specific gravity of the GFRP rebars, 1.92, is less than the specific gravity of fresh concrete, 2.4. Consequently, it is possible that the GFRP rebars could float before the concrete sets.

Floating of the reinforcement was not observed during construction of the mock bridge deck reinforced with GFRP. The slump of the concrete was between 50 mm and 75 mm which is too low to allow free movement of the GFRP rebars. Floating of the reinforcement could be an issue if the concrete had a higher slump, as in cases where a concrete pump is used.

As a second check for rebar floatation, concrete cores were taken from the mock bridge decks, after the concrete had set, to determine the final vertical location of the rebars. Figure 3.10 shows a core being removed from the mock deck reinforced with GFRP rebars. An illustration of how the cores were used to determine the vertical location of the rebars is shown in Figure 3.11. The measurements from the cores showed that the vertical location of the GFRP rebars met Kentucky construction specifications, within +/- 6 mm (Standard Specifications for Road and Bridge Construction 1998). Therefore, the GFRP rebar mat did not float appreciably.

The GFRP rebars were not observed to float during the Roger's Creek bridge deck construction. GFRP rebars were tied in with the ECS rebars in other regions of the mat preventing floatation.



Figure 3. 10: Concrete Core Removed from the GFRP Reinforced Mock Bridge Deck



Figure 3. 11: Measuring to Determine the Vertical Location of the GFRP Rebars in the Mock Bridge Deck (Note: Ruler dimensions are in inches, 1 inch = 25.4 mm)

3.5 REBAR DAMAGE DURING CONSTRUCTION

There were concerns that construction mishaps could lead to damage of the GFRP rebars. Observations showed that the construction tools, i.e. shovels, vibrators, etc., could scratch the outer surface of the rebars, but no major physical damage such as the loss of surface deformations was encountered during the test. ECS rebars sustained similar minor damage from construction tools

Though there was no obvious physical damage, the small scratches on the surface of the rebars could lead to long term deterioration. The small scratches removed the protective coating applied to the rebars during the manufacturing process to prevent deterioration in harsh environments.

3.6 CONTRACTOR/ENGINEER COMMENTS ON THE ROGER'S CREEK BRIDGE DECK

Information recorded during the initial stages of the constructability test conducted on the mock bridge decks was provided to the contractors prior to placement of the GFRP rebars in the Roger's Creek bridge deck. The contractor was informed of different chair requirements due to the flexibility of the material and other differences in ECS and GFRP rebars.

The contractor's foreman and almost every laborer commented on how much easier the GFRP rebars were to install compared to conventional ECS rebars. They praised the GFRP rebar's light weight. Construction workers did not wear gloves to protect from splinters while handling the GFRP rebars and they did not encounter any itching or cuts on their hands.

3.7 BRIDGE DECK REPAIR

Although GFRP reinforcement is used to prevent corrosion-related degradation of bridge decks, long term wear could affect the integrity of the concrete deck regardless of the type of reinforcement. Such wear could include truck impact loads, poor quality concrete, alkali-silica reactivity, etc. Repair of these problems could include removal of concrete surrounding the reinforcement. Two different concrete removal schemes were evaluated in the constructability assessment; jackhammers and hydro-demolition equipment.

3.7.1 Jackhammer

As shown in Figure 3.12, a jackhammer was used to remove concrete from the mock bridge decks. Two holes were hammered in the mock bridge deck reinforced with GFRP. The first hole was used for practice to acquaint the research technicians with the equipment. The second hole, shown in Figure 3.13, was used to record observations. An additional hole was hammered into the ECS deck.

In a bridge deck reinforced with ECS rebars a pachometer can be used to detect the location of the steel reinforcement. This allows the jackhammer operator to avoid the rebars from the beginning of the concrete removal process. A pachometer cannot be used to determine the location of GFRP rebars in a bridge deck. Therefore, a jackhammer operator must find the location of the rebars while removing concrete, often damaging rebars in the process.

Since GFRP rebars have a low hardness when compared to ECS rebars, caution was used during the removal of concrete to prevent damage. As Figure 3.14 shows, allowing the jackhammer to rest on a GFRP rebar, would easily nick or fully cut through the rebar. Care was taken to avoid the rebar as much as possible. Similarly, allowing the jackhammer to rest on an ECS rebar would also lead to damage, as shown in Figure 3.15. However, it takes more time to inflict major damage to ECS rebars than GFRP rebars, and this allows the jackhammer operator time to locate the rebars and work around them during the concrete removal process.

Another advantage of repairing an ECS deck over a GFRP deck is that the ECS rebars can be used as a guide for the jackhammer during concrete removal. Since the ECS rebars are hard, the jackhammer operator often wedged the tip of the jackhammer against the ECS rebar when removing concrete around it. This did little more to the rebar than scratch the epoxy coating. GFRP rebars could not be used as a guide during concrete removal. First, the GFRP rebars were not stiff enough to firmly wedge the tip of the jackhammer. When the jackhammer was operating, it would shake the rebar and the jackhammer would slip. Second, the use of a GFRP rebar as a jackhammer guide resulted in damage to the rebar, often removing surface deformations.

To minimize the damage to the GFRP rebars, the operator would have to jackhammer until a rebar in each horizontal direction was found. Once the rebars were found, the operator could estimate the location of adjacent rebars based on the reinforcement spacing if available. In every test case performed on the mock bridge deck the operator would inflict damage to the GFRP rebar before realizing that the hammer was resting on the rebar. After the first rebar was located the operator was better able to avoid the other rebars.

It was very difficult for the operator to remove concrete near the surface of the GFRP rebar. When the jackhammer would shake, the point of the jackhammer would slip, changing position. Often the change in position would move the tip of the jackhammer directly on the rebar resulting in substantial damage.

Though damage to the ECS rebars also occurred, in most cases it was limited to removal of the epoxy coating and small nicks. Figure 3.15 shows the hole hammered into the mock deck reinforced with ECS rebars. Most of the damage done to the mock deck reinforced with ECS rebars could be corrected by applying a new epoxy coating to the nicked surfaces, assuming that all of the damaged surfaces are easily detected. The large cut shown in the Figure 3.15 was the result of intentional damage with the jackhammer to determine the ECS rebar's resistance to cutting.



Figure 3. 12: Hammering Concrete during Repair Feasibility Study. A GFRP Rebar is Exposed near the Hammer Tip.

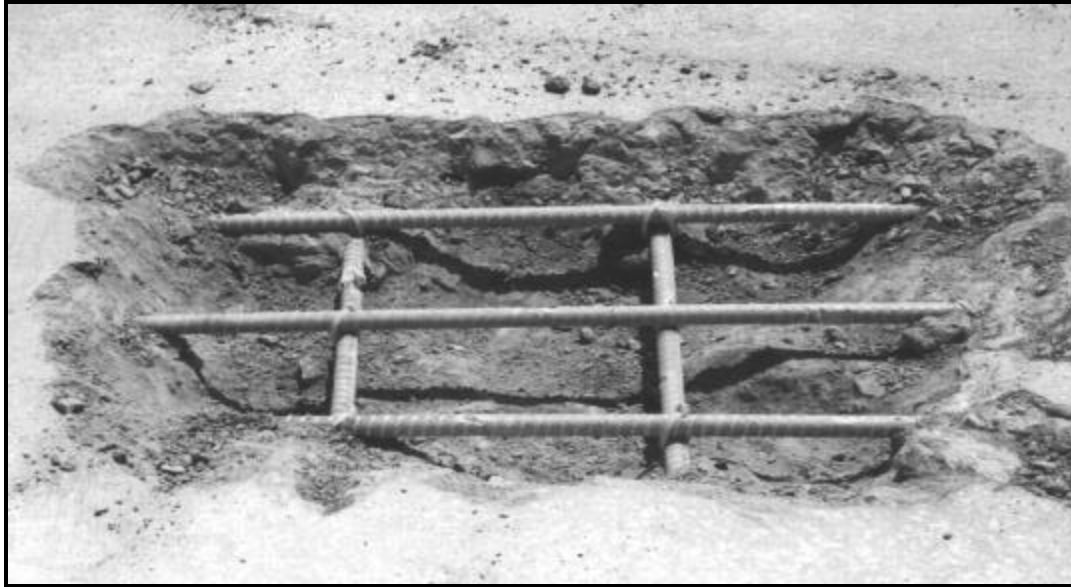


Figure 3. 13: Second Hole Hammered into Mock Bridge Deck Reinforced with GFRP Rebars

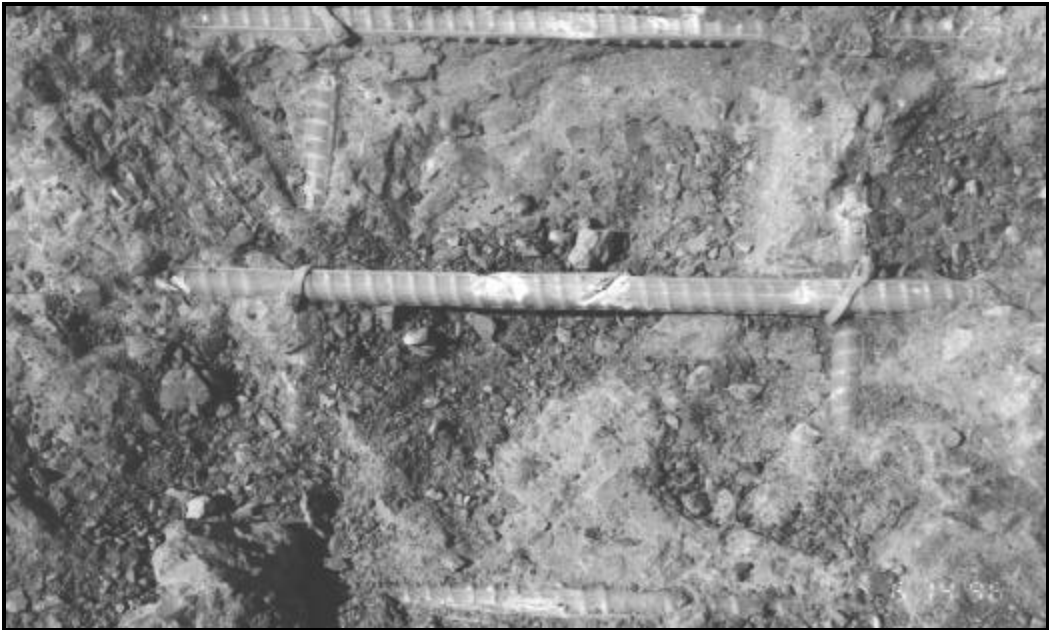


Figure 3. 14: Detail of Jackhammer Damage to the GFRP Mock Bridge Deck

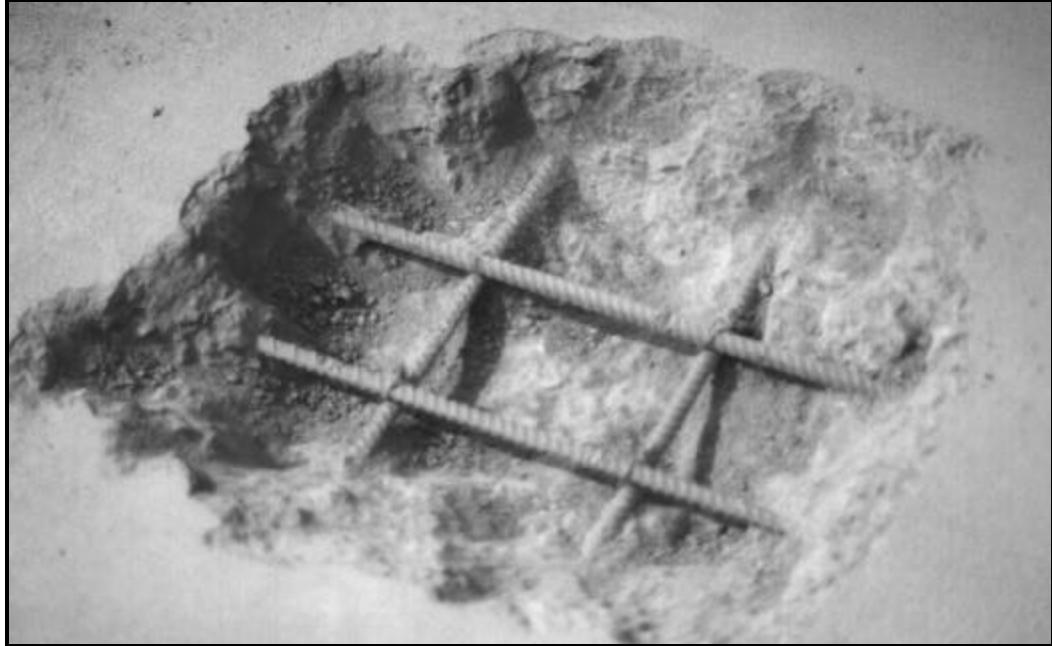


Figure 3. 15: Hole Hammered into Mock Bridge Deck Reinforced with ECS Rebars

3.7.2 Hydro-Demolition

Figure 3.16 shows a photograph of the hydro-demolition equipment used in the study. The equipment consisted of the apparatus that removes the concrete shown in the foreground and a semi-trailer to produce the required hydraulic pressure. Water at high pressure is released under the base of the apparatus breaking up and removing concrete. During the removal process the water moves sand and gravel around with the water at high speed. This acts as an abrasive, removing the epoxy coating from ECS rebars commonly used in bridge decks. After the concrete has been removed, the rebar's epoxy coating must be replaced to provide long term reinforcement protection.

To evaluate the hydro-demolition process as a potential repair solution to bridge decks reinforced with GFRP, an individual loose GFRP rebar was placed under the machine while it was in operation. The abrasive action of the sand and gravel damaged the GFRP rebar shown in Figure 3.17. As the figure shows, the hydro-demolition equipment simply tore the rebar apart. For this reason hydro-demolition should not be considered a viable option for the repair of bridge decks reinforced with GFRP rebars.

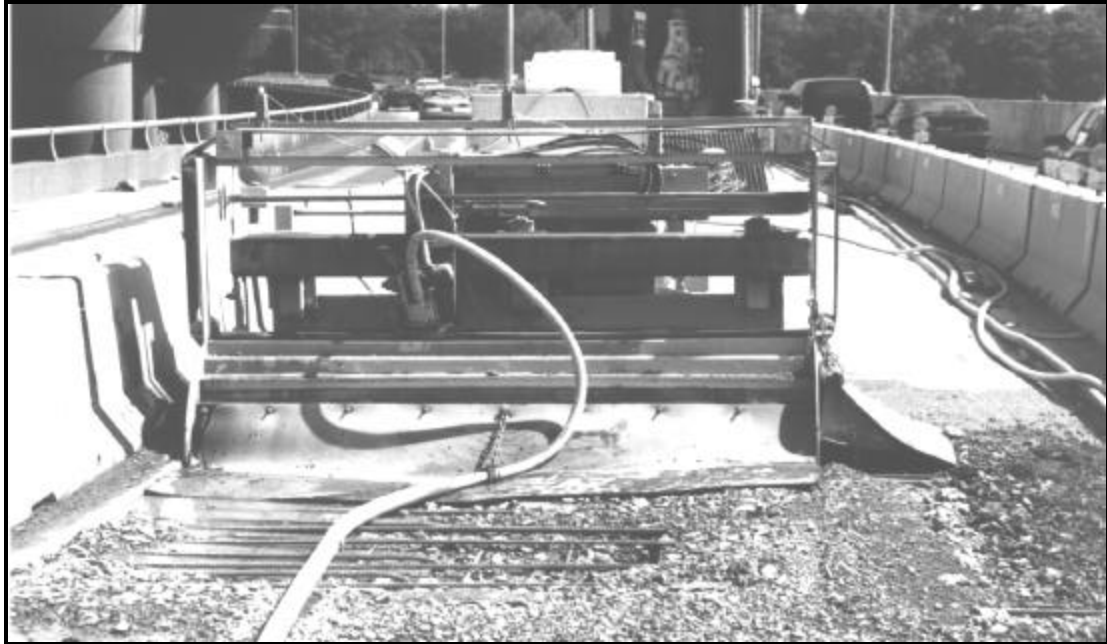


Figure 3. 16: Hydro-Demolition Equipment

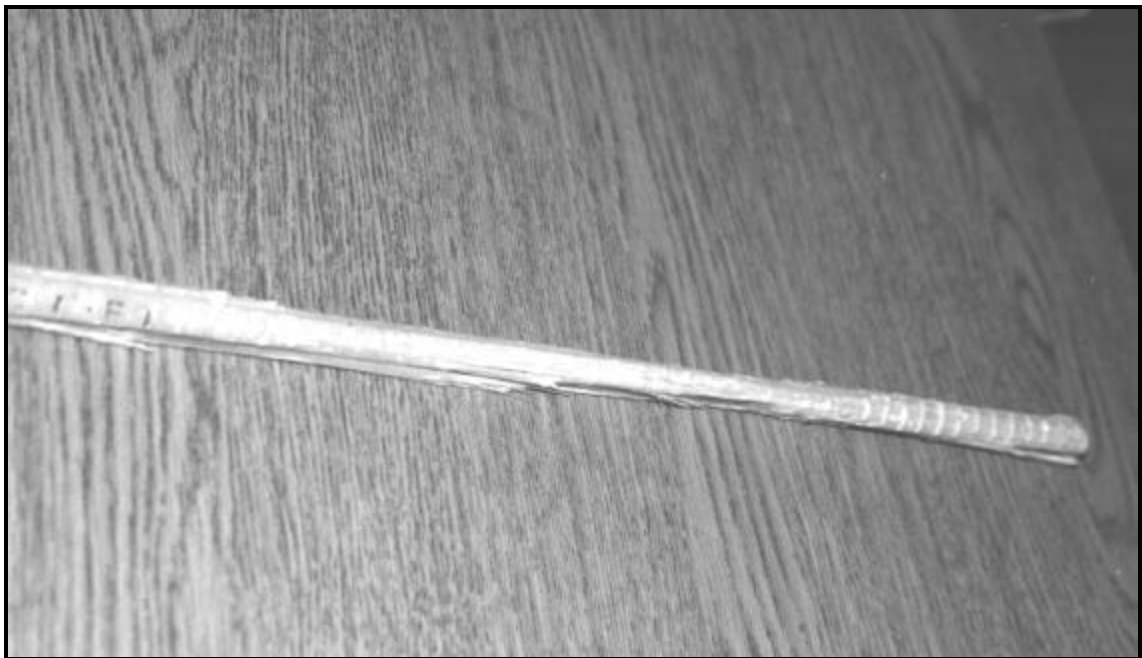


Figure 3. 17: Rebar after being Exposed to the Hydro-Demolition Equipment

3.7.3 Recommended Repair Procedure

Hydro-demolition is not a viable alternative in the repair of bridge decks reinforced with GFRP rebars. Therefore, the use of a jackhammer is required for the removal of concrete in repair operations. The following steps can be used as a guide in the concrete removal procedure:

- Step 1.** Locate a GFRP rebar in each of the two horizontal directions. Remove concrete in thin layers until at least one rebar in each direction is exposed.
- Step 2.** Using the rebars found in Step 1 as a guide, mark positions of adjacent rebars based on the spacing in the bridge plans.
- Step 3.** Remove the concrete around and underneath the rebars while taking precautions to avoid resting the tip of the hammer on the GFRP rebars. During the procedure the operator should avoid using the GFRP rebars as a guide for the jackhammer because this will remove surface deformations.

3.8 CONCLUSIONS AND RECOMMENDATIONS

During the constructability assessment, critical issues regarding the construction of concrete bridge decks with GFRP and ECS rebars were evaluated. It was found that direct application of the GFRP rebars in an actual bridge deck required few changes from conventional construction practice. The GFRP rebars can adequately support the weight of construction workers and equipment moving around on the GFRP reinforcing mat. In addition, the same reinforcement tying procedures and types of chair supports can be used with conventional ECS rebars and GFRP rebars.

The constructability test proved that the GFRP rebars could withstand bridge deck construction. Results showed that most problems encountered during the construction of the mock bridge deck reinforced with GFRP rebars were due to the plastic zip ties and the plastic chairs, rather than the GFRP rebars themselves. Problems with these plastic components could be overcome by using ECS chairs and ties instead. ECS ties are also much quicker and easier to use than the plastic zip ties, saving valuable construction time. Additional ECS chairs would still be required to reduce the flexibility of the GFRP mat. Deterioration of the steel ties and chairs due to the application of deicing salts is possible. However, the chances of full scale deck deterioration are small due to the relatively small volume of steel in the deck.

Differences in the GFRP rebar mat and conventional ECS rebar mats included the amount of required chair supports. In the constructability test, roughly three times as many individual plastic chair supports were required in the GFRP deck as individual steel chair supports in the ECS reinforced deck. Even with the large number of individual plastic chairs in the GFRP reinforced deck, the flexibility of the GFRP mat was much

greater than the ECS deck. During the construction of the Roger's Creek bridge deck approximately twice as many steel runner chairs were required to support the regions of the deck reinforced with GFRP rebars compared to areas reinforced with ECS rebars to provide the same stiffness.

No problems with floatation of the GFRP rebars in the wet concrete were observed in this study. However, floatation could be an issue when using high slump concrete.

The use of a jackhammer was identified as a viable method for removing concrete from a deck reinforced with GFRP rebars. Guidelines for the removal of concrete from a GFRP reinforced bridge deck were presented in the study (see Section 3.8.3). It was also determined that hydro-demolition should not be considered in the removal of concrete from a GFRP reinforced deck. Hydro-demolition damages the GFRP rebars during the concrete removal process.

Another difference in the GFRP and ECS reinforcing mats was the light weight of the GFRP rebars. Most of the construction workers on the Roger's Creek bridge commented on how much easier GFRP rebars were to place than ECS rebars. The light weight of the GFRP rebars reduced fatigue of the workers and sped up construction time.

4.0 EXPERIMENTAL DECK PANEL TESTING

4.1 INTRODUCTION

Figure 4.1 shows a cross section of a typical bridge deck designed to transfer vehicle loads from the riding surface to the main support girders of a bridge superstructure. Typically, bridge decks are designed to transfer loads to main support girders in a direction transverse to traffic flow. Twelve concrete deck panels were tested to evaluate the behavior of bridge decks in the transverse direction reinforced with different combinations of glass fiber reinforced polymer (GFRP) and epoxy coated steel (ECS) rebars.

The deck panels were constructed to simulate the two regions of a bridge deck highlighted in Figure 4.1. Different deck panel specimens were required to simulate conditions in these two regions due to different load orientations.

Three different reinforcing schemes were considered in the study. First, an ECS reinforcing scheme containing a top and bottom mat of ECS rebars. Second, a GFRP reinforcing scheme composed of a top and a bottom mat of GFRP rebars. Third, a Hybrid reinforcing scheme reinforced with a top mat of GFRP rebars and a bottom mat of ECS rebars.

This chapter includes a discussion of the experimental test methods used in the study and comparisons of recorded data from the different deck panels specimens including; (1) load versus displacement, (2) moment versus maximum concrete compressive strain, (3) crack behavior, and (4) failure mode. Comparisons of the test results to various analytical predictions and code specifications are provided in Chapter 5.

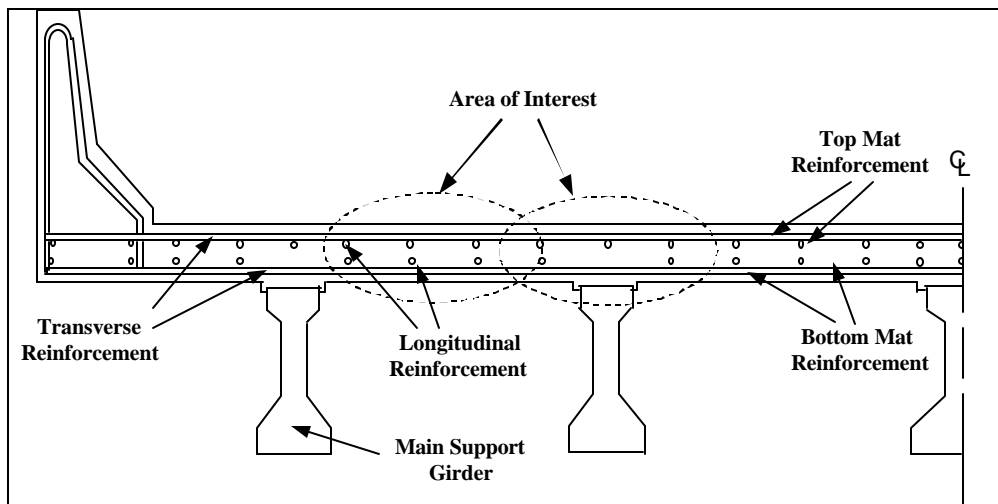


Figure 4. 1: Bridge Deck Cross Section Showing Regions of Interest

4.2 DECK PANEL SPECIMEN DESCRIPTION

This section provides details of the deck panels tests, including deck panel dimensions, reinforcement layouts, and material properties.

4.2.1 Deck Panel Dimensions

Twelve deck panel sections were load tested in the laboratory. Each deck panel had the same exterior dimensions shown in Figure 4.2, 2970 mm x 305 mm x 190 mm. The 2970 mm length of the deck panel was chosen to represent a 2740 mm clear span length during load testing. The span length is an average Kentucky main support girder spacing. Typically, Kentucky bridge decks are constructed with a 205 mm thickness. However, in design the top 15 mm of the deck is assumed to wear away during the service life of the bridge resulting in the remaining 190 mm thick deck used in the laboratory specimens. The width of the deck panels was selected based on an English unit width of 1 foot, or 305 mm.

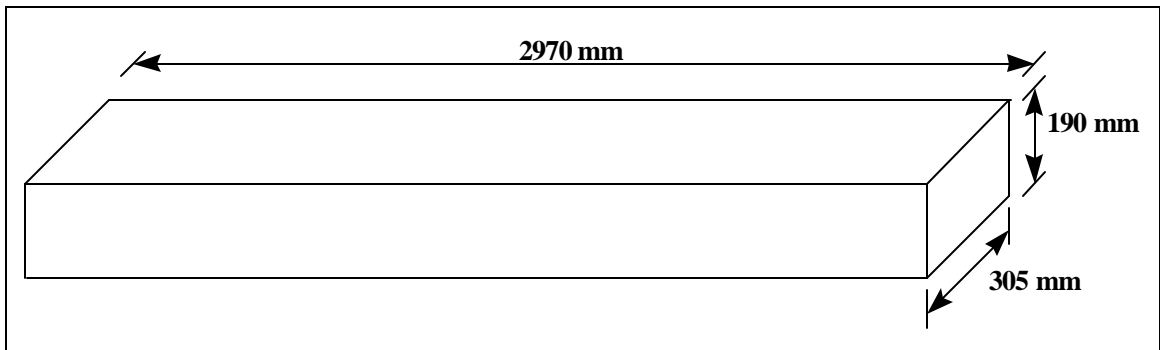


Figure 4. 2: Deck Panel Dimensions

4.2.2 Reinforcement Patterns

Figure 4.3 shows the orientation of the reinforcement in the ECS, GFRP, and Hybrid deck panels tested. This figure can be compared to Figure 4.1 to relate how the deck panel reinforcement layouts to an actual bridge deck. All three types of deck panels had the same reinforcement spacing in both the transverse and longitudinal directions shown in Figure 4.4. This spacing was based on the design of a simply supported Kentucky bridge deck reinforced with ECS rebars. The main girder spacing of this bridge deck corresponded with the 2740 mm span length used in the deck panel load tests. Identical reinforcement spacing was used in all specimens to permit a direct comparison of test results. It should be noted that the spacing of transverse reinforcement in an actual bridge deck reinforced with GFRP rebars would be less than a similar bridge deck reinforced with ECS rebars. However, Kentucky guidelines

recommend a minimum center to center spacing of bridge deck reinforcement of 125 mm.

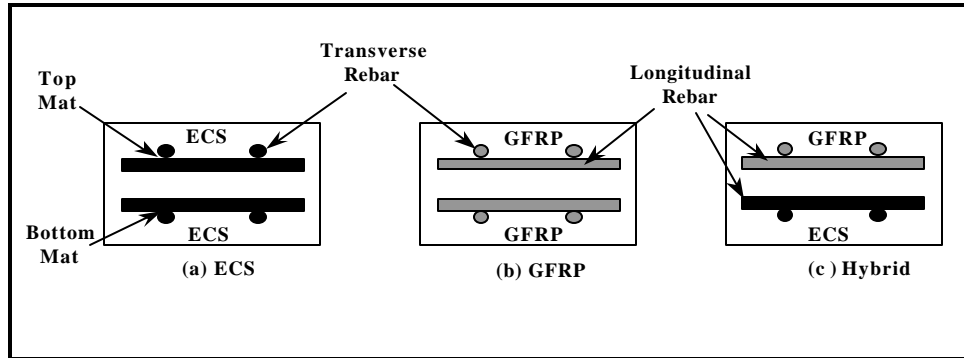


Figure 4. 3: Deck Panel Cross Sections

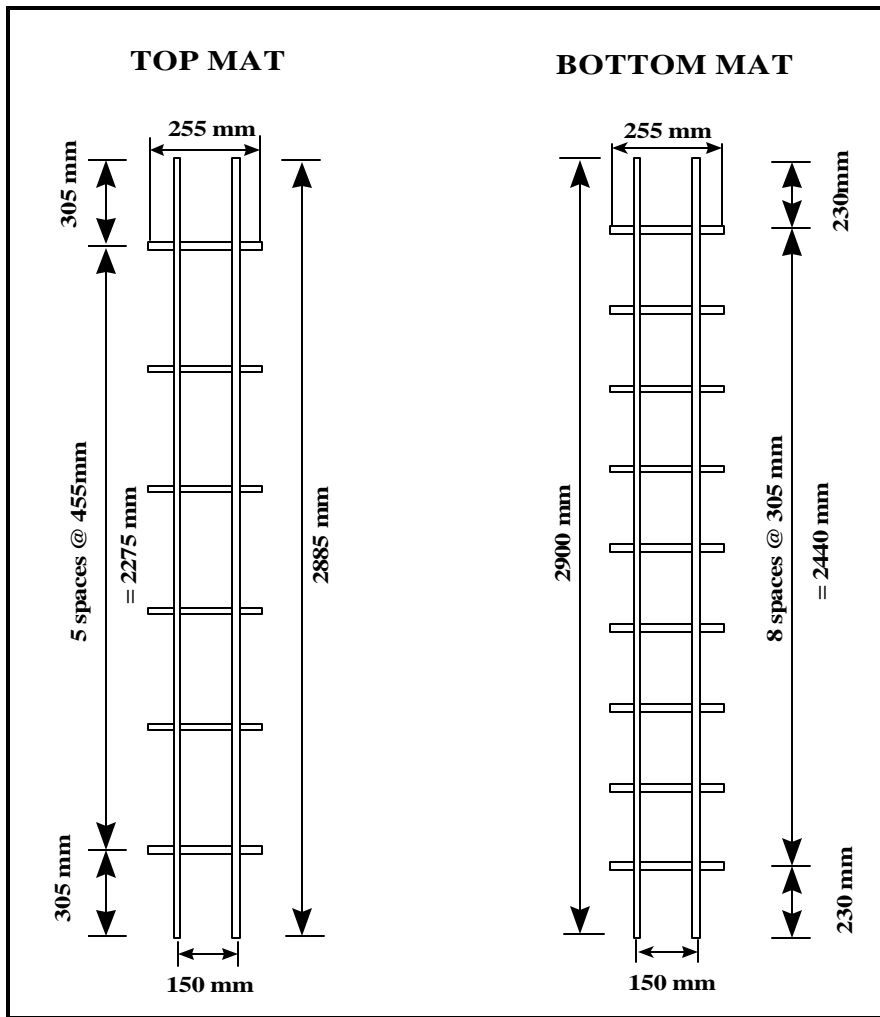


Figure 4. 1: Plan View of Reinforcing Pattern

Though the spacing of reinforcement was the same for all three deck panel types, the clear cover and reinforcement type varied as shown in Figure 4.5. The top clear cover for all of the specimen types was reduced by 15 mm from that of the to account for the future wearing surface discussed in Section 4.2.1. Four ECS reinforced deck panels were tested with a top clear cover of 50 mm and a bottom clear cover of 25 mm. These clear covers were based on Kentucky specifications. A larger top clear cover is specified to slow or prevent reinforcement corrosion related deterioration of the bridge deck.

Three GFRP reinforced deck panels were constructed with a top and bottom clear cover of 25 mm. The top clear cover was decreased by 25 mm compared to the ECS deck panels, since reinforcement corrosion should not be encountered in a bridge deck reinforced with GFRP rebars.

For the same reason, the 25 mm top clear cover used in the GFRP reinforced deck panels was used in the five Hybrid reinforced deck panels. A 25 mm bottom clear cover was also used in the Hybrid deck panels.

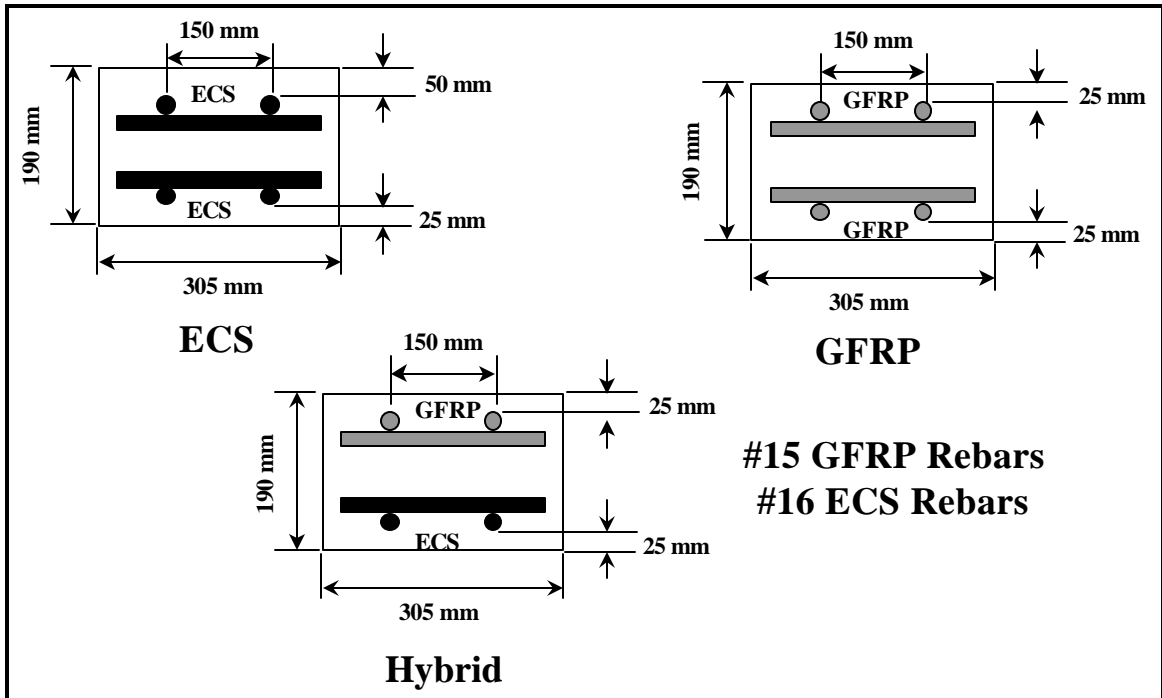


Figure 4. 5: Deck Panel Cross Sections

4.2.3 Moment Orientations in a Bridge Deck

A bridge deck acts as a continuous beam over the main support girders, as illustrated in Figure 4.6. Consequently, some regions of the bridge deck are subjected to positive moment (between main support girders) while other regions are subjected to

negative moment (over main support girders). Both moment orientations were considered in the deck panel load testing.

Due to differences in cover and reinforcement types, separate ECS and Hybrid reinforced deck panels were required to simulate the different moment orientations. Since both clear cover and reinforcement for the GFRP specimens were the same for the top and bottom mats there was no need to distinguish between positive and negative moment orientations. Hereafter, ECS and Hybrid reinforced deck panels are referred to based on their moment orientation during testing, i.e. negative moment ECS reinforced deck panels.

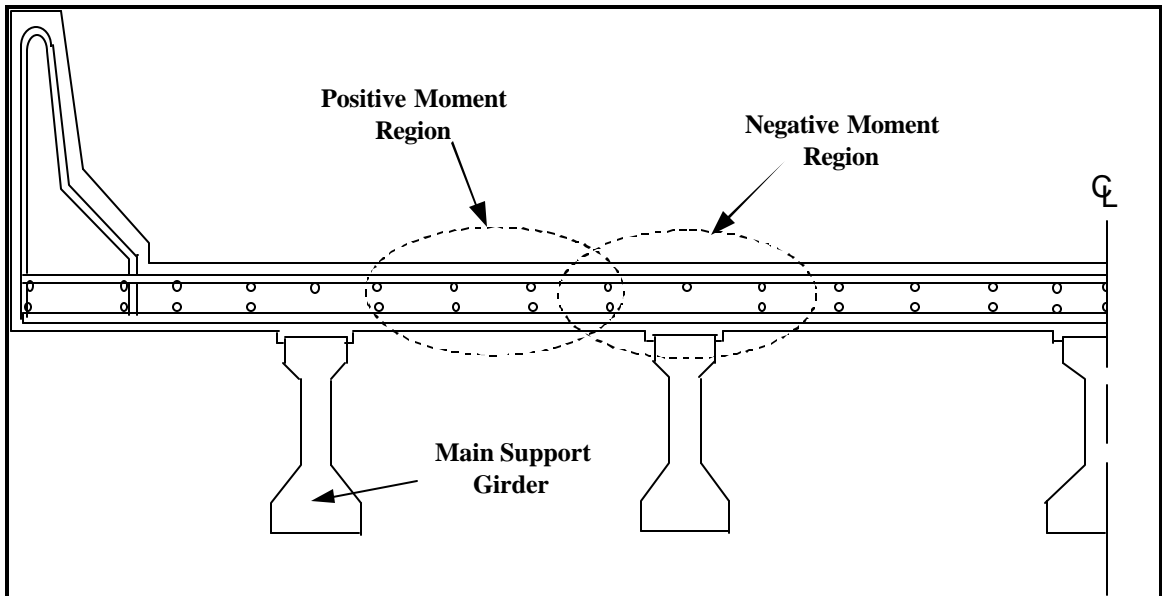


Figure 4. 6: Moment Orientations in an Actual Bridge Deck

4.2.4 Specimen Labeling

Each deck panel specimen was labeled using a sequence of three characters denoting the specimen type, moment condition, and specimen number. The first character denoted the deck panel type, an "E" for ECS, "F" for GFRP, and "H" for hybrid. The second character identified the representative moment orientation. A "P" was used for a positive (plus) moment, simulating flexural conditions between main support girders in an actual bridge deck. An "M" was used for a negative (minus) moment, simulating flexural loading conditions over main support girders in an actual bridge deck (see Section 4.2.3). The third character represented the specimen number. Table 4.1 shows the deck panel label, deck panel type, moment orientation, reinforcement geometry, and reinforcement location for the twelve specimens tested.

TABLE 4.1 SUMMARY OF DECK PANELS TESTED

Deck Panel Label	Panel Type	Moment Orientation	Compression Reinforcement		Tension Reinforcement	
			Rebars	Clear Cover (mm)	Rebars	Clear Cover (mm)
EM2 EM3	ECS	Negative ^a	2 - #16 ECS	25	2 - #16 ECS	50
EP1 EP3	ECS	Positive ^b	2 - #16 ECS	50	2 - #16 ECS	25
F1 F2 F3	GFRP	N. A.	2 - #15 GFRP	25	2 - #15 GFRP	25
HM1 HM2	Hybrid	Negative ^a	2 - #16 ECS	25	2 - #15 GFRP	25
HP1 HP2 HP3	Hybrid	Positive ^b	2 - #15 GFRP	25	2 - #16 ECS	25

^a deck panels were tested to simulate negative moment conditions existing in a bridge deck over main support girders (see Section 4.2.3).
^b deck panels were tested to simulate positive moment conditions in a bridge deck between main support girders (see Section 4.2.3).

4.2.5 Material Properties

Kentucky's standard Class AA concrete bridge deck concrete mix was used in the construction of the deck panels. Table 4.2 shows a summary of the mix design taken from the Kentucky's Standard Specifications for Road and Bridge Construction (1998).

Two 150 mm x 305 mm concrete cylinders were cast for each deck panel and tested within a day of the respective deck panel test. Table 4.3 shows a summary of the compression test results for each of the deck panel's cylinders. As the table shows, there was a substantial difference in concrete strength between deck panels. The variation was due mainly to the length of time required to cast the specimens. It took the research team approximately 2 hours to place the concrete. Cylinders for three of the deck panels, F1, F3, and HM1, failed to meet the 28-day compressive strength criterion shown in Table 4.2.

Properties for the ECS and GFRP rebars used in the study are presented in Table 4.4 and Figure 4.7.

TABLE 4.2 CONCRETE MIX DESIGN
(Taken from the Kentucky Standard Specifications for Road and Bridge Construction (1998))

Class of Concrete	Approximate Percent Fine to Total Aggregate		Maximum Free Water (kg/kg)	28-Day Compressive Strength (MPa)	Slump (mm)	Minimum Cement Factor (kg/m ³)
	Gravel	Stone				
AA	36	40	0.42	30	50-100	368

TABLE 4.3 CONCRETE CYLINDER COMPRESSION STRENGTHS

Deck Panel Label	Compressive Strength ^a (MPa)		
	Cylinder 1	Cylinder 2	Average
EM2	41.97	40.20	41.44
EM3	45.99	46.36	46.17
EP1	41.67	N. A.	41.67
EP3	46.92	45.16	46.03
F1	29.53	27.65	28.59
F2	29.65	30.58	30.11
F3	27.36	26.68	27.02
HP1	46.50	48.80	47.65
HP2	46.38	50.06	48.22
HP3	41.26	44.55	42.91
HM1	28.04	28.41	28.23
HM2	31.34	30.26	30.80

^a Concrete Age at time of cylinder tests ranged between 9 and 11 months.

TABLE 4.4 REBAR PROPERTIES

Rebar Type	Diameter of Rebar (mm)	Area of Rebar (mm ²)	Yield Strength (MPa)	Stress Orientation	Ultimate Strength (MPa)	Modulus of Elasticity (MPa)
#16 ECS	16	199	486.9	Tension/ Compression	653.4	196,490
#15 GFRP	15	176	N. A.	Tension	612	40,045
				Compression	325	42,510

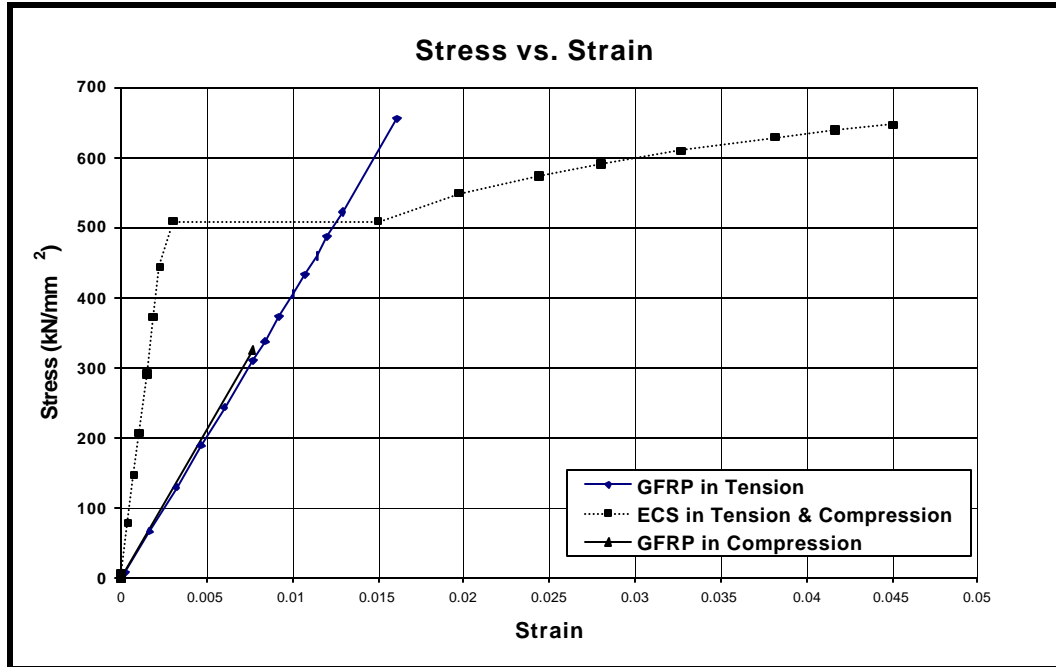


Figure 4. 7: Stress versus Strain Properties of the Rebars Used

4.2.6 Preparation of Deck Panel Specimens

Form-work for the twelve deck panel specimens was constructed with plywood and timber sections. Rebars were anchored inside the forms with individual steel chairs and wire ties. All twelve specimens and their respective concrete cylinders were cast with a single load of concrete. After the concrete was placed, the exposed surfaces of the specimens and the compressive cylinders were sprayed with a curing compound to prevent water from evaporating at the surface. The specimens were then covered with plastic sheeting.

The deck panel specimens and concrete cylinders were left at the casting site for approximately one month. Then they were moved to the laboratory, a distance of approximately 15 km. Testing of the deck panels began approximately 9 months after the concrete was placed. The final specimen was tested about 11 months after the deck panels were cast.

4.3 DECK PANEL TEST SETUP

4.3.1 Test Frame

Figure 4.8 shows a schematic elevation view of the deck panel test frame whose photo is shown in Figure 4.9. The deck panels were loaded upward rather than downward in the tests to facilitate collection of crack data and to increase safety. Equally

spaced four point loading was used to provide a constant moment region between the load application points. Dimensions of the test setup were the same for all of the deck panels except for specimen F1.

A 445 kN hydraulic jack operated with a small electric pump was used to apply load. Since the of load was applied under load control, no post ultimate behavior of the deck panels could be documented.

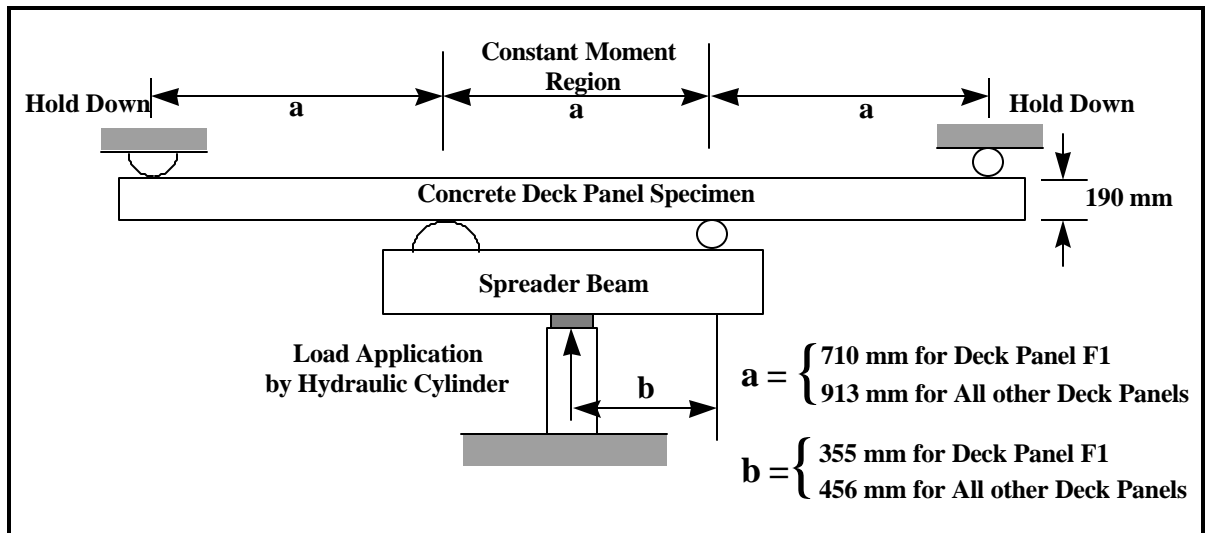


Figure 4. 8: Deck Panel Load Test Setup



Figure 4. 9: Deck Panel Load Test Setup

4.3.2 Instrumentation and Measurements Recorded

The instrumentation used during the deck panel testing is shown in Figure 4.10. One load cell, six linear variable displacement transducers (LVDTs), and two strain gages were used in all of the tests. Two additional strain gages were used in the test of deck panel F1.

Figure 4.10 shows the position of the load cell during the deck panel test. The load measured was equal to the total load applied by the hydraulic cylinder. This load was then divided by the spreader beam into two equal loads applied to the deck panel. All of the load data presented is based on the total load applied by the hydraulic jack.

Since the supports of the load frame could displace a substantial amount during testing, displacement measurements were required at the supports in addition to the midspan. Twisting of the deck panel during the test was also a consideration requiring two LVDTs at each location. Midspan displacements presented in later discussions were computed by averaging the displacement of the two midspan LVDTs and subtracting the average of the four support LVDTs.

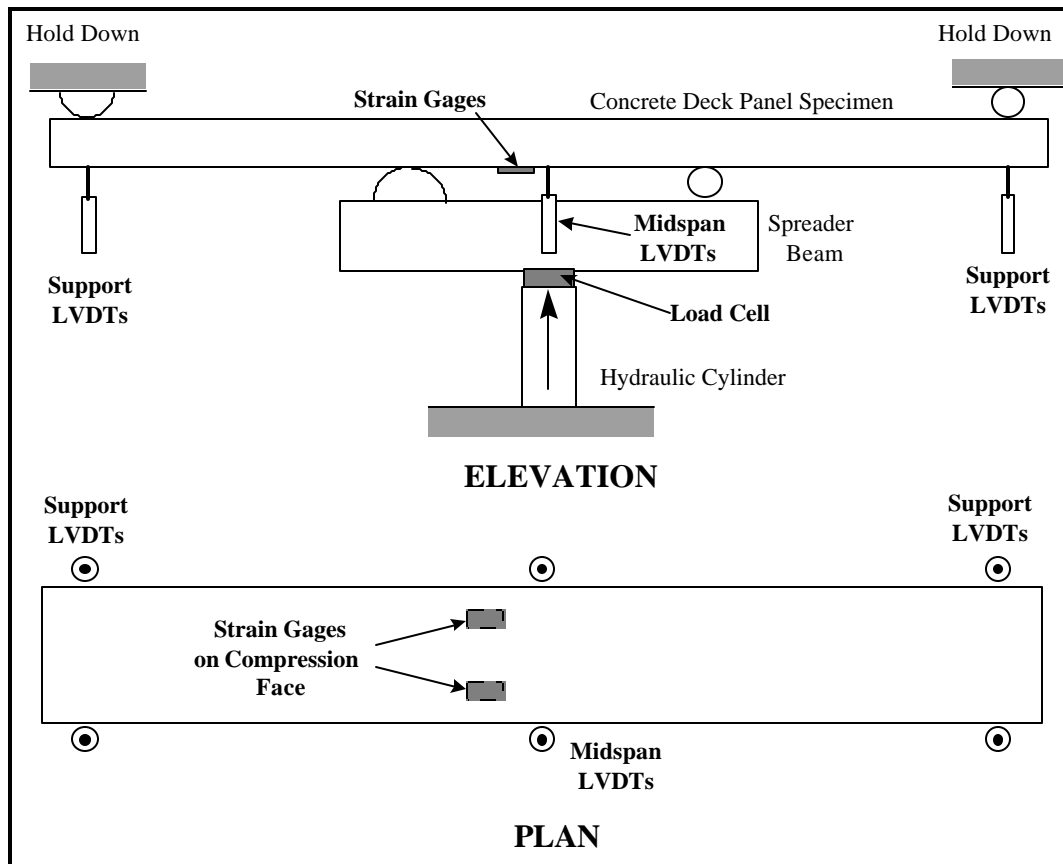


Figure 4. 10: `Instrumentation Locations

4.3.2.1 Strain Measurements

Figure 4.10 shows the location of the strain gages used on the compressive face of the deck panels. For the majority of the tests, two reusable strain gages were employed. Micro-Measurements foil strain gages were used to measure compressive strains during the testing of deck panels F1 and F2.

Figure 4.11 shows a reusable strain gage used during the study. The gages had an active length of 75 mm equal to approximately four times the maximum concrete aggregate size of 19 mm. To prevent the reusable strain gages from being damaged they were removed at approximately 60% of the predicted deck panel failure load. Therefore, no values of concrete compressive strain were recorded by the reusable gages at or near the ultimate load of the deck panels.

Disposable 100 mm foil strain gages were used in the testing of deck panels F1 and F2. The active length of these gages was approximately 5 times the maximum concrete aggregate size. These were not removed during load testing. In every case the strain gages, reusable and foil, were applied in pairs. The data presented in subsequent sections is the average of the two gages in the respective pair.

Tensile strains were not recorded during the deck panel load tests, since it would have required mounting gages on the rebars. Mounting the gage on a rebar and the wires associated with it would alter the cracking behavior of the deck panel. Since crack information was a focus of the study, it was decided to omit rebar tensile strains.

During the deck panel testing, it was observed that the relative distance between the strain gage and the nearest crack influenced the recorded strains. This was apparent when the strain data and the crack mapping information were compared for various load levels.



Figure 4. 11: Reusable Strain Gage

4.3.2.2 Crack Measurements

Crack width and locations were recorded manually during the testing of the deck panels. Figure 4.12 shows the grid used to facilitate crack recording during testing of the specimens tested with a 2740 mm span length. Grid dimensions were altered slightly during the test of deck panel F1 with a span length of 2130 mm.

During the testing, load application was halted at the initiation of the first crack. Crack widths and locations relative to the grid were then measured at the three points circled in Figure 4.12 for each transverse crack within the grid. After initiation of the first crack, load application was halted at several levels (at approximately 5 kN increments). This was continued up to a load of approximately 60% of the predicted ultimate load. At this point it was considered unsafe to be near the specimens and measurements were no longer recorded.

Crack widths were measured using the crack comparator shown in Figure 4.13. Locations of the cracks were measured using a carpenters' scale with increments to the nearest 1.5 mm ($1/16^{\text{th}}$ inch).

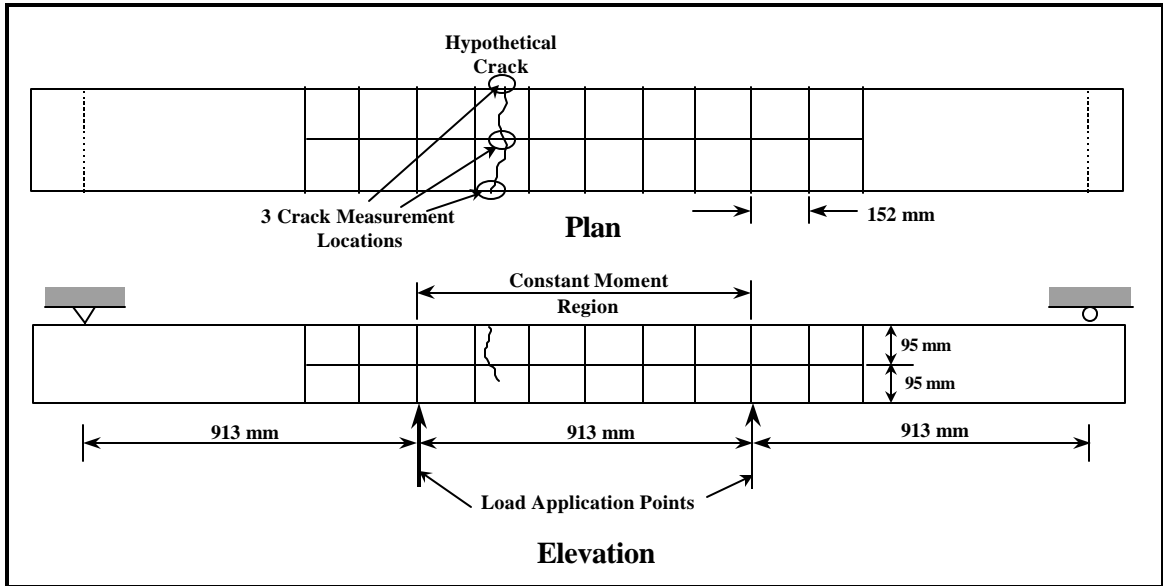


Figure 4. 12: Crack Recording Grid & Measurement Locations

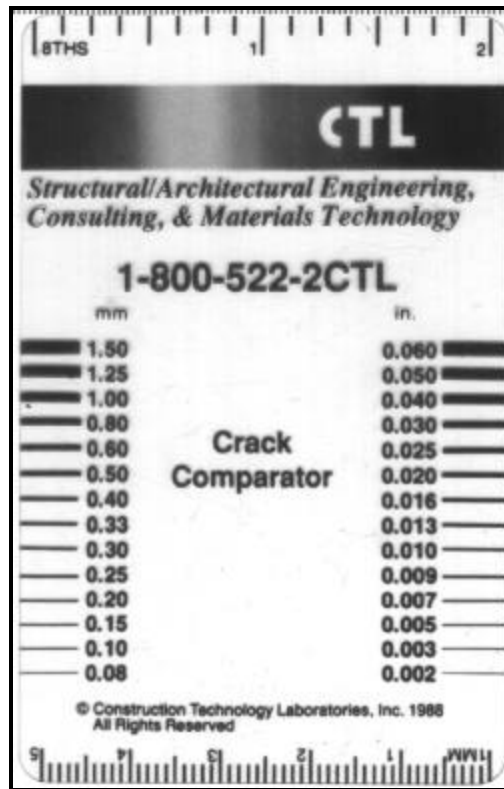


Figure 4. 13: Crack Comparator used to Measure Crack Widths during the Deck Panel Testing

4.4 DECK PANEL LOAD TEST RESULTS

This section presents the test results for each deck panel type. Comparisons of test results between the different deck panels are provided in Section 4.5. Deck panel test results include: load versus displacement behavior, moment versus compressive strain relations, and crack behavior.

4.4.1 Load versus Midspan Displacement

Figure 4.14 shows the load versus midspan displacement results for the two negative moment (i.e. simulating load conditions over main support girders in an actual bridge deck, see Section 4.2.3) ECS reinforced deck panels. Slopes of the two curves are similar in every region of the plot, but, the values differ by a constant load. This is also shown in the numerical data of Table 4.5. Figure 4.15 shows a similar phenomenon when comparing the positive moment (i.e. simulating load conditions between main support girders in an actual bridge deck, see Section 4.2.3) ECS specimens, EP1 and EP3. As the figures show, the stiffness represented by the slopes of the curve, is the same for the respective specimen types. Two possible explanations for the differences in load could be: (1) a mix up in compressive cylinder information resulting in significant differences in concrete strength between the two specimens, or (2) an initialization error of the load cells prior to testing.

Load versus displacement curves for the three GFRP deck panels are shown in Figure 4.16. The deck panels were not tested in numerical order. Deck panel F3 was tested first, followed by deck panel F2. Results of the first two deck panels prompted a change in span length for the final deck panel labeled F1. The difference in span length is reflected by a difference in stiffness shown in the figure.

The failure load and behavior of the GFRP specimens could not be predicted with confidence prior to the testing of specimen F3. For this reason most of the electronic measuring equipment (e.g., LVDTs and strain gages) was removed well before failure, at a load of about 34 kN, to avoid instrument damage. Note the termination of the curve in Figure 4.16. Since the load cell was not removed, the failure load was recorded and shown in Table 4.5.

After observing the failure mode of deck panel F3 it was decided that deck panel F2 could be tested to failure without risk to the instrumentation. The test results presented in Figure 4.16 show that the responses of the two deck panels, F3 and F2, follow each other closely up to the point where the equipment was removed from deck panel F3.

Specimens F3 and F2 failed between an active load point and a support in a shear-flexure region of the deck panel. The load was less than predicted by ACI 318M-95 relations for shear and flexural failure. To determine what affect the span length had on ultimate strength of the GFRP panels, the span length of deck panel F1 was reduced from

2740 mm to 2130 mm. The change in span length is reflected in the load displacement plot by the difference in slope and the displacement at failure. The failure results for these deck panels are discussed in Section 4.5.6.

The load versus displacement plots for the negative moment Hybrid deck panels tested are shown in Figure 4.17. During the testing of deck panel HM2 a LVDT plunger was prevented from moving resulting in a region of erroneous data. The data that should be disregarded is circled in the figure. At approximately 50 kN the LVDT obstruction was removed. Data after the circled region is still considered accurate. Except for the circled region of curve HM2, the two Hybrid deck panels show good correlation.

Results of the positive moment Hybrid deck panels are shown in Figure 4.18. The test results show good correlation. The curve paths follow closely up to near failure, where some differences occur. The figure also shows the hysteresis exhibited during the unloading of deck panel HP3.

TABLE 4.5 SUMMARY OF DECK PANEL SPECIMENS LOAD VERSUS DISPLACEMENT BEHAVIOR

Deck Panel Label	Panel Reinforcement		Cracking Load, P	Ultimate Load, P	Displacement @ Corresponding Load	
	Rebars in Compression	Rebars in Tension	(kN)	(kN)	Cracking (mm)	Ultimate (mm)
EM2	2 #16 ECS	2 #16 ECS	25.09	64.94	1.50	61.47
EM3	2 #16 ECS	2 #16 ECS	17.14	55.42	1.14	59.69
EP1	2 #16 ECS	2 #16 ECS	24.36	80.96	1.78	55.37
EP3	2 #16 ECS	2 #16 ECS	20.12	73.35	2.00	53.32
F1	2 #15 GFRP	2 #15 GFRP	21.71	53.56	1.68	37.34
F2	2 #15 GFRP	2 #15 GFRP	21.18	56.58	1.16	80.01
F3	2 #15 GFRP	2 #15 GFRP	19.46	58.36	1.30	N. A.
HM1	2 #16 ECS	2 #15 GFRP	19.59	57.07	2.64	79.50
HM2	2 #16 ECS	2 #15 GFRP	20.85	55.20	1.56	82.04
HP1	2 #15 GFRP	2 #16 ECS	20.12	80.00	0.99	83.57
HP2	2 #15 GFRP	2 #16 ECS	21.91	77.44	1.00	58.42
HP3	2 #15 GFRP	2 #16 ECS	24.62	77.88	1.44	19.81

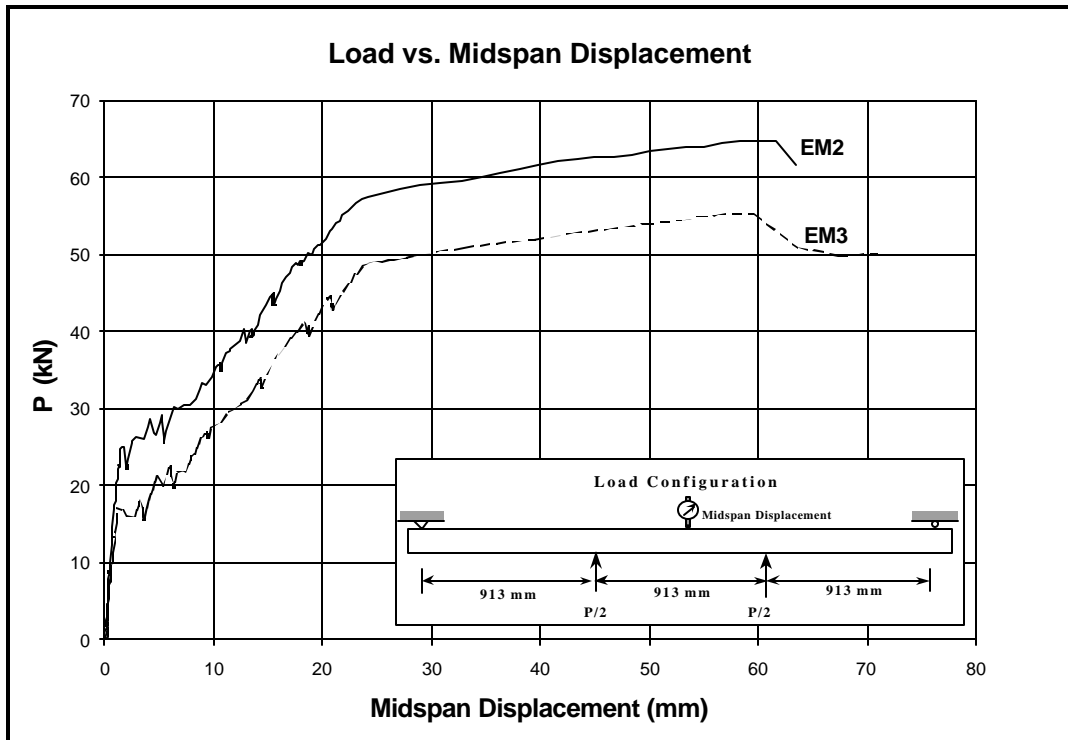


Figure 4. 14: Load versus Midspan Displacement for the Negative Moment ECS Reinforced Deck Panels

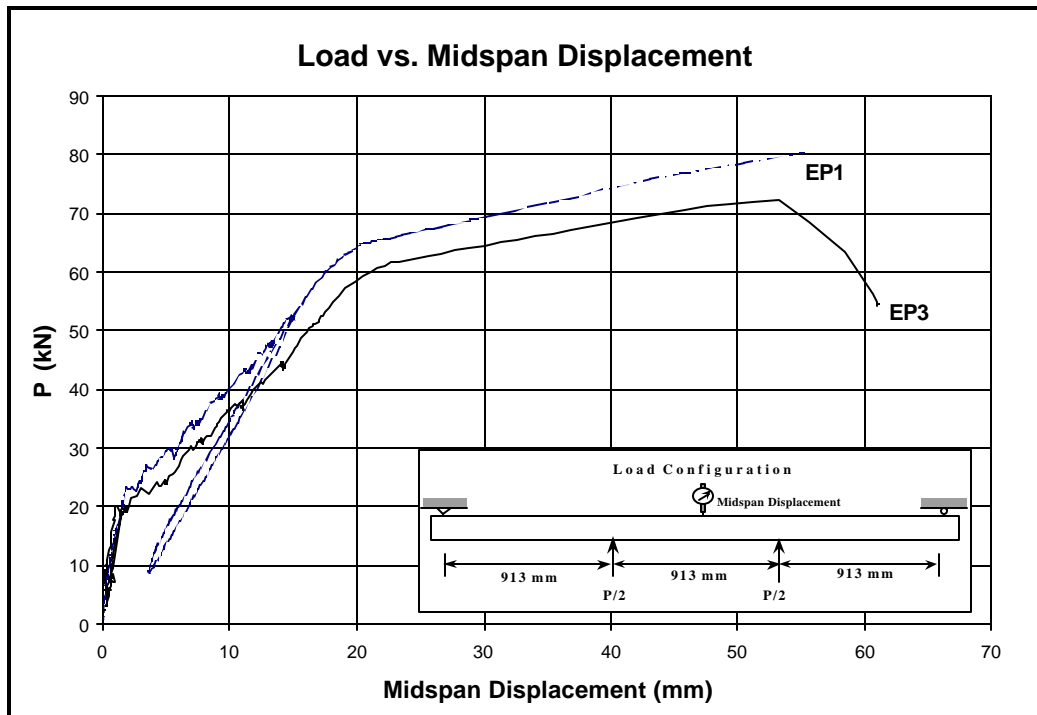


Figure 4. 15: Load versus Midspan Displacement for the Positive Moment ECS Reinforced Deck Panels

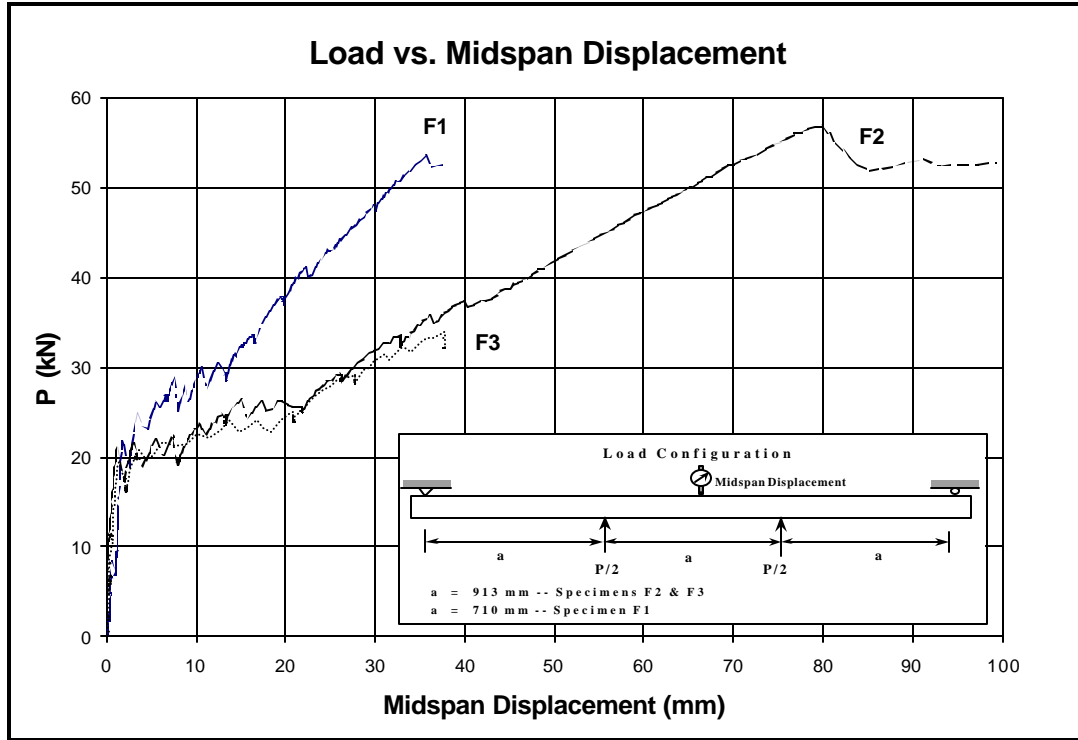


Figure 4. 16: Load versus Midspan Displacement for the GFRP Reinforced Panels

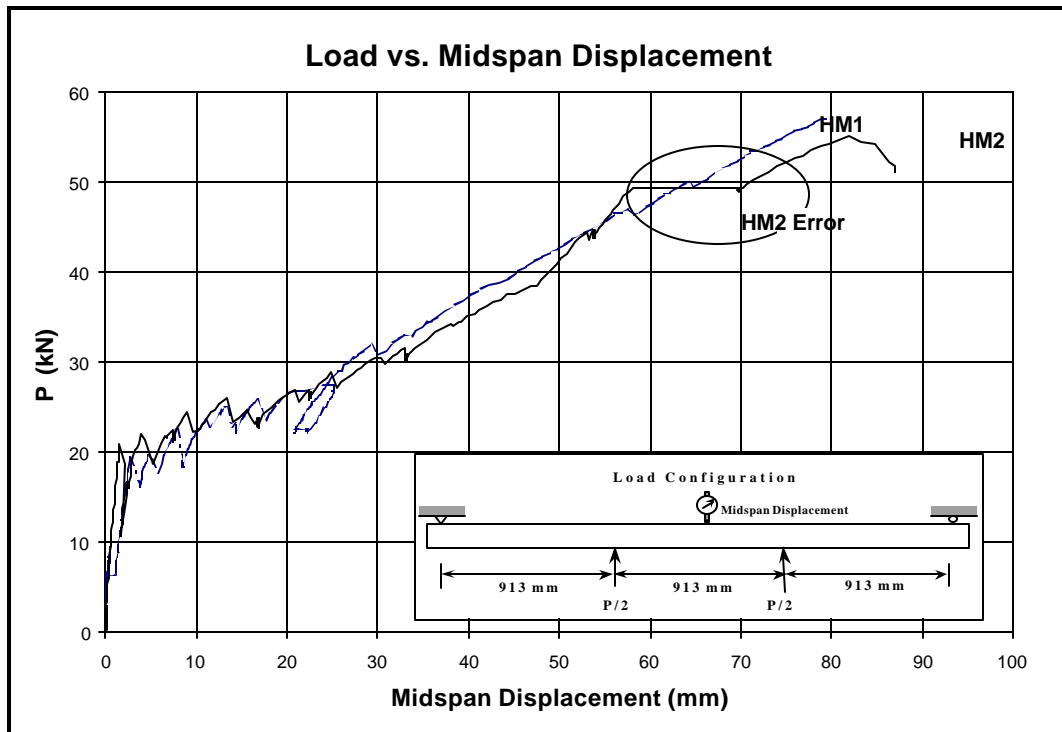


Figure 4. 17: Load versus Midspan Displacement for the Negative Moment Hybrid Reinforced Deck Panels

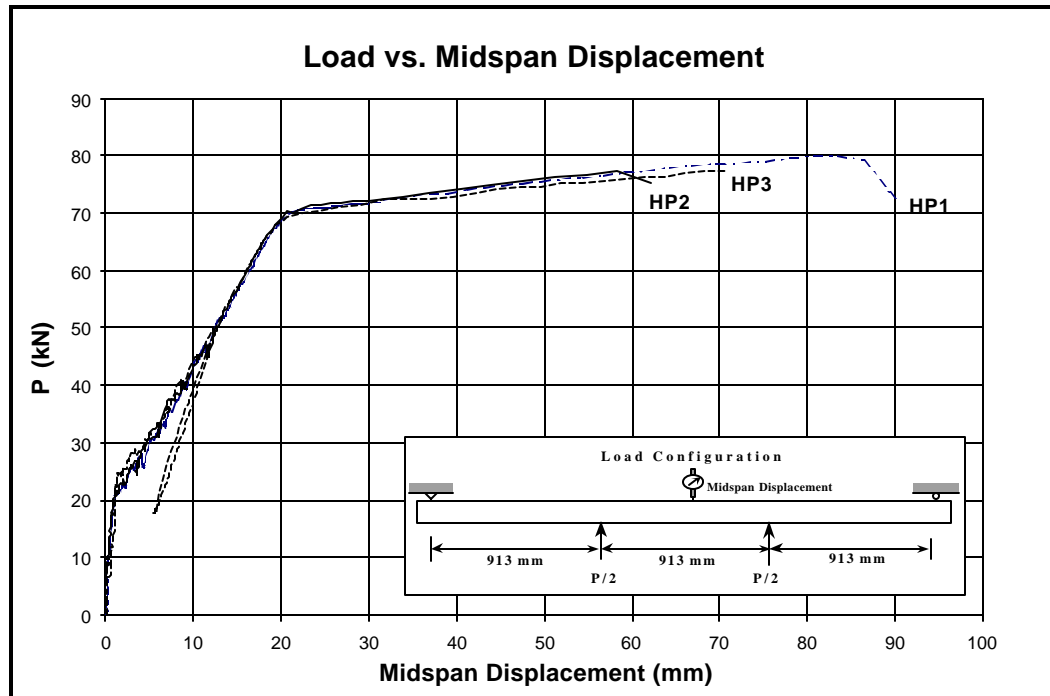


Figure 4. 18: Load versus Midspan Displacement for the Positive Moment Hybrid Reinforced Deck Panels

4.4.2 Moment versus Maximum Compressive Strain in Concrete

Figures 4.19 through 4.24 show the moment versus maximum compressive strain results for the deck panels grouped by panel type. As mentioned in Section 4.3.2.1, termination of the moment versus compressive strain plots does not represent failure except in specific cases discussed subsequently.

Moment versus maximum compressive strain behavior for the two negative moment ECS deck panels, EM2 and EM3, is shown in Figure 4.19. Tests of the two deck panels do not correlate well. This was most likely due to differences in concrete strength shown in Table 4.3 or the location of cracks relative to the strain gages or a combination of the two (See Section 4.3.2.1).

Figure 4.20 shows the maximum compressive strain behavior of the two positive moment ECS reinforced deck panels. The plot correlates well between the specimens up to a moment of approximately 17,500 kN-mm. At that point, the EP1 curve shows a sudden reduction. This was most likely the result of either a crack forming at the gage location a slip in the glue attaching a strain gage to the specimen or a combination of both.

Figure 4.21 shows moment versus maximum compressive strain in the concrete for deck panel F1. Since the span length of deck panel F1 was less than the span length

of deck panels F2 and F3, it is presented separately. A total of four strain gages were used during the test of deck panel F1, two reusable and two foil gages. The respective strain gage results were averaged and presented as two curves on the plot in Figure 4.21. The two curves show good agreement up to the cracking load where they diverge slightly, most likely due to the relative distance between the nearest crack to the strain gages. For this specimen, the foil strain gages recorded strain up to failure of the deck panel.

Results for deck panels F2 and F3 are shown in Figure 4.22. Data was collected for deck panel F2 using foil strain gages. The gages recorded the compressive strain of the specimen up to a moment of approximately 21,800 kN-mm when the voltage of the strain gage surpassed the measuring capacity of the data acquisition equipment. Therefore, the termination of the F2 curve does not represent the conditions at deck panel failure. Reusable strain gages were used in the test of deck panel F3 and were removed at a moment of approximately 12,800 kN-mm. Curves for deck panels F2 and F3 do not show good agreement due to differences in the relative distance between the strain gages and nearest crack locations.

Moment versus maximum compressive concrete strain for the negative moment Hybrid deck panels is shown in Figure 4.23. The curves follow each other closely up to the point where the strain gages were removed.

Results for the positive moment Hybrid deck panels are shown in Figure 4.24. All three deck panels show good agreement with the exception of the jump in deck panel HP2 strain at a moment of approximately 17,600 kN-mm. The jump was the result of a slip in the glue attaching the reusable strain gage to the deck panel.

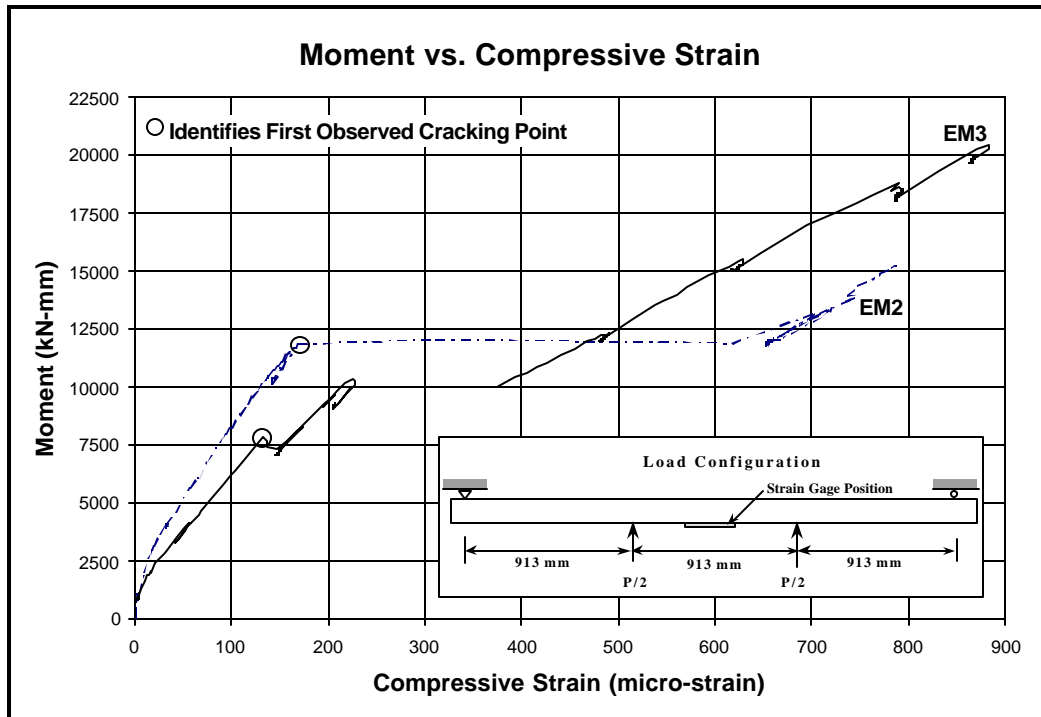


Figure 4.19: Moment versus Maximum Compressive Strain in Concrete for the Negative Moment ECS Reinforced Deck Panels

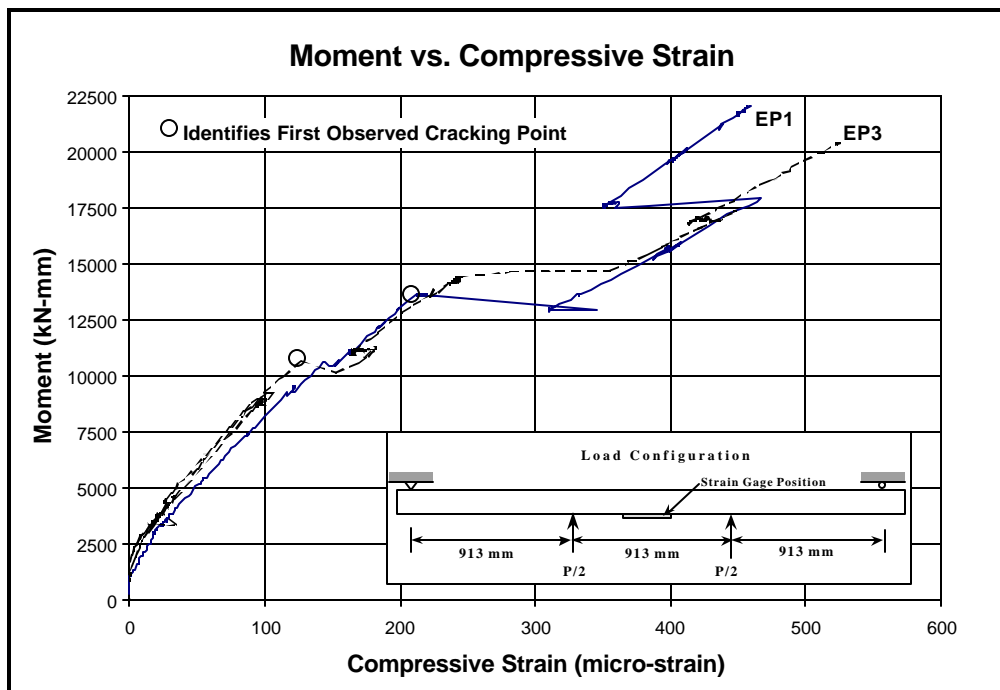


Figure 4.20: Moment versus Maximum Compressive Strain in Concrete for the Positive Moment ECS Reinforced Deck Panels

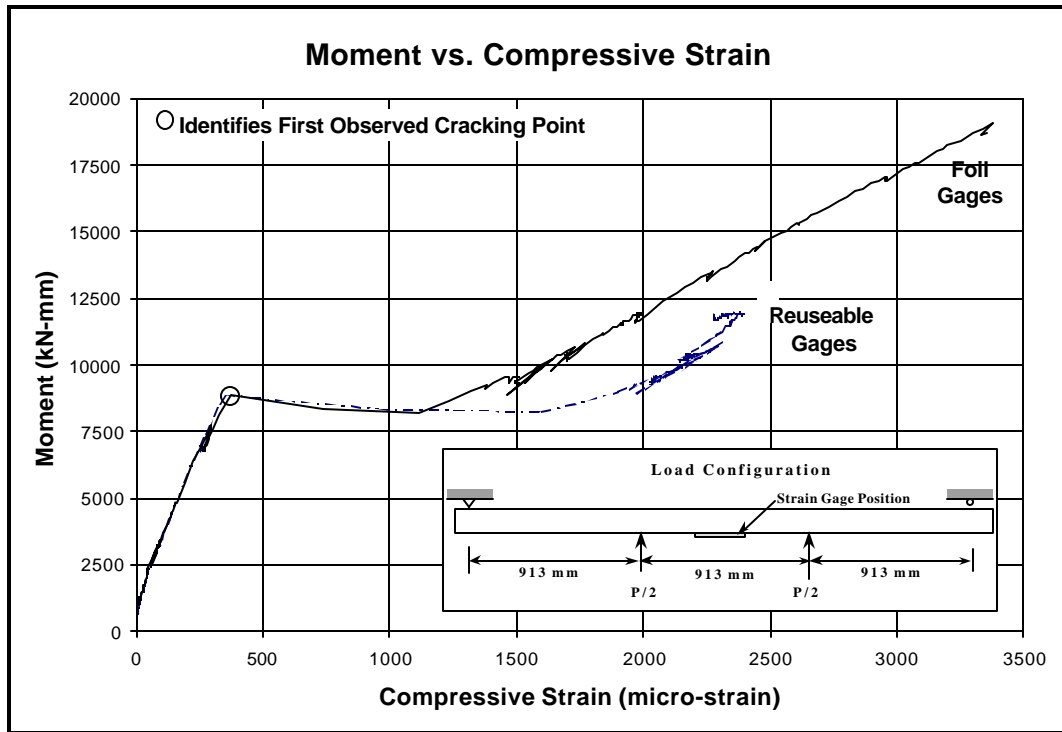


Figure 4. 21: Moment versus Maximum Compressive Strain in Concrete for the GFRP Reinforced Deck Panel F1

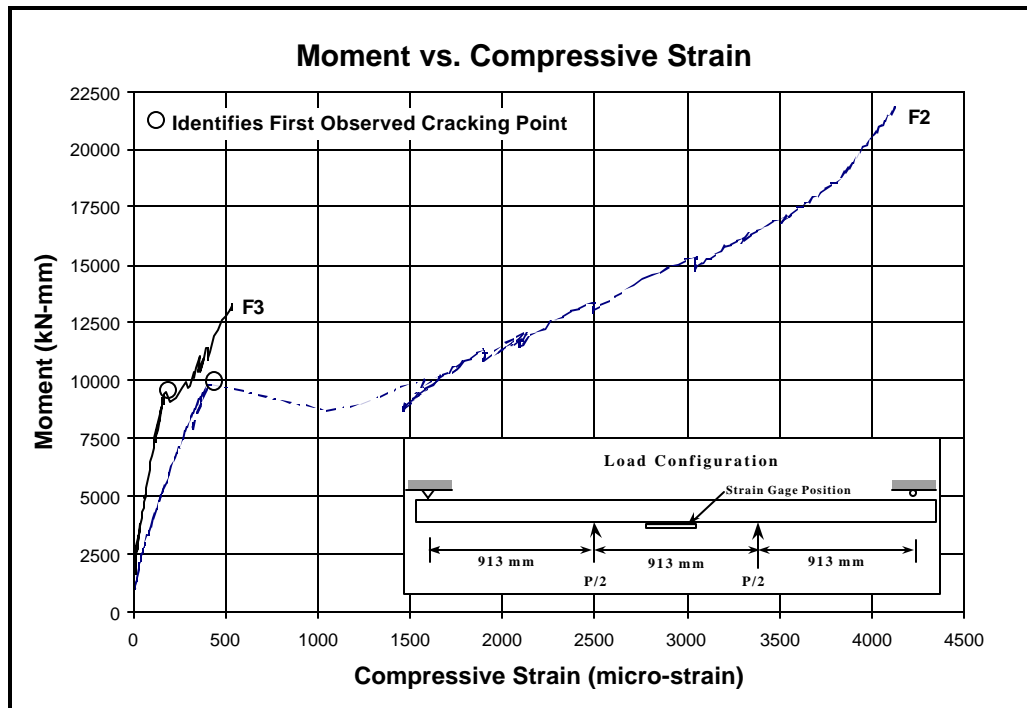


Figure 4. 22: Moment versus Maximum Compressive Strain in Concrete for the GFRP Reinforced Panels F2 & F3

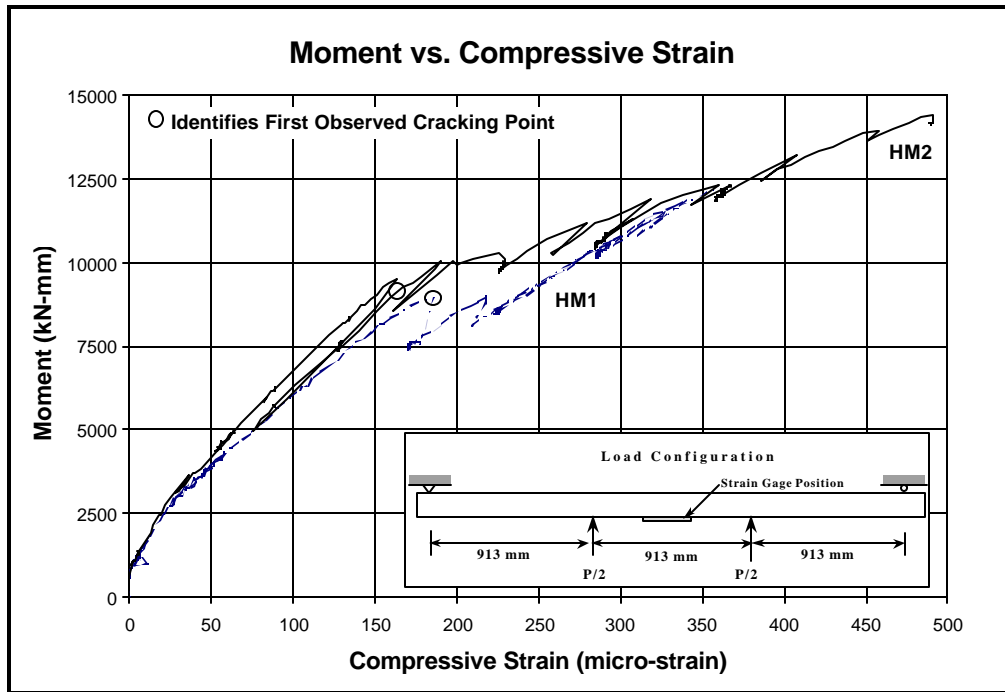


Figure 4. 23: Moment versus Maximum Compressive Strain in Concrete for the Negative Moment Hybrid Deck Panels

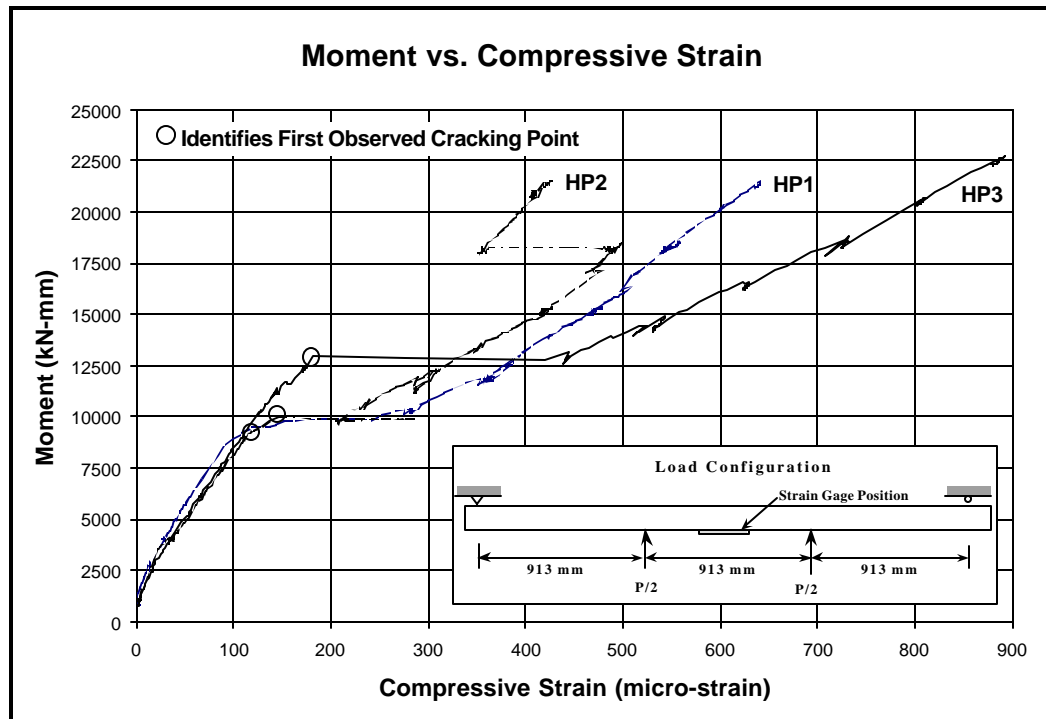


Figure 4. 24: Moment versus Maximum Compressive Strain in Concrete for the Positive Moment Hybrid Deck Panels

4.4.3 Maximum Crack Widths

Using the crack information taken during the load tests (see Section 4.3.2.2 for details of the data gathering techniques) maximum and average crack widths at each load point were determined. The final crack widths were recorded at approximately 60% of the deck panels predicted ultimate load. After this load, it was considered unsafe to be near the test specimen.

Both ACI and AASHTO specifications limit maximum crack widths. Therefore these are presented here rather than average crack widths. A comparison of maximum and average crack width results for specimens EP1 and F2 is shown in Figure 4.25. This plot can be considered representative of all the deck panel specimens. Appendix A includes moment versus average crack width at each load level for all of the specimens tested.

Results for both the positive and negative moment ECS reinforced deck panels are shown in Figure 4.26. The plot shows that in general, the negative moment deck panels had a greater maximum crack width than the positive moment deck panels for a given load. This was due to the difference in reinforcement clear cover shown in Table 4.1. Figure 4.27 shows the moment versus maximum crack width data for the all GFRP reinforced deck panels. As shown in Figure 4.8, the span length during the test of deck panel F1 was reduced from 2740 mm used in the other deck panel tests to 2130 mm. Deck panel F1 had a smaller maximum crack width at a given load than the other two GFRP reinforced deck panels, however, the difference was less than that between the other two. Based on these test results, the maximum crack width for deck panels of this type is a function of the applied moment.

Results for the hybrid deck panels are shown in Figure 4.28. The maximum crack widths for the negative moment deck panels are greater than those of the positive moment deck panels for a given moment. This was due to the different top and bottom mat rebar types for two specimens shown in Table 4.7.

In several instances, the measured maximum crack width measured did not increase with an increase in moment. This phenomenon was observed in deck panels, EP1, HP1, and HP2, and is circled in Figures 4.26 and 4.28. The formation of new, smaller, cracks was observed in those regions of the deck panels near the largest maximum crack width.

TABLE 4.6 SUMMARY OF MAXIMUM CRACK WIDTH DATA

Deck Panel Label	Reinforcement		First Crack Measurement		Final Crack* Measurement	
	Compression	Tension	Moment	Max. Crack Width	Moment	Max. Crack Width
			(kN-mm)	(mm)	(kN-mm)	(mm)
EM2	2 #16 ECS	2 #16 ECS	11,592	0.1270	20,336	0.5080
EM3	2 #16 ECS	2 #16 ECS	8134	0.1778	20,336	0.7620
EP1	2 #16 ECS	2 #16 ECS	9151	0.0508	23,387	0.4064
EP3	2 #16 ECS	2 #16 ECS	9151	0.0762	20,336	0.4064
F1	2 #15 GFRP	2 #15 GFRP	9964	0.2286	15,252	0.8890
F2	2 #15 GFRP	2 #15 GFRP	9660	0.1778	15,252	1.2700
F3	2 #15 GFRP	2 #15 GFRP	8541	0.2286	15,252	1.2700
HM1	2 #16 ECS	2 #15 GFRP	9151	0.25	12,800	1.00
HM2	2 #16 ECS	2 #15 GFRP	9600	0.20	14,200	1.50
HP1	2 #15 GFRP	2 #16 ECS	10,000	0.05	21,400	0.2286
HP2	2 #15 GFRP	2 #16 ECS	11,400	0.05	21,400	0.2286
HP3	2 #15 GFRP	2 #16 ECS	10,200	0.05	22,600	0.2286

* Final Crack Width was measured at approximately 60% of the predicted ultimate load

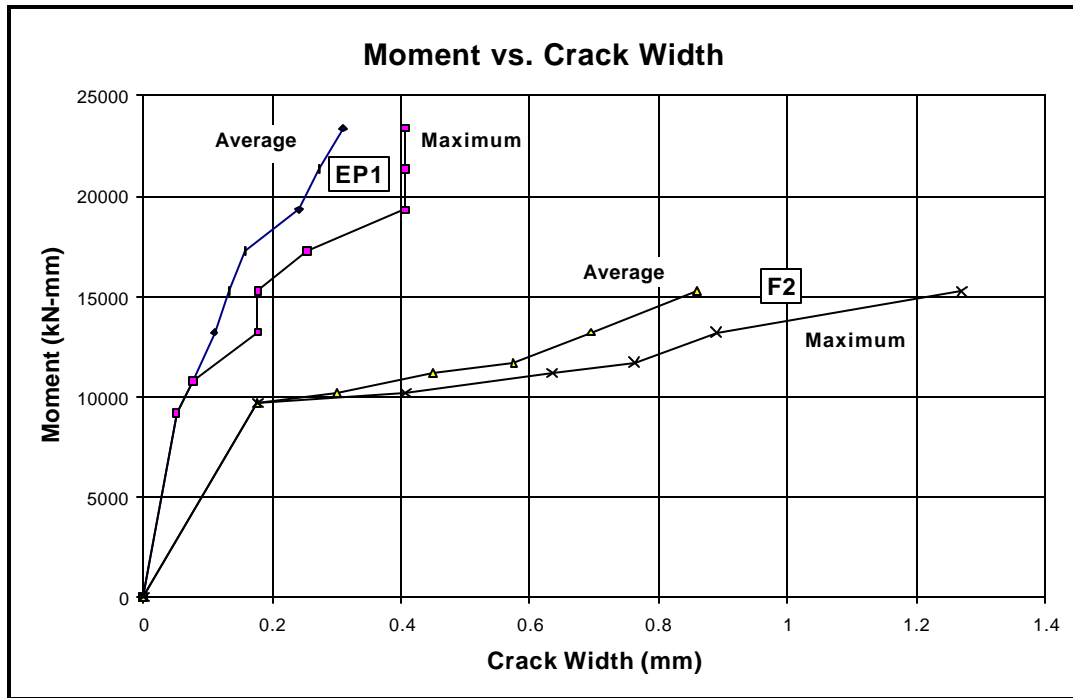


Figure 4. 25: Moment versus Crack Width Illustrating Maximum and Average Crack Width Results for Deck Panels EP1 and F2

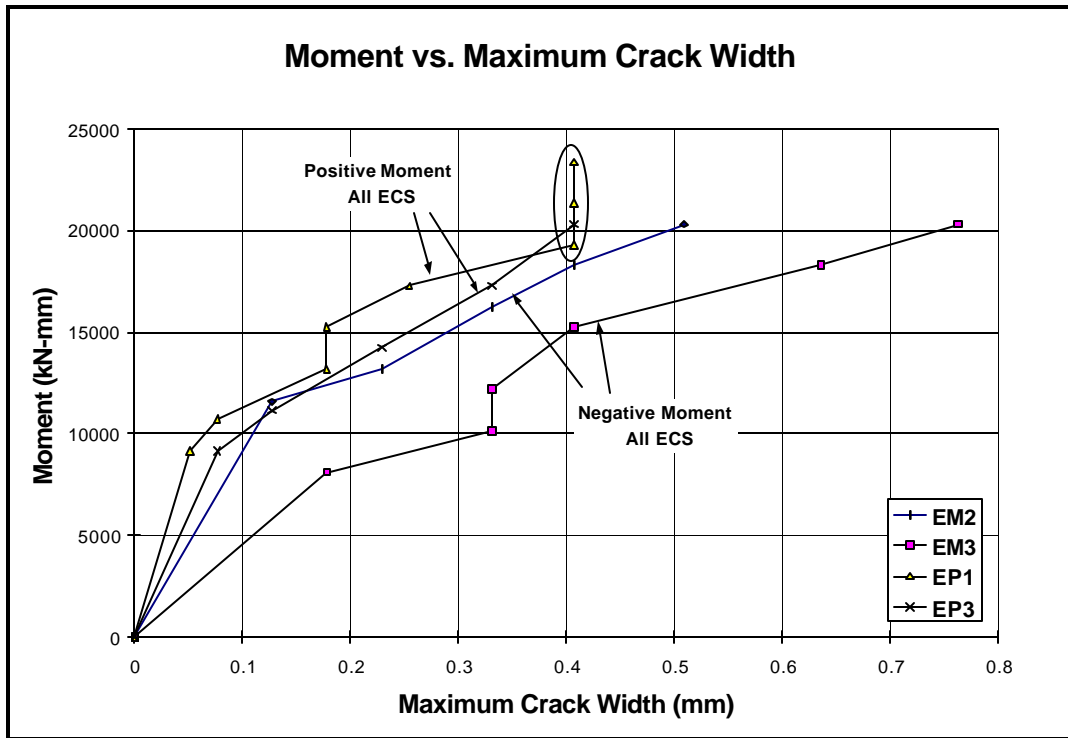


Figure 4. 26: Moment versus Maximum Crack Width for the ECS Reinforced Deck Panels

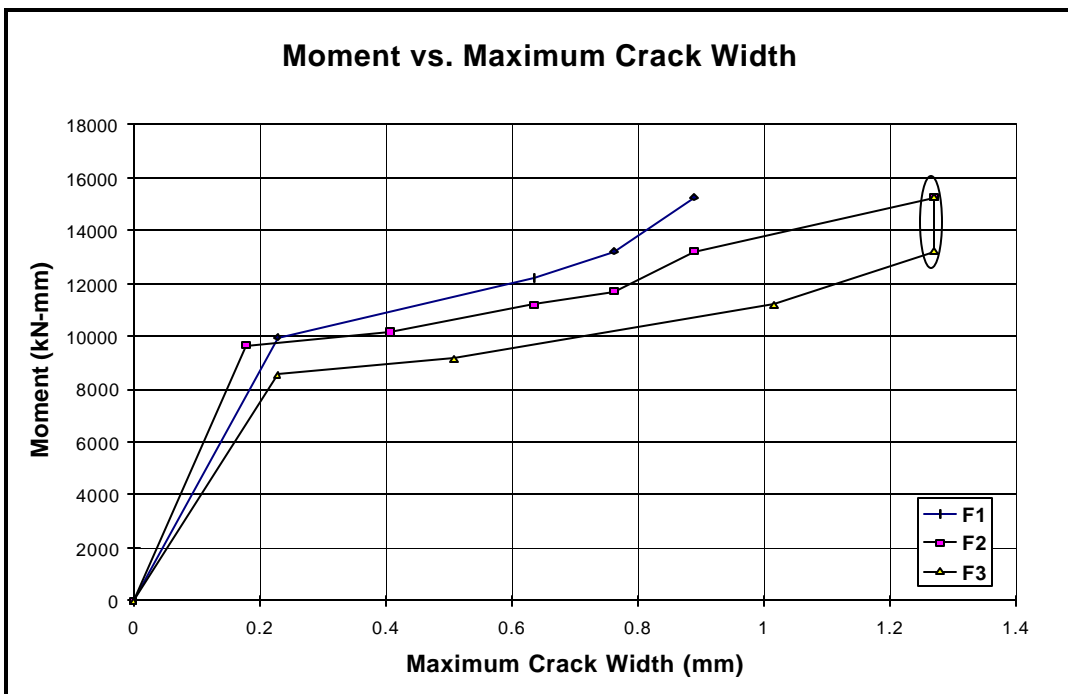


Figure 4. 27: Moment versus Maximum Crack Width for the GFRP Reinforced Deck Panels

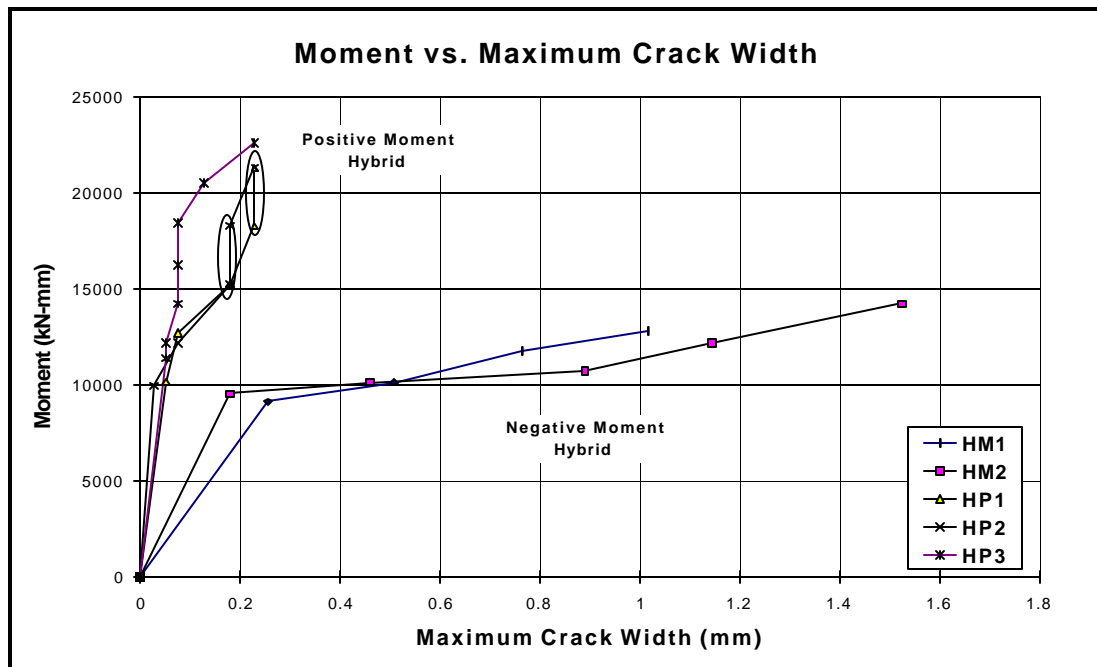


Figure 4. 28: Moment versus Maximum Crack Width for the Hybrid Reinforced Deck Panels

4.5 DECK PANEL LOAD TEST RESULTS (COMPARISON OF DECK PANEL TYPES)

Comparisons of results for the different deck panel types discussed in this section include: Load versus displacement, moment versus maximum compressive concrete strain, crack behavior, and failure mode. Results are grouped by moment orientation, i.e. positive and negative moment deck panel specimens (see Section 4.3.2.1).

4.5.1 Load versus Displacement

Results of three deck panels representing regions of the bridge deck under negative moment (regions above main support girders, see Section 4.3.2.1) are shown in Figure 4.29. Deck panels EM3, F2, and HM1 were selected as representative of the negative moment ECS, GFRP, and Hybrid deck panels respectively. Numerical results and reinforcement information for the deck panels is presented in Table 4.7.

All three specimens follow the same load versus displacement path up to the cracking load. After the cracking load, the plots for deck panels HM1 and F2 remain essentially collinear up to the ultimate load. Both of these specimens had similar GFRP tensile reinforcement.

Since deck panel EM3 has ECS tensile reinforcement, its load versus displacement behavior was different than deck panels HM1 and F2 with GFRP tensile reinforcement. After cracking, the curve for deck panel EM3 has a much greater slope, indicating a larger stiffness than deck panels HM1 and F2. At a load of approximately 48 kN, the ECS rebars in tension yielded resulting in a sudden decrease in the slope of the load displacement curve. After yielding the load resisted by deck panel EM3 continued to increase due to inelastic behavior up to the ultimate load.

Results for the deck panels representing regions of a bridge deck under positive moment (regions between main support girders, see Section 4.3.2.1) are presented in Figure 4.30. Deck panels EP1, F2, and HP1 were selected as representative of the ECS, GFRP, and Hybrid deck panels respectively. As Figure 4.30 shows, the deck panels had the same load versus displacement behavior up until the cracking load. After the cracking load, deck panels EP1 and HP1 with ECS tensile reinforcement continued to follow a similar path exhibiting apparent yielding of the tensile reinforcement followed by inelastic behavior of the specimen. Differences in the displacements of deck panels EP1 and HP1 can be attributed to the differences in compression reinforcement type. The ECS compression reinforcement in deck panel EP1 results in a larger ductility (i.e. area under the load-displacement curve) than the GFRP compression reinforcement in deck panel HP1.

After cracking, the load versus displacement curve of deck panel F2 follows a smaller slope than curves of deck panels EP1 and HP1 due to differences in tensile reinforcement. Since ECS rebars have a modulus equal to approximately five times the GFRP rebar modulus, deck panels EP1 and HP1 had a greater stiffness (i.e. slope in Figure 4.30) than deck panel F2.

Results showed that the overall load versus displacement behavior of the deck panels was determined by the type of tensile reinforcement. Compression reinforcement had a negligible effect on the stiffness and ultimate loads of the deck panels. Compression reinforcement did have an effect on the post yield behavior of the deck panels, but only in the case of the deck panels with ECS tensile reinforcement.

TABLE 4.7 DECK PANEL SPECIMENS LOAD VERSUS DISPLACEMENT BEHAVIOR

Deck Panel Label	Rebars in:		Load, P		Displacement @ Corresponding Load	
	Compression	Tension	Cracking	Ultimate	Cracking	Ultimate
			(kN)	(kN)	(mm)	(mm)
EM3	2 #16 ECS	2 #16 ECS	17.14	55.42	1.14	59.69
EP1	2 #16 ECS	2 #16 ECS	24.36	80.96	1.78	55.37
F2	2 #16 GFRP	2 #16 GFRP	21.18	56.58	1.16	80.01
HM1	2 #16 ECS	2 #16 GFRP	19.59	57.07	2.64	79.50
HP1	2 #16 GFRP	2 #16 ECS	20.12	80.00	0.99	83.566

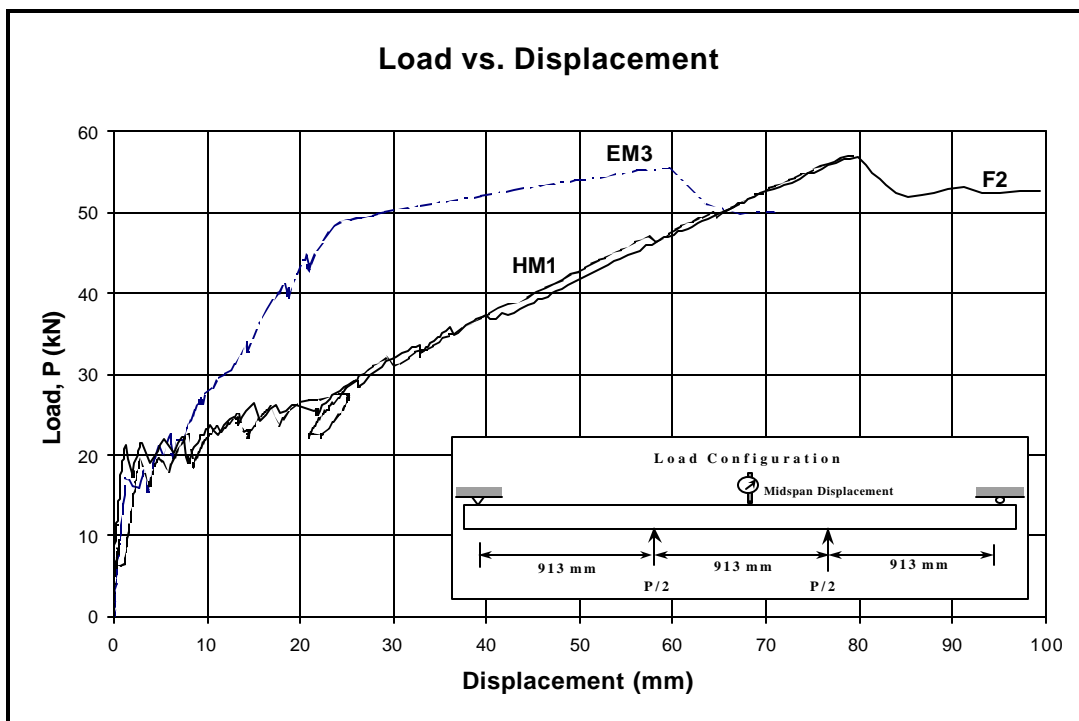


Figure 4. 29: Load versus Displacement for Negative Moment Deck Panels

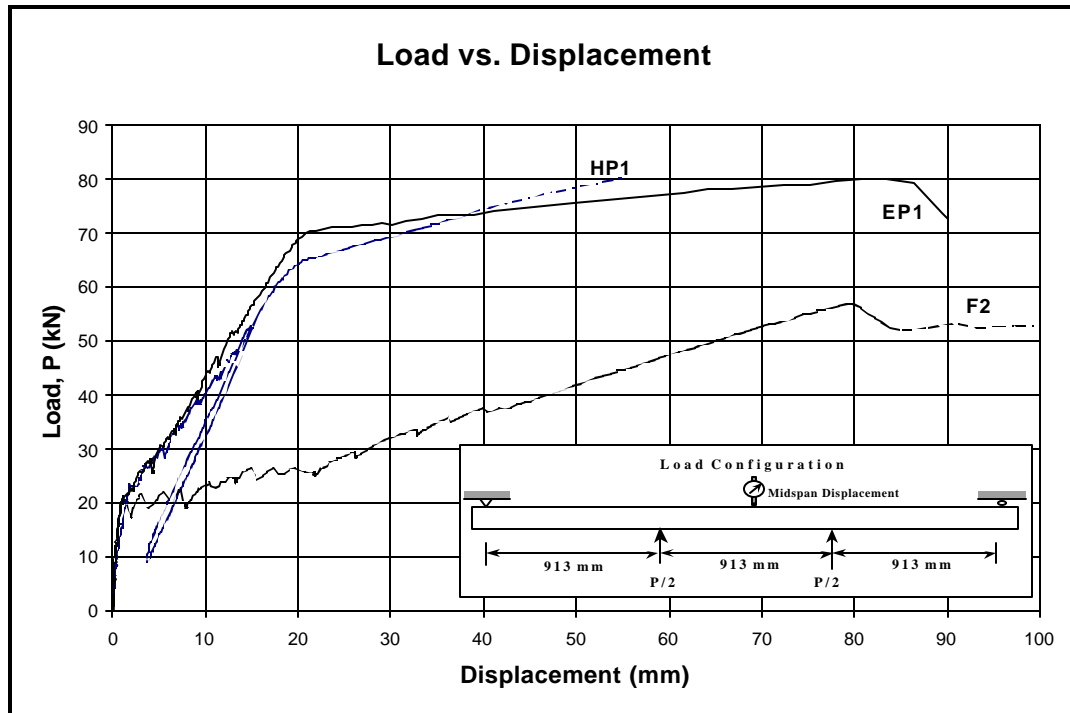


Figure 4. 30: Load versus Displacement for Positive Moment Deck Panels

4.5.2 Moment versus Maximum Compressive Strain in the Concrete

The nature of the strain readings (see Section 4.3.2.1) made it difficult to draw specific conclusions from the test results. Observations showed that the strain data were greatly influenced by the locations of cracks relative to the strain gage during testing. None of the results presented in this section reflects the maximum concrete compressive strain at failure. In the ECS and Hybrid reinforced deck panel tests the strain gages were removed prior to failure to prevent damage. In the GFRP reinforced deck panel tests the disposable foil gages passed the limits of the data acquisition equipment prior to failure.

Moment versus maximum compressive strain (i.e. strain at the compression face) results for the negative moment specimens are shown in Figure 4.31. Deck panels EM3, F2, and HM1 were selected as representative of the ECS, GFRP, and Hybrid reinforced deck panels respectively. Curves for deck panels HM1 and EM3 are similar up until the removal of the HM1 strain gages. Since these specimens have different tensile reinforcement (see Table 4.8), the behavior of the two deck panels should be significantly different. However, after examining crack locations recorded, it was found that no cracks formed near the strain gages on deck panel HM1 resulting in an exaggerated stiffness for the deck panel. This is characterized by the small difference in slope of the HM1 curve after the cracking load. The curve for the GFRP reinforced deck panel F2 has a much lower slope than curves for deck panels HM1 and EM3. This was due to the exaggerated

stiffness of deck panel HM1, discussed previously, and the ECS tensile reinforcement in deck panel EM3.

Figure 4.32 shows the moment versus maximum compressive strain in the concrete for deck panels EP3, F2, and HP1 representing the ECS, GFRP, and Hybrid deck panels respectively. Curves HP1 and EP3 follow each other closely both before and after cracking because both specimens had the same tensile reinforcement as shown in Table 4.8. The small differences in the curve paths could be attributed to either the differences in compression reinforcement or relative distances between cracks and the strain gages. Deck panel F2 had a lower stiffness, and smaller slope of curve, than specimens HP1 and EP3 due to differences in tensile reinforcement (see Table 4.7).

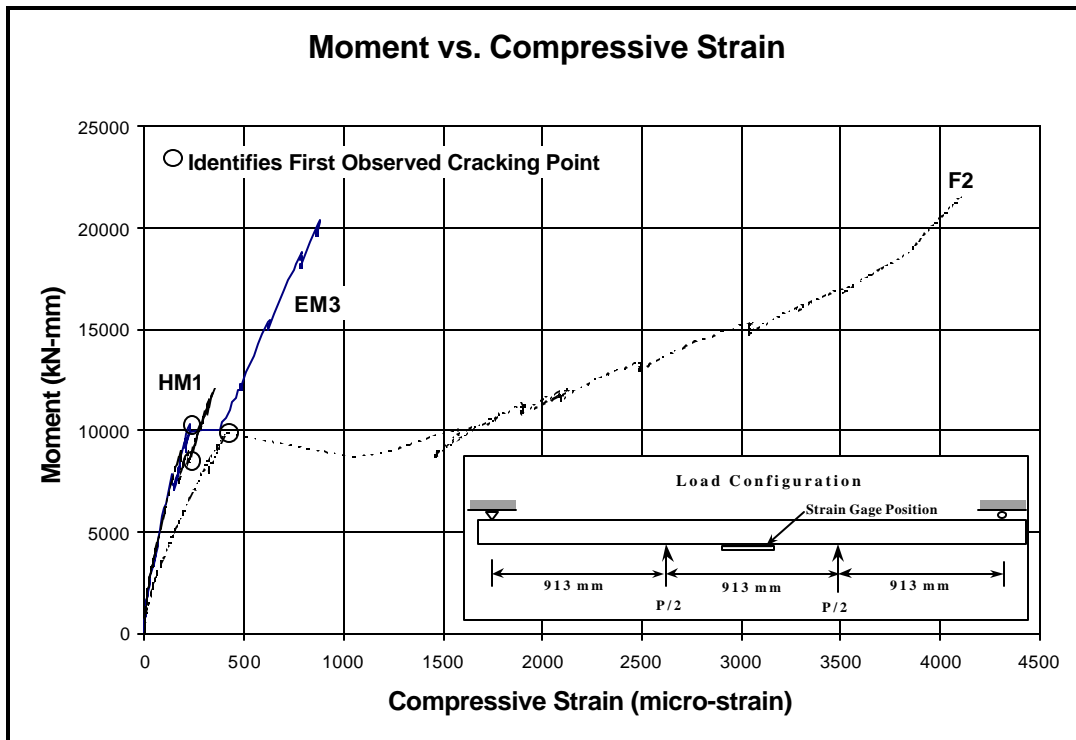


Figure 4. 31: Moment versus Maximum Compressive Strain for the Negative Moment Deck Panels

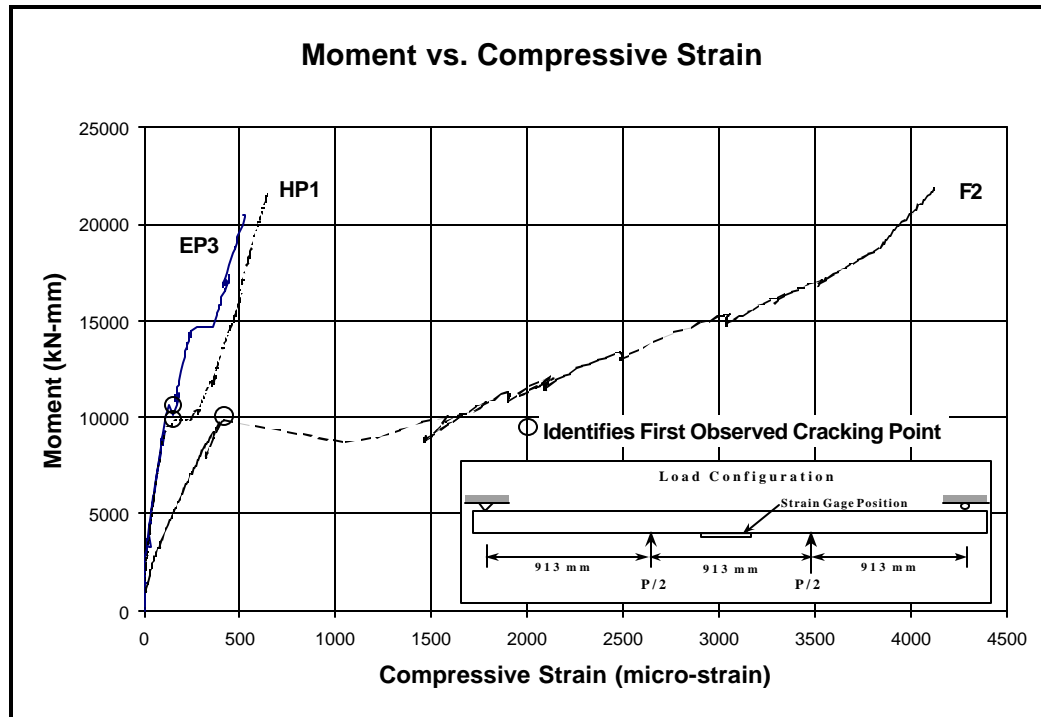


Figure 4. 32: Moment versus Maximum Compressive Strain for the Positive Moment Deck Panels

4.5.3 Moment versus Maximum Crack Width

Crack width data for each deck panel type are grouped together for discussion in this section. Figures 4.33 and 4.34 show the moment versus maximum crack width results for the different deck panel types along with lines representing the least squares linear regression results of the data.

Figure 4.33 shows the moment versus maximum crack width test results for the negative moment deck panels. As the figure shows, the behavior of the GFRP and Hybrid deck panels was similar, and quite different from that of the ECS deck panels. This is due to the type of tensile reinforcement present in the different deck panels specimens. The GFRP and Hybrid reinforced deck panels have GFRP tensile reinforcement while the ECS deck panels have ECS tensile reinforcement. Since the ECS rebar's stiffness was approximately five times greater than the GFRP rebar's, the maximum crack width in the ECS deck panels was much less than that of the GFRP and Hybrid deck panels at a given moment.

Figure 4.33 also shows that the crack widths for the Hybrid reinforced deck panels were greater overall than those of the GFRP reinforced deck panels at a given moment. This is because of the difference in compression reinforcement (see Table 4.7). Since the Hybrid reinforcement had stiffer ECS rebars as compression reinforcement, the

neutral axis of the deck panels was shifted away from the tensile face of the deck panels. This resulted in larger crack openings on the tensile face of the Hybrid deck panels.

Figure 4.34 shows the moment versus maximum crack width results for the positive moment deck panels. Maximum crack widths at a given moment for the ECS and Hybrid specimens were similar and much smaller compared to the GFRP deck panels.

In general, at a given applied moment, maximum crack widths for the Hybrid reinforced deck panels were smaller than those of the ECS reinforced deck panels. This again was most likely due to a difference in compression reinforcement (see Table 4.7). The ECS reinforced specimens had stiffer ECS rebars as compression reinforcement shifting the neutral axis of the specimens away from the tensile face of the deck panel. This resulted in larger crack widths for the ECS deck panels at a given moment.

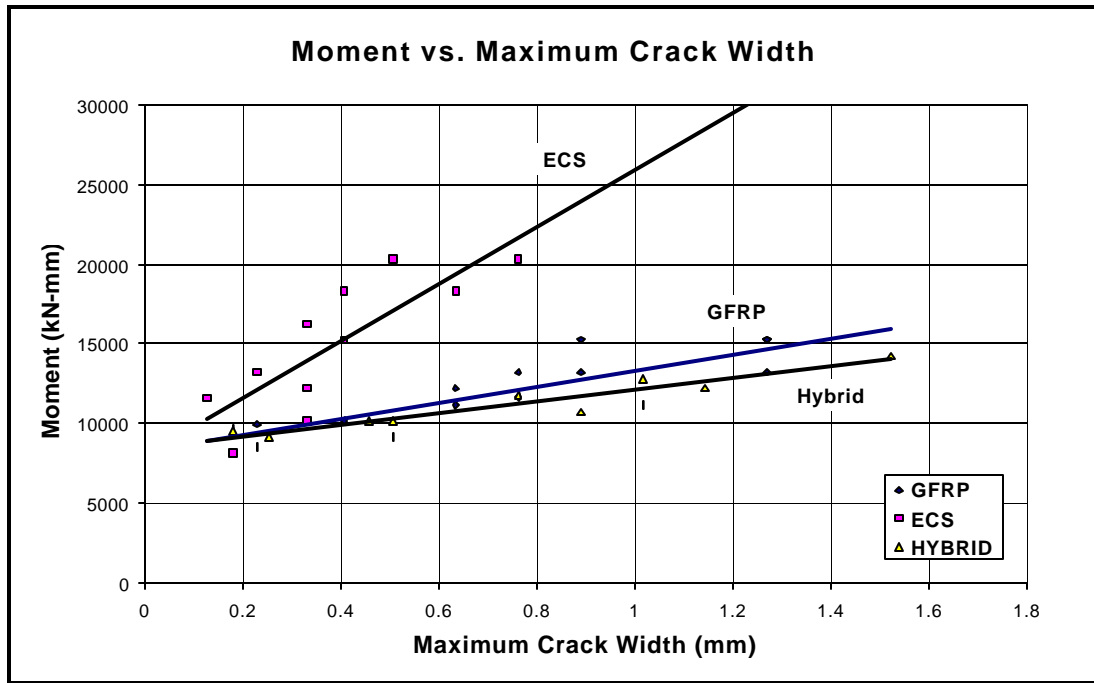


Figure 4. 33: Moment versus Maximum Crack Width for the Negative Moment Deck Panels

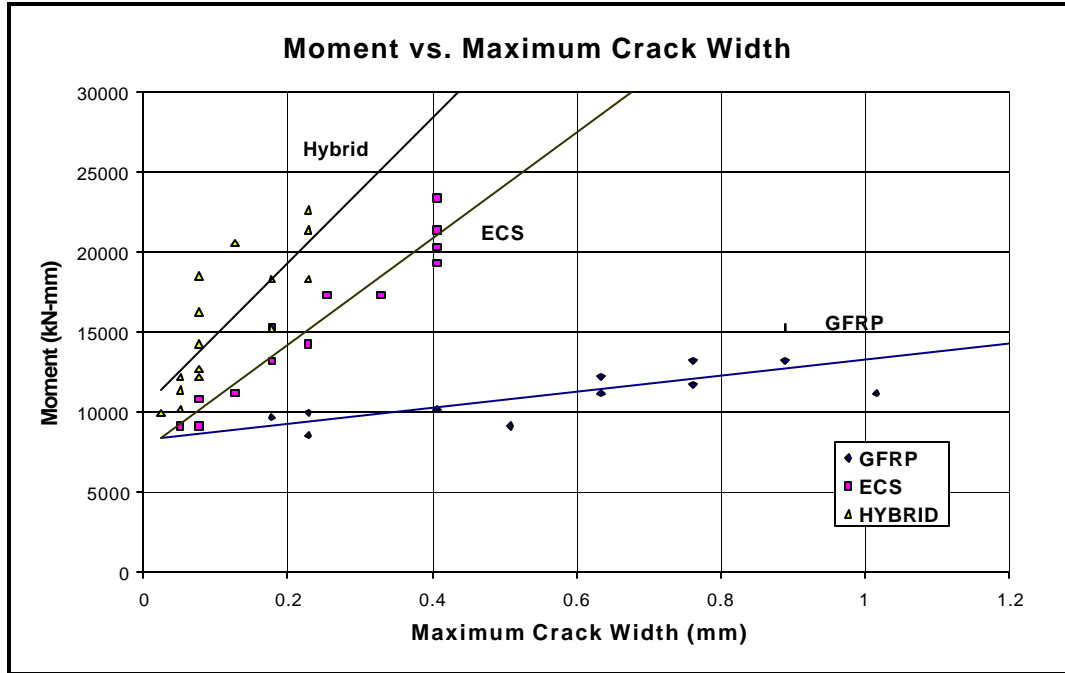


Figure 4. 34: Moment versus Maximum Crack Width for the Positive Moment Deck Panels

4.5.4 Average Crack Spacing

The chart in Figure 4.35 shows the average crack spacing at a deck panel moment of 14,200 kN-mm. For some deck panels, crack measurements were not taken at this particular moment level and an interpolated value was used. Data for deck panels HM1, F1, and F3 are not shown because crack measurements were halted prior to a moment of 14,200 kN-mm.

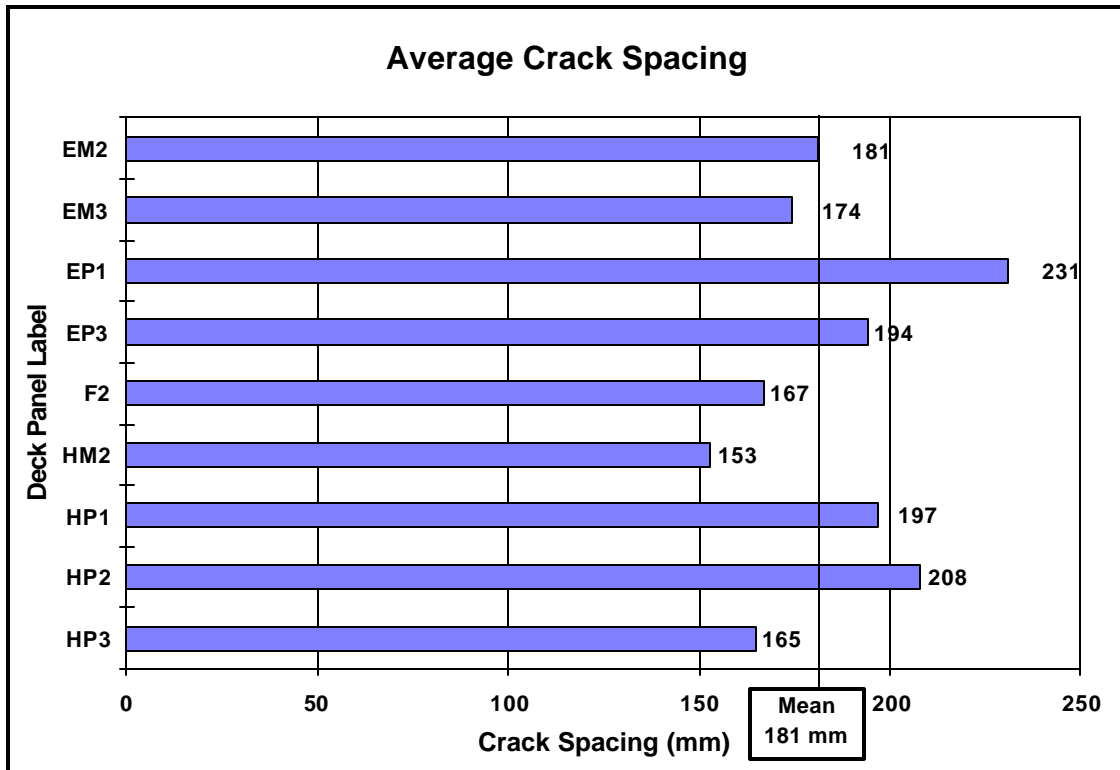


Figure 4. 2: Average Crack Spacing for Deck Panels at a Moment of 14,200 kN-mm

4.5.5 Crack Patterns

Figures 4.36 and 4.37 show the crack patterns observed for deck panels F2 and HP1 at approximately 60% of the respective failure loads. Crack formation was mainly dictated by the type of tensile reinforcement used in the deck panels. Therefore, deck panel F2 can be considered representative of all the deck panels with GFRP tensile reinforcement shown in Table 4.7. Deck panel HP1 can be considered representative of all the deck panels with ECS tensile reinforcement.

One difference in the crack patterns of Figures 4.36 and 4.37 is shown in the plan view. Many transverse cracks that do not cross the entire deck panel section can be seen for deck panel F2 that are not apparent in deck panel HP1. The cracks occurred in locations above the main reinforcement.

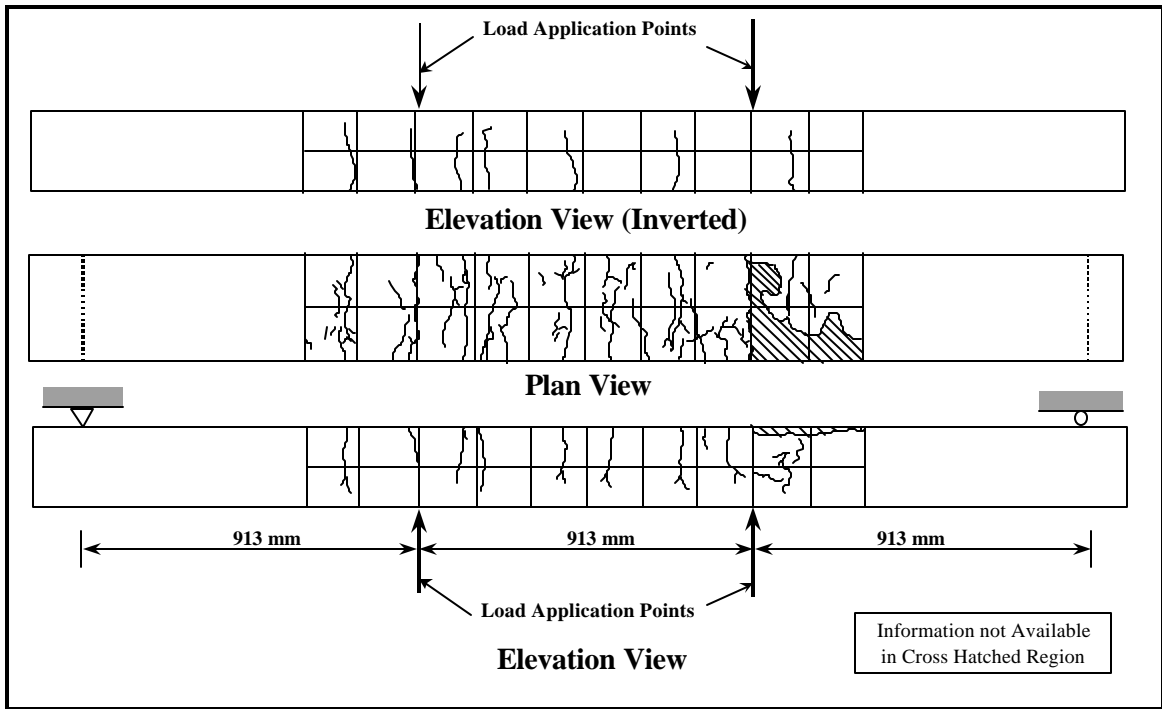


Figure 4. 36: Crack Pattern for Deck Panel F2 at Approximately 60% of the Ultimate Load

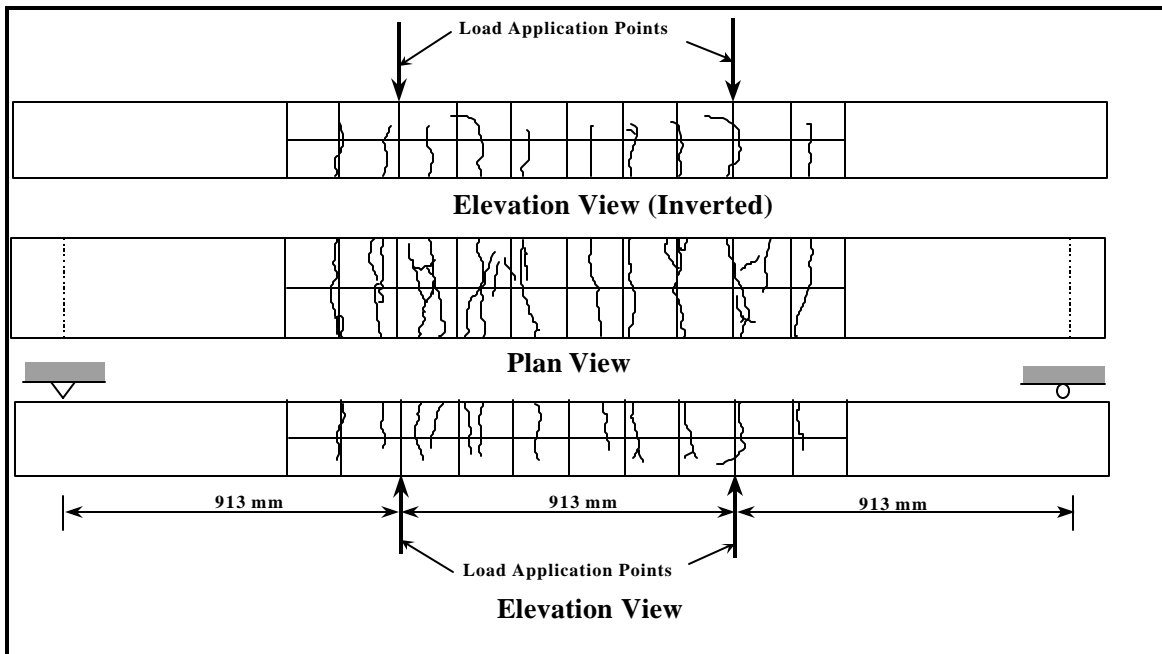


Figure 4. 37: Crack Pattern for Deck Panel HP1 at Approximately 60% of Ultimate Load

4.5.6 Failure Mode

Two different failure modes were observed in the deck panel testing and are shown in Figures 4.38 and 4.39. The failure modes were dictated by the type of tensile reinforcement. First, the shear-diagonal tension failure shown in Figure 4.38 was observed for all of the deck panels with GFRP tensile reinforcement as summarized in Table 4.9. Though the specimens did display ductility in the form of large displacements and wide flexural cracks. The diagonal failure crack shown in Figure 4.38 began forming approximately 5 kN prior to failure, or at approximately 90% of the failure load for these specimen types.

The flexural failure shown in Figure 4.39 occurred in all of the deck panels with ECS tensile reinforcement (see Table 4.8). This failure was characterized by yielding of the ECS tensile reinforcement followed by a compressive failure of the concrete. Ductility was apparent in this failure mode due to the apparent yielding of the ECS rebars and inelastic post yield behavior of the specimen. The yielding provided an easily identifiable warning of deck panel failure.

Table 4.8 shows good agreement in ultimate loads for the different deck panel types. The reduced span length used in the testing of deck panel F1 did nothing to increase the load carrying capacity of the deck panel. Based on the results of this study, it can be concluded that the failure is controlled by shear alone. Any effect of flexure appears to be negligible.

All of the negative moment deck panels had approximately the same ultimate load regardless of reinforcement type or orientation.

For the positive moment deck panels the ECS and Hybrid reinforced deck panels had approximately the same ultimate loads. However, there was a significant difference in the ultimate loads for the ECS and GFRP reinforced deck panels. On average, the GFRP reinforced deck panel ultimate load was approximately 70% of the ECS reinforced deck panel ultimate load.

4.6 SUMMARY & CONCLUSIONS

The objective of this chapter was a to determine if GFRP rebars were a potential alternative to conventional ECS rebars as concrete bridge deck reinforcement. To achieve this objective twelve doubly reinforced deck panels were constructed and tested under four point loading. Eleven of the deck panels were load tested with a span length of 2740 mm. The final deck panel, F1, was tested with a reduced span length of 2130 mm.

Three different reinforcement schemes were studied, an ECS configuration, a GFRP configuration, and a Hybrid configuration reinforced with a combination of ECS and GFRP rebars. Details of the reinforcement schemes used in the twelve panels tested are provided in Table 4.1. Both positive (regions between main support girders) and negative (regions above main support girders) moment orientations existing in the transverse direction in an actual bridge deck were considered in the study. During deck panel testing, the following were observed: load versus displacement, moment versus maximum concrete compressive strain, cracking behavior, and failure mode of the deck panels.

TABLE 4.8 SUMMARY OF FAILURE MODES

Deck Panel Label	Rebars in:		Failure Mode	Ultimate Load
	Compression	Tension		(kN)
EM2	2 #16 ECS	2 #16 ECS	Flexure	64.94
EM3	2 #16 ECS	2 #16 ECS	Flexure	55.42
EP1	2 #16 ECS	2 #16 ECS	Flexure	80.96
EP3	2 #16 ECS	2 #16 ECS	Flexure	73.35
F1	2 #15 GFRP	2 #15 GFRP	Shear – Diagonal Tension	53.56
F2	2 #15 GFRP	2 #15 GFRP	Shear – Diagonal Tension	56.58
F3	2 #15 GFRP	2 #15 GFRP	Shear – Diagonal Tension	58.36
HM1	2 #16 ECS	2 #15 GFRP	Shear – Diagonal Tension	57.07
HM2	2 #16 ECS	2 #15 GFRP	Shear – Diagonal Tension	55.20
HP1	2 #15 GFRP	2 #16 ECS	Flexure	80.00
HP2	2 #15 GFRP	2 #16 ECS	Flexure	77.44
HP3	2 #15 GFRP	2 #16 ECS	Flexure	77.88

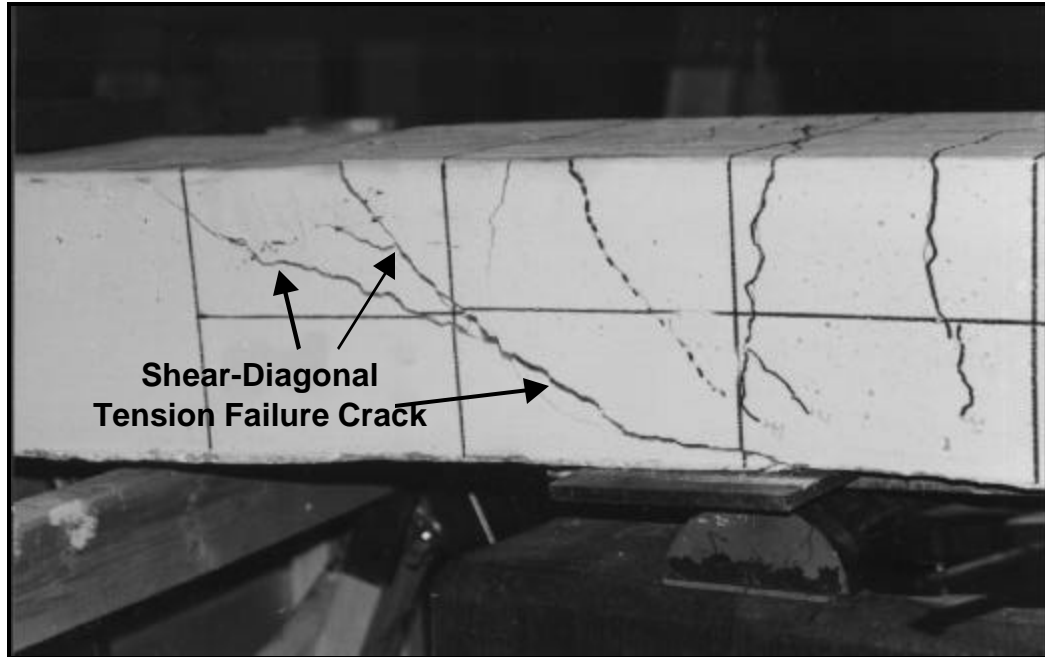


Figure 4. 38: Shear – Diagonal Tension Failure of Deck Panels with GFRP Tensile Reinforcement

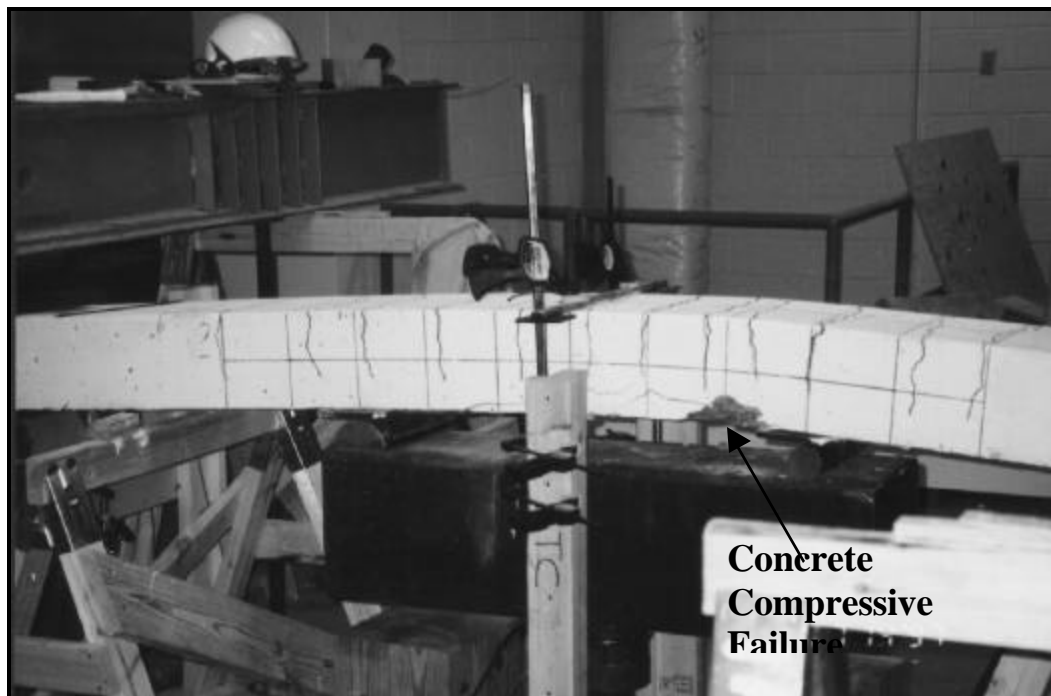


Figure 4. 39: Flexural Failure of Deck Panels with ECS Tensile Reinforcement

Overall, the results showed that the type of tensile reinforcement governed the ultimate load, load versus displacement at service levels (i.e. prior to yielding), moment versus maximum concrete compressive strain, and failure mode of the deck panels. The type of compressive reinforcement had negligible effect on these parameters. However, compression reinforcement did have a limited effect on the maximum crack widths recorded and a significant effect on the ductility of the deck panels reinforced with ECS tensile reinforcement.

During testing, all of the deck panels exhibited the same load versus displacement and moment versus strain characteristics prior to cracking. After cracking, deck panels with ECS tensile reinforcement had a greater stiffness than the deck panels with GFRP tensile reinforcement. The deck panels with GFRP tensile reinforcement had much greater displacements, strains, and crack widths at a given load than the ECS tensile reinforced deck panels.

All of the deck panels had similar crack patterns and spacing (but not crack widths) until near ultimate load levels were achieved. At those levels, small cracks transverse to the main reinforcement began forming on the GFRP tensile reinforced deck panels. These cracks formed in locations away from the final catastrophic failure crack. Therefore, the small transverse cracks did not result in the final catastrophic failure of the deck panels.

Two failure modes were observed in the testing of deck panels. First, all of the ECS tensile reinforced deck panels failed in the constant moment region between the active load points. The deck panels exhibited ductility, providing adequate warning through apparent yielding prior to the final compressive failure of the concrete. Second, all of the deck panels with GFRP tensile reinforced failed between the active load point and support in a region of high shear and flexure. The failure was ductile in nature providing warning of failure with large crack widths and displacements. The final failure cracks shown in Figure 4.38 did not form until approximately 90% of the ultimate load.

Results showed that all the negative moment deck panels failed at approximately the same ultimate load regardless of the reinforcing scheme. It can be concluded that the negative moment ECS, GFRP, and Hybrid deck panels can provide the same load resistance. For the positive moment deck panels, the ECS and Hybrid reinforced deck panels failed at approximately the same load. However, on average, the ultimate load of the GFRP reinforced deck panels was approximately 70% of the ECS reinforced deck panels.

The reduced span length of the GFRP reinforced deck panel, specimen F1, increased the stiffness of the deck panel significantly. However, the reduction in span length had little or no effect on the maximum crack widths and failure loads observed. Based on the limited experimental results herein, it can be concluded that the failure observed in the GFRP reinforced deck panels was governed by shear for the span lengths tested, since altering the span length had negligible affect on the ultimate strength.

5.0 DECK PANEL THEORETICAL CORRELATION

5.1 INTRODUCTION

To evaluate the behavior of concrete bridge decks reinforced with GFRP and ECS rebars, twelve reinforced concrete deck panels were constructed and tested. The following three reinforcement schemes were examined in the study: (1) an ECS reinforced concrete deck panel representing conventional bridge deck construction, (2) a GFRP reinforced deck panel, and (3) a hybrid reinforcing scheme with a top mat of GFRP and a bottom mat of ECS reinforcement.

The deck panels were constructed to simulate bridge deck load conditions. An actual bridge deck transfers vehicle load to the main support girders in the transverse direction through one-way action, as illustrated in Figure 5.1. The deck panels simulate a transverse unit width of deck.

This chapter has two main objectives. First, to determine if the experimental results from the deck panel tests meet design requirements of the American Association of State Highway and Transportation Officials (AASHTO 1996) and the American Concrete Institute (ACI-318M-95). Second, to determine if the experimental results can be predicted adequately using various available theoretical methods.

Ultimate loads of the deck panels are compared to design load specifications provided in AASHTO (1996). Results of the comparison determine if the deck panels with the different reinforcing schemes can withstand necessary load levels and provide adequate factors of safety. In addition, ACI-318M-95 specifications and various other models are compared to the observed experimental failure loads.

Experimental displacements at service loads are compared to code provisions limiting displacements. Theoretical models are used to determine if the load versus displacement behavior of the deck panels could be adequately predicted.

Maximum crack widths at service load, observed during the tests, are compared to AASHTO and ACI specifications for limiting crack widths. In addition, three published theoretical models for predicting maximum crack widths are compared to the experimental results.

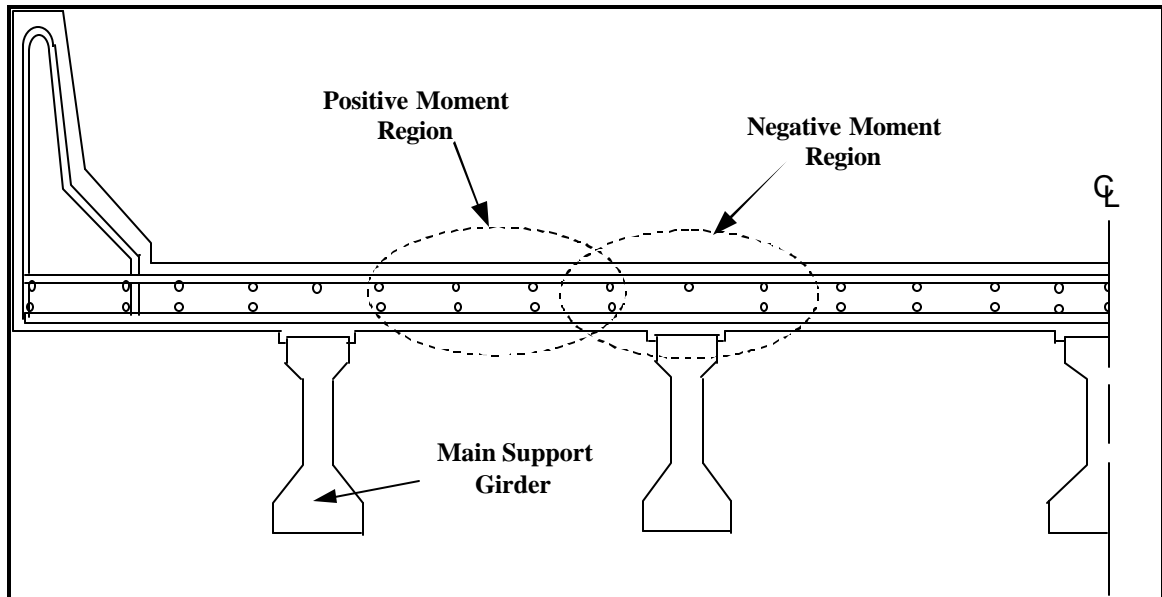


Figure 5.1: Bridge Superstructure Cross Section

5.2 CONCRETE REINFORCED WITH GFRP VERSUS ECS REBARS

The most obvious difference between concrete reinforced with GFRP rebars and that reinforced with ECS rebars is due to the difference in Young's modulus of the two rebar types. Young's modulus of ECS rebars is approximately five times greater than that of the GFRP rebars used in this study. This difference directly affects the behavior of reinforced concrete deck panels in flexure, shear, displacement, and crack formation.

The flexural behavior of the deck panels is influenced by the difference in Young's modulus of the rebar types. Figure 5.2 shows qualitative strain diagrams for two reinforced concrete beams with the same geometry under the same applied moment. The first beam is reinforced with ECS rebars, while the second is reinforced with GFRP rebars. One difference in the diagrams is the larger strain required in the GFRP rebars than in the ECS rebars to resist the same moment.

Another difference is the reduction in depth of concrete in compression, kd . As Figure 5.2 shows, the larger strain in the GFRP rebars than in the ECS rebars at a given moment results in a smaller distance from the neutral axis to the compression face. Figure 5.3 illustrates the difference in compression region depth versus moment for two of the deck panels tested, GFRP reinforced specimen F2, and ECS reinforced specimen, EP1 (see Table 5.1). After cracking the neutral axis depth of the GFRP reinforced specimen is approximately $\frac{1}{2}$ that of the ECS reinforced specimen.

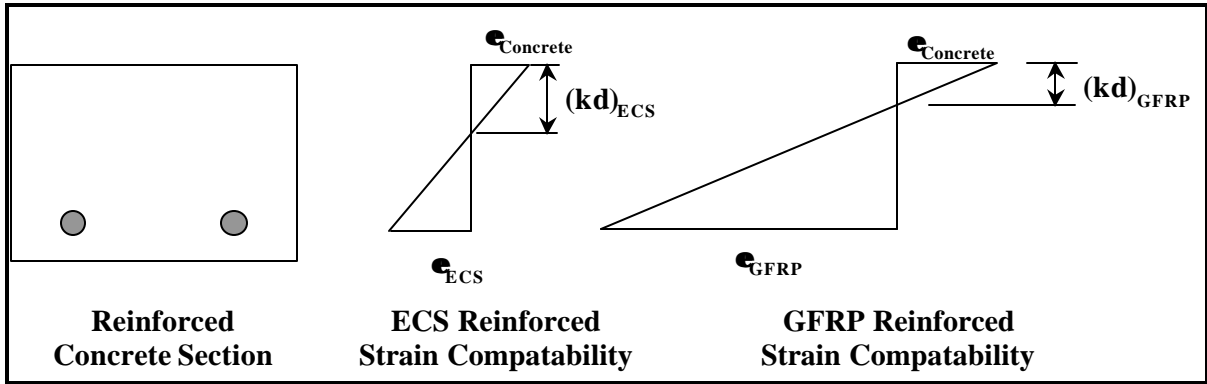


Figure 5. 2: Qualitative Strain Compatibility for Concrete Reinforced with ECS and GFRP rebars at the Same Applied Moment

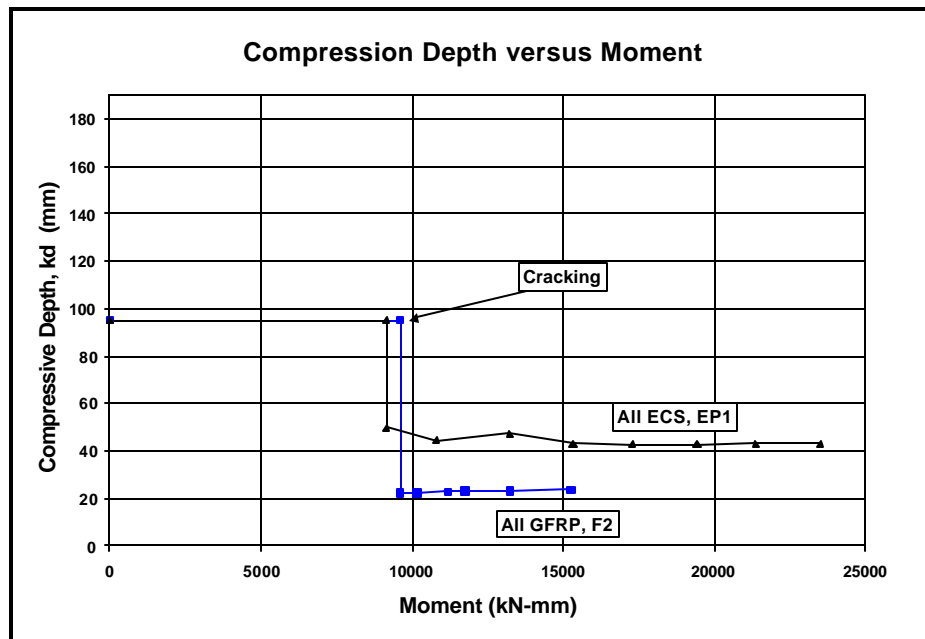


Figure 5. 3: Theoretical Compressive Depth versus Moment for ECS and GFRP Reinforced Concrete Deck Panels

These differences in curvature, depth of compression block, and increase in concrete strains can result in a large reduction in shear strength of concrete sections reinforced with GFRP rebars instead of ECS rebars. Figure 5.4, from MacGregor (1992), illustrates the mechanisms that resist shear forces after a combined flexure and shear crack has formed. First, the section resists shear in the region of concrete still in compression, represented by V_{cz} . Second, there is dowel action, V_d , which depends greatly on the flexural stiffness of the rebar. Third, the vertical component of the aggregate interlock, V_{ay} , also provides a significant amount of shear resistance. In fact, dowel action and aggregate interlock can resist as much as 40% to 60% of the total shear in conventional steel reinforced concrete deck panels (MacGregor 1992). Other forces

existing in the sketch result from flexure, including tensile forces in the rebar T_2 and the compressive force in the concrete C_1 .

In GFRP reinforced flexural members, all of these shear transfer mechanisms are reduced significantly compared to an ECS reinforced member. First, as illustrated in Figure 5.2, the amount of concrete above the neutral axis, still in compression, is reduced greatly due to larger strains existing in the GFRP rebars reducing V_{cz} . Second, the larger tensile strain in the GFRP rebars and larger curvature, decrease the amount of shear that can be resisted by aggregate interlock due to large crack widths reducing V_{ay} . Third, the flexural stiffness of the GFRP rebar is small compared to that of a steel rebar, thereby inhibiting dowel action and so reducing V_d . These reductions in the shear resistance components result in a significant decrease in shear strength of a GFRP reinforced deck panel overall. This is evidenced in the results presented in this study. Concrete deck panels with GFRP rebars failed in shear at approximately 60% of the shear failure predicted by ACI equations for conventional steel reinforced concrete.

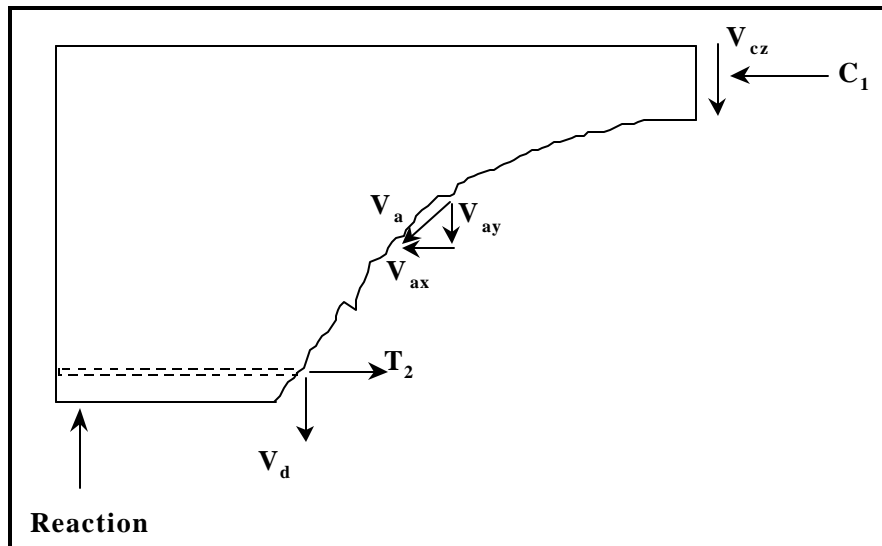


Figure 5. 4: Shear Resisting Mechanisms in a Reinforced Concrete Deck Panel (Adapted from MacGregor (1992))

Displacements of GFRP reinforced concrete members are also significantly greater than ECS reinforced concrete members due to difference in curvature of GFRP reinforced deck panels. Figure 5.5 qualitatively illustrates this difference showing sections used to compute the cracked moment of inertia for an equivalent ECS and a GFRP reinforced deck panel at the AASHTO service moment. The area of the deck panel under compression is greatly reduced, by a factor of 2, as illustrated in Figure 5.2. This greatly reduces the moment of inertia of the panel section. The reduction is compounded by the difference in Young's modulus of the reinforcement. These two differences resulted in a cracked section moment of inertia for an ECS reinforced specimen that is 4.3 times greater than that of an equivalent GFRP reinforced specimen.

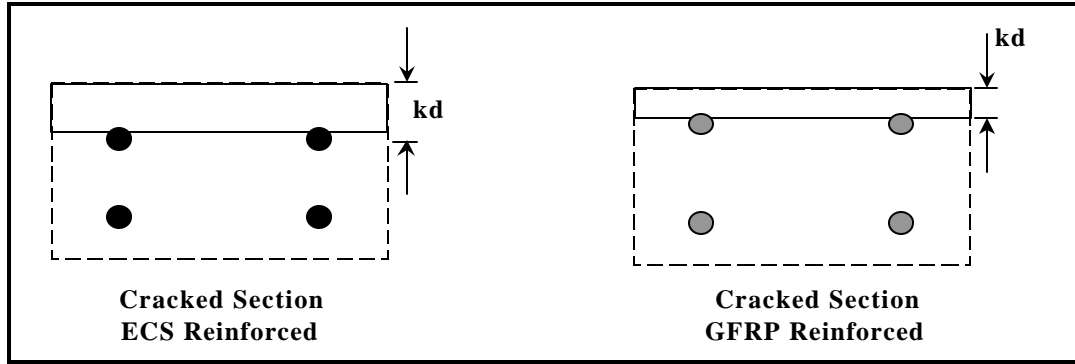


Figure 5.5: Qualitative Cracked Transformed Sections

Crack widths of the GFRP specimens are also greater than those of an equivalent ECS reinforced specimens. Crack widths are influenced by many parameters, such as bond quality of rebar, depth of cover, effective area of concrete surrounding the rebar, etc. However, stress in the rebar was found to be the greatest variable by Gergely and Lutz (1968). Gergely and Lutz's derivation was based on steel reinforced specimens. Since GFRP reinforced rebars have a different modulus of elasticity, the measure of strain would be more appropriate when comparing specimens with the two reinforcement types. Crack widths are directly related to reinforcement strain; therefore the larger strains present in a GFRP reinforced member would result in larger cracks than in an equivalent ECS reinforced member.

5.3 REVIEW OF EXPERIMENTAL PROCEDURE

A review of the testing parameters is provided in this section. For a more detailed discussion, refer to Section 4.2 of Chapter 4.

5.3.1 Deck Panel Geometry

Twelve 2970 mm x 305 mm x 190 mm deck panels were constructed to study the behavior of concrete bridge decks reinforced with ECS and GFRP rebars under load. The length of the deck panels was selected to accommodate a span length of 2740 mm during testing. This was considered an average Kentucky main support girder spacing. Typically, Kentucky bridge decks are constructed with a thickness of 205 mm. However, in the design of bridge decks 15 mm of this thickness is an assumed wearing surface that is not considered in the structural computations. The deck panels were constructed to represent design conditions with a thickness of 190 mm. The assumed 15 mm wearing surface was subtracted from the clear cover of the top reinforcing mat for all the specimens.

Three different reinforcing schemes were used in the deck panels and are shown in Figure 5.6. First, four ECS reinforced deck panels were constructed. Main

reinforcement of these specimens consisted of two mats of #16 ECS rebars. Clear covers for the top and bottom mats were 50 mm and 25 mm respectively and were selected to correspond to Kentucky design specifications. The larger top clear cover is specified mainly to protect the reinforcement in the bridge deck from corrosion related deterioration.

The second reinforcing scheme studied was the GFRP reinforced deck panel. Three of these specimens were fabricated with two mats of #15 GFRP rebars. Clear cover for both the top and bottom mats was 25 mm. The top clear cover was reduced by 25 mm compared to the ECS reinforced deck panels since corrosion related deterioration should not be encountered in a GFRP reinforced bridge deck.

The third reinforcing scheme was the Hybrid reinforced deck panel. Five of these specimens were tested. The top mat of the specimens was made up of #15 GFRP rebars with a clear cover of 25 mm as in the GFRP reinforced deck panels. The bottom mat of reinforcement consisted of two #16 ECS rebars with a 25 mm clear cover. Table 5.1 provides a summary of the reinforcement details for all of the deck panels tested.

A bridge deck transfers loads from the riding surface to the main support girders acting as a continuous beam in the transverse direction. Therefore, both positive and negative moment regions exist as illustrated in Figure 5.1. Different ECS and Hybrid deck panels were constructed to test these different moment orientations due to differences in clear cover and rebar types. Hereafter the deck panels are referred to based on the moment orientation, e.g. positive moment ECS reinforced deck panel. Since the GFRP reinforced deck panels had the same top and bottom clear cover, there is no need to distinguish between positive and negative moment orientation.

The deck panels specimens were labeled using a three character sequence. The first letter identifies the specimen type, “E”, “F”, and “H”, represent the ECS, GFRP, and Hybrid deck panels respectively. The second character identifies the moment orientation, “M” for negative (minus) and “P” for positive (plus) moment. The third character is a number distinguishing specific deck panels.

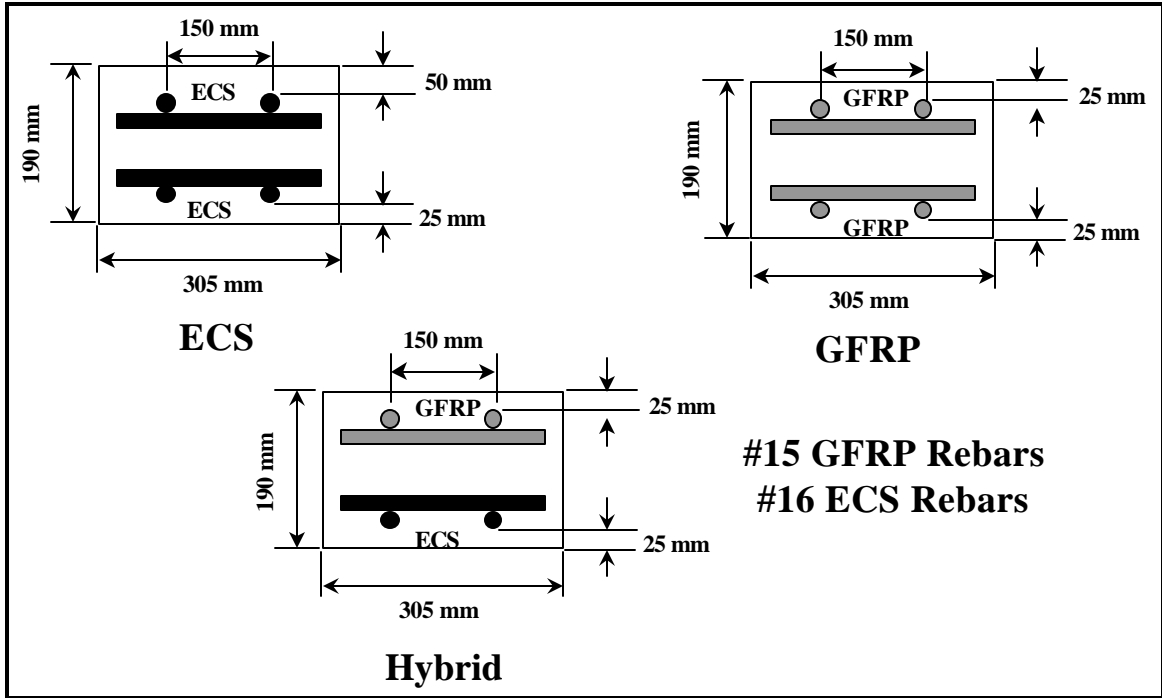


Figure 5. 6: Deck Panel Cross Sections

TABLE 5.1 DECK PANELS IDENTIFICATION AND PROPERTIES

Deck Panel Label	Panel Type	Moment Orientation	Compression Reinforcement		Tension Reinforcement	
			Number of Rebars	Clear Cover (mm)	Number of Rebars	Clear Cover (mm)
EM2 EM3	ECS	Negative	2 - #16 ECS	25	2 - #16 ECS	50
EP1 EP3	ECS	Positive	2 - #16 ECS	50	2 - #16 ECS	25
F1 F2 F3	GFRP	N. A.	2 - #15 GFRP	25	2 - #15 GFRP	25
HM1 HM2	Hybrid	Negative	2 - #15 ECS	25	2 - #15 GFRP	25
HP1 HP2 HP3	Hybrid	Positive	2 - #15 GFRP	25	2 - #16 ECS	25

5.3.2 Material Properties

During the fabrication of the deck panels, two standard compression cylinders were made for each deck panel. Compression tests were conducted on the cylinders the same day the respective deck panels were tested. Table 5.2 presents the results of the concrete strengths for the cylinders tested.

Table 5.3 and Figure 5.7 show the material properties of the rebars used in the study.

TABLE 5.2 CONCRETE CYLINDER COMPRESSIVE STRENGTH

Deck Panel Label	Compressive Strength ^a (MPa)		
	Cylinder 1	Cylinder 2	Average
EM2	41.97	40.20	41.44
EM3	45.99	46.36	46.17
EP1	41.67	N. A.	41.67
EP3	46.92	45.16	46.03
F1	29.53	27.65	28.59
F2	29.65	30.58	30.11
F3	27.36	26.68	27.02
HP1	46.50	48.80	47.65
HP2	46.38	50.06	48.22
HP3	41.26	44.55	42.91
HM1	28.04	28.41	28.23
HM2	31.34	30.26	30.80

^a Concrete Age at time of cylinder tests ranged between 9 and 11 months.

TABLE 5.3 REBAR PROPERTIES

Rebar Type	Diameter of Rebar	Area of Rebar (mm ²)	Yield Strength (MPa)	Stress Orientation	Ultimate Strength	Modulus of Elasticity
	(mm)				(MPa)	(MPa)
#16 ECS	16	199	486.9	Tension/ Compression	653.4	196,490
#15 GFRP	15	176	N. A.	Tension	612	42,045
				Compression	325	42,510

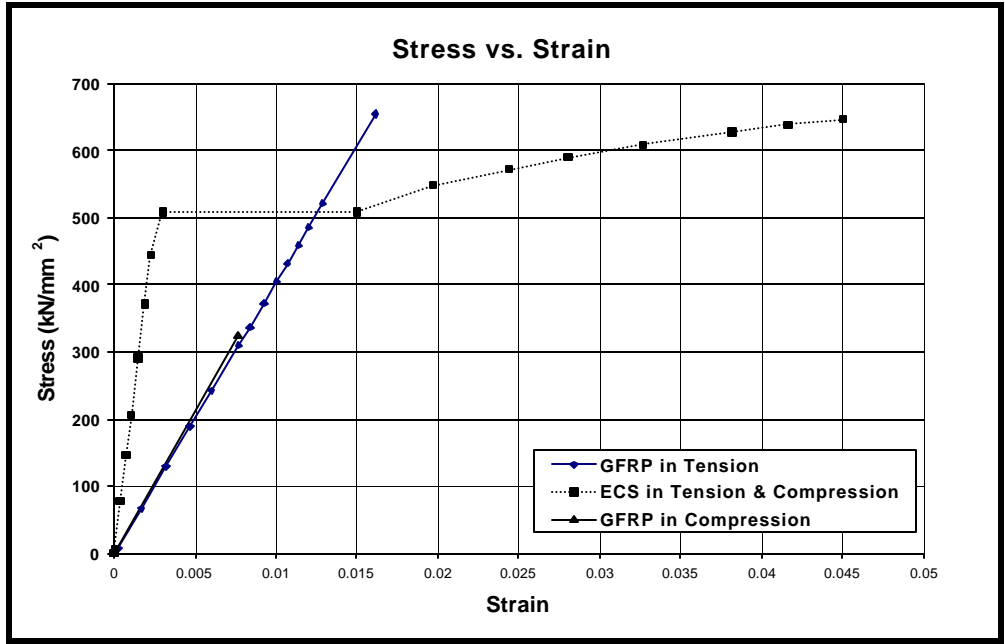


Figure 5.7: Stress versus Strain Properties of the Rebars Used

5.3.3 Deck Panel Test Setup

Figure 5.8 illustrates the four point load configuration used during the deck panel tests. As the figure shows, the load spacing was reduced from 913 mm to 710 mm for testing of deck panel F1. Instrumentation was placed to record the load and midspan displacement of the deck panels. In addition, crack measurements were recorded in the constant moment region at load intervals of approximately 4500 kN. For more details of the test setup refer to Section 4.3 of Chapter 4.

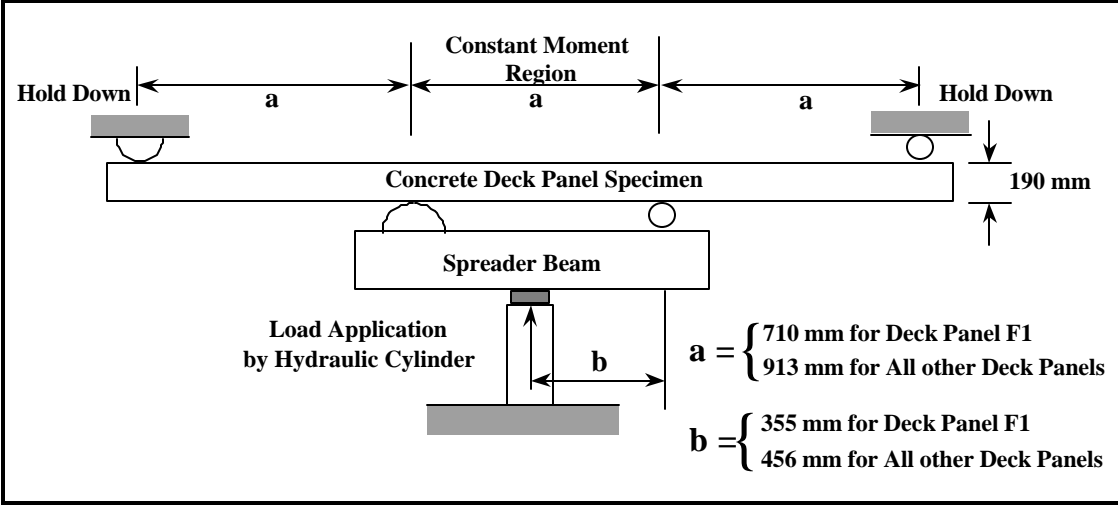


Figure 5.8: Elevation View of Test Setup

5.3.4 Dead Load Considerations

Since the deck panel specimens were tested in an inverted position, consideration of dead load was important in the test results. During the testing, the hydraulic jack lifted the deck panel up to bear against the supports and the dead load of the deck panels was included in the measured load. Load, shear, and moment diagrams for the test setup prior to lifting the entire weight of the deck panel are shown in Figure 5.9a (dead load). The load, shear, and moment diagrams after the weight of the deck panels specimen was bearing against the supports are shown in Figure 5.9b (live load). During the reduction of the test data, the dead load moment diagram was assumed to have the same shape as the live load moment diagram. This resulted in a small error in measured moment as illustrated Figure 5.10. The maximum percent error of this assumption at the midspan at AASHTO service load conditions is 1.3% and considered negligible.

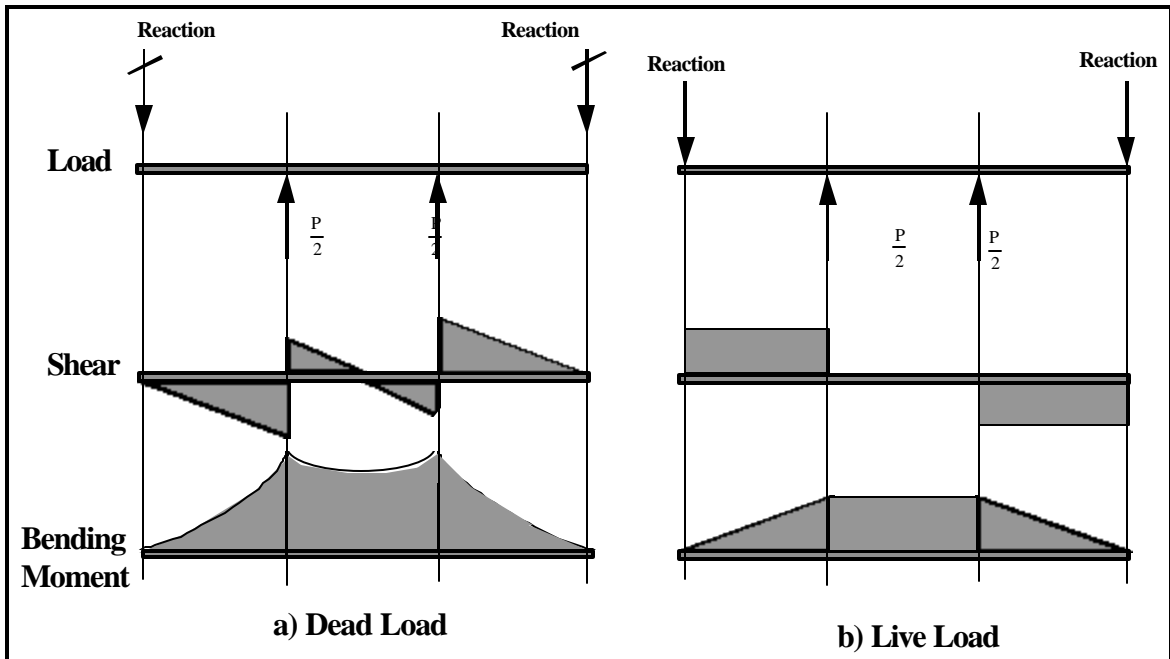


Figure 5.9: Qualitative Load, Shear, and Bending Moment Diagrams for the Load Test Setup

5.4 CORRELATION OF ULTIMATE LOAD WITH CODE PROVISIONS & THEORY

This Section provides comparisons of experimental ultimate load with: (1) design load requirements of current AASHTO specifications, (2) ACI-318M-95 provisions for predicting ultimate load, and (3) two published expressions for predicting shear failure in GFRP reinforced deck panels.

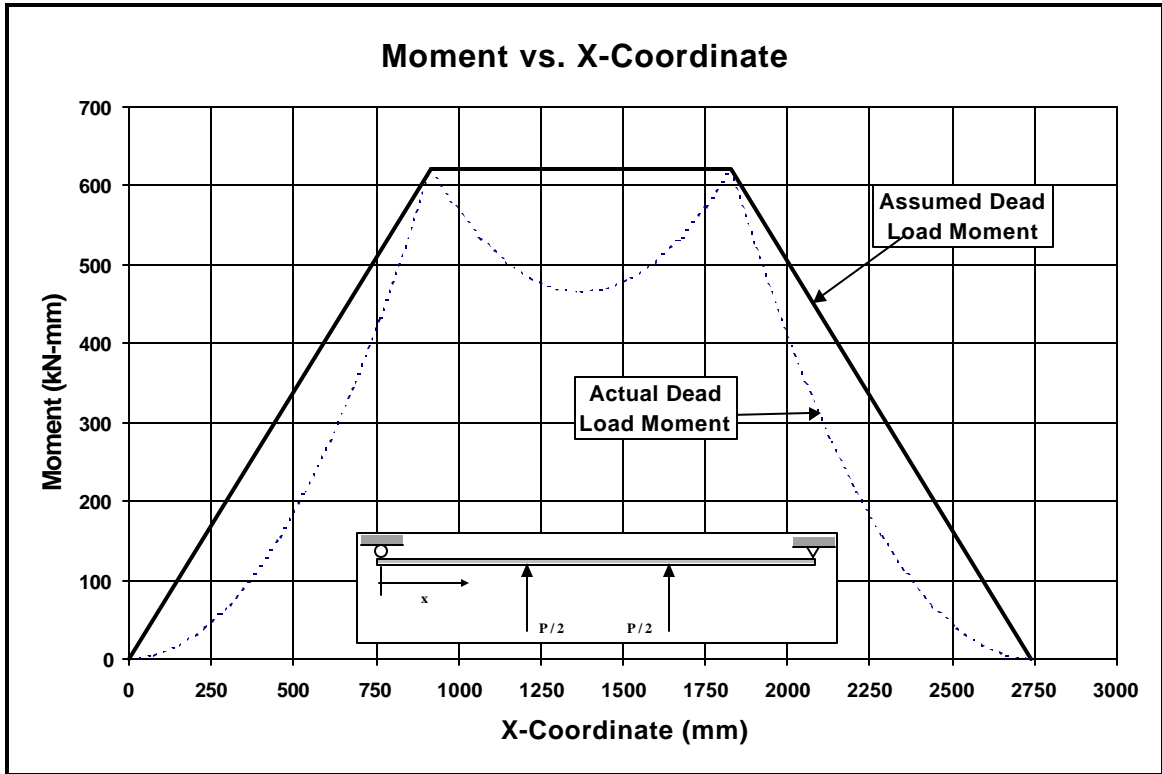


Figure 5. 10: Assumed Dead Load Moment versus Actual Dead Load Moment

5.4.1 AASHTO Design Load Requirements

Article 3.24 of AASHTO (1996) provides guidelines for the design of concrete bridge slabs with reinforcement perpendicular to traffic. Flexural requirements for the deck panels studied are provided in Article 3.24.3.1. AASHTO specifies that concrete slabs are to be designed for both a positive and negative live load moment computed using the following expression in English units:

$$M_{LL} = \left(\frac{S + 2}{32} \right) \cdot P_{25} \quad (5.1)$$

where,

- M_{LL} = Live Load Moment in foot-pound per foot slab width
- P_{25} = 20 kips (90 kN) for HS-25 Loading
- S = Span Length in feet

AASHTO further specifies that in cases where the slabs are continuous over three or more supports a continuity reduction factor of 0.8 shall be applied to Equation (5.1). This factor was applied to the deck panels, resulting in a required design live load moment of 7460 kN-mm for the specimens with a 2740 mm span length. Similarly, the design live load moment for specimen F1 with the 2130 mm span length was 6100 kN-mm.

AASHTO specifies an impact fraction, I, in Article 3.8.2.1 that applies to concrete bridge decks and is a magnification factor to live loads. For the deck panels, the impact fraction was the maximum allowed value of 30% resulting in a live load plus impact moment of 7930 kN-mm for specimen F1 and 9700 kN-mm for the remaining deck panels.

Design dead load moments were computed using the moment equation for a simply supported span with a uniformly distributed load. A 205 mm thick bridge deck with a 15 mm wearing surface (see Section 4.2.1) was assumed in the computations rather than the 190 mm thick deck panels tested. In addition the dead load moment included an 720 Pa allowance for future wearing surfaces. This resulted in a required dead load moment of 955 kN-mm for deck panel F1 and 1580 kN-mm for the remaining deck panels.

Combining the dead and live load plus impact moments resulted in design service moments of 8885 kN-mm for specimen F1 and 11,280 kN-mm for the other deck panels. Factored design moments were computed using load factors specified in AASHTO Article 3.22. The resulting factored design moments were 18,460 kN-mm for specimen F1 and 23,115 kN-mm for the remaining specimens. Figures 5.11 and 5.12 depict the ratio of experimental ultimate moment to the AASHTO service and factored design moments.

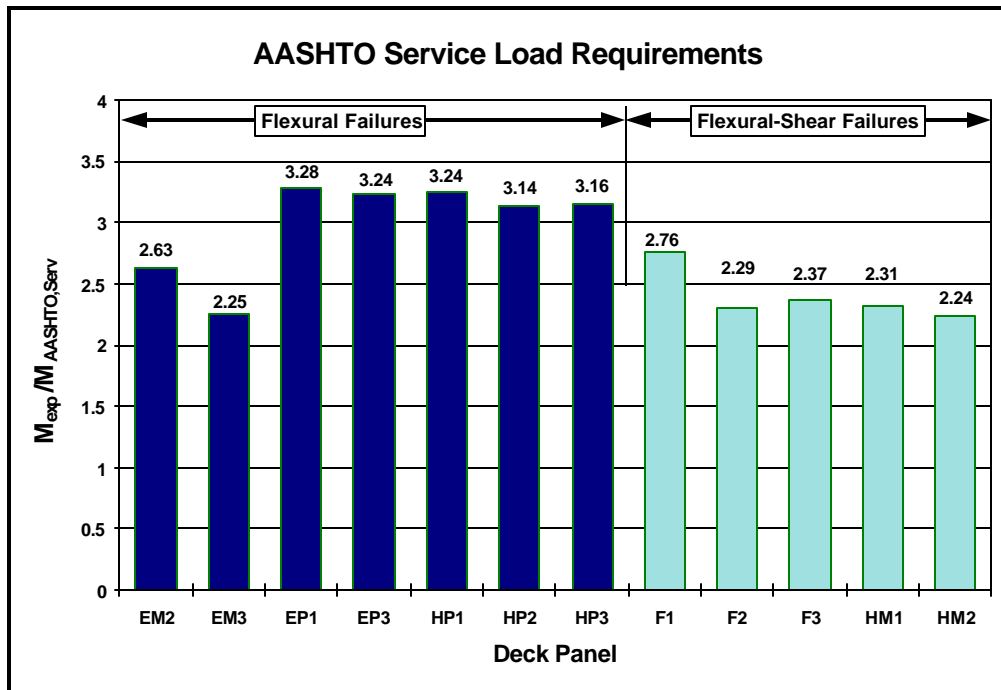


Figure 5. 11: Comparison of Experimental Ultimate Moment and AASHTO Service Moment

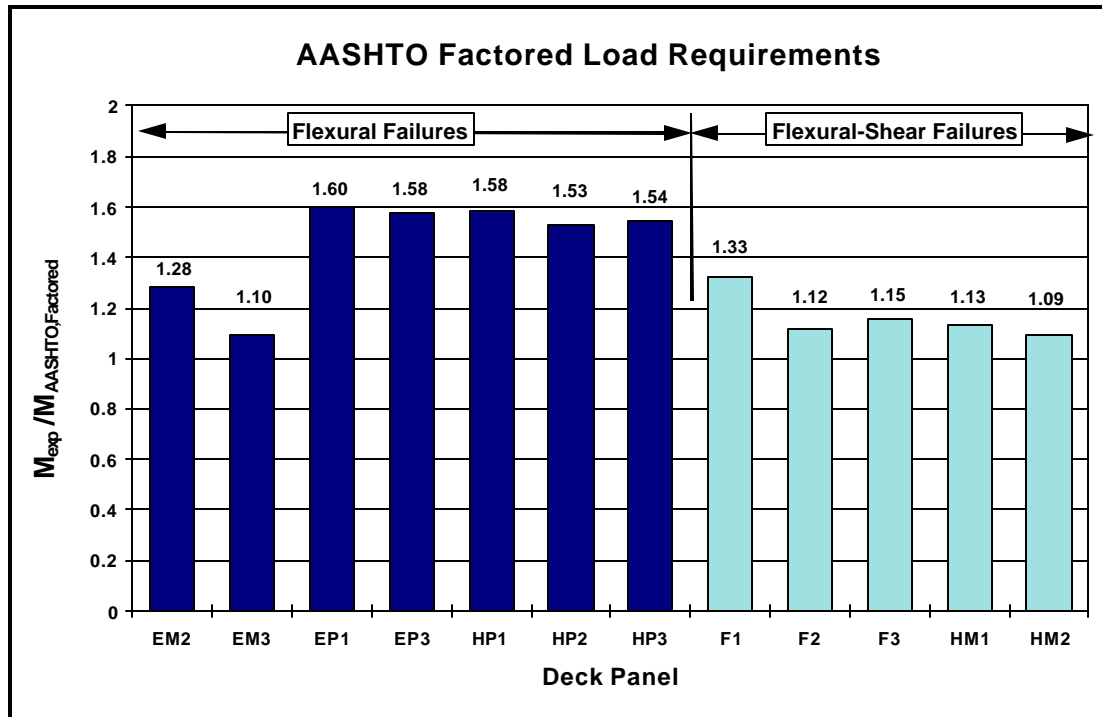


Figure 5.12: Comparison of Experimental Ultimate Moment and AASHTO Factored Moment

The deck panels are separated in Figures 5.11 and 5.12 based on the two observed failure modes. The flexure failure mode was observed for all the deck panels with ECS tensile reinforcement, see Table 5.1. This failure mode was characterized by yielding of the tensile reinforcement followed by a compression failure of the concrete between the active load points. The flexure-shear failure was observed in all the deck panels with GFRP tensile reinforcement. This failure occurred between the active load point and the support reaction.

Figure 5.11 shows that all deck panels met AASHTO flexural service load requirements with minimum ratios of experimental ultimate moment to design service moment of 2.25 and 2.24 for specimens with flexural and shear-flexural failure modes, respectively. Similarly, Figure 5.12 shows that the minimum ratios of experimental ultimate to factored AASHTO design moments for the specimens are 1.1 and 1.09 for the flexural and flexure-shear failure modes, respectively.

For the specimens failing in the flexural mode, the negative moment ECS specimens, EM2 and EM3 have the lowest ratio of experimental to design service and factored moments. This is due to the greater clear cover to tensile reinforcement in these specimens than in the positive moment specimens with ECS tensile reinforcement shown in Table 5.1.

Of the specimens failing in the flexure-shear failure mode, deck panel F1 has the largest ratio of experimental to design service load and of experimental to design factored load. This was due to the lower design moment requirements for specimen F1 with the reduced span of 2130 mm. The remainder of the specimens with the 2740 mm span length failed at comparable ratios of experimental to design moments, an average ratio of 2.3 and 1.12 for service and factored loads, respectively.

Despite the differences in failure mode and type of tensile reinforcement, all of the deck panels tested under negative moment have approximately the same ratios of experimental ultimate load to design service load and design factored load.

AASHTO provides no direct provisions for the shear design of bridge decks. Instead, Article 3.24.4 specifies that “slabs designed for bending moment in accordance with Article 3.24.3 (Equation 5.1) shall be considered satisfactory in bond and shear” (AASHTO 1996). Since all deck panels meet the design flexural requirements, they meet AASHTO specifications with regard to strength.

5.4.2 Correlation of Experimental Ultimate Load with Theory

Experimental ultimate loads were compared with predicted failure loads based on current ACI-318M-95 provisions and other published theoretical relations. As discussed in the previous section, two failure modes were exhibited in the deck panels, flexure and flexure-shear failure modes. The subsequent discussion of predicted ultimate load is separated for these two failure modes. Material properties identified in Tables 5.2 and 5.3 were used in all theoretical computations in the following sections.

5.4.2.1 Flexural failure mode

Predictions of the flexure failure mode were computed based on design assumptions presented in Section 10.2 of ACI-318M-95. The assumptions include: (1) satisfaction of equilibrium and compatibility conditions, (2) a maximum usable concrete strain of 0.003, (3) a reinforcement stress equal to f_y , and (4) an equivalent rectangular stress block. In addition, ACI-318M-95 specifies a strength reduction factor of 0.9 for members under flexure without axial load. This factor was not applied to the theoretical results presented in this section.

Figure 5.13 shows the ratio of experimental failure moment to the predicted failure moment computed with the above assumptions for specimens failing in flexure. Ratios computed vary between 1.02 and 1.23. Results show that the ultimate strength of these specimens can be predicted accurately with current ACI provisions.

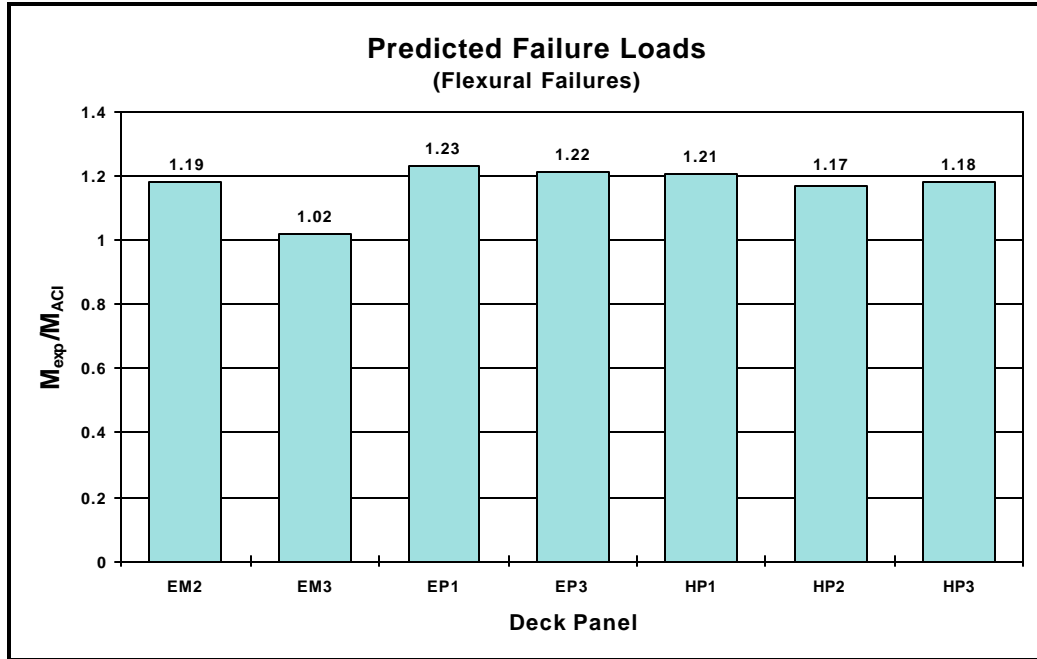


Figure 5. 13: Comparison of Experimental Ultimate Load to Predicted Ultimate Load based on ACI Provisions – Flexural Failures

5.4.2.2 Flexural shear failure mode

ACI-318M-95 provides the following two equations for computing the shear capacity of members subjected to shear and flexure in Section 11.3:

$$V_c = \left(\frac{\sqrt{f'_c}}{6} \right) b_w d \quad (5.2)$$

$$V_c = \left(\sqrt{f'_c} + 120 \rho_w \frac{V_u d}{M_u} \right) \frac{b_w d}{7} \leq 0.3 \sqrt{f'_c} b_w d \quad (5.3)$$

where,

- V_c = nominal shear strength provided by concrete in Newtons
- f'_c = specified concrete strength
- b_w = member width
- d = distance from extreme compression fiber to centroid of tensile reinforcement
- ρ_w = reinforcement ratio
- V_u = factored shear at section considered
- M_u = factored moment occurring simultaneously with V_u at section considered

As shown in Figure 5.14, these two expressions greatly overestimate the shear strength of the GFRP tensile reinforced deck panels. Ratios of experimental ultimate

strength to predicted ultimate strength using Equations (5.2) and (5.3) range between 0.63 and 0.70.

Tests performed by Michaluk et al., (1998) produced similar results. Michaluk tested slabs under an equally spaced four point loading with a span length of 3000 mm. The slabs had a width of 100 mm and depths of 150 mm and 200 mm. Transverse reinforcement was included in the specimens with longitudinal reinforcing ratios ranging from 0.23% to 0.955% for the GFRP reinforced specimens. The author recommended modification of the existing ACI equations by the ratio of the elastic moduli of GFRP and steel reinforcements, $E_{\text{GFRP}}/E_{\text{STEEL}}$. This modification applied to the ACI-318M-95 relations, Equations (5.2) and (5.3), results in:

$$V_c = \left(\frac{E_{\text{GFRP}}}{E_{\text{ECS}}} \right) \left(\frac{\sqrt{f'_c}}{6} \right) b_w d \quad (5.4)$$

$$V_c = \left(\frac{E_{\text{GFRP}}}{E_{\text{ECS}}} \right) \left(\sqrt{f'_c} + 120\rho_w \frac{V_u d}{M_u} \right) \frac{b_w d}{7} \leq 0.3\sqrt{f'_c} b_w d \quad (5.5)$$

Equations 5.4 and 5.5 predicted the failure strength of Michaluk's deck panels with ratios of experimental to predicted ultimate shear strength ranging from approximately 1.15 to 1.95.

Figure 5.14 shows a comparison of observed experimental design loads of this study to equations (5.4) and (5.5) proposed by Michaluk et al., (1998). Ratios range from values of 3.05 to 3.45, which means Michaluk's expressions significantly underestimate the shear strength of the deck panels tested.

5.4.2.3 Proposed shear equation modifications

Due to inadequacies of the above shear relations, a proposed shear equation modification based on the test data is proposed in Equations (5.6) through (5.8). It is proposed that the ACI-318M-95 shear relations be modified by the following ratio:

$$3 \left(\frac{E_{\text{GFRP}}}{E_{\text{ECS}}} \right) \quad (5.6)$$

resulting in the following relations for predicting shear capacity:

$$V_c = 3 \left(\frac{E_{\text{GFRP}}}{E_{\text{ECS}}} \right) \left(\frac{\sqrt{f'_c}}{6} \right) b_w d \quad (5.7)$$

$$V_c = 3 \left(\frac{E_{\text{GFRP}}}{E_{\text{ECS}}} \right) \left(\sqrt{f'_c} + 120\rho_w \frac{V_u d}{M_u} \right) \frac{b_w d}{7} \leq 0.9 \left(\frac{E_{\text{GFRP}}}{E_{\text{ECS}}} \right) \sqrt{f'_c} b_w d \quad (5.8)$$

Comparisons of the experimental results and the proposed relations are shown in Figure 5.14. In addition, numerical comparisons of the results from both Michaluk et al., (1998) study and the present study are given in Table 5.4. Ratios of experimental results to the proposed shear relations ranged from 1.04 to 1.17 for the deck panels of this study.

TABLE 5.4 RESULTS OF PROPOSED SHEAR EQUATION

	Specimen	V_{exp} (kN)	Proposed Equation			
			(5.7)		(5.8)	
			V_c (kN)	V_{exp}/V_c (kN)	V_c (kN)	V_{exp}/V_c (kN)
Michaluk et al. (1998)	1	74.6	96.4	0.77	83.87	0.89
	2	158.1	142.75	1.11	124.6	1.27
Present Study	F1	53.56	51.42	1.04	51.24	1.04
	F2	56.58	52.77	1.07	52.52	1.08
	F3	58.36	49.98	1.17	49.89	1.17
	HM1	57.07	51.09	1.11	50.94	1.12
	HM2	55.20	53.36	1.03	53.09	1.04

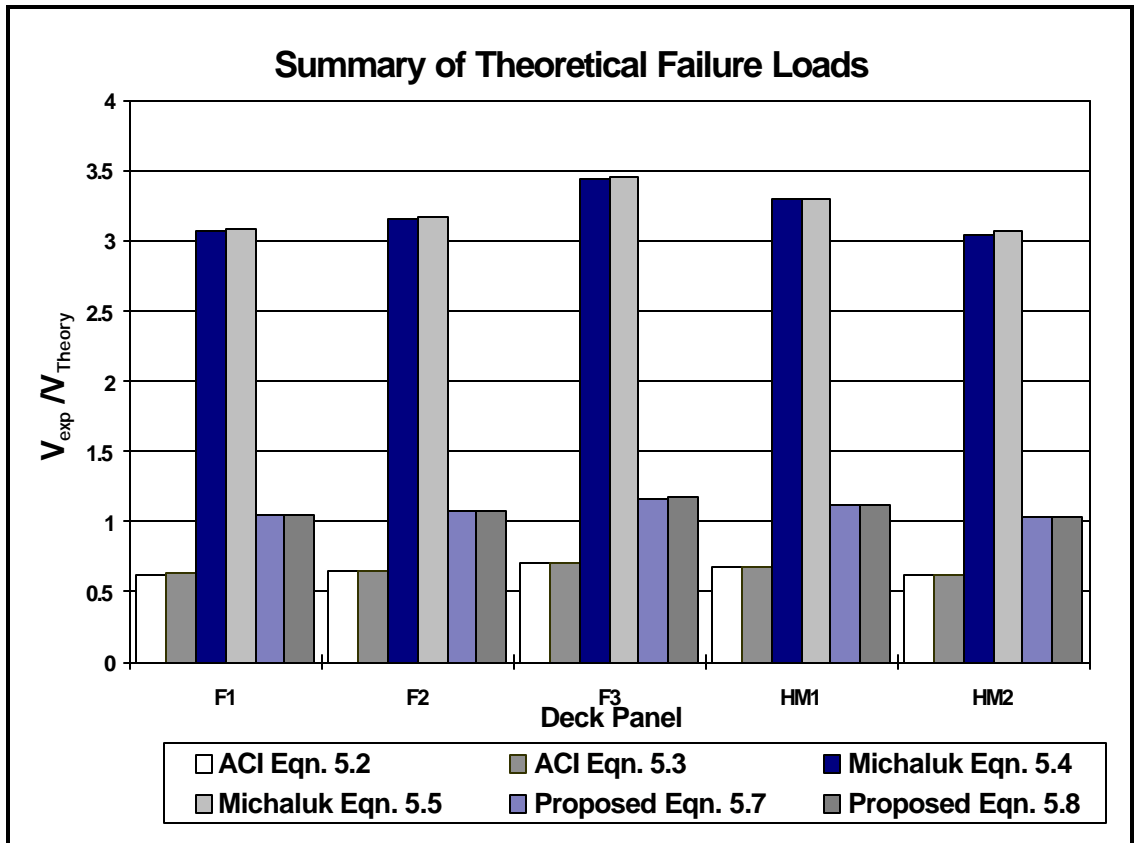


Figure 5. 14: Summary of Comparisons of Experimental Ultimate Load to Predicted Shear Capacity (Flexural Shear Failures)

5.5 PREDICTION OF MIDSPAN DISPLACEMENT

Both AASHTO and ACI design recommendations for one way slabs are discussed in this section. In addition, four different theoretical methods for computing load versus displacement are compared to the experimental results. These theoretical methods include: (1) integration of moment curvature relations using the moment area method, (2) an approximate method provided in ACI-318M-95 and its predecessors for many years, (3) a method proposed by Masmoudi, Theriault, and Benmokrane(1996), and (4) a method proposed by GangaRao and Faza (1991).

5.5.1 AASHTO & ACI Maximum Displacements at Service Load

AASHTO (1996) provides design recommendations for displacements of concrete structures in Articles 8.9 and 8.13. No specifications are provided for individual superstructure components such as the bridge deck. Rather, displacement specifications are based on the entire superstructure acting as a whole. Article 8.13 specifies that computed displacements should be based on the entire superstructure section and that the

superstructure acts together having an equal displacement. The provisions provided are not set up to limit localized displacements, such as bridge deck displacements relative to the main support girders.

ACI-318M-95 specifies a minimum slab thickness that, if equaled or exceeded, obviates displacement computations. Based on ACI Section 9.5.2, no displacement computations are required for the deck panels if the thickness of the deck panels exceeds $L/20$, where L is the span length. For the spans tested, the minimum thickness $L/20$, equals 107 mm and 137 mm for the 2130 mm span of specimen F1 and the 2740 mm span of the remaining specimens respectively. All of the specimens tested exceed this minimum thickness with a thickness 190 mm. Therefore, displacement computations are not required for the deck panels according to ACI-318M-95 requirements.

Though no displacement computations were required by code specifications, a comparison of the service load displacements for the deck panels tested is provided in Figure 5.15. The AASHTO service loads for the deck panels were presented in Section 5.4.1 and were 8885 kN-mm for deck panel F1 and 11,280 kN-mm for the other deck panels. Service dead loads for the deck panels were 955 kN-mm and 1580 kN-mm respectively. The displacements used in Figure 5.15 were computed by subtracting the displacements of the specimens at the service dead load from the displacements at the total service load.

Results for the deck panels with ECS tensile reinforcement varied widely. The deck panels with the smallest δ/L at service live load were EM2 and HP3. Studies of the load displacement results showed that these deck panels did not crack prior to reaching the service load while all of the other specimens did crack. Deck panel EM3 had a very large ratio compared to the other ECS reinforced deck panels because it had a significantly lower cracking load. EP3 also had a lower cracking load than the other positive moment ECS deck panel, EP1.

Of the deck panels reinforced with GFRP rebars, deck panel F1 had the smallest δ/L at service live load. This was because the smaller span length made the deck panel stiffer and reduced the service live load (see Equation (5.1)). The remaining GFRP tensile reinforced deck panels had similar ratios that were much larger than ratios for the ECS reinforced deck panels.

Since code specifications for displacements were based on steel reinforced members, it is recommended that they be modified for GFRP reinforced members.

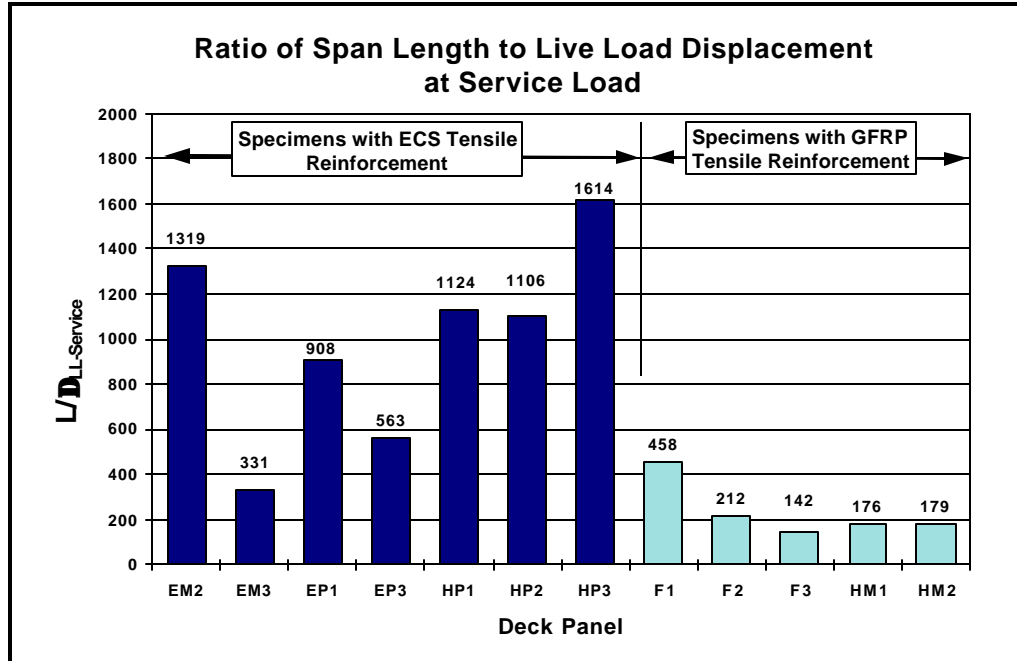


Figure 5.15: Span Length, L , to Service Live Load Displacement, $D_{LL-Service}$, Ratios of Deck Panels

5.5.2 Moment Curvature Analysis

To obtain a more accurate prediction of displacement, moment curvature relations were required for each specimen. Assumptions and theories used in the moment curvature analyses are presented below.

Figure 5.16 shows the concrete compressive stress strain model proposed by Kent and Park (1971) used in the development of the moment curvature relations. The concrete cylinder strengths shown in Table 5.2 were used for the maximum concrete compressive stress, f'_c . Maximum stress in the concrete was assumed to occur at a strain of 0.002 as recommended by Kent and Park. The model is defined by the following expressions in English units:

$$f_c = f'_c \left[\frac{2\varepsilon_c}{\varepsilon_0} - \left(\frac{\varepsilon_c}{\varepsilon_0} \right)^2 \right] \quad (5.11)$$

$$\varepsilon_{50U} = \frac{3 + 0.002f'_c}{f'_c - 1000} \quad (5.12)$$

where,

- ε_c = concrete strain
- ε_0 = concrete strain at stress f'_c

g_{50U}	=	strain at 0.5 of maximum stress on descending branch of stress-strain curve for unconfined concrete
f'_c	=	compressive strength of a concrete cylinder [psi]

The Kent Park model was selected for this study because it is widely accepted and is easily programmed.

Tension tests, such as split cylinder or beam tests, were not performed on the concrete. Initially, the expression for tensile strength of concrete recommended in Section 9.5.2.3 of ACI-318M-95 was used in the moment curvature derivations. However, after comparison of the experimental and theoretical load displacement diagrams, it was decided to calculate the tensile strength of the concrete from the cracking load observed during the tests.

Tensile properties of the ECS and GFRP rebars were determined experimentally. Stress strain relations were derived from tension tests of three ECS rebars and four GFRP rebars. Table 5.3 and Figure 5.7 give details of the tensile properties used. A more detailed discussion of the tension test methods is provided in Chapter 2.

The ECS rebars were assumed to display the same compression and tension stress/strain properties. However, the GFRP rebars were likely to have significantly different properties in tension and compression. The compression properties of the GFRP rebars were determined experimentally (see Chapter 2) and are presented in Table 5.3 and Figure 5.7.

Theoretical moment/curvature plots for three negative moment deck panels are shown in Figure 5.17 and for three positive moment deck panels in Figure 5.18. The figures reflect the yielding of the ECS rebars and post yielding behavior of the deck panels with ECS tensile reinforcement. No experimental moment/curvature results are presented because rebar tensile strains were not recorded during the testing. Placement of strain gages on the rebars would interfere with the crack behavior of the deck panels which was a major focus of the study. Moment curvature diagrams for the remainder of the deck panels are given in Section B.1 of Appendix B.

The compression reinforcement apparently did little to alter the behavior of the specimens at service load levels. In most cases the reinforcement closest to the compression face of the deck panel was located near the neutral axis of the specimen and consequently was under little stress. After yielding of the ECS tensile reinforcement, the compression reinforcement of the ECS deck panels did affect the deck panel behavior. Figure 5.18 shows representative positive moment ECS and hybrid specimens. Both specimens contained ECS tension reinforcement. However, the all ECS specimen had ECS compression reinforcement while the Hybrid specimen had GFRP compression reinforcement (see Table 5.1). The plot shows that the ECS specimen had a greater post-yielding strength than the Hybrid specimen due to the presence of the ECS compression reinforcement.

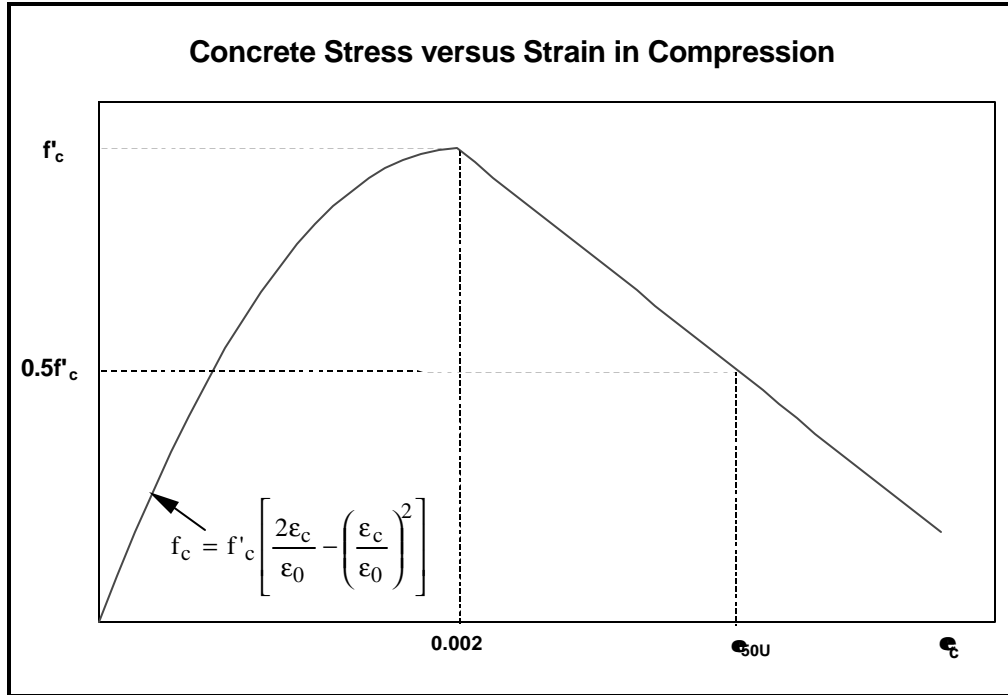


Figure 5.16: Kent Park Model for Concrete in Compression

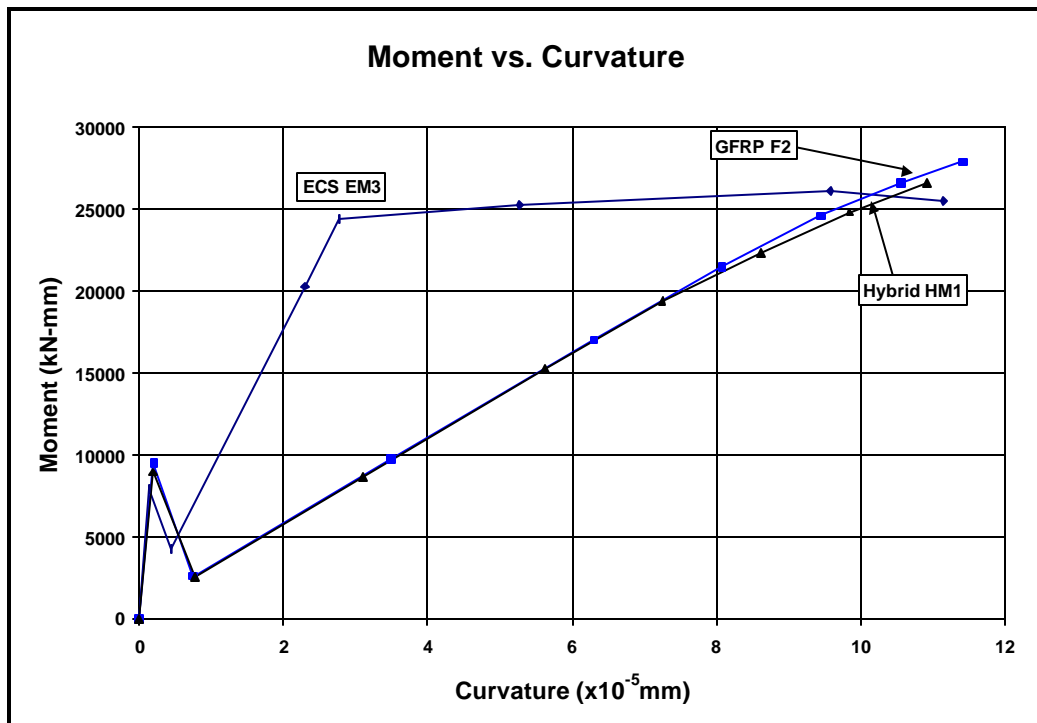


Figure 5.17: Theoretical Moment Curvature for Negative Moment Deck Panels

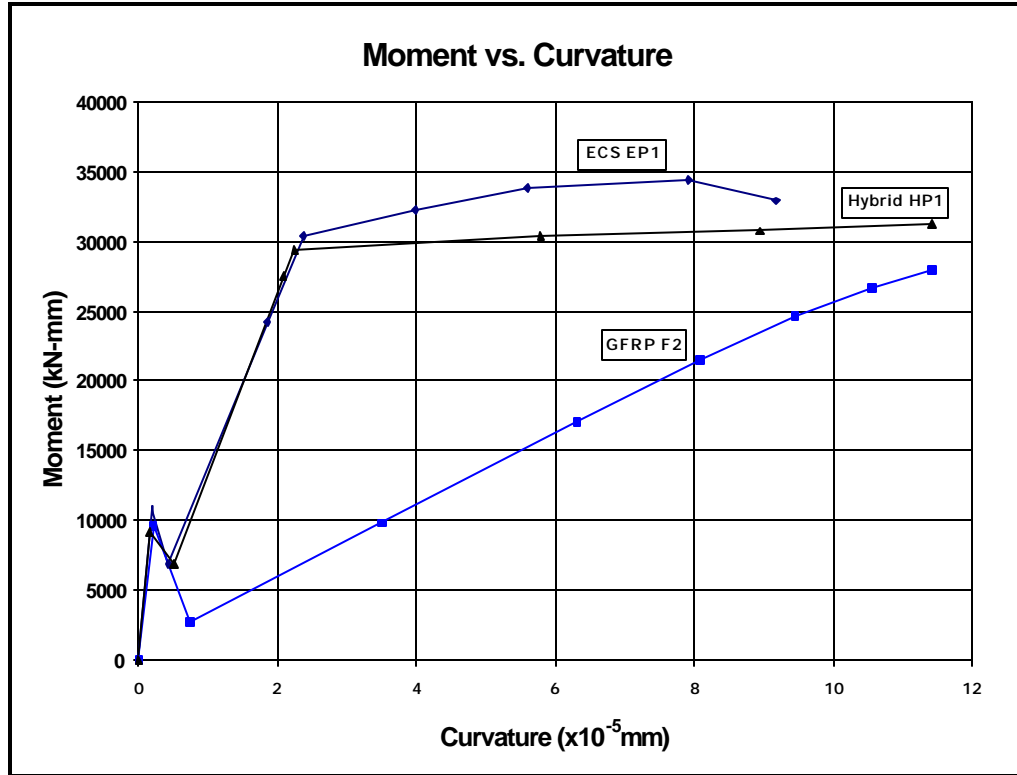


Figure 5.18: Theoretical Moment versus Curvature for Positive Moment Deck Panels

5.5.3 Theoretical Estimates of Displacement for Deck Panels with ECS Tensile Reinforcement

Two methods were used to compute displacements for the deck panels with ECS tensile reinforcement. First, the moment area method was used to compute the theoretical load displacement curves shown in Figures 5.19 through 5.21. Moment/curvature relations discussed in Section 5.5.2 were integrated in correlation with the moment area method to compute displacements accounting for: nonlinearity of the concrete, concrete still in tension before and after cracking, yielding of the reinforcing steel, and compression reinforcement.

Second, the method presented in Section 9.5.2.3 of ACI-318M-95 is used. This involves an effective moment of inertia computed with the following relations:

$$I_e = I_{cr} + (I_g - I_{cr}) \left(\frac{M_{cr}}{M_a} \right)^3 \leq I_g \quad (5.13)$$

$$M_{cr} = \frac{f_r I_g}{y_t} \quad (5.14)$$

where,

- I_e = effective moment of inertia
- M_{cr} = cracking moment
- M_a = maximum moment in member at stage displacement is computed

I_g = moment of inertia of gross concrete section neglecting reinforcement
 I_{cr} = moment of inertia of cracked section transformed to concrete
 f_r = modulus of rupture of concrete, MPa (see Section 5.5.2)
 y_t = distance from centroidal axis of gross section, neglecting reinforcement, to extreme fiber in tension.

Figures 5.19 through 5.21 provide comparisons of the experimental results with the two theoretical methods for three of the deck panels tested. The three panels were selected to represent each of the different reinforcement schemes with ECS tensile reinforcement.

Results of the moment area method show good correlation for all of the deck panels with ECS tensile reinforcement up to yielding. After yielding, the theoretical results followed the experimental results well for deck panel EP1. However, there was some difference in the theoretical and experimental post yielding results for deck panels EM2 and HP1. The difference in load was never greater than 15% in either case and was a result of inaccuracies in the models used. Hysteresis due to the unloading of deck panel EP1 had no effect on the load versus displacement results presented here.

Results from the ACI model show good agreement with experimental results up to the point where the concrete stress/strain curve can no longer be assumed nonlinear, approximately $0.45f'_c$. After this point, the method no longer applies without considering nonlinearity in the concrete stress/strain curve.

Section B.2 of Appendix B provides similar plots for the remaining specimens.

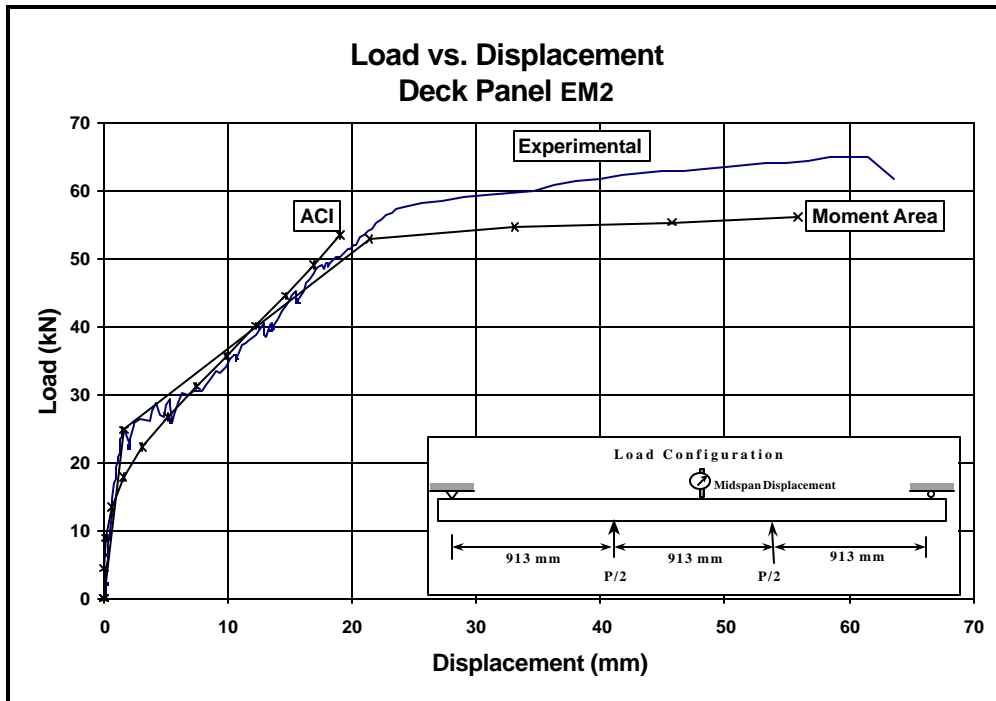


Figure 5. 19: Comparison of Experimental and Theoretical Load versus Displacement for Deck Panel EM2

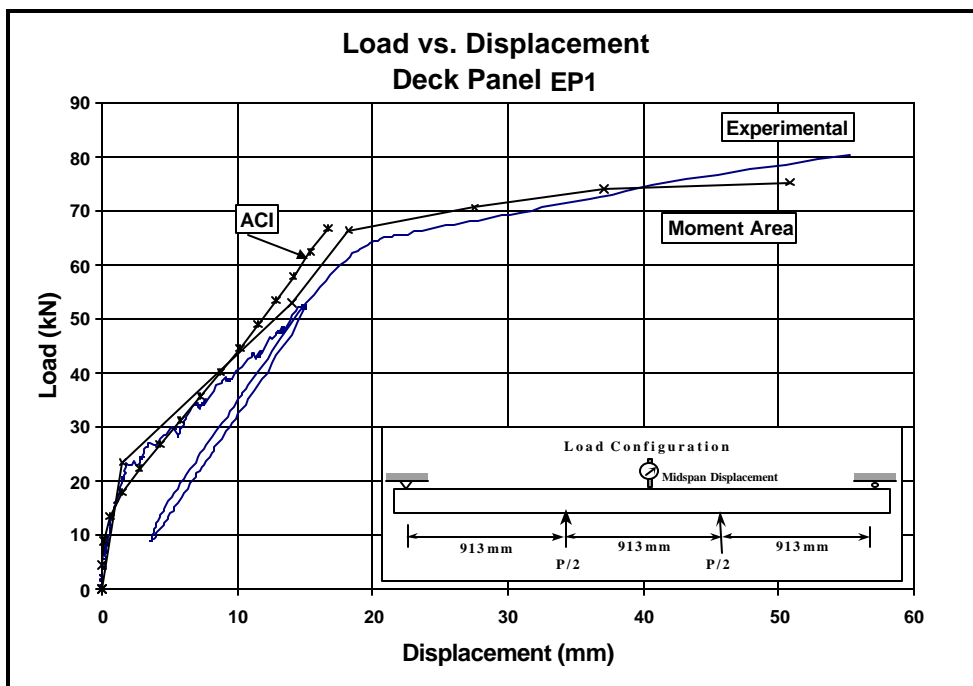


Figure 5. 20: Comparison of Experimental and Theoretical Load versus Displacement for Deck Panel EP1

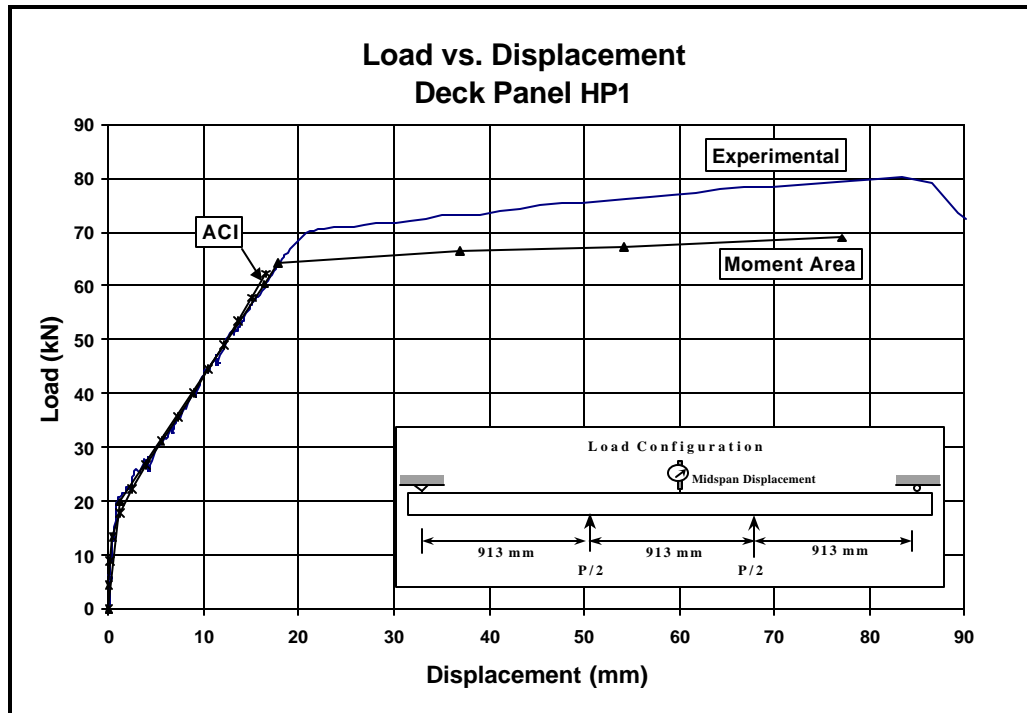


Figure 5. 21: Comparison of Experimental and Theoretical Load versus Displacement for Deck Panel HP1

5.5.4 THEORETICAL ESTIMATES OF DISPLACEMENT FOR DECK PANELS WITH GFRP TENSION REINFORCEMENT

Displacements of the deck panels with GFRP tension reinforcement were predicted using three methods. First, the moment area method was used with the moment curvature diagrams discussed in Section 5.5.2. To compute the theoretical load/displacement curves shown in Figures 5.22 and 5.23 the moment/curvature relations were integrated as part of the moment area method to compute displacements including the effects of nonlinearity of the concrete, concrete still in tension before and after cracking, yielding of the reinforcing steel, and compression reinforcement.

The other two methods for estimating displacements of the deck panels were based on published research. Several research studies have found that the ACI-318M-95 effective inertia relation, Equation (5.13), significantly overestimates the effective moment of inertia of beams reinforced with GFRP rebars due to the large rise of the neutral axis following cracking. This overestimation of effective inertia results in a significant underestimation of displacements.

The second method used to estimate displacements of the GFRP tensile reinforced specimens was proposed by Masmoudi, Theriault, and Benmokrane (1996). In his study, four point load tests were performed on beams with a 3300 mm span with 500 mm between load points. The specimen cross sections were 300 mm deep and 200 mm wide

with reinforcing ratios ranging from 0.50% to 1.07%. Shear stirrups were provided in the specimens at a 80 mm spacing. Based on test results a coefficient, β , was derived that reduced the computed gross moment of inertia in Equation (5.14). Using it in correlation with Equation (5.13) results in the following expression:

$$I_e = I_{cr} + (\beta I_g - I_{cr}) \left(\frac{M_{cr}}{M_a} \right)^3 \leq I_g \quad (5.15)$$

where,

I_e = reduction coefficient

Masmoudi recommended a reduction coefficient of 0.6 for I_g of members reinforced with the GFRP rebars used in this study.

The third method used for the computation of displacements was proposed by GangaRao and Faza (1991) for GFRP reinforced beams. In this experimental study, load tests were performed on 305 mm deep and 150 mm wide beams reinforced with different reinforcing ratios and reinforcement types. The beams were tested under four point loading with a 2750 mm span. All of the specimens contained shear stirrups. The types of reinforcement used in the study included smooth, sand coated, and deformed GFRP rebars as well as conventional deformed steel rebars.

Based on the test results, GangaRao and Faza developed a load displacement model. For the four point loading used in the deck panel testing, their model assumes that the moment of inertia of the deck panel between load points is equal to the cracked transformed moment of inertia, I_{cr} . The remainder of the deck panel, between the load point and support, is assumed to be partially cracked with an ACI-318M-95 effective moment of inertia, I_e . This results in a modified moment of inertia, I_m , applicable only to an equally spaced four point loading given by:

$$I_m = \frac{23I_{cr}I_e}{8I_{cr} + I_e} \quad (5.16)$$

where,

I_m = modified moment of inertia

Figures 5.22 and 5.23 show comparisons of the displacements recorded during the load tests of the two specimen types with GFRP tensile reinforcement and the three methods discussed. The most rigorous analysis method, the moment area method, shows good correlation.

Both the model developed by Masmoudi, Theriault, and Benmokrane (1996) and the model developed by GangaRao and Faza (1991) were terminated in Figures 5.22 and 5.23 where the stress/strain curve for concrete was assumed nonlinear, a concrete stress of approximately $0.45f_c$. After this stress level, the models are no longer applicable without considering the nonlinearity of the concrete stress/strain. This type of analysis was not performed in this study.

The effective moment of inertia method proposed by Masmoudi Theriault, and Benmokrane (1996), Equation (5.15), shows good agreement with the experimental data throughout the load range. However, the method underestimates the displacements recorded during the tests. The modified moment of inertia method proposed by GangaRao and Faza (1991), Equation (5.16), does not show good agreement around the cracking load. However, in regions after cracking the model does approximate the experimental data reasonably well. (See Section B.2 of Appendix B for the remainder of the test results).

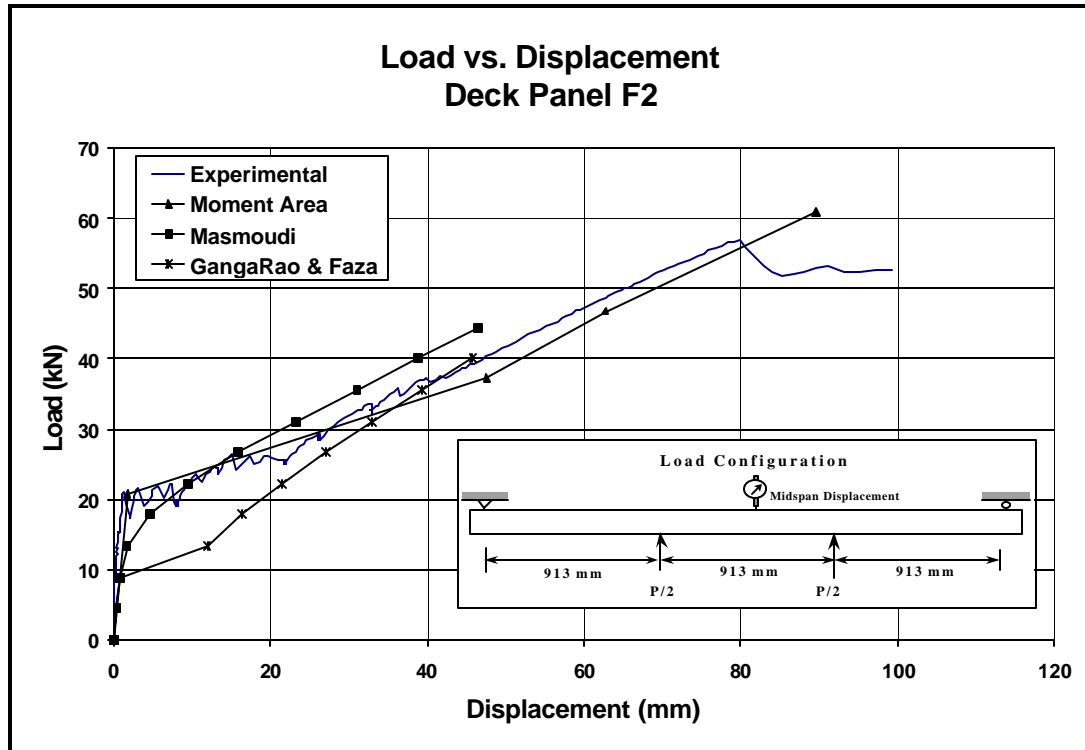


Figure 5. 22: Comparison of Experimental and Theoretical Load versus Displacement for Deck Panel F2

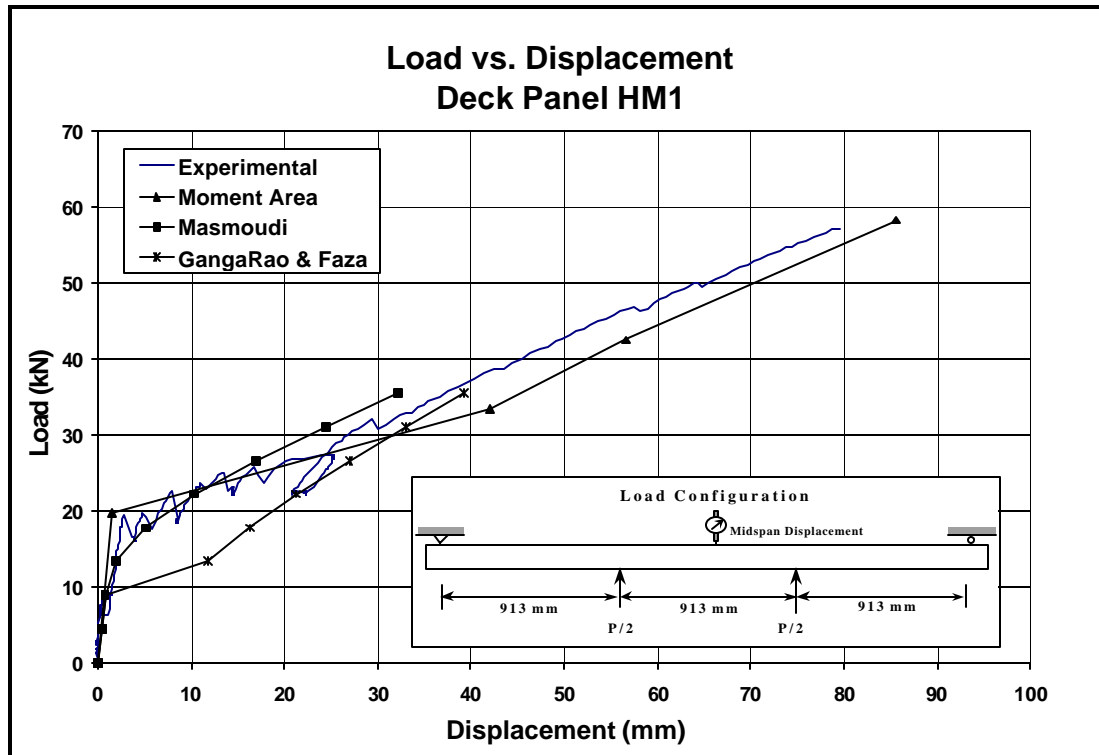


Figure 5. 23: Comparison of Experimental and Theoretical Load versus Displacement for Deck Panel HM1

5.6 CRACK WIDTH CORRELATION

This section first discusses maximum crack width limitations and specifications provided in ACI-318M-95 and AASHTO (1996) design guidelines. Comparisons are made between the maximum crack widths specified in the code provisions and those observed during experimental testing. Next, maximum crack spacings measured for the deck panels with ECS tensile reinforcement are compared to theoretical crack widths based on the cracking theory proposed by Gergely and Lutz (1968).

Experimental maximum crack widths observed on the deck panels with GFRP tension reinforcement are compared with three theoretical maximum crack width models. First, a model proposed by Masmoudi, Benmokrane, and Challal (1996) based on the Gergely and Lutz relation. Second, a model proposed by Faza and GangaRao (1991). And third, a model proposed based on the results of the deck panels tested in this study.

5.6.1 AASHTO and ACI Maximum Crack Widths

Both AASHTO and ACI specifications do not limit maximum crack widths directly. Instead, they provide expressions that control the distribution and size of

reinforcement, which in turn control flexural cracking. These expressions are based on the maximum crack width model proposed by Gergely and Lutz (1968) in English units:

$$w = 0.076\beta f_s \sqrt[3]{d_c A} \quad (5.17)$$

where,

w	=	crack width (units of 0.001 in)
	=	ratio of distances to the neutral axis from the extreme tension fiber and from the centroid of the main reinforcement
f_s	=	reinforcement stress calculated by elastic cracked section theory (ksi)
d_c	=	tensile reinforcement cover measured from the outermost rebar (in)
A	=	average effective concrete area around a reinforcing bar (in ²)

Section 10.6.4 of ACI-318M-95 specifies that reinforcement should be sized and distributed such that the quantity z, does not exceed 30 MN/m for interior exposure and 25 MN/m for exterior exposure. The quantity z is given by the metric version of Equation (5.17):

$$z = f_s \sqrt[3]{d_c A} \quad (5.18)$$

where,

z	=	quantity limiting distribution of flexural reinforcement
f_s	=	calculated stress in reinforcement at service load

Commentary on the provision in R10.6.4 of ACI-318M-95 states that these two limits for the quantity z correspond to maximum crack widths of 0.4 mm and 0.33 mm, respectively, assuming an average ratio of 1.35 for floor slabs.

For a bridge deck, the stricter specification for exterior exposure, 0.33 mm, would apply to the negative moment specimens reinforced with ECS tensile reinforcement. In negative moment regions of a bridge deck the tensile reinforcement is located near the riding surface and is exposed to a harsher environment. Interior specifications, 0.4 mm, would apply to positive moment regions of the bridge deck where the tensile reinforcement is located near the bottom of the slab. This would apply to the positive moment deck panels.

GFRP rebars are not vulnerable to aggressive ions and therefore corrosion. For this reason, the limiting maximum crack widths for GFRP reinforced concrete members should be based entirely on aesthetics and serviceability (i.e. the crack width limit should be small enough to prevent impact damage from passing vehicles and prevent freeze-thaw deterioration). Additional research is required to determine practical limits. At this time, it is recommended that the maximum crack width specification for interior exposure, 0.4 mm, apply to GFRP reinforced concrete members regardless of exposure condition.

Figure 5.24 provides a comparison of maximum crack widths, encountered at service load, with the ACI-318M-95 provisions. Three of the deck panels, specimens

EM2, F1, and HP3, did not crack until after the service load was surpassed and do not have values depicted in the figure. Of the remaining deck panels, all of the specimens with ECS tensile reinforcement met the ACI specifications for maximum crack width at service load. None of the remaining specimens with GFRP tension reinforcement met ACI specifications, even though the maximum crack width limitation was increased for interior exposure conditions.

AASHTO (1996) limits the allowable stress in steel reinforcement at service load. In English units, Article 8.16.8.4 provides the following relation for distribution of reinforcement:

$$f_s = \frac{z}{\sqrt[3]{d_c A}} \leq 0.6f_y \quad (5.19)$$

where,

f_y = yield stress of reinforcement

AASHTO specifies that the factor z shall not exceed 170 kips/inch for members in moderate exposure conditions and 130 kips/inch for members in severe exposure conditions. Maximum crack widths apparently intended by the AASHTO specifications were computed using the value of $\beta = 1.35$ assumed in the ACI-318M-95 specifications in conjunction with Equation (5.17). This resulted in apparent intended maximum crack widths of 0.4 mm for moderate exposure conditions and 0.3 mm for severe exposure conditions.

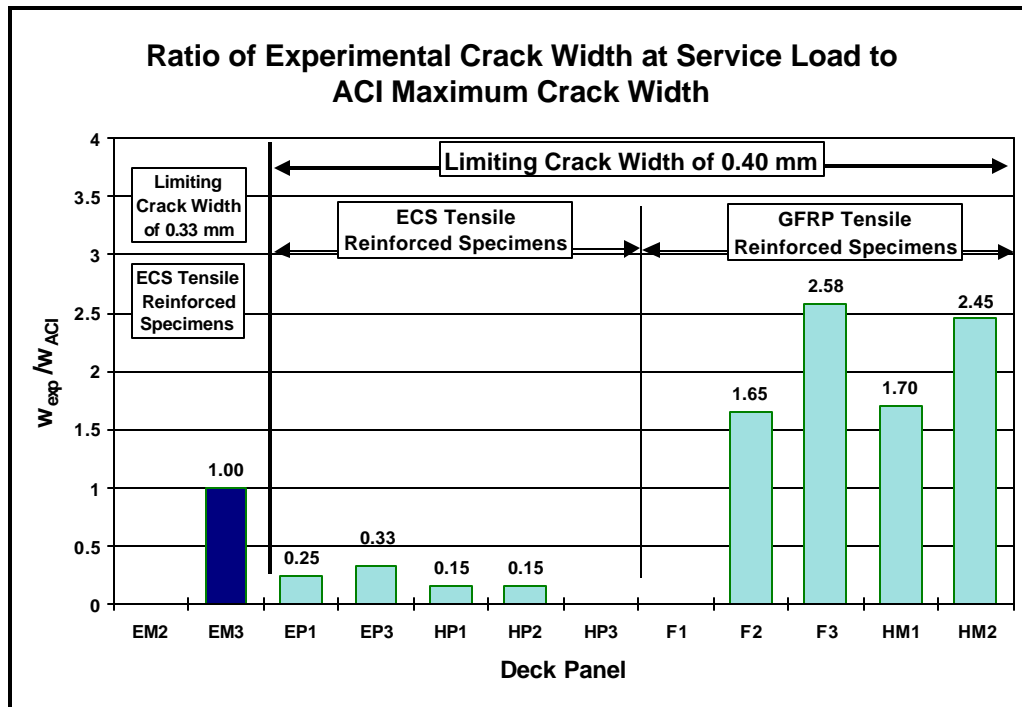


Figure 5.24: Ratio of Experimental Crack Width at Service Load to ACI Specified Maximum Crack Width

The AASHTO maximum crack width limits were calculated for the deck panels in a similar fashion to the ACI limits previously discussed. Consequently AASHTO severe exposure specifications, 0.3 mm, were assumed for the deck panels with ECS tension reinforcement under negative moment. Moderate exposure conditions, 0.4 mm, were applied to the remaining deck panels.

Ratios of maximum experimental crack width at service load to the maximum crack width intended by AASHTO are presented in Figure 5.25. Specimens EM2, F1, and HP3 did not crack prior to reaching service load and are depicted in the figure with values of zero. All of the remaining deck panels tested with ECS tensile reinforcement met AASHTO specifications with the exception of deck panel EM3. None of the remaining specimens reinforced with GFRP reinforcement met the AASHTO specifications for intended maximum crack width.

5.6.2 Theoretical Estimates of Maximum Crack Width for Deck Panels with ECS Tensile Reinforcement

The model proposed by Gergely and Lutz (1968), Equation (5.17), was used to predict maximum crack widths for the deck panels tested with ECS tensile reinforcement. Steel stresses required for the model were calculated using the assumptions and models described in 5.5.2. Stresses were computed at load levels where cracks were measured during the deck panel testing.

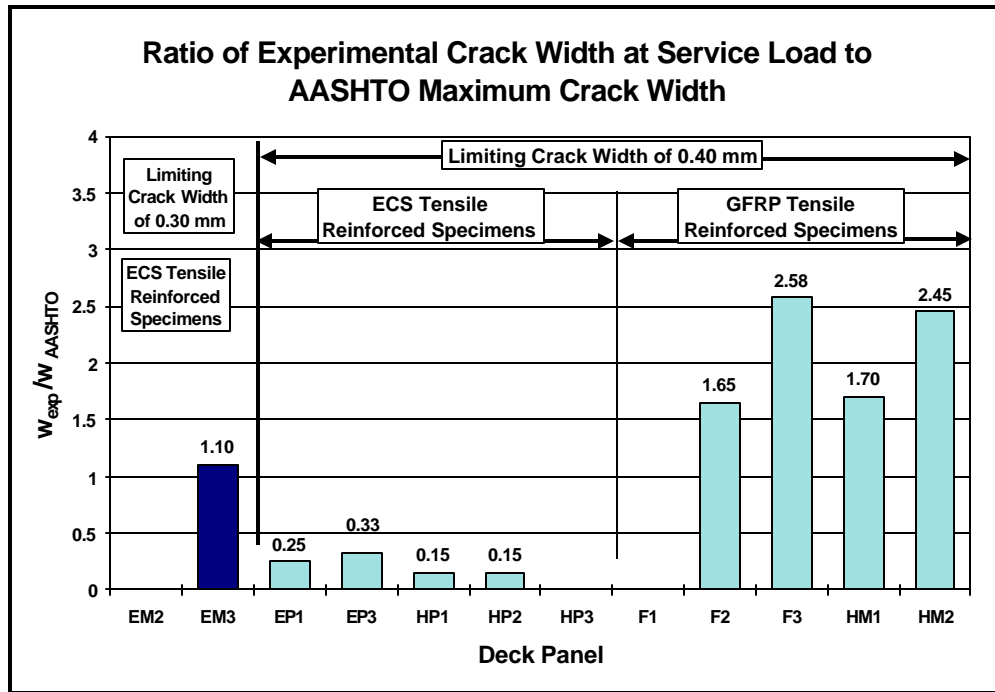


Figure 5. 25: Ratio of Experimental Crack Width at Service Load to AASHTO Apparently Intended Maximum Crack Width

Figures 5.26 through 5.28 show the experimental and theoretical results for representative specimens of the three deck panel types with ECS tensile reinforcement. Experimental and theoretical predictions show reasonable agreement for both ECS reinforced specimens in Figures 5.26 and 5.27. However, theoretical predictions of the maximum crack width overestimate the measured crack width for the positive moment Hybrid specimen, as shown in Figure 5.28. Differences in theoretical and experimental data should be expected when attempting to predict highly variable parameters such as maximum crack width.

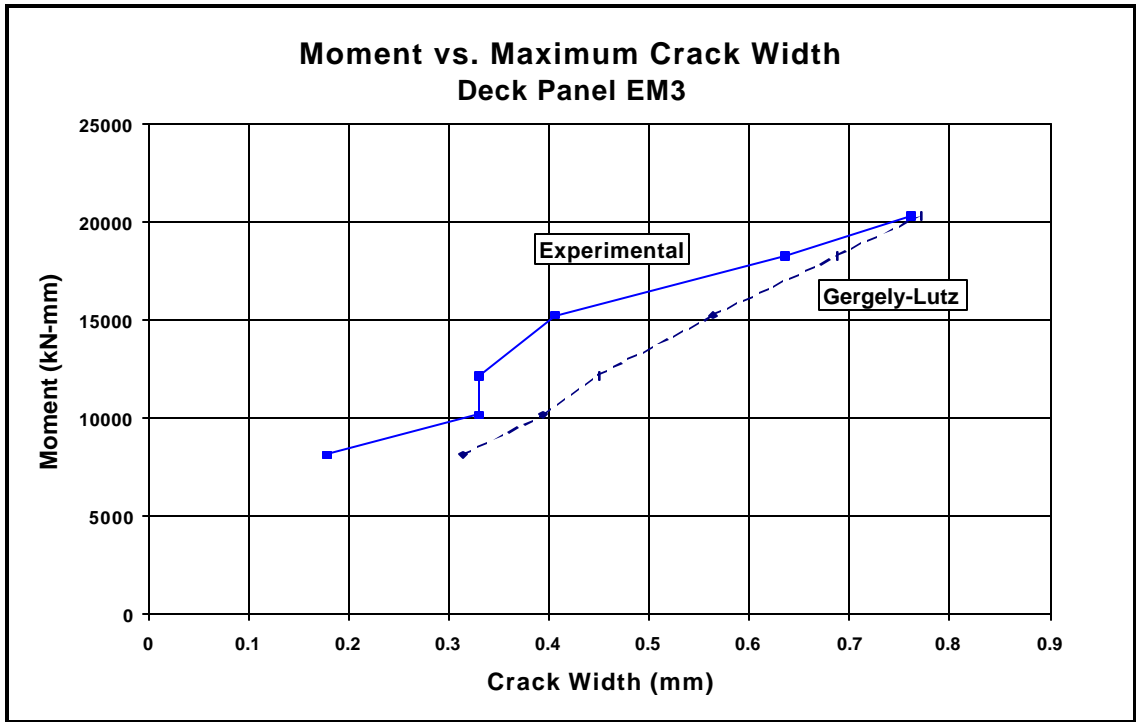


Figure 5. 26: Experimental and Theoretical Maximum Crack Width for Negative Moment ECS Deck Panel EM3

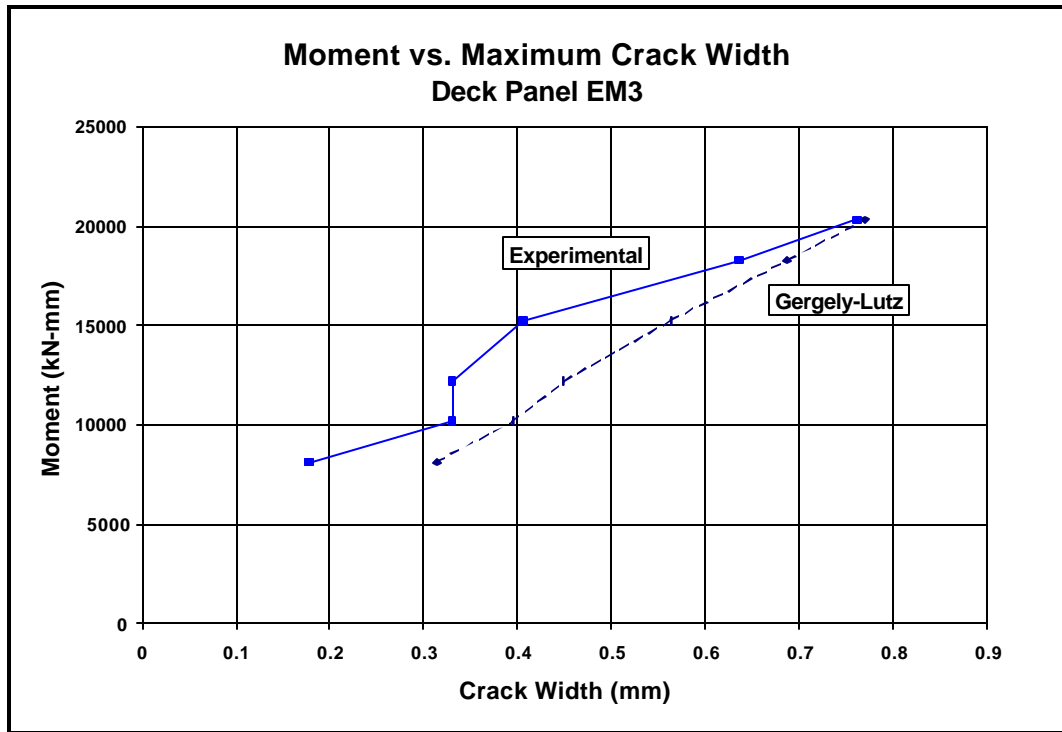


Figure 5. 27: Experimental and Theoretical Maximum Crack Width for Positive Moment ECS Deck Panel EP1

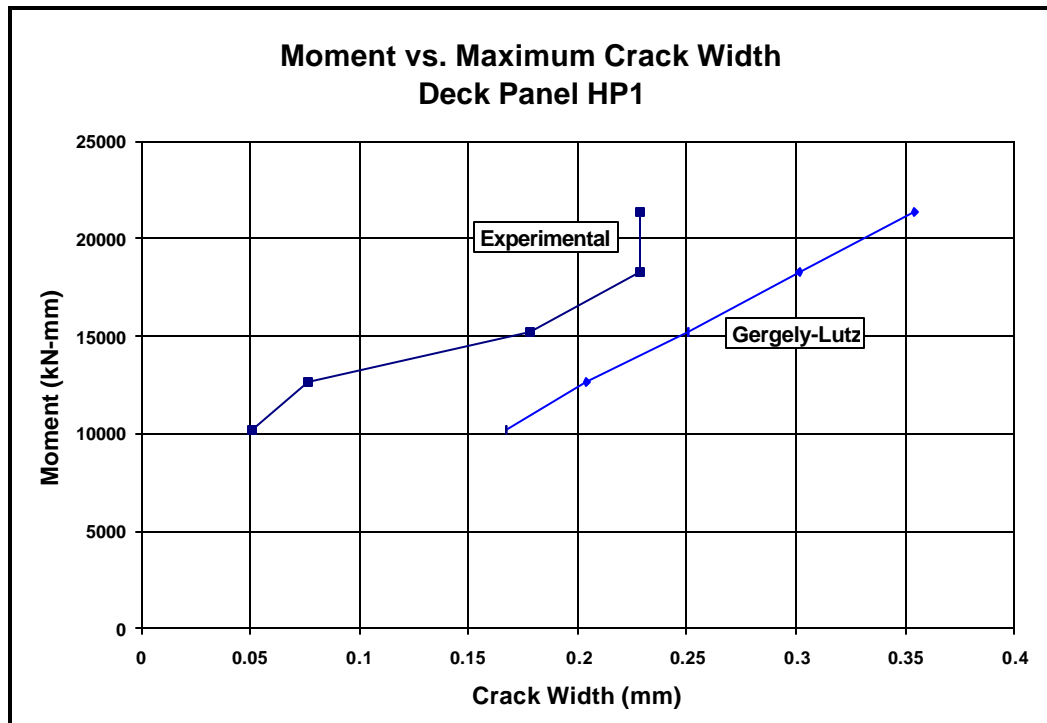


Figure 5.28: Experimental and Theoretical Maximum Crack Width for Positive Moment Hybrid Deck Panel HP1

5.6.3 Theoretical Estimates of Maximum Crack Width for Specimens with GFRP Tensile Reinforcement

Three models are used to estimate maximum crack width for the two specimen types with GFRP tensile reinforcement. First, a model developed by GangaRao and Faza (1991) is used which was based on the Watstein and Bresler model:

$$w_{\max} = \frac{2f_f f_r A}{E_f \mu_m \pi D} \quad (5.20)$$

where,

- w_{\max} = maximum crack width
- f_f = GFRP rebar stress
- f_r = tensile strength of concrete
- E_f = modulus of GFRP rebar
- μ_m = bond strength
- D = rebar diameter
- A = previously specified

Stress in the GFRP rebar, f_f , modulus of the GFRP rebar, E_f , and the tensile strength of the concrete, f_r , are based on information provided in the discussion of the moment curvature derivations in Section 5.5.2. A bond strength, μ_m , of 18 MPa and a rebar diameter of 15 mm provided by the manufacturer are used in the analysis. Equation (5.20) was obtained from tests of beams with a span length similar to those of this study. However, the beams contained shear stirrups that were not used in the experiments conducted here. In addition the cross sections of the beams tested by Faza and GangaRao had a thickness of 305 mm and a width of 150 mm compared to the thickness of 190 mm and width of 305 mm for the deck panels tested in this study.

The second model used to estimate the experimental crack widths was proposed by Masmoudi, Benmokrane, and Chaallal (1996) and was based on the familiar Gergely Lutz relation, Equation (5.17). The relationship proposed was given as:

$$w = K_g f_f \beta \sqrt[3]{d_c A} \quad (5.21)$$

where,

K_g = a coefficient derived from experimental data. The remaining parameters have previously been defined

The coefficient K_g depends on the type of GFRP reinforcement. Theriault and Benmokrane (1996) recommended a value of 40.9 mm²/N for the GFRP rebars used in this study. The relationship was based on beams tested with stirrups spaced at 80 mm throughout the specimens. The specimens were tested under four point loading at a span length of 1500 mm compared to the 2740 mm and 2130 mm span lengths used in this study. Cross sectional dimensions of the specimens used to derive K_g were similar to those of the deck panels tested here.

Figures 5.29 through 5.31 compare experimental results to the two maximum crack width models described above. Both models show good agreement with deck panel F1 in Figure 5.31, which was tested at the reduced span length of 2130 mm. However, neither model shows good agreement with the experimental data for the other two GFRP tensile reinforced deck panels tested with a 2740 mm span length. Figures 5.30 and 5.31 show that results of both theoretical models provide approximate single lines that, if extrapolated, would intercept the y-axis (representing moment) near the origin. However, the y-intercept for the experimental data does not pass near the origin. In addition, the slopes of the curves do not match; the slopes of the experimental data are considerably smaller than those of the proposed models.

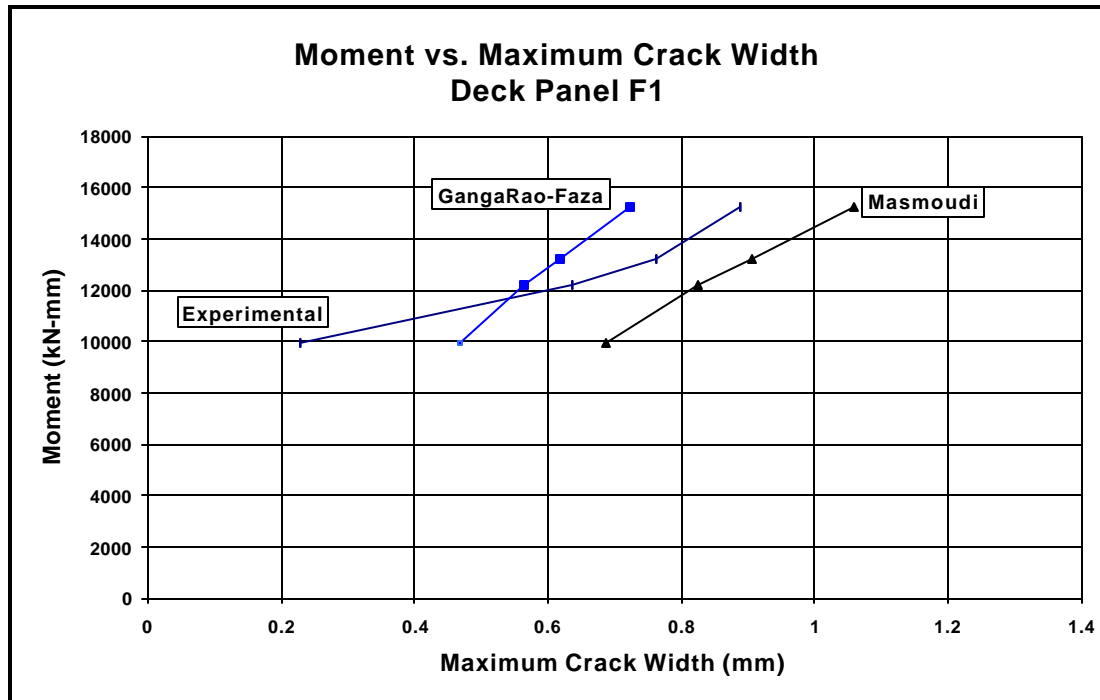


Figure 5. 29: Experimental and Theoretical Maximum Crack Width for the GFRP Deck Panel F1 Tested with a Reduced Span Length of 2130 mm

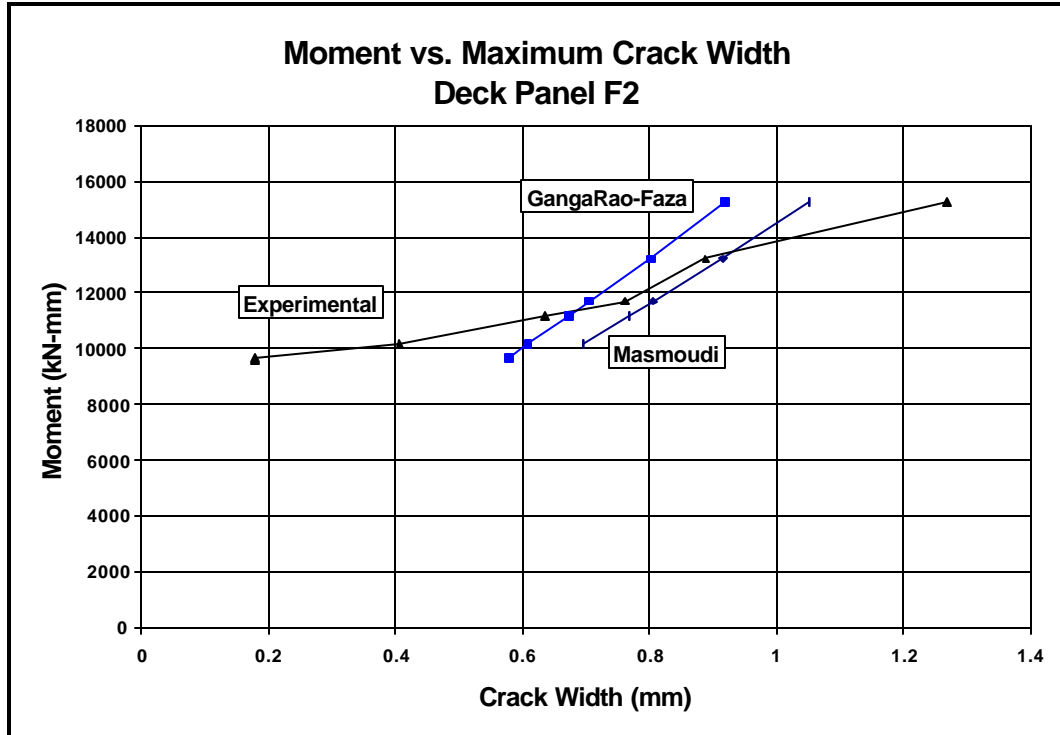


Figure 5. 30: Experimental and Theoretical Maximum Crack Width for the GFRP Reinforced Deck Panel F2

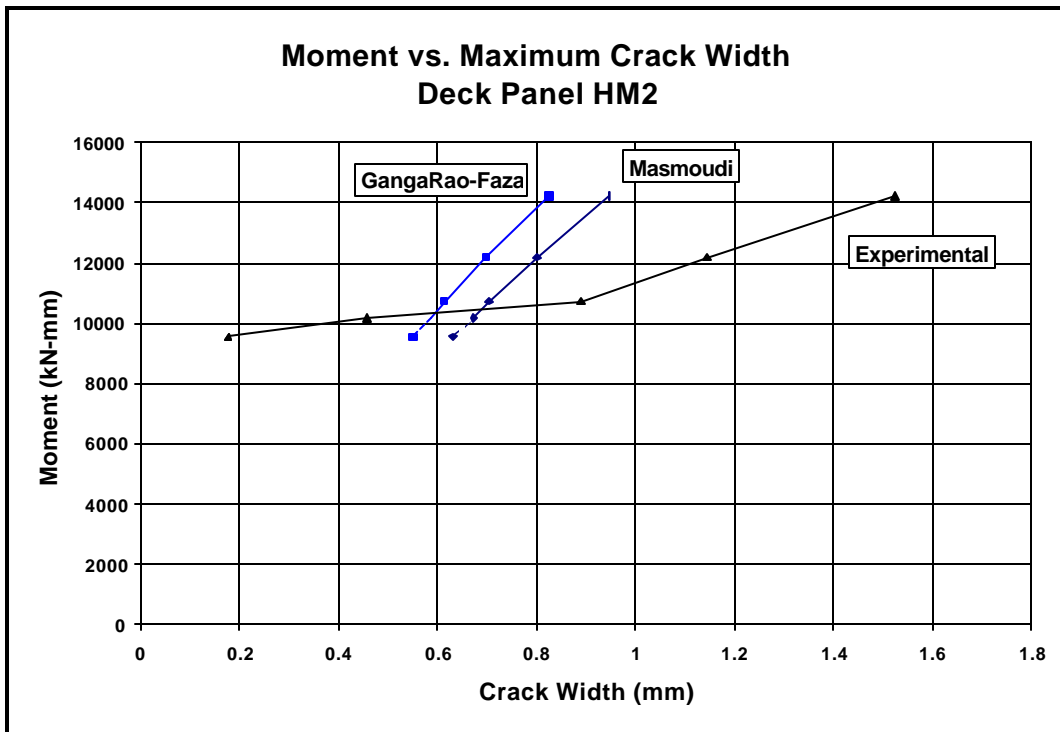


Figure 5. 31: Experimental and Theoretical Maximum Crack Width for the Negative Moment Hybrid Deck Panel HM2

A third model, proposed here, is derived to account for the two differences described above and is also based on the Gergely and Lutz relation (1968). It is:

$$w = 0.09(f_f - f_{f,crack})\beta^3\sqrt{d_c A} \quad (5.22)$$

where,

$f_{f,crack}$ = stress in the reinforcement at cracking computed for the cracked transformed section. The remaining parameters were defined previously.

The coefficient 0.09 was computed from experimental maximum crack data for all the GFRP tensile reinforced deck panels, including deck panel F1. Figure 5.32 shows a plot of the maximum measured crack widths versus the quantity, $f_f(d_c A)^{1/3}$. Least squares linear regression was used to compute the value of the coefficient equal to the inverse of the experimentally obtained 11.2 N/mm, or 0.09 mm/N. This coefficient corrects for differences in slope of the experimental and proposed models given by Equations (5.20) and (5.21).

Equation (5.22) accounts for the non zero value of the y-intercept using the term, $(f_f - f_{f,crack})$. The value $f_{f,crack}$ represents the stress in the GFRP reinforcement after cracking, at the magnitude of the cracking moment. Values of the cracking moment were taken from the experimental data for the deck panels tested in this study.

Figures 5.33 through 5.35 show comparisons of the three models and the experimental data for three of the test specimens with GFRP tensile reinforcement. Relations developed by GangaRao and Faza and by Masmoudi show much better agreement than the proposed model for deck panel F1, with the reduced span length of 2130 mm. However, the proposed model provides a better estimate of maximum crack width for the specimens with the longer 2740 mm span in Figure 5.34 and 5.35. Section B.3 of Appendix B presents the results for the other three deck panels.

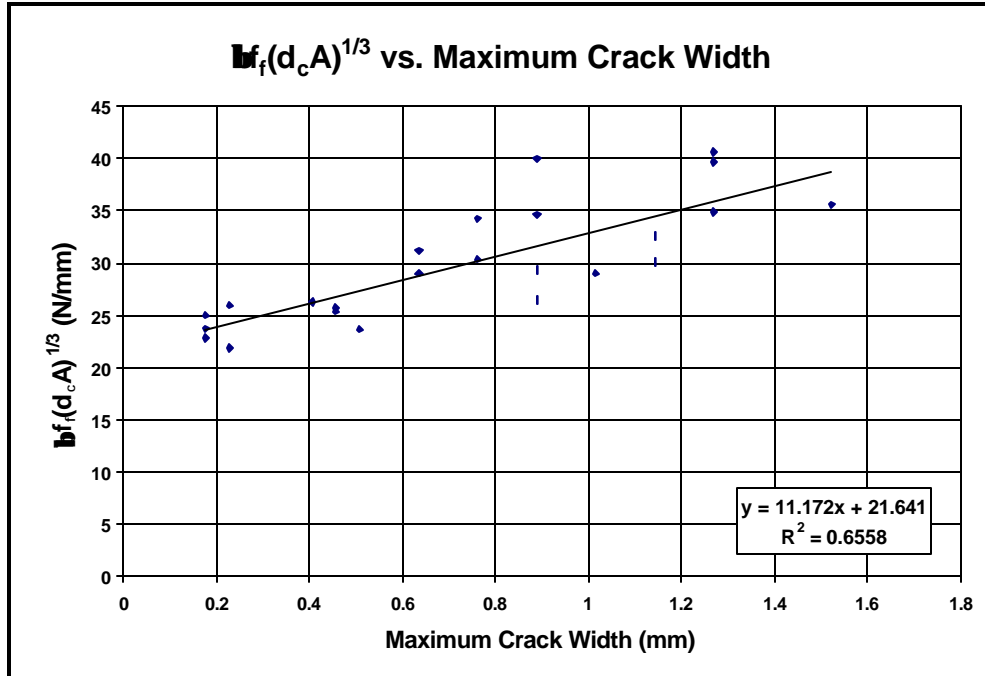


Figure 5. 32: $bf_s(d_cA)^{1/3}$ versus Maximum Crack Width for Deck Panels with GFRP Tensile Reinforcement

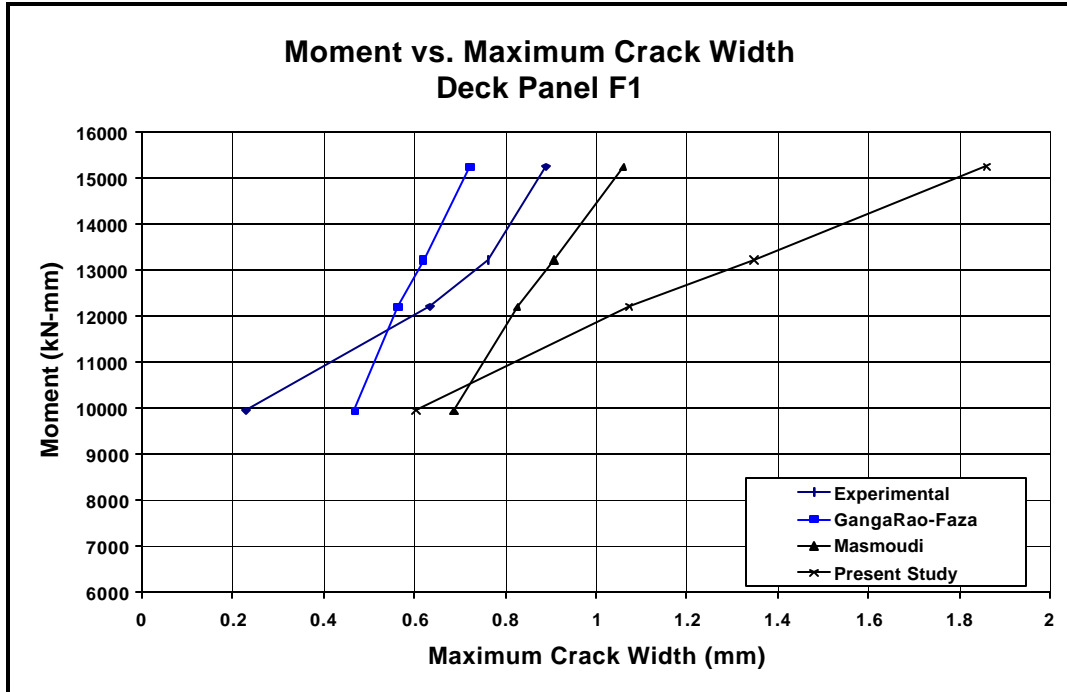


Figure 5. 33: Experimental and Predicted Maximum Crack Width for the GFRP Reinforced Deck Panel Tested with a Reduced Span of 2130 mm

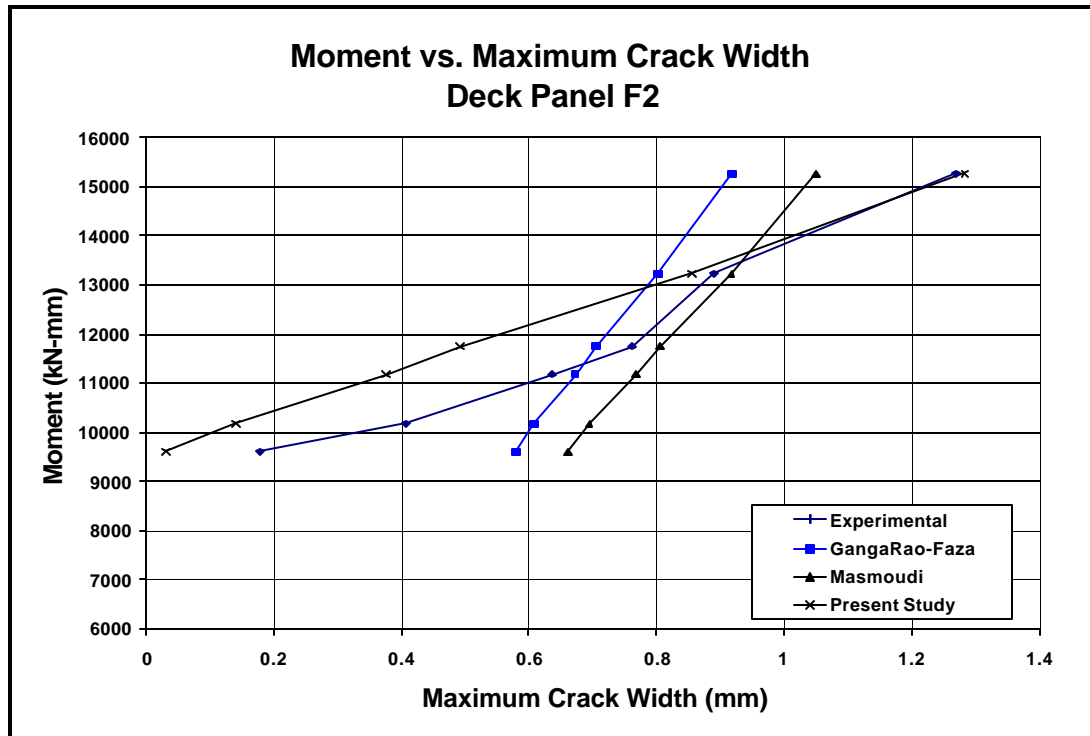


Figure 5. 34: Experimental and Predicted Maximum Crack Width for the GFRP Reinforced Deck Panel F2

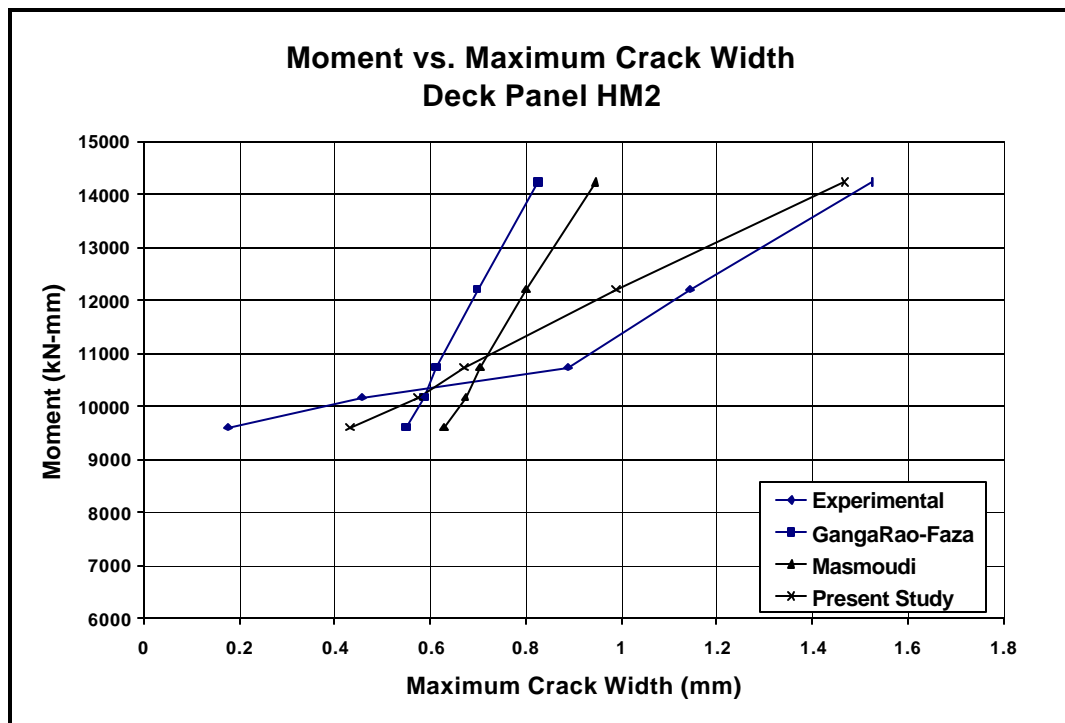


Figure 5. 35: Experimental and Predicted Maximum Crack Width for the Negative Moment Hybrid Reinforced Deck Panel HM2

5.7 SUMMARY AND CONCLUSIONS

Twelve full scale reinforced concrete deck panels were tested, simulating conditions in an actual bridge deck to determine if GFRP rebars are a viable alternative to conventional ECS rebars as concrete bridge deck reinforcement. Three different reinforcing schemes are considered in the study: (1) an ECS reinforcing scheme with two mats of ECS rebars, (2) a GFRP reinforcing scheme with two mats of GFRP rebars, and (3) a Hybrid reinforcing scheme with a top mat of GFRP rebars and a bottom mat of ECS rebars. The different reinforcing schemes were tested in the laboratory with both the positive and negative moment orientations existing in an actual bridge deck (see Section 5.3.1).

The objective of this chapter is to compare the deck panel test results to pertinent code specifications and theoretical predictions. Failure loads, displacements, and maximum crack widths are considered.

All of the deck panels meet AASHTO (1996) design specifications with regard to ultimate load. It can be concluded that the GFRP deck panels can meet load requirements in an actual bridge deck. However, the AASHTO design specifications are based on flexural failures of under-reinforced steel reinforced members which would collapse in flexure after yielding of the reinforcement. Since the GFRP tensile reinforced deck panels of this study failed in a flexure/shear failure mode, it is recommended that AASHTO consider broadening its current specifications with regard to failure mode.

ACI-318M-95 design guidelines for ultimate load accurately predicted the failure load of the ECS reinforced deck panels failing in flexure. However, current ACI predictions of the failure shear, based on concrete contribution alone, significantly overestimate the failure load of the GFRP tensile reinforced deck panels. A theory for predicting ultimate shear proposed by Michaluk et al., (1998) is also compared to the test data. Results show his shear failure theory significantly underestimates the shear strength of the deck panels. Since the above theories cannot adequately predict the shear strength of the GFRP reinforced deck panels, two relations for predicting the shear strength are proposed herein, based on the results of Michaluk et al., (1998) and the present study.

Service live load displacements are compared to AASHTO and ACI code provisions. AASHTO provisions were written to limit full superstructure displacements rather than localized displacements. No relative bridge deck displacement limitations are specified in the code. ACI-318M-95 specifies that deflection computations are not required for slabs meeting a minimum thickness provided in the code. The deck panels tested in this study met the minimum depth requirement; therefore displacement computations were not required. Modifications to both code specifications are warranted in this case, since GFRP reinforced concrete members have greater displacements at service load than ECS reinforced specimens on which present provisions are based. It is recommended that computations of prospective displacements for GFRP reinforced concrete members be required.

Theoretical estimates of displacements are calculated by integrating the moment/curvature relations in combination with the moment area method. Comparisons of the theoretical and experimental displacements show good agreement for all of the deck panels considered. Displacements are also predicted for the deck panels with ECS tensile reinforcement using the ACI-318M-95 effective moment of inertia. Theoretical and experimental results show good agreement up to yielding of the reinforcement after which the method no longer applies.

Displacements of the specimens with GFRP tensile reinforcement are estimated using two proposed theoretical models, one by Masmoudi, Theriault, and Benmokrane (1996) the other by GangaRao and Faza (1991). The method proposed by Masmoudi et al. shows good agreement with the experimental results, slightly underestimating the displacements. The method developed by GangaRao and Faza correlates well with the experimental data, except for regions near the cracking load.

Of the seven deck panels with ECS tension reinforcement, six meet both AASHTO and ACI maximum crack width requirements. None of the GFRP tensile reinforced deck panels that cracked prior to service load meet AASHTO or ACI maximum crack width requirements. Both codes specify strict maximum crack widths to protect steel reinforcement from corrosion related deterioration. GFRP reinforced concrete members are not subject to corrosion. Therefore, the maximum allowable crack widths should be based on aesthetics and serviceability (i.e. ability to withstand repeated loading and freeze-thaw cycles without physical degradation).

Theoretical maximum crack widths computed using the Gergely Lutz equation (1968) show good correlation with the experimental results for the deck panels with ECS tension reinforcement. Models proposed by GangaRao and Faza (1991) and Masmoudi, Benmokrane, and Chaallal (1996) for predicting maximum crack widths for GFRP reinforced deck panels are also compared to the test results. The model shows good correlation for the specimen tested with a reduced span length, deck panel F1. However, there are significant differences in slope and y-intercept for the remaining deck panels with GFRP tensile reinforcement. A model that better fits these data is proposed.

6.0 BARRIER WALL IMPACT SIMULATION

6.1 INTRODUCTION

Figure 6.1 shows the superstructure of a typical bridge deck. A bridge deck is required to support loads of passing traffic and must also resist forces caused by barrier wall impacts. In the event of a barrier wall impact the portion of the deck highlighted in Figure 6.1 is subjected to a tensile-flexural load combination that could not be simulated using the deck panels discussed in Chapters 4 and 5. To evaluate the behavior of deck overhang during a vehicle barrier impact, nine reinforced concrete barrier wall specimens were constructed and tested.

The decks of the barrier wall specimens were reinforced with three different combinations of rebars. First, three specimens were constructed reinforced with ECS reinforced deck typical of conventional design practice. Second, three specimens with a deck reinforced entirely with GFRP rebars were fabricated. Third, three barrier wall specimens with a hybrid deck reinforcing scheme were constructed. The Hybrid reinforcement scheme consisted of a top mat of GFRP rebars and a bottom mat of ECS rebars.

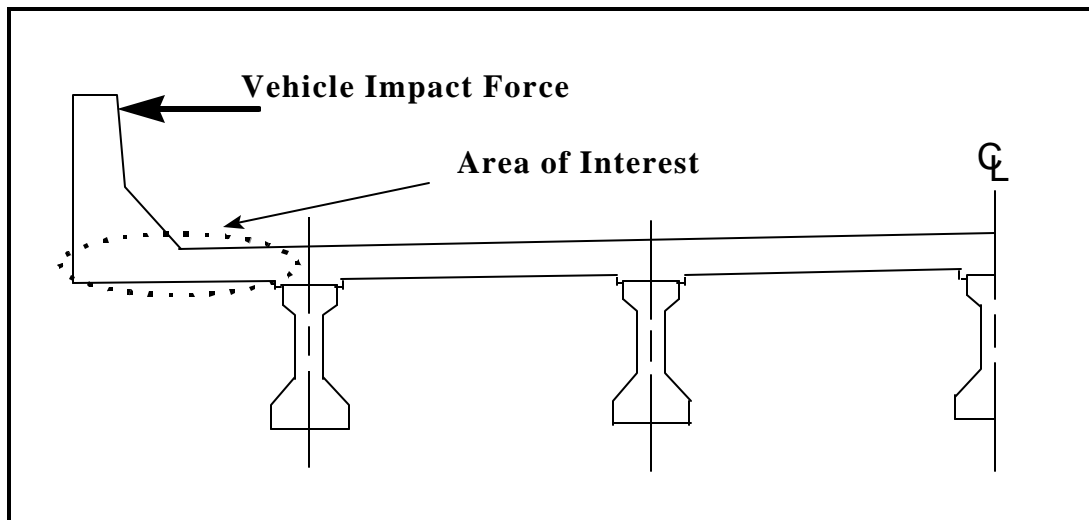


Figure 6. 1: Typical Bridge Superstructure Cross Section

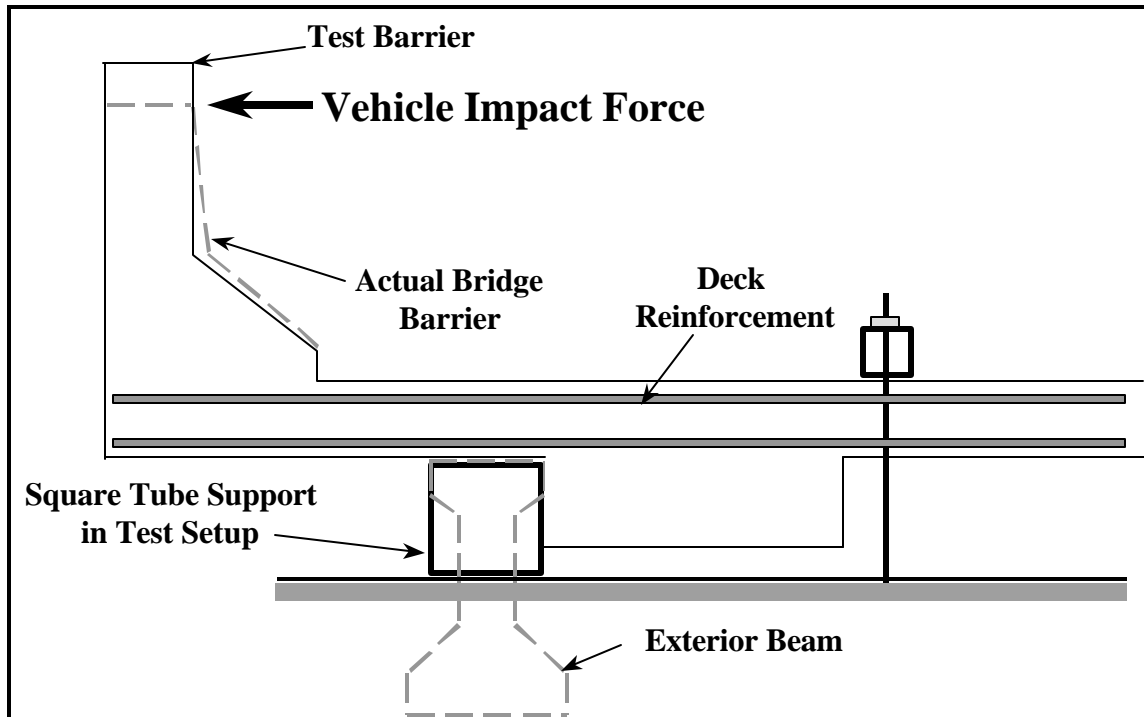


Figure 6. 2: Relation of a Test Specimen to an Actual Bridge (Reinforcement details are given in Figure 6.3)

6.2 BARRIER WALL SPECIMEN DESCRIPTION

Figure 6.2 illustrates how the constructed barrier wall specimens relate to an actual bridge deck. This section provides specific details concerning geometry and reinforcement of the nine barrier wall specimens.

6.2.1 Barrier Wall Dimensions

The geometry of the barrier wall specimens was taken from the plans of the US-460 bridge over Roger's Creek in Bourbon County Kentucky. The bridge was constructed in July and August of 1997. Exterior dimensions of the bridge's barrier walls were altered in two ways to fabricate the test specimens illustrated in Figures 6.2 and 6.3. First, the height of the barrier walls was increased by 89 mm to provide adequate bearing area at the load point, as shown in Figure 6.3. AASHTO specifies that the barrier wall design load be applied at the top of the barrier, 1067 mm in the actual bridge deck. Second, one of the tapers of the barrier wall was omitted to facilitate formwork (see Figure 6.1). This was not a problem since the barrier wall itself is not of interest in the study.

The reaction block shown in Figure 6.3 was provided to transfer the reaction force to the test frame. In addition the reaction block provided a counterweight for the wall

facilitating movement of the specimens in the laboratory. The additional length past the smaller support tube was designed to insure adequate development length for the deck reinforcement in the specimen.

The thickness of the actual Roger's Creek bridge deck was 205 mm. However, 15 mm of the actual deck thickness is an assumed wearing surface and is not considered in design. This resulted in a deck thickness of 190 mm for the barrier wall specimens.

A specimen width of 395 mm was selected to accommodate the three reinforcement spacings used in the study discussed in the next section.

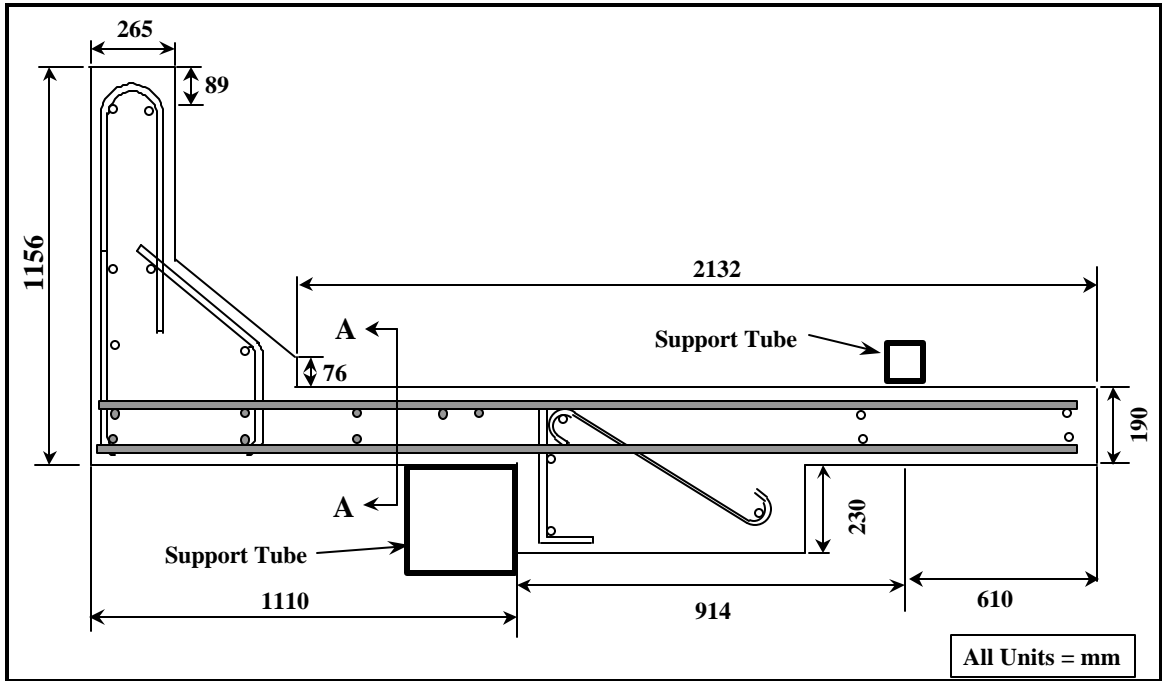


Figure 6.3: Barrier Wall Specimen Dimensions

6.2.2 Reinforcement Layout

Figure 6.4 shows cross section A-A of Figure 6.3 for the different reinforcement layouts. The 15 mm wearing surface discussed in Section 6.2.1 was subtracted from the top clear cover of all the specimens.

Reinforcement layouts were selected based on three proposed designs of the Roger's Creek bridge deck. Figure 6.4a shows the proposed ECS design consisting of two mats of ECS rebars. Both the bottom and top mats were made up of 2 #19 ECS rebars spaced at 203 mm. A 25 mm clear cover to the bottom mat and a 50 mm clear cover to the top mat were used for these barrier wall specimens.

Figure 6.4b shows the GFRP design proposal made up of two GFRP reinforcing mats. Top and bottom mats consisted of 3 #15 GFRP rebars spaced at 127 mm. A clear cover to both the top and bottom mat of 25 mm was selected for these specimens.

Finally, Figure 6.4c shows the hybrid design proposal. These specimens had a bottom mat made up of 2 #19 ECS rebars spaced at 203 mm with a clear cover of 25 mm. The top mat consisted of 3 #15 GFRP rebars spaced at 127 mm with a clear cover of 25 mm.

Transverse reinforcement spacing was taken from the Roger’s Creek bridge design plans and was the same for all of the specimens. All of the transverse rebars in the ECS mats were #16 ECS rebars. All of the transverse rebars in the GFRP mats were #15 GFRP rebars.

The barrier wall reinforcement shown in Figure 6.3 was made up of 2 #16 bent ECS rebars spaced at 305 mm. All nine of the specimens possessed identical barrier wall reinforcement.

The reaction block hook reinforcement, shown in Figure 6.3, consisted of #13 uncoated Grade 420 steel rebars. Three sets of the double hooked were placed at a spacing of 127 mm through the reaction block width. Reaction block reinforcement was the same for all the barrier wall specimens.

Table 6.1 provides a summary of the three different deck reinforcement layouts were used during the study.

TABLE 6.1 SUMMARY OF BARRIER WALL SPECIMEN REINFORCEMENT

Specimen Type	Bottom Mat Reinforcement		Top Mat Reinforcement		Clear Cover to Bottom Mat (mm)	Clear Cover to Top Mat (mm)
	Rebars	Spacing (mm)	Rebars	Spacing (mm)		
ECS	2 #19 ECS	203	2 #19 ECS	203	25	50
GFRP	3 #15 GFRP	127	3 #15 GFRP	127	25	25
Hybrid	2 #19 ECS	203	3 #15 GFRP	127	25	25

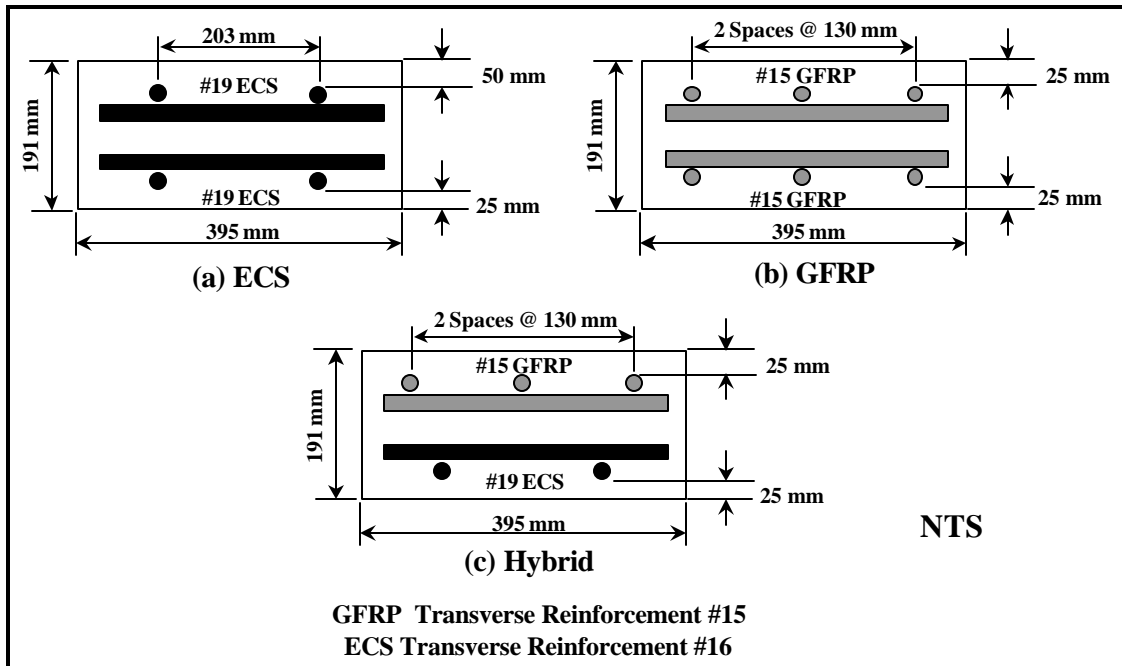


Figure 6. 4: Cross Section of Barrier Wall Specimen Deck

6.2.3 Specimen Labeling

Specimens were identified by a three character sequence. The first character for all of the specimens was the letter “B” for barrier wall specimen. This differentiated them from the deck panel specimens discussed in Chapters 4 and 5. The second character denoted specimen deck reinforcement type, “E” for ECS, “F” for GFRP, and “H” for the Hybrid barriers. The third character was a number, 1, 2, or 3, differentiating specimens with the same reinforcement type.

6.2.4 Material Properties

A standard Kentucky Class AA concrete mix was selected for the barrier wall specimens. Table 6.2 provides details of the mix design.

All of the barrier wall specimens were cast using a single load of concrete. Two standard 305 mm x 152 mm compression cylinders were made for each of the barrier wall specimens. These were broken the day each respective barrier wall was tested. Table 6.3 shows a summary of the compression strengths. All of the cylinders had a greater compressive strength than the 30 MPa identified in Kentucky Standard Specifications for Road and Bridge Construction (1998).

The properties for the ECS and GFRP rebars used in the barrier wall specimens are given in Table 6.4 and Figure 6.5.

TABLE 6.2 CONCRETE MIX DESIGN

(Taken from Kentucky Standard Specifications for Road and Bridge Construction)

Class of Concrete	Approximate Percent Fine to Total Aggregate		Maximum Free Water by W/C Ratio	28-Day Compressive Strength	Slump	Minimum Cement Factor
	Gravel	Stone	(kg/kg)	(MPa)	(mm)	(kg/m ³)
AA	36	40	0.42	30	50-100	368

TABLE 6.3 CONCRETE CYLINDER COMPRESSION STRENGTHS

Deck Panel Label	Compression Strength, f'_c (MPa)		
	Cylinder 1	Cylinder 2	Average
BE1	44.64	44.64	44.64
BE2	40.99	N. A.	40.99
BE3	45.50	46.62	46.06
BF1	41.19	40.41	40.80
BF2	38.28	39.91	39.10
BF3	31.67	31.11	31.40
BH1	33.62	37.94	35.78
BH2	32.67	37.55	35.11
BH3	34.52	36.79	35.66

TABLE 6.4 REBAR PROPERTIES

Rebar Type	Diameter of Rebar	Area of Rebar	Yield Strength	Stress Orientation	Ultimate Strength	Modulus of Elasticity
	(mm)	(mm ²)	(MPa)		(MPa)	(MPa)
#19 ECS	19	284	486.9	Tension & Compression	653.4	196,490
#15 GFRP	15	176	N. A.	Tension	612	40,045
				Compression	325	42,510
Refer to Chapter 2 for details of the reinforcement properties.						

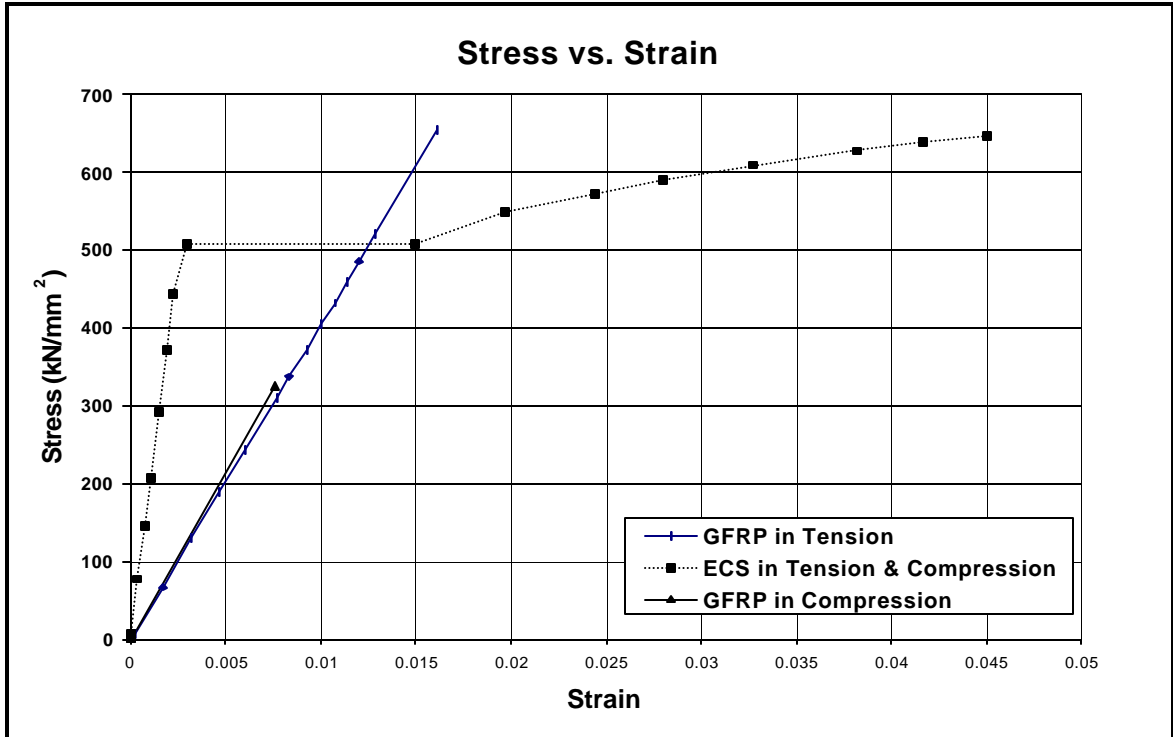


Figure 6. 5: Stress versus Strain for ECS and GFRP Rebars
 (Refer to Chapter 2 for the derivation of these curves)

6.2.5 Test Specimen Preparation

Forms for the nine barrier wall specimens were constructed with plywood and timber sections. Rebars were anchored inside the forms with individual steel chairs and wire ties. All nine specimens and their respective concrete cylinders were cast with a single load of concrete. The wide variation of concrete compression strengths shown in Table 6.3 was due to the large amount of time required to place the concrete. After the concrete was placed, the exposed surfaces of the barrier wall specimens and compressive cylinders were sprayed with a curing compound to prevent water from evaporating at the surface. The specimens were then covered with plastic sheeting.

The barrier wall specimens and concrete cylinders were left at the pour site for approximately one month. Then they were moved from the pour site to the laboratory, a distance of approximately 15 km. Testing of the barrier wall specimens began approximately 10 months after the concrete was placed. The final specimen was tested about 11 months after the specimens were cast.

6.3 BARRIER WALL TEST SETUP & INSTRUMENTATION

Figure 6.6 shows an elevation of the test setup. The barrier walls were tested in a normal vertical position as illustrated in Figures 6.7 and 6.8. A building column in the laboratory served as a reaction block for the load frame. The load cell was placed against the wall adjacent to the hydraulic jack as shown in Figure 6.6. Hydraulic pressure was controlled under load control, therefore, no post ultimate behavior of the specimens could be recorded. The load was transferred from the hydraulic jack to the barrier wall with a timber section. The location of load application was selected to satisfy AASHTO specifications as discussed in Section 6.2.1

Two steel tubes resisted the applied load. The larger 305 mm square tube acted as the exterior beam and the smaller tube resisted the uplift that would be resisted by flexure in the remainder of the bridge deck in an actual bridge. Figure 6.9 shows qualitative shear, tensile, and bending moment diagrams for the barrier wall under load.

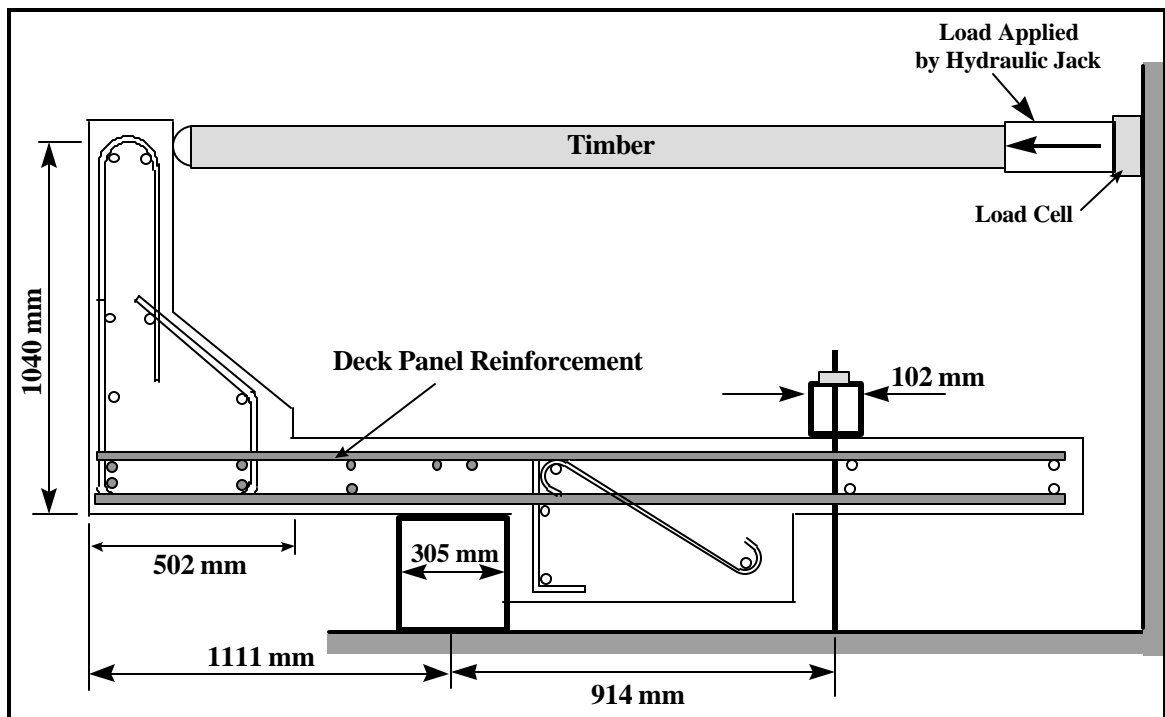


Figure 6. 6: Barrier Wall Test Setup



Figure 6.7: Barrier Wall Test Setup



Figure 6.8: Barrier Wall Test Setup

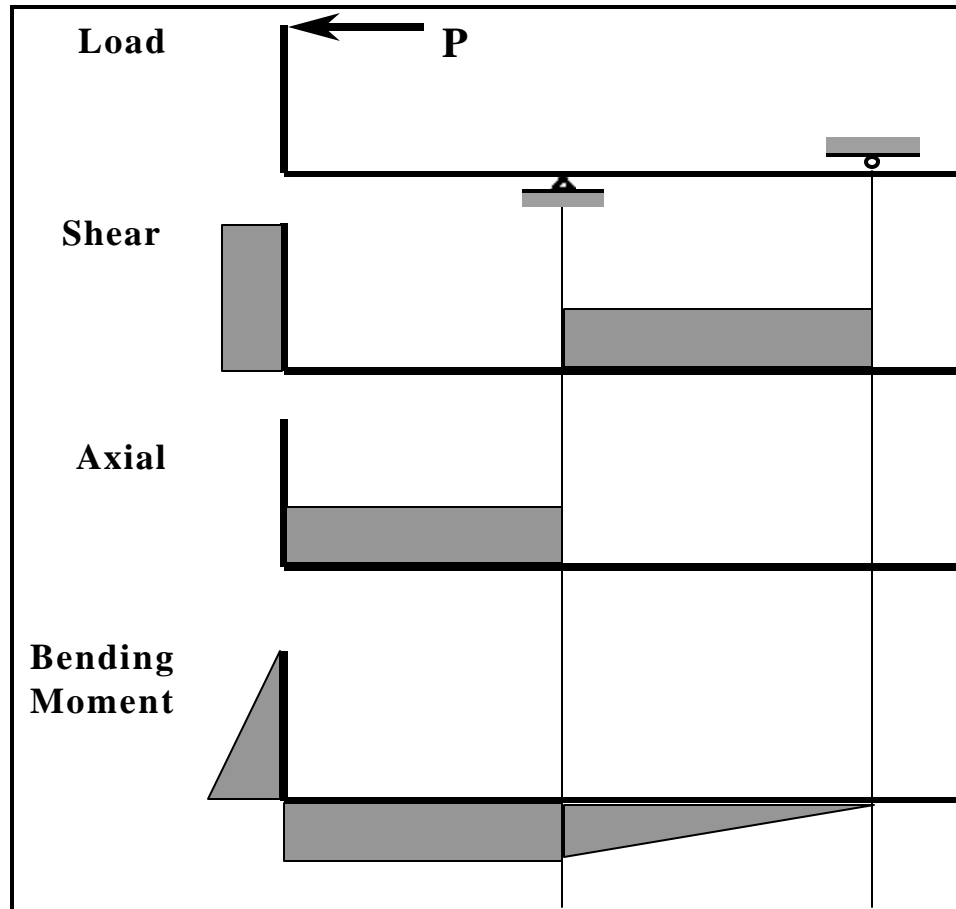


Figure 6. 9: Qualitative Shear, Axial, and Moment Diagrams for the Barrier Wall Subjected to Load P

Twelve LVDTs, two dial gages, and a load cell were used during the barrier wall tests. As Figure 6.10 shows, the LVDTs and dial gages were placed in pairs, one on each side of the specimens. This allowed for measurements of specimen twist under load. In the data reduction, the pairs were averaged to subtract the twist from the recorded data. Data results showed that the twist encountered during the tests was negligible.

Measurements were recorded at a rate of 1 sample every 2 seconds from the LVDTs and the load cell. These measurements continued to be taken through failure of the specimens. Dial gages were used to record the horizontal displacement at the top of the barrier wall. Loading was stopped in increments of approximately 4500 kN to manually record the dial gage readings. Readings were recorded up to approximately 60% of the predicted failure load. At that point the gages were removed to prevent their damage.

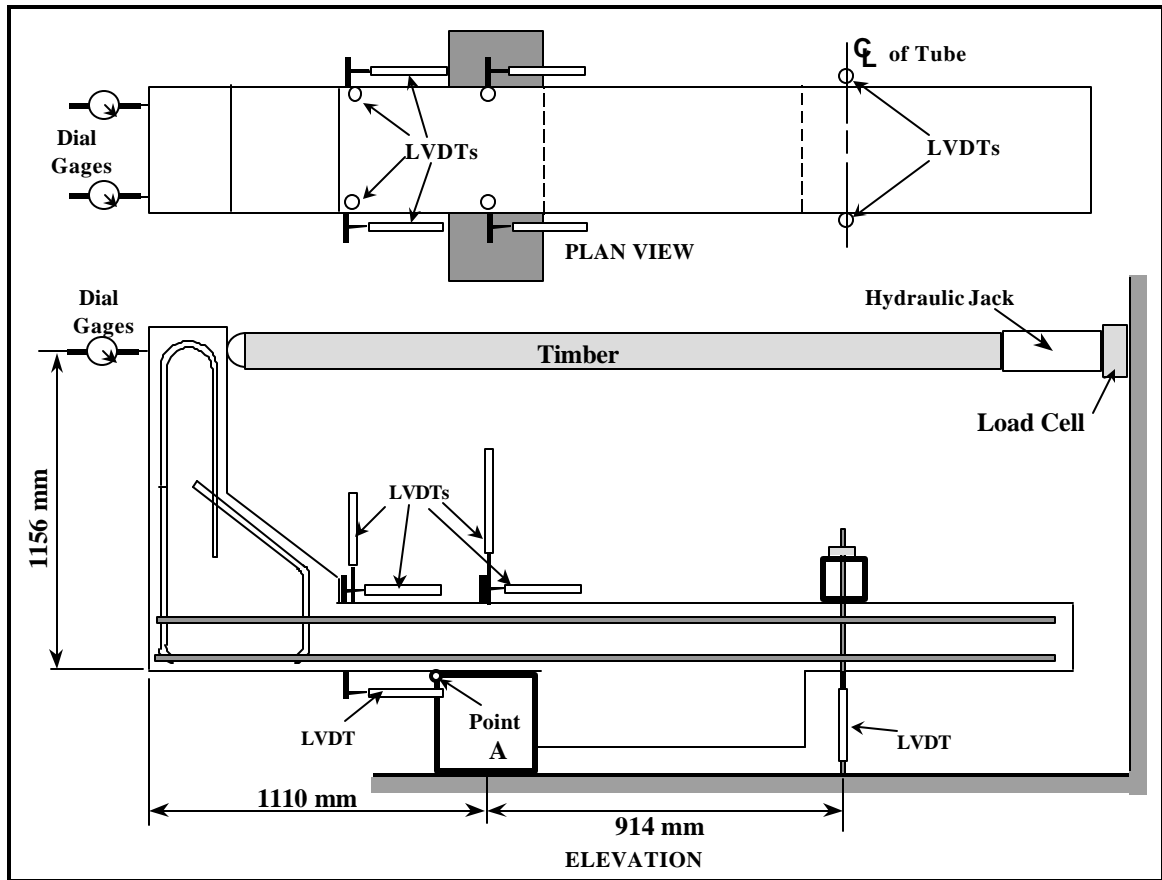


Figure 6. 10: Illustration of Instrumentation Locations

6.4 COMPARISON OF BARRIER WALL STIFFNESS

To evaluate the behavior of the different barrier wall specimens, the recorded data were used to determine relative stiffnesses of the specimens. Relative stiffness was evaluated in three ways: 1) horizontal displacement at the top of the barrier wall, 2) vertical displacement at the toe of the barrier wall, and 3) approximate average curvature between section A-A and the back of the large tube shown in Figure 6.3.

Dead load of the barrier wall specimens was not considered in the analysis. Instrumentation was positioned after the specimens were subjected to their own weight.

6.4.1 Load versus Displacement at Top of Barrier Wall

Figures 6.11 through 6.13 show the load versus displacement results for the nine specimens that are grouped by deck reinforcement type. The dial gages measuring displacement were removed prior to failure to prevent damage. Therefore, termination of

the curves in the figures does not reflect failure conditions of the barriers. The figures show good consistency between specimens with the same reinforcement.

Figure 6.14 displays the load versus displacement response of three specimens, BE3, BF2, and BH2. These were selected to represent the load displacement behavior of the ECS, GFRP, and Hybrid reinforced barrier specimens, respectively. All three curves follow similar paths up to cracking of the concrete in the deck, denoted by the change in slope. After cracking behavior of the three specimens varies.

The ECS barrier, BE3, has the largest slope of the three specimens reflecting the largest stiffness of the specimens with regard to displacement at the top of the barrier. Despite differences in bottom mat reinforcement, shown in Table 6.1, curves BF2 and BH2 follow similar paths after cracking. Results show that the top mat of reinforcement (or negative bending reinforcement) governs the behavior of the barrier wall specimens.

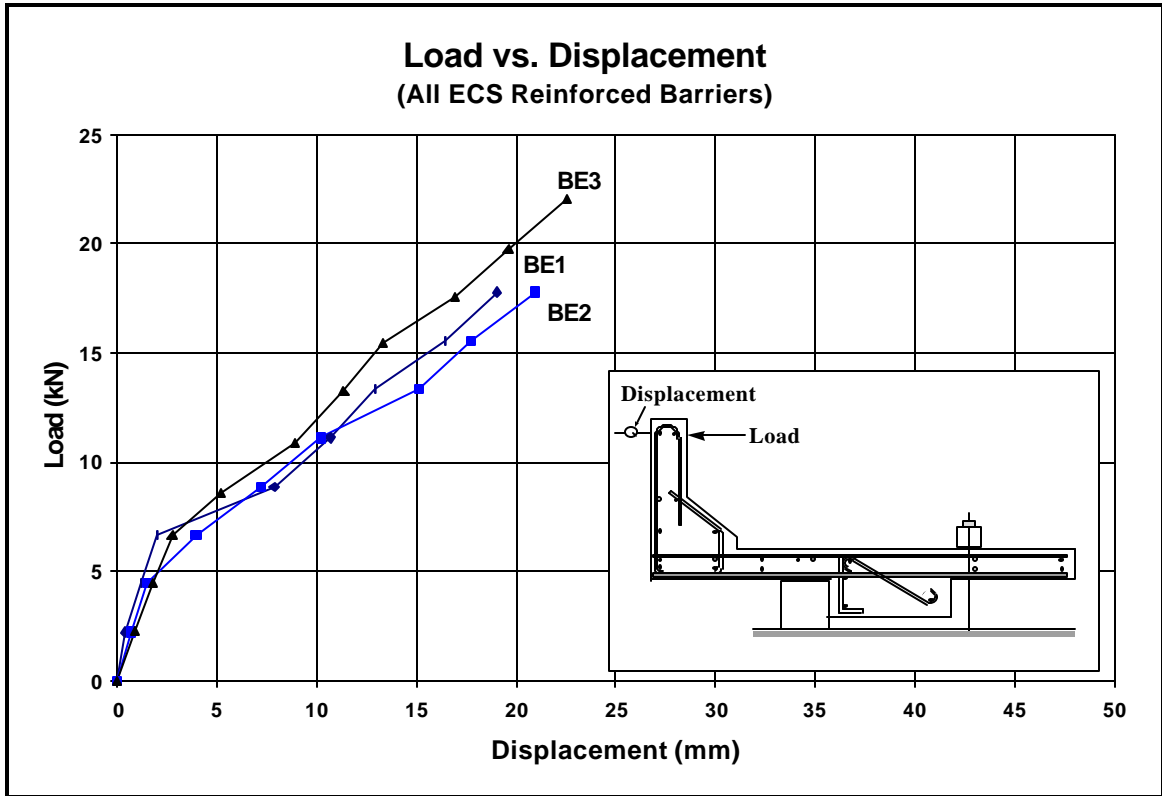


Figure 6. 11: Load versus Displacement at Barrier Top, ECS Barriers

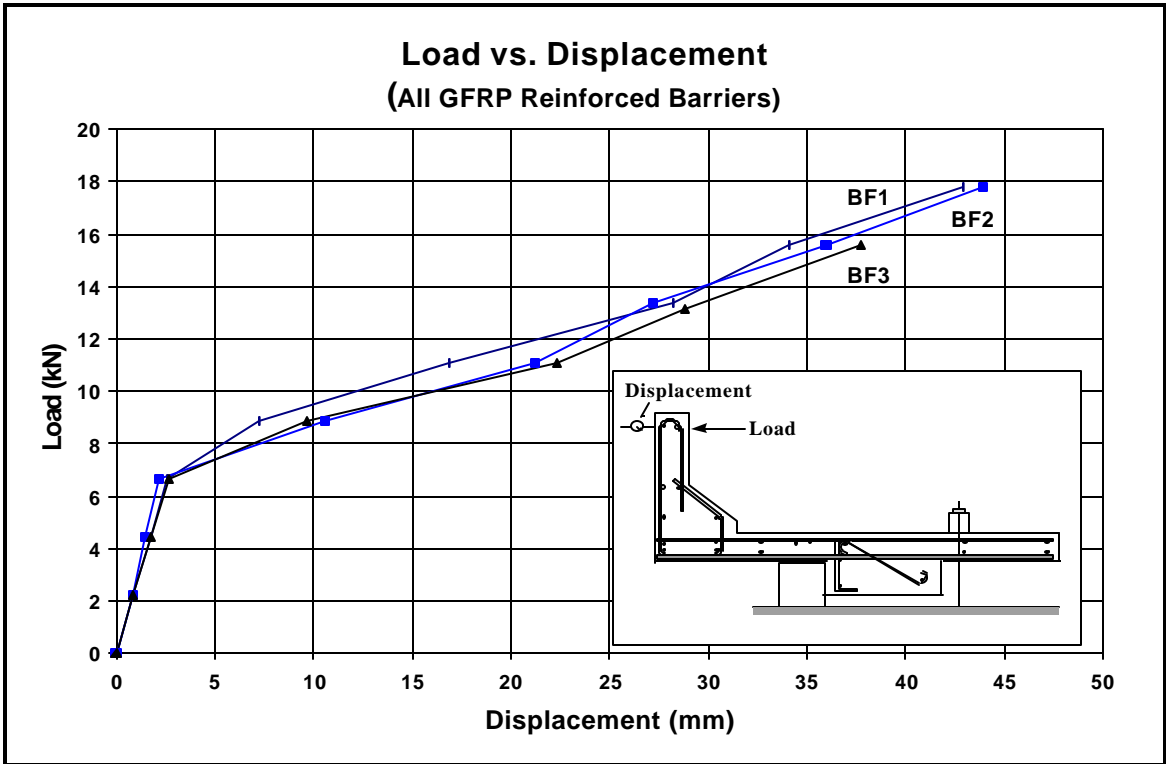


Figure 6. 12: Load versus Displacement at Barrier Top, GFRP Barriers

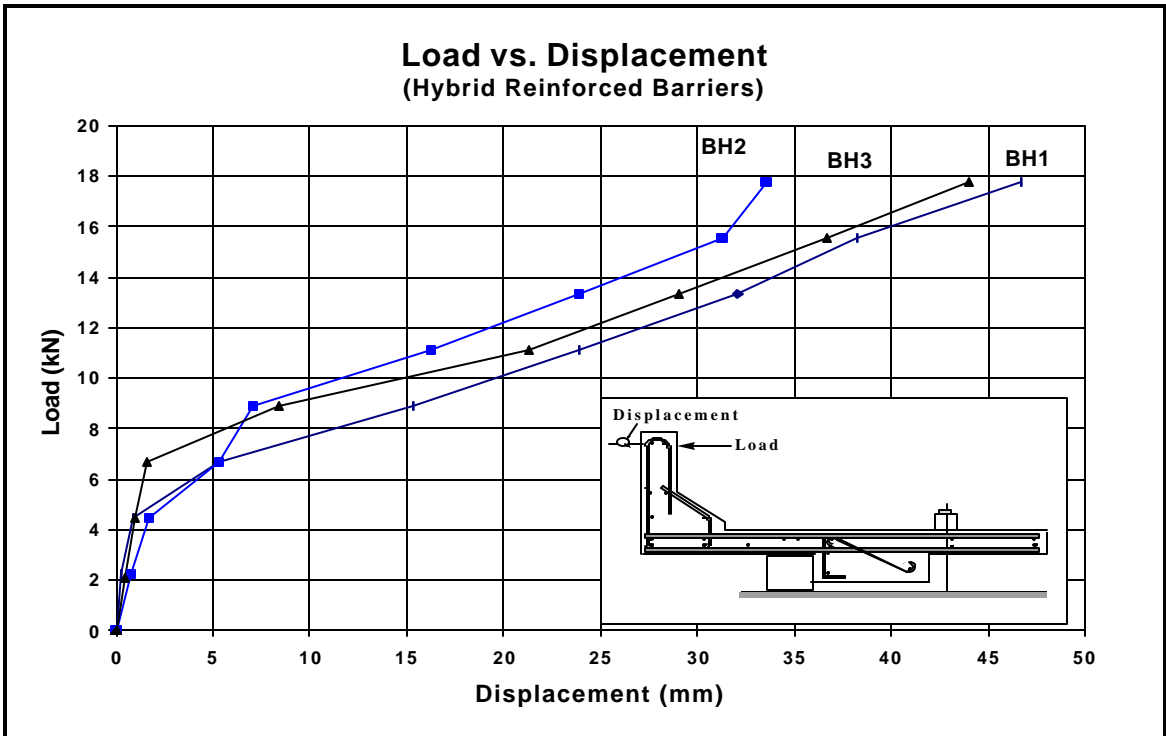


Figure 6. 13: Load versus Displacement at Barrier Top, Hybrid Barriers

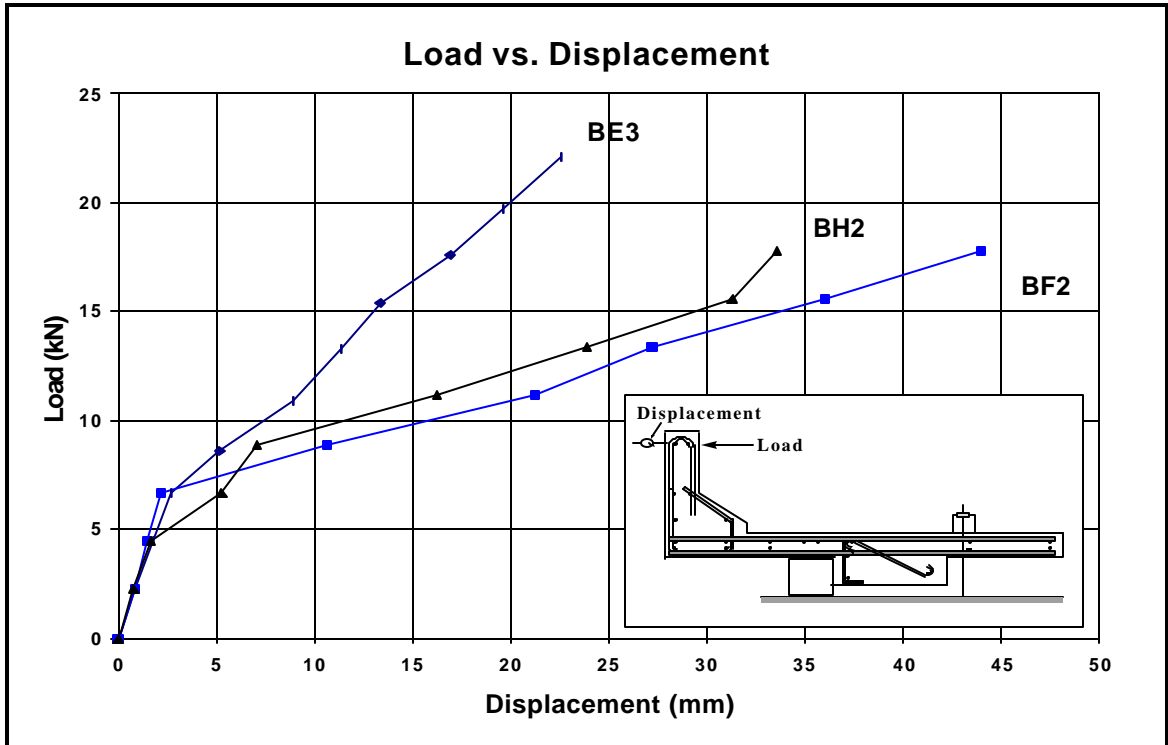


Figure 6. 14: Comparison of Load versus Displacement at Barrier Top for the ECS, GFRP, and Hybrid Specimens; BE3, BF2, and BH2 Respectively

6.4.2 Vertical Displacement at Toe of Barrier Wall

A second comparison of stiffness was based on the vertical displacement of the specimen at the toe of the barrier wall. Figure 6.15 illustrates the parameters required in the evaluation of displacement at the toe. Data from four LVDTs were used to compute the displacement. First, the two LVDTs at the location labeled LVDT₁ in the figure were averaged and used as a measure of displacement at the toe. Second, the average of the pair of LVDTs at location LVDT₂ were used. After analyzing the data it was found that the specimen was rotating as a rigid body around Point A due to displacement at the small tube support located at the rear of the specimen. To correct the data for rigid body displacements the following relation was used:

$$\delta = \Delta_1 - \left(\frac{L_1}{L_2} \right) \Delta_2 \quad (5.1)$$

where,

- δ = corrected vertical displacement at barrier wall toe, Point B
- Δ_1 = displacement measured with LVDT₁
- Δ_2 = displacement measured measure with LVDT₂
- L_1 = 455 mm

$$L_2 = 1040 \text{ mm}$$

All of these parameters are illustrated in Figure 6.15.

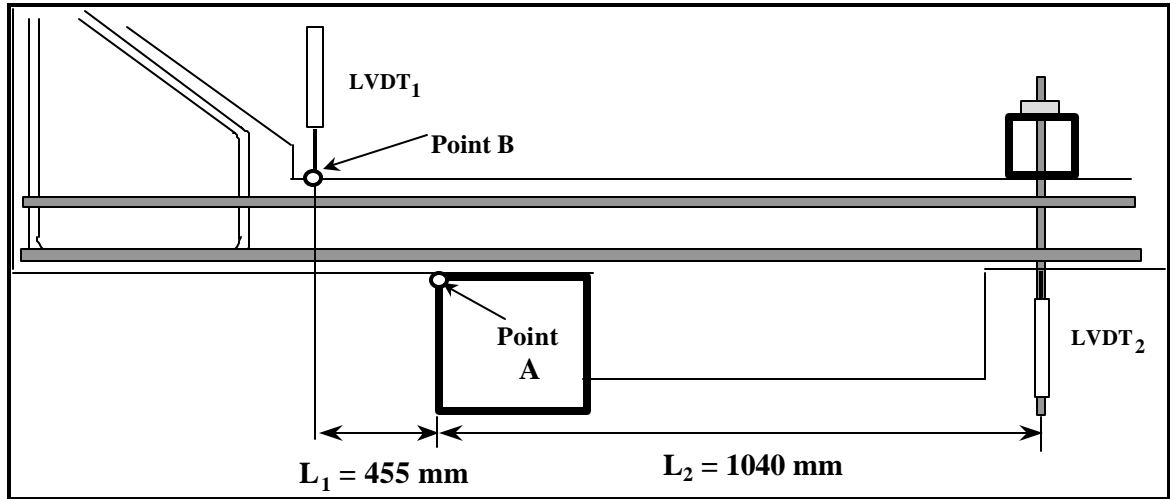


Figure 6. 15: Detail showing Parameters used to compute Vertical Displacement at the Toe of the Barrier

Load versus displacement results for the three types of barrier specimens are shown in Figures 6.16 through 6.18. Good agreement of test results is shown for all the specimen types. Data for specimen BF1 were accidentally erased and are not presented with the other test results.

Load displacement curves in Figure 6.19 are representative of the three barrier types in the study. Specimens BE3, BF2, and BH2 were chosen to represent the ECS, GFRP, and Hybrid barrier specimens respectively. After cracking the specimens show differences in slope. As in Section 6.4.1, the ECS specimen data show a larger slope, and therefore larger stiffness, than the other two specimen types. In addition, specimen BE3 shows inelastic characteristics due to apparent yielding of the ECS rebars in the deck. This effect is not exhibited in specimens BF2 and BH2 with GFRP reinforcement in the deck.

The similarity in slope after cracking of the GFRP and Hybrid specimens again shows that the stiffness of the barrier is dictated largely by the type and location of reinforcement in the top mat. Specimens BF2 and BH2 had the same top mat reinforcement, with different bottom mat reinforcement as presented in Table 6.1.

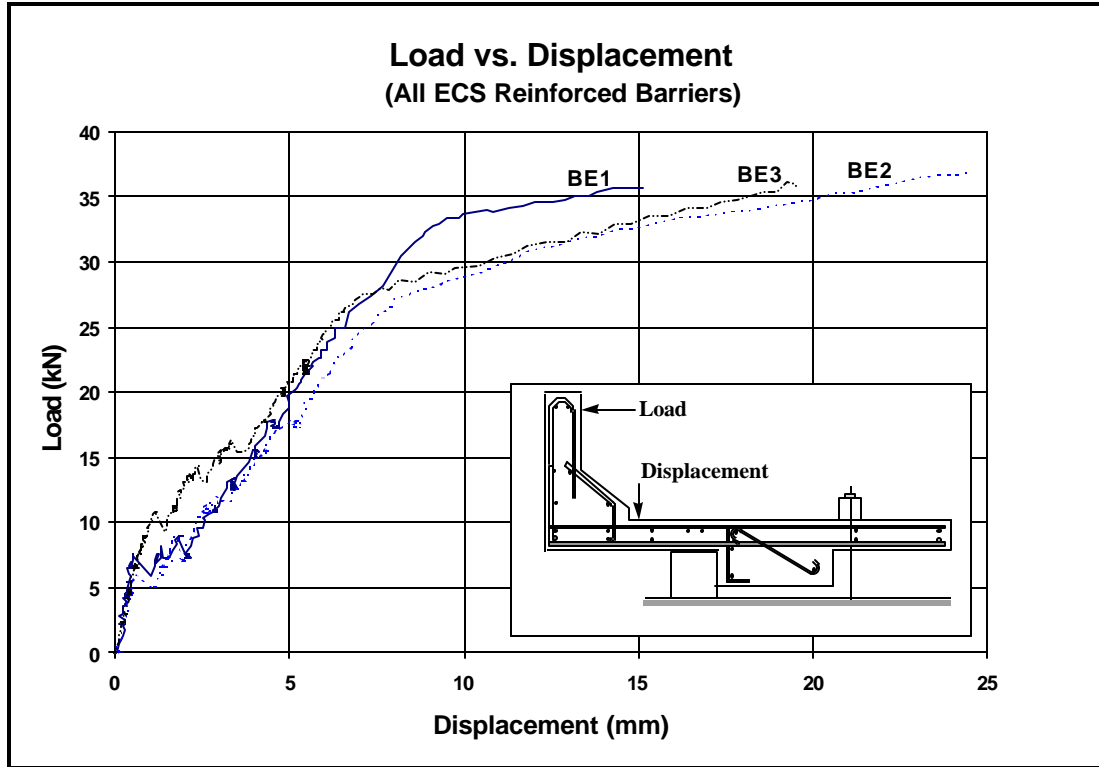


Figure 6. 16: Load versus Vertical Displacement at Toe of Barrier, ECS Barriers

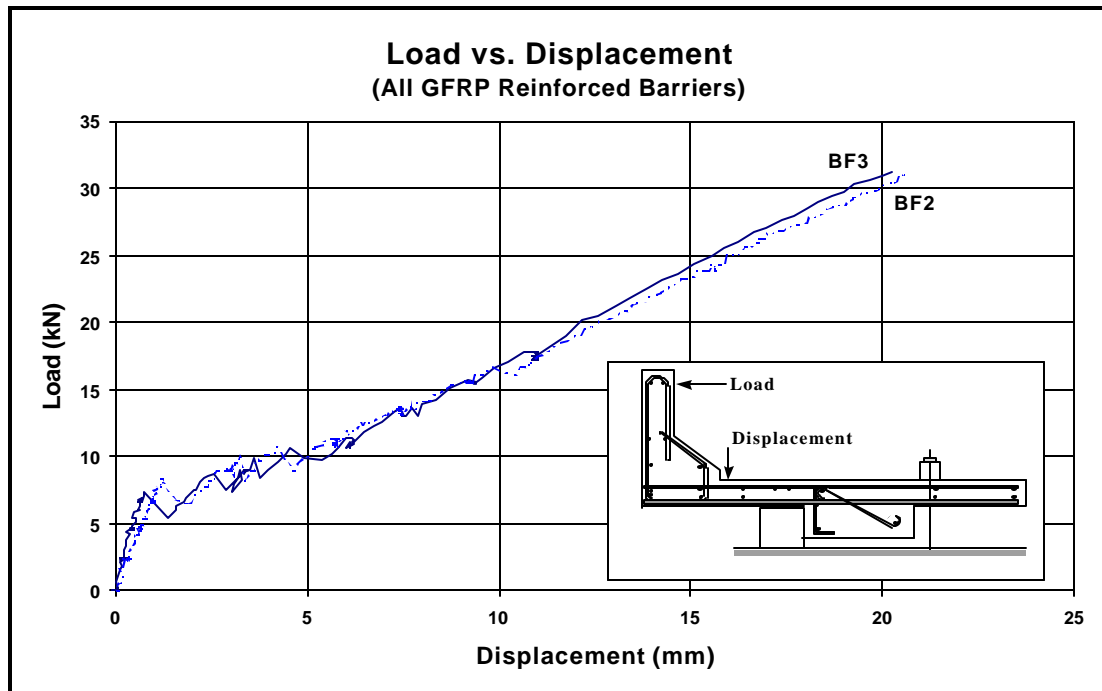


Figure 6. 17: Load versus Vertical Displacement at Toe of Barrier, GFRP Barriers
(Note: Data for Specimen BF1 were accidentally erased and are not shown)

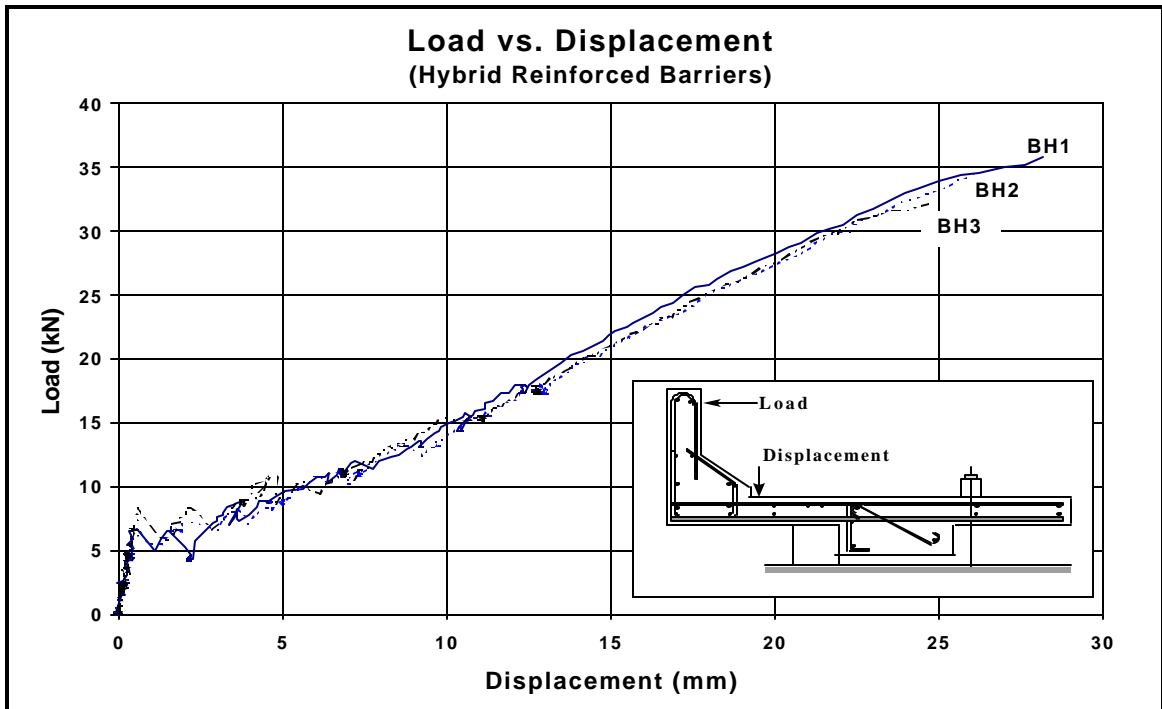


Figure 6. 18: Load versus Vertical Displacement at Toe of Barrier, Hybrid Barriers

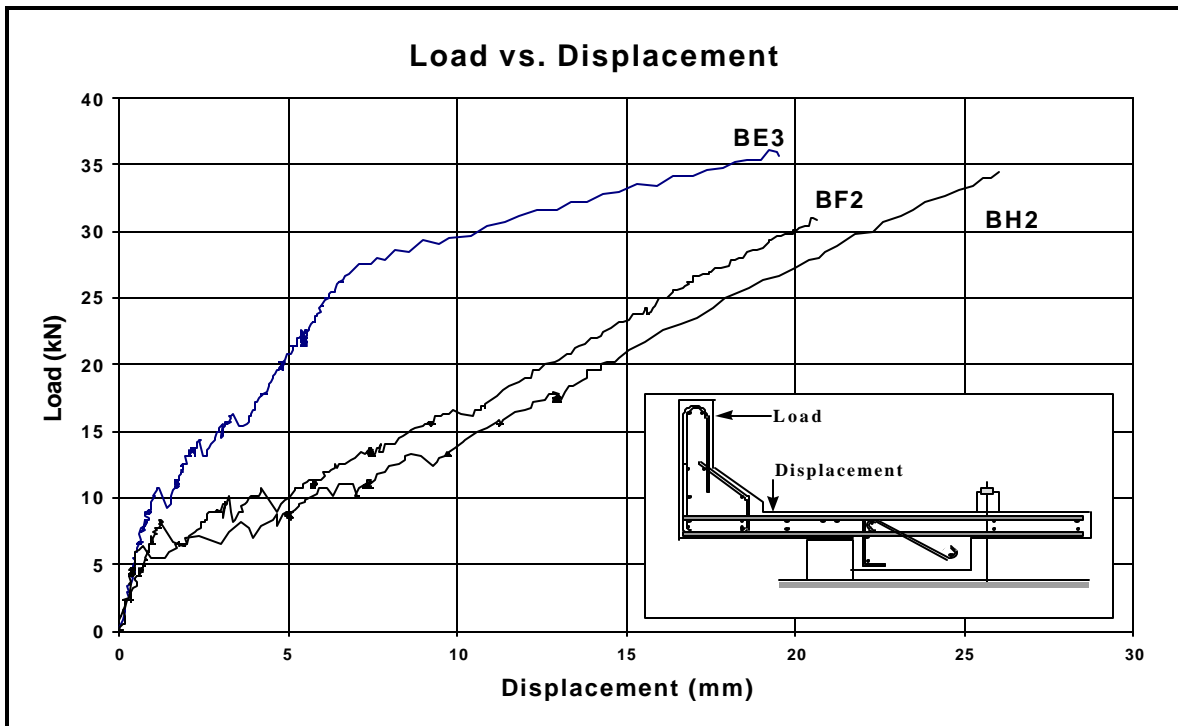


Figure 6. 19: Load versus Vertical Displacement at Toe of Barrier for the ECS, GFRP, and Hybrid Specimens; BE3, BF2, and BH2 Respectively

6.4.3 Load versus Curvature

The third measure of relative stiffness used as a basis of comparison for the barrier wall specimens was the load curvature response between section A-A and the back of the large tube in Figure 6.3. The parameters shown in Figure 6.20 were used to calculate the curvature.

Since the entire section of the deck from the position of the LVDTs to the back of the large square support tube was considered a constant moment region, the flexural strains required to compute curvature can be assumed constant across the section. Displacements measured using LVDT₁ and LVDT₂ in Figure 6.20 were divided by the length from the large tube end to the location of the gages, $L_3 = 735$ mm, converting them into strains. The strains were then used to compute the curvature by subtracting the strain at the top of the barrier deck from the strain at the bottom and dividing by the distance between the gages, $H_1 = 215$ mm. This procedure reduces to the following equation:

$$\phi = \left(\frac{\Delta_3 - \Delta_4}{H_1 \cdot L_3} \right) \quad (6.2)$$

where,

- f = curvature at Section A-A
- Δ_3 = displacement measured with LVDT₃
- Δ_4 = displacement measured with LVDT₄
- L_3 = 735 mm, distance from section A-A to back of square support tube
- L_4 = 215 mm distance from LVDT₃ to LVDT₄

All of these parameters are shown below in Figure 6.20.

Curvature results grouped by specimen type are shown in Figures 6.21 through 6.23. Termination of the curves shown in the figures represents failure of the specimens. All of the specimens of each type show good consistency of behavior. Data for barrier BF1 were accidentally erased, so they are omitted from Figure 6.22.

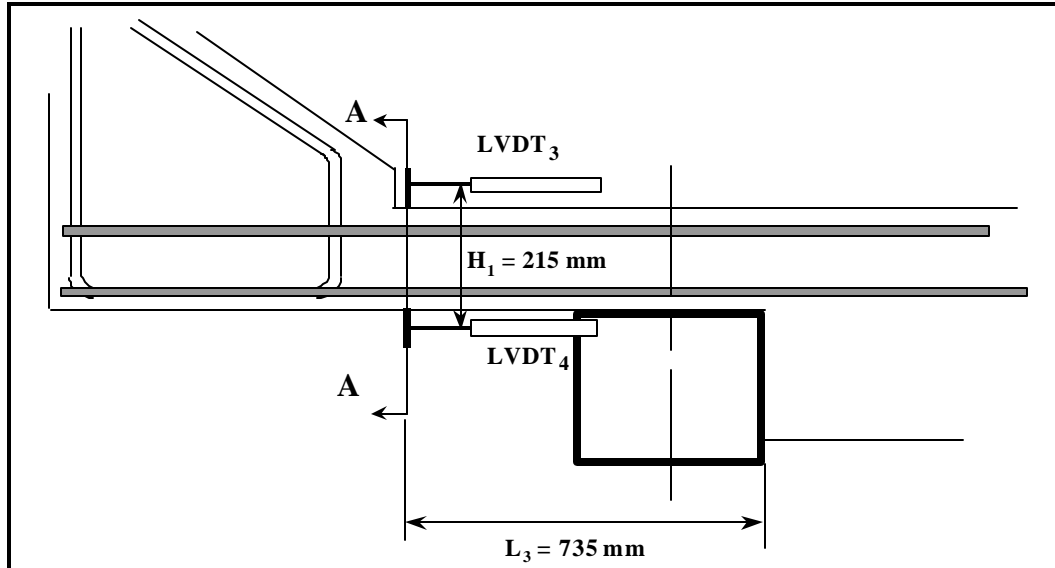


Figure 6. 20: Detail showing Parameters used to Compute Curvature at Section A-A

A comparison of the different barrier wall types is shown in Figure 6.24. Three specimens were selected as characteristic of the different barriers tested, BE3, BF2, and BH2. These represented the ECS, GFRP, and Hybrid deck panels respectively. Until cracking, all of the specimens displayed similar behavior. After cracking, the slope of the BE3 curve was greater than the slopes of curves BF2 and BH2, reflecting greater stiffness. This was due to the larger stiffness of the ECS rebars used in the top mat of the barrier wall specimen compared to the stiffness of the GFRP rebars used in the top mat of the other specimens (see Table 6.1). In addition, the presence of the ECS rebars in the top mat of specimen BE3 produced ductility due to yielding of reinforcement. This is shown in Figure 6.24. Large curvatures exhibited by specimens BF2 and BH2, with GFRP rebars as top mat reinforcement, are due to the low elastic modulus of the GFRP rebars.

The curves for barriers BF2 and BH2 follow approximately the same slope after cracking. This is because both specimens have the same type and location of top mat reinforcement, as described in Table 6.1. The figure shows that the bottom mat reinforcement has little effect on the stiffness of the barrier wall specimens.

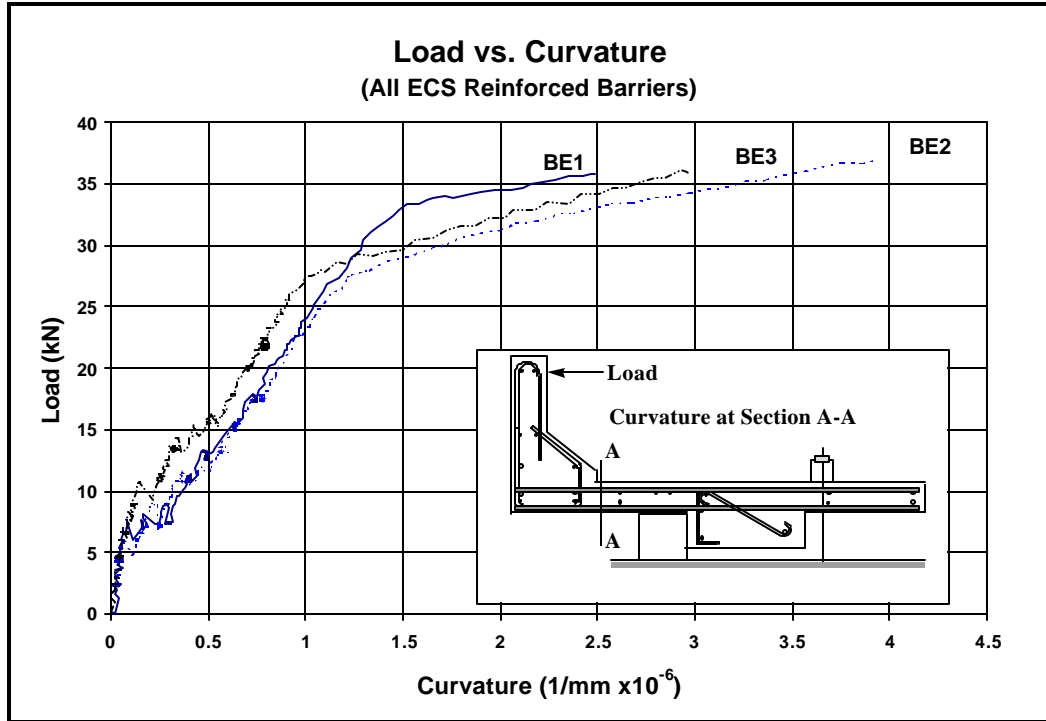


Figure 6. 21: Load versus Curvature of Deck, ECS Barriers

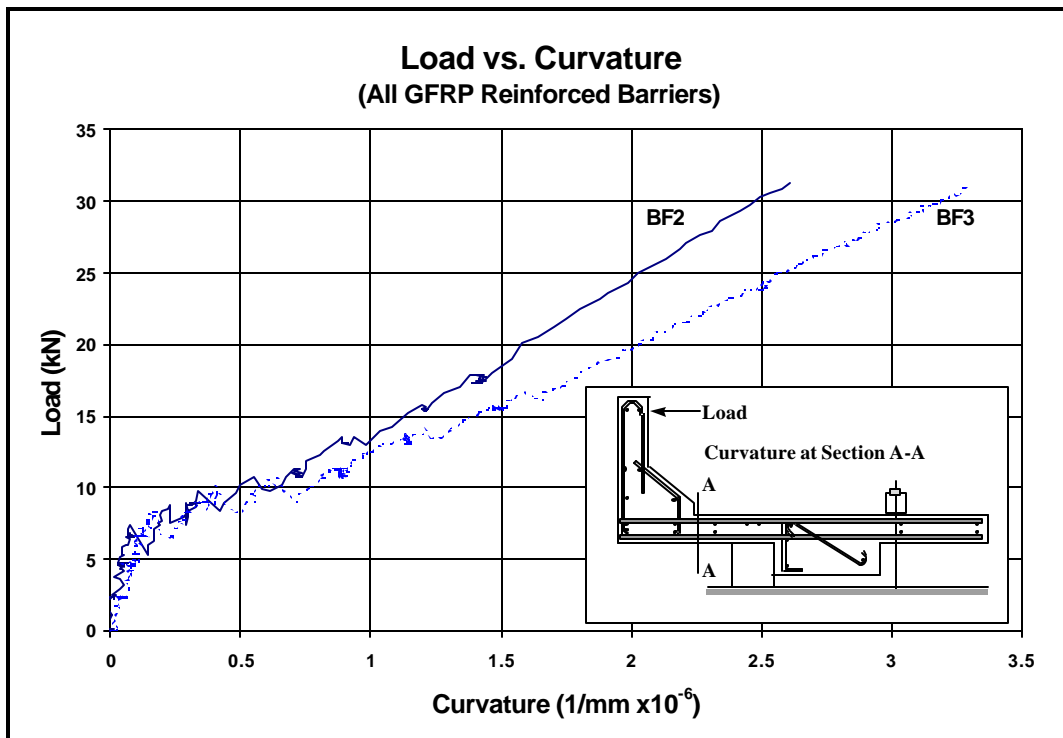


Figure 6. 22: Load versus Curvature of Deck, GFRP Barriers (Note: Data for Specimen BF1 were accidentally erased and is not shown)

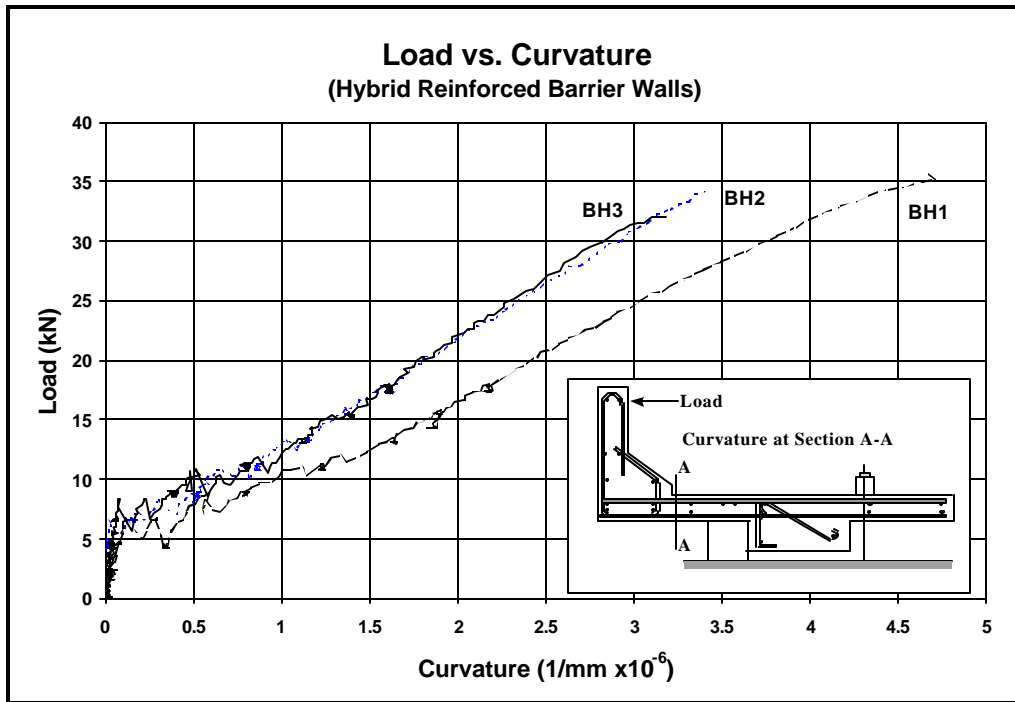


Figure 6. 23: Load versus Curvature of Deck, Hybrid Barriers

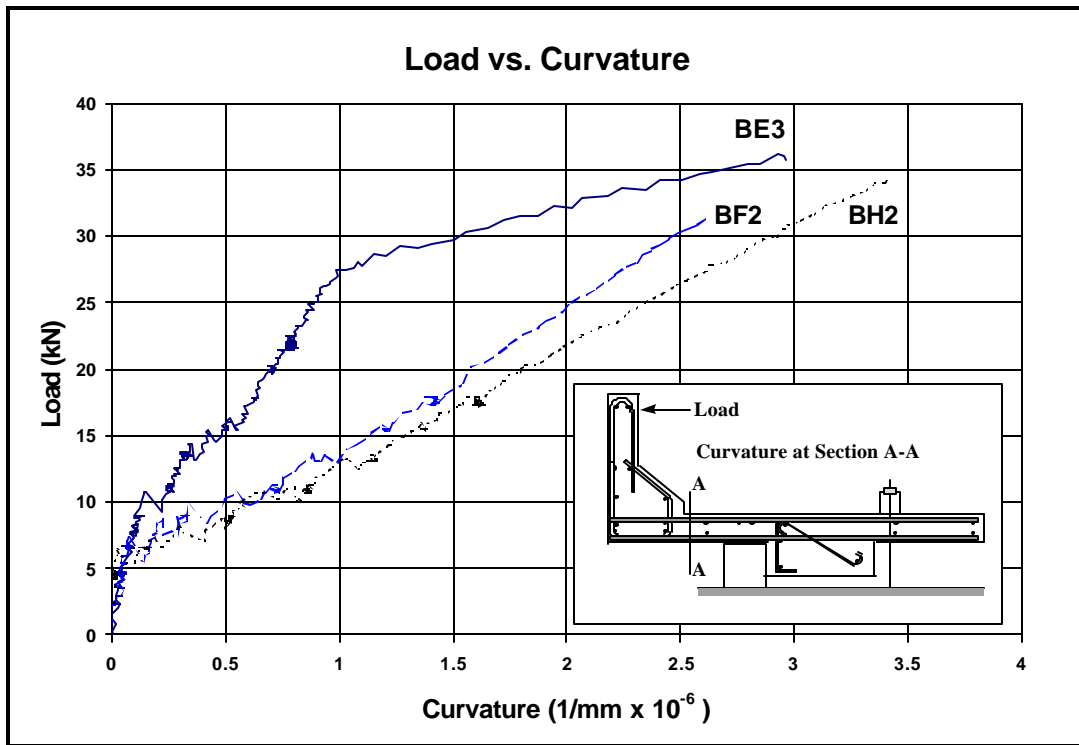


Figure 6. 24: Load versus Curvature of Deck Top for the ECS, GFRP, and Hybrid Specimens; BE3, BF2, and BH2 Respectively

6.5 FAILURE OF BARRIER WALL SPECIMENS

This section compares the ultimate load observed in the specimens to the design loads required by AASHTO specifications. In addition, the different failure modes observed in the tests are discussed.

6.5.1 AASHTO Load Requirements

Provisions for design load requirements are provided in Chapter 2 of the AASHTO (1996) specifications. Article 2.7 stipulates that the bridge barrier wall plan used in the test specimens must resist an unfactored service load of 47 kN, or factored load of 102 kN. AASHTO specifies that the load be distributed over a 1725 mm length of deck, at the gutter line. This reduces to a required unfactored service load of 10.7 kN. Using the AASHTO specified live load factor of 2.17 results in a factored design load of 23.3 kN for the barriers tested.

Only live load is considered in the discussion of barrier wall results because the recorded data was zeroed with the barrier wall specimens under their own weight. As mentioned in Section 6.2.1, the dimensions of the barrier wall specimens were altered from the actual barrier wall of the US-460 bridge deck to provide adequate bearing area and to facilitate form construction. The difference in geometry increased the load on the barrier wall specimens by 0.03 kN/m over the actual bridge deck barrier wall, a 0.04% increase. This was considered negligible and both the barrier wall specimens and the actual barrier wall can be assumed to have the same dead load, which is negligible compared to live load effects.

6.5.2 Ultimate Strength of Barrier Wall Specimens

The main focus of the study was the ability of the bridge decks, reinforced with the three different layouts, to resist required barrier wall impacts. Serviceability concerns were not considered as important as the safety requirements associated with the ability to resist design loads.

Table 6.5 provides a summary of specimen ultimate loads observed during the test. As discussed in the previous section the AASHTO design unfactored service and factored live loads for the specimens were 10.7 kN and 23.3 kN respectively. Every barrier tested exceeded these design loads. Failure modes in Table 6.5 are discussed in Section 6.5.3.

Figures 6.25 and 6.26 show graphical comparisons of experimental ultimate load to the design service and factored loads, respectively. The ratio of experimental ultimate load to design service load was an average of 2.96, 2.55, and 2.79 for the ECS, GFRP, and Hybrid specimens, respectively. This reflects a minimum average safety factor of 2.55 for the specimens. The chart in Figure 6.26 shows the ratio of observed specimen

load compared to factored design load was an average of 1.37, 1.18, and 1.30, for the ECS, GFRP, and Hybrid reinforced specimens. The results show that the capacity of the specimens exceeded the AASHTO design loads in every case.

TABLE 6.5 SUMMARY OF FAILURE LOADS OBSERVED

Type	Label	Reinforcement		Ultimate Load (kN)	Failure Mode
		Bottom Mat	Top Mat		
ECS	BE1	2 #19 ECS	2 #19 ECS	35.74	Anchorage
	BE2	2 #19 ECS	2 #19 ECS	36.93	Anchorage
	BE3	2 #19 ECS	2 #19 ECS	35.71	Anchorage
GFRP	BF1	3 #15 GFRP	3 #15 GFRP	N.A.	Flexure – Tension
	BF2	3 #15 GFRP	3 #15 GFRP	31.3	Flexure- Tension
	BF3	3 #15 GFRP	3 #15 GFRP	30.97	Shear-Tension-Bond
Hybrid	BH1	2 #19 ECS	3 #15 GFRP	35.74	Anchorage
	BH2	2 #19 ECS	3 #15 GFRP	34.45	Anchorage
	BH3	2 #19 ECS	3 #15 GFRP	32.07	Shear-Tension-Bond

6.5.3 Failure Mode

Three different failure modes were observed during the tests. However, all of the modes occurred at similar loads. This is reflected in Figure 6.26 showing ratios of the observed experimental ultimate loads and AASHTO design factored.

All three of the ECS reinforced barriers experienced an anchorage failure under the barrier wall. Figure 6.27 shows a photograph of the anchorage failure. Cracks formed in the deck region below the barrier wall running parallel to and at the location of the deck reinforcement. The crack patterns observed suggest that anchorage failures occurred at both the top and bottom reinforcing mats. In addition, failures of the specimens were ductile in nature, as reflected in the graph showing load versus vertical displacement at the toe of the barrier in Figure 6.17. This provided warning of the impending specimen failure.

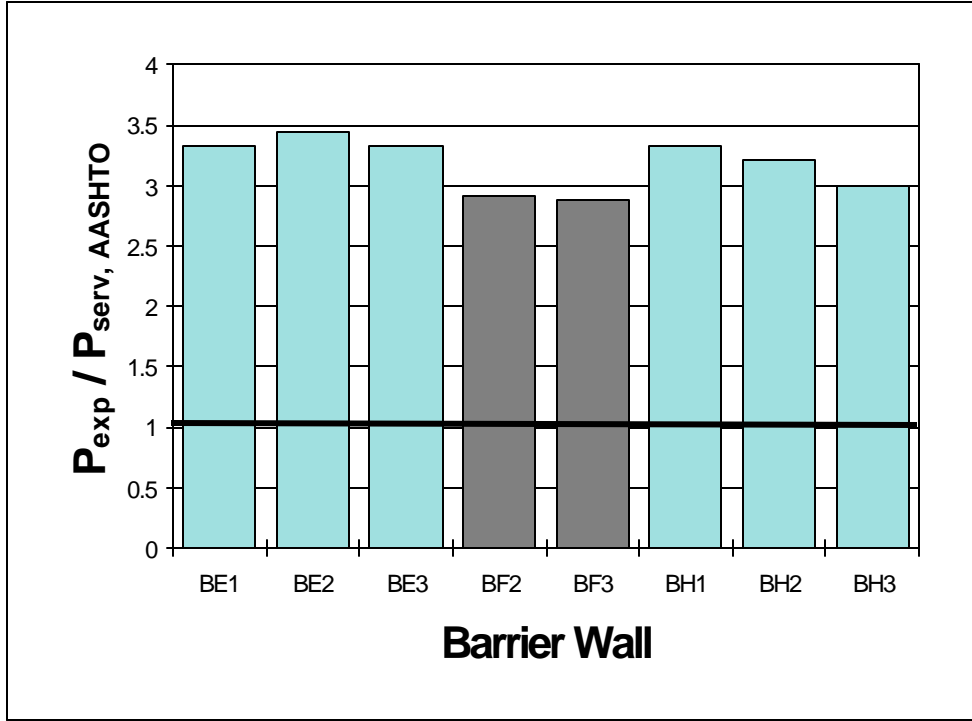


Figure 6. 25: Comparison of Experimental Load Ultimate Load and AASHTO Service Design Load

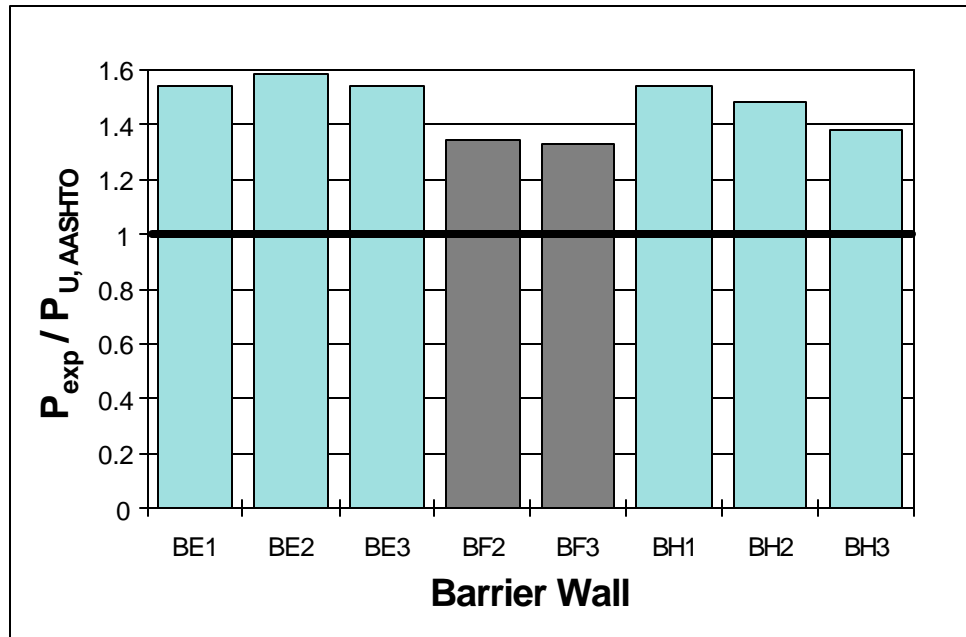


Figure 6. 26: Comparison of Experimental Ultimate Load and AASHTO Factored Design Load

The development length provided in the barrier wall specimens was 460 mm. This was greater than the maximum required AASHTO development length of 400 mm for the three ECS specimens computed assuming a 415 MPa yield strength for the reinforcement. Therefore, by AASHTO specifications, the barrier specimens had adequate development length using the commonly assumed yield strength of 415 MPa. Tests of the ECS reinforcement showed that the actual yield point of the reinforcement was 486.9 MPa. Using this in correlation with AASHTO provisions resulted in a maximum required development length of 480 mm for the ECS specimens, 20 mm more than provided.

Two of the Hybrid specimens, BH1 and BH2, also exhibited an anchorage failure in the deck below the barrier wall similar to the ECS specimens. However, a large diagonal crack in the region behind the large support tube was beginning to form in specimens BH1 and BH2, which was not observed in the ECS specimens. The cracks, similar to that shown in Figure 6.28, apparently formed due to the combined shear, tensile, and bond forces occurring in that region. The final Hybrid specimen, BH3, failed due to the combined forces in the region behind the support tube with the crack pattern shown in Figure 6.28. Despite the difference in failure mechanisms for the specimens, the ultimate loads of the Hybrid reinforced barriers were approximately the same, as shown in Table 6.5. The Hybrid specimen failure was also ductile in nature providing warning of failure in the form of large crack widths and large displacements.

The GFRP reinforced barrier BF3 failed due to the flexural, shear, and bond force combination similar to barrier BH3. Figure 6.28 shows the crack pattern observed in the failure. The remaining two GFRP reinforced specimens, BF1 and BF2, failed between the toe of the barrier wall and the edge of the larger support tube, as shown in Figure 6.29. The failure zone is in the photograph where the concrete piece has been removed. In this region the specimen deck is under a combination of flexural and tensile forces, as graphically illustrated in Figure 6.9.

As mentioned previously, no failure or load displacement data were available for barrier BF1. However, Table 6.5 shows that both of the other GFRP reinforced barriers failed at approximately the same load despite the difference in failure mechanism. As in the Hybrid specimens, ductility was present in the behavior of specimens BF2 and BF3 as shown by large crack widths and large displacements.

Though there was a significant variation in barrier wall specimen concrete strength, the concrete strength had little affect on the ultimate strengths of the deck panels for any specific reinforcing scheme. Differences in the reinforcement types made it difficult to comment on the influence in concrete strengths between different deck panels types. Overall, comparisons of concrete strength to ultimate load or failure mode show no trends in barrier wall behavior.



Figure 6. 27: Crack Pattern of Anchorage Failure beneath the Barrier Wall



Figure 6. 28: Crack Pattern of Combined Shear-Tension-Bond Failure

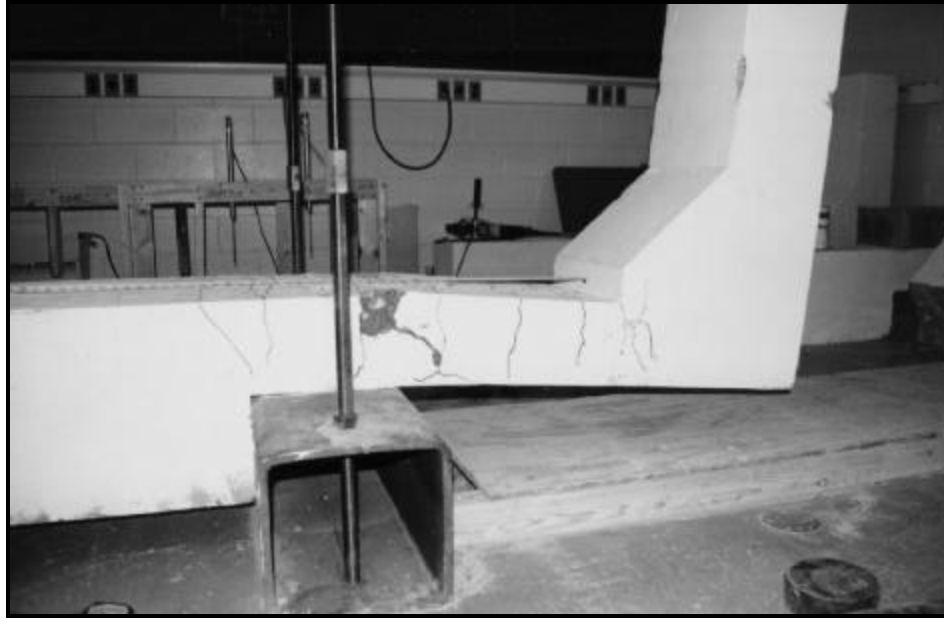


Figure 6. 29: Crack Pattern of Combined Flexural-Tension Failure

6.6 SUMMARY AND CONCLUSIONS

To evaluate the behavior of concrete bridge deck overhangs reinforced with GFRP rebars, nine barrier wall specimens were constructed and tested. The specimens were designed to simulate force conditions in a bridge deck overhang in the event of a vehicle barrier wall impact. Three different deck reinforcing schemes were tested in the study. These included a deck reinforced entirely with ECS rebars, a deck reinforced entirely with GFRP rebars, and a Hybrid deck with a top mat of GFRP rebars and a bottom mat of ECS rebars. Details of the reinforcing types are given in Table 6.1. The objectives of the study included the comparative stiffness, ultimate strength, and failure mode of the specimen types.

The test setup was based on an actual Kentucky bridge deck and designed according to AASHTO specifications.

Measurements were taken to compare the stiffnesses of the barrier walls in three ways: (1) horizontal displacement at the level of load application; (2) vertical displacement at the barrier toe; and (3) curvature of the deck. Results from the three methods showed that all of the specimens exhibited the same behavior up until cracking of the deck. After cracking the ECS reinforced specimens had greater stiffness than either the GFRP and Hybrid reinforced specimens. In addition, the ECS reinforced specimens exhibited an apparent yielding failure not observed in the GFRP or the Hybrid specimens. Both of these results were due to the presence of the ECS rebars in the top mat of the ECS barriers. Both the GFRP and Hybrid specimens had top mats made up of GFRP rebars as shown in Table 6.6. Comparing stiffness results also showed that the

GFRP and Hybrid specimens displayed similar behavior after cracking despite the difference in compression reinforcement of the two specimens.

Table 6.6 shows that all of the specimens met AASHTO load requirements. Ratios of experimental failure to design service load for all the specimens were greater than 2.9 for all the specimens. Similarly, ratios of experimental failure to factored design load for all the specimens were greater than 1.3.

Three different failure modes were observed during the tests. First, an anchorage failure (Figure 6.27) in the deck beneath the barrier wall was observed for all three ECS reinforced specimens and two of the Hybrid reinforced specimens, as summarized in Table 6.6. Results showed that adequate development length based on AASHTO provisions was provided for the #19 ECS rebars assuming a yield point of 415 MPa. However, tests of the rebar showed that the actual yield strength was 486.7 MPa. Using this yield strength with AASHTO specifications for development length showed that the provided development length was 20 mm less than required. Though the specimens did not provide adequate development length in this case, an increase in development length is not recommended since the barrier wall specimens met AASHTO design load specifications prior to failure.

The third hybrid reinforced and one of the GFRP reinforced specimens failed in a region past the support tube simulating the exterior girder (Figure 6.28). In this region the deck was under a combined shear, tension, and bond force combination. The two final GFRP reinforced specimens failed in the deck between the toe of the barrier wall and the support tube simulating the exterior girder (Figure 6.29). This failure was the result of a combined flexural tension load combination.

Despite the variation in failure mode, all nine of the specimens failed at approximately the same ultimate load.

All of the specimens regardless of reinforcement type provided some warning of impending failure. Failure of the ECS reinforced specimens exhibited yielding, with sudden large displacement occurring as the applied load approached ultimate load. The GFRP and hybrid specimens provided warning of failure by large displacements and crack widths.

Based on the experimental results all three proposed reinforcing schemes, e.g. ECS, GFRP, and Hybrid, can be recommended for use in actual bridge decks since they provided adequate resistance in case of a barrier wall impact. Each reinforcing scheme met AASHTO specifications for barrier wall resistance and provided adequate warning of failure with ductile behavior.

TABLE 6.6 SUMMARY TEST RESULTS

Type	Label	Reinforcement		Ultimate Load (kN)	P _{EXP} /P _{AASHTO}		Failure Mode
		Bottom	Top		Service	Factored	
ECS	BE1	ECS	ECS	35.74	3.33	1.54	Anchorage
	BE2	ECS	ECS	36.93	3.44	1.59	Anchorage
	BE3	ECS	ECS	35.71	3.33	1.54	Anchorage
GFRP	BF1	GFRP	GFRP	N. A.	N. A.	N. A.	Flexure - Tension
	BF2	GFRP	GFRP	31.3	2.92	1.34	Flexure- Tension
	BF3	GFRP	GFRP	30.97	2.89	1.33	Shear-Tension-Bond
Hybrid	BH1	ECS	GFRP	35.74	3.33	1.54	Anchorage
	BH2	ECS	GFRP	34.45	3.21	1.48	Anchorage
	BH3	ECS	GFRP	32.07	2.99	1.38	Shear-Tension-Bond

7.0 CONCLUSIONS, RECOMMENDATIONS, AND FUTURE RESEARCH

7.1 OBJECTIVES

The objective of this study is to evaluate the use of glass fiber reinforced polymer (GFRP) rebars in concrete bridge decks. The objective was achieved by conducting the following tasks: (1) Constructability assessment; (2) Laboratory testing of GFRP rebars to determine their material properties; (3) Laboratory testing of concrete deck panels and barrier walls reinforced with GFRP and/or epoxy coated steel to evaluate the behavior and compliancy with the AASHTO and ACI Codes; and (4) Deployment of the GFRP rebars in a portion of the top reinforcing mat in the Roger's Creek deck.

7.2 SUMMARY OF RESEARCH FINDINGS

7.2.1 Constructability Assessment

The constructability assessment phase of the research project proved that GFRP rebars can withstand bridge deck construction with very few changes from conventional construction techniques. In addition, results show that GFRP rebar mats can support construction loads.

Recommendations based on the research findings include the use of ECS chairs and plastic coated steel wire ties with GFRP rebars. It is estimated that approximately twice as many ECS chairs will be required to achieve adequate mat stiffness in a GFRP rebar mat.

No floatation of the reinforcing mat was observed during the constructability assessment; however, this problem could be encountered during placement of high slump concrete. To avoid floatation, the GFRP reinforcing mat could be tied to the concrete forms.

In case repairs on a deck are needed (e.g. potholes), the use of a jackhammer was identified as a viable method for removing concrete from a GFRP reinforced bridge deck during repair operations. Hydro-demolition was also considered as a repair procedure but was found to damage the GFRP rebars during the concrete removal process. Therefore, it should not be considered for removal of deteriorated concrete reinforced with GFRP rebars.

7.2.2 Rebar Material Properties

Standard methods are not available for determining the compression elastic modulus and compression strength of GFRP rebars. A method was developed to experimentally determine these parameters. Based on the test results of more than 50

GFRP rebar specimens in compression, an ultimate compression strength versus unbraced length design curve is proposed. Test results also show that the compression modulus of elasticity is approximately the same as the tensile modulus of elasticity for the GFRP rebars used in the study. However, for design, the compression strength of the GFRP rebars should be 50% of the tension strength.

7.2.3 Testing of Bridge Deck Panels

Twelve full-scale reinforced concrete deck panels were tested to simulate transverse bridge deck load conditions. Three different reinforcing schemes were evaluated in the study: (1) an ECS reinforcing scheme with a top and bottom mat of ECS rebars, (2) a GFRP reinforcing scheme with a top and bottom mat of GFRP rebars, and (3) a Hybrid reinforcing scheme with a top mat of GFRP rebars and a bottom mat of ECS rebars.

Results show that the ultimate load, load versus displacement at service levels (i.e. prior to yielding), moment versus maximum concrete compression strain, and deck panel failure mode were governed by the type of tensile reinforcement. The type of compression reinforcement had little effect on these parameters. Compression reinforcement did have a limited effect on the ductility of the deck panels with ECS tension reinforcement and the maximum observed crack widths.

Observations show that all twelve deck panels exhibited the same load versus displacement and moment versus strain characteristics prior to cracking. After cracking, the deck panels with ECS tension reinforcement exhibited significantly greater stiffness and smaller crack widths than the deck panels with GFRP tensile reinforcement.

All of the deck panels with ECS tension reinforcement failed in a flexural mode. The failure mode exhibited ductility and provided adequate warning of failure through apparent yielding of the reinforcement. All deck panels with GFRP reinforcement collapsed in a combined flexure and shear failure mode. The failure of these deck panels was ductile, and provided warning of impending collapse with large crack widths and displacements.

7.2.3.1 Comparison with AASHTO Specifications

Comparisons of the deck panel results to current AASHTO provisions for bridge deck design show that all of the deck panels met AASHTO guidelines for ultimate load. However, AASHTO specifications are based on under-reinforced concrete specimens with steel reinforcement, failing after yielding of the reinforcing steel. Since GFRP specimens do not exhibit yielding, and in this study failed in shear, it is recommended that specifications be broadened to include a shear failure mode.

ACI-318M-95 design specifications accurately predicted the failure load of the ECS reinforced deck panels, which failed in flexure. However, neither current ACI provisions nor a model developed by other researchers adequately predicted the combined shear and flexural failure strength of the GFRP reinforced deck panels. Two equations for predicting the shear strength of the specimens are proposed in this study.

Experimental maximum crack widths were compared to theoretical models developed by others, and the result show that these models adequately predicted crack widths for the GFRP reinforced deck panel with a span length of 2130 mm. However, these models did not predict crack widths for the deck panels with the longer span length of 2740 mm. A maximum crack width model based on the results of this study is proposed based on the Gergely-Lutz expression.

7.2.4 Barrier Wall Impact Simulation

In addition to the deck panel specimens, nine barrier wall specimens were constructed and tested to evaluate the behavior of concrete bridge deck overhangs with the three different reinforcing schemes discussed in Section 7.1.3. Results show that all of the specimens met AASHTO load specifications. In addition, all of the specimens exhibited a ductile failure type that provided adequate warning of the impending failure. The ECS reinforced specimens exhibited ductility through apparent reinforcement yielding, large displacements, and large crack widths, while the GFRP reinforced deck panels exhibited ductility through large displacements and crack widths.

7.3 RECOMMENDED REINFORCING SCHEME

Results of this study show that both the GFRP and Hybrid deck panel reinforcing schemes meet all AASHTO load requirements. Either of these reinforcing schemes can be depended on from a strength standpoint. However, the results also show that the GFRP and Hybrid deck panels did not meet AASHTO requirements for maximum crack widths. In addition, though AASHTO does not specify maximum displacements for concrete bridge decks, the displacements observed for the GFRP and Hybrid deck panels were significantly greater than those of the ECS reinforced deck panels and warrant consideration.

The Hybrid reinforcing scheme is recommended for use in bridge decks even though it did not meet serviceability requirements. This reinforcing scheme provides the dependability of ECS rebars with the corrosion immunity of the GFRP rebars. Since reinforced concrete bridge decks transfer load transversely over main support girders as a continuous beam, ECS rebars in the bottom of the bridge deck will decrease the deflection of the deck under loading observed in this study. In addition, crack width limitations for the top reinforcing mat could be increased for GFRP reinforced deck panels due to their immunity from corrosion.

REFERENCES

- AASHTO (1996). *Standard Specifications for Highway Bridges, 16th Edition*. American Association of State Highway and Transportation Officials, Washington, D.C.
- Alysayed, S., Almusallam T., Al-Salloum, and Amjad, M. (1995). "Flexural Behavior of Concrete Elements Reinforced by GFRP Bars." *Non-Metallic (FRP) Reinforcement for Concrete Structures*. E & FN Spon, London England.
- American Concrete Institute (ACI) (1995). *Building Code Requirements for Reinforced Concrete and Commentary ACI 318M/318RM-95*. Detroit, Michigan.
- Anderson, R., Bank, L., and Munley, E. (1994). "Durability of Concrete Reinforced with Pultruded Fiber Reinforced Plastic Grating." *Composites Institute 49th Annual Conference*. The Society of the Plastics Industry.
- Bank, L., Frostig, Y., and Shapira, A. (1997). "Three-Dimensional Fiber-Reinforced Plastic Grating Cages for Concrete Beams: A Pilot Study." *ACI Structural Journal*. 94(6).
- Benmokrane, B., Masmoudi, R. (1996). "Tensile Properties of Deformed FRP C-BAR Reinforcing Rod." *Technical Report No. 1*, Submitted to Marshall Industries, Lima, OH.
- Benmokrane, B., Chaallal, O., and Masmoudi, R. (1996). "Flexural Response of Concrete Beams Reinforced with FRP Reinforcing Bars." *ACI Structural Journal*. 91(2).
- Benmokrane, B., Tighiouart B., and Chaallal, O. (1996). "Bond Strength and Load Distribution of Composite GFRP Reinforcing Bars in Concrete." *ACI Materials Journal*. 93(3).
- Bridge Design Guidance Manual* (1997). Kentucky Transportation Cabinet. Frankfort, KY.
- Brown, V. and Bartholomew, C. (1996). "Long-Term Deflections of GFRP-Reinforced Concrete Beams." *Fiber Composites in Infrastructure, Proc. of the First International Conference on Composites in Infrastructure*. Tucson, AZ.
- Burke, D. (1994). "Performance of Epoxy-Coated Rebar, Galvanized Rebar, and Plain Rebar with Calcium Nitrite in a Marine Environment." *CSRI Research Series-2*. Concrete Reinforcing Steel Institute, Schaumburg, IL.
- Castro, P., and Carino, N. (1998). "Tensile and Nondestructive Testing FRP Bars." *Journal of Composites for Construction*." 2(1).

Cosenza, E., Manfredi, G., and Realfonzo, R. (1997). "Behavior and Modeling of Bond of FRP Rebars to Concrete." *Journal of Composites for Construction*. 1(2).

Deitz, D. H. (1995). *Parametric Study of Prestressed Concrete Box Beam Bridges*. Masters Thesis, University of Cincinnati, Cincinnati, Ohio.

Faza, S. and GangaRao, H. (1991). "Bending and Bond Behavior of Concrete Beams Reinforced with Plastic Rebars." *Transportation Research Record Number 1290*. Transportation Research Board, Washington, D.C.

Fraczek, J. (1987). "A Review of Electrochemical Principles as Applied to Corrosion of Steel in a Concrete or Grout Environment." *Corrosion, Concrete, and Chlorides: Steel Corrosion in Concrete: Causes and Restraints*, ACI SP-102, American Concrete Institute, Detroit, MI.

Galvanized Rebar Advisory Board (1995). "Galvanized Reinforcing Bar... The Rebar that Sticks to the Job on Highways and Bridges." Washington, D.C.

GangaRao, H, and Faza, S. (1991). "Bending and Bond Behavior and Design of Concrete Beams Reinforced with Fiber Reinforced Plastic Rebars." *Technical Report Submitted to the FHWA, WVDOH, International Grating, Inc., and Vega Technologies, Inc.* West Virginia Constructed Facilities Center, Morgantown, WV.

Gergely, P. and Lutz, L. (1968). "Maximum Crack Width in Reinforced Concrete Flexural Members." *Causes, Mechanism, and Control of Cracking in Concrete*, SP-20, American Concrete Institute, Detroit.

Hartle, R., Amrhein, W., Wilson, K., Baughman, D., and Tkacs, J. (1990). *Bridge Inspectors Training Manual*. FHWA-PD-91-015. McLean, VA.

Hasan, H., Ramirez, J., and Cleary, D. (1995). "Field Evaluation of Concrete Bridge Decks Reinforced with Epoxy-Coated Steel in Indiana." *Transportation Research Record 1476*. Transportation Research Board, Washington, D.C.

"Interim Recommendations for Specifying Soft Metric Reinforcing Bars." (1995). CRSI, Concrete Reinforcing Steel Institute, Schaumburg, IL.

Kanakubo, T., Yonemaru, K., Fukuyama, H., Fujisawa, M., and Sonobe, Y. (1993). "Bond Performance of Concrete Members Reinforced with FRP Bars." *Fiber Reinforced Plastic Reinforcement for Concrete Structures, International Symposium*. American Concrete Institute SP 138-46, Detroit Michigan.

Kent D. and Park R. (1971). "Flexural Members with Confined Concrete." *Journal of the Structural Division, Proceedings of the American Society of Civil Engineers*. 97(ST7).

- Kobayashi, K., and Fujisaki, T. (1995). "Compressive Behavior of FRP Reinforcement in Non-Prestressed Concrete Members." *Non-Metallic (FRP) Reinforcement for Concrete Structures*. E & FN Spon, London England.
- Kumar, S. (1996). Telephone communication regarding methods of gripping GFRP rebars during tensile tests. West Virginia Constructed Facilities Center, Morgantown, WV.
- Loud, S. (1995). "Rebar: Steel Vs. Composites." *Composites Technology*". May/June.
- MacGregor, J. (1992). *Reinforced Concrete Mechanics and Design*. Prentice Hall, Saddle River, NJ.
- Malvar, J. (1995). "Tensile and Bond Properties of GFRP Reinforcing Bars." *ACI Materials Journal*. 92(3).
- Masmoudi, R., Benmokrane, and Chaallal, O. (1996). "Cracking Behavior of Concrete Beams Reinforced with Fiber Reinforced Plastic Rebars." *Canadian Journal of Civil Engineering*, 23, 1172-1179.
- Masmoudi, R., Theriault, M., and Benmokrane, B. (1996). "Flexural Behavior of Concrete Reinforced with FRP C-BAR Reinforcing Rod." *Technical Report No. 2*, Submitted to Marshall Industries, Lima, OH.
- Matkitai, E., Irisawa, I., and Nishiura, N. (1992). "Investigation of Bond in Concrete Member with Fiber Reinforced Plastic Bars." *Fiber Reinforced Plastic Reinforcement for Concrete Structures, International Symposium*. American Concrete Institute SP 138-46, Detroit Michigan.
- McDonald, D., Virmani, Y., and Pfeifer, D. (1996). "Testing the Performance of Copper-Clad Reinforcing Bars." *Concrete International*, 18(9).
- Michaluk, C. (1996). *Flexural Behavior of One Way Concrete Slabs Reinforced by Glass Fibre Reinforced Plastic Bars*. Masters Thesis, University of Manitoba, Winnipeg, Manitoba, Canada.
- Michaluk, C., Rizcalla, S., Tadros, G., Benmokrane, B. (1998). "Flexural Behavior of One-Way Concrete Slabs Reinforced by Fiber Reinforced Plastic Reinforcements." *ACI Structural Journal*. 95(3).
- Microsoft FORTRAN PowerStation (1993). User's Guide, Microsoft Corporation, Redmond, Washington.

Nanni, A. (1993). "Flexural Behavior and Design of RC Members using FRP Reinforcement." *ASCE, Journal of Structural Engineering*. 119(11).

Nawy, E. (1996). *Reinforced Concrete A Fundamental Approach*. Prentice Hall, Inc., Upper Saddle River New Jersey.

Purvis, R., Khossrow, B., Clear, K., and Markow, M. (1994). "Life-Cycle Cost Analysis for Protection and Rehabilitation of Concrete Bridges Relative to Reinforcement Corrosion." *Strategic Highway Research Program, SHRP-S-377*, National Research Council, Washington, D.C.

Standard Specifications for Road and Bridge Construction. (1998). Kentucky Transportation Cabinet, Frankfort, KY.

Theriault, M. and Benmokrane, B. (1998). "Effects of FRP Reinforcement Ratio and Concrete Strength on Flexural Behavior of Concrete Beams." *Journal of Composites for Construction*, 2(1).

Thippeswamy, H., Franco, J., and GangaRao, H. (1998). "FRP Reinforcement in Bridge Deck." *Concrete International*. 20(6).

Treece, R., and Jirsa, J. (1989). "Bond Strength of Epoxy-Coated Reinforcing Bars." *ACI Materials Journal*. 86(2).

West Virginia Department of Transportation Division of Highways (1994). "Evaluation of Bridge Decks Using Epoxy Coated Reinforcement. *CRSI Research Series-1*. Concrete Reinforcing Steel Institute, Schaumburg, IL.

Weyers, R. Prowell, B., Sprinkel, M., and Vorster, M. (1993). "Concrete Bridge Protection, Repair, and Rehabilitation Relative to Reinforcement Corrosion: A Methods Application Manual." *Strategic Highway Research Council, SHRP-S-360*. National research Council, Washington, D.C.